# Interactions of Quinoline Antimalarial Drugs with Ferrihaem: Structural and Kinetic Insights into the Inhibition of Malaria Pigment Formation

by
Johandie Gildenhuys

Dissertation presented for the degree of *Doctor of Science in the Faculty of Chemistry and Polymer Science at Stellenbosch University*
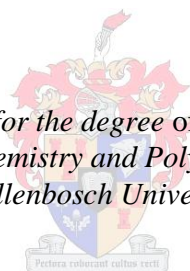
Supervisor: Dr Katherine de Villiers-Chen
Co-supervisor: Dr Tanya le Roex

December 2013

Declaration

By submitting this dissertation electronically, I, Johandie (Kaliefie) Gildenhuys, declare that the entirety of the work contained therein is my own, original work, that I am sole author thereof (save to the extent explicitly otherwise stated), that reproduction and publication thereof by Stellenbosch University will not infringe any third party rights and that I have not previously in its entirety or in part submitted it for obtaining any qualification.

December 2013

Abstract

The work in this dissertation provides structural and kinetic insight into the mechanism of action of quinoline antimalarial drugs which may aid rational drug design. Quinoline antimalarial drug-ferrihaem (Fe(III)PPIX) complexes were investigated. Single crystal X-ray diffraction (SCD) structures of the complexes formed between Fe(III)PPIX and the quinoline methanol antimalarials quinine, quinidine and mefloquine have been determined, and are the first observed structures of complexes formed between free Fe(III)PPIX and quinoline antimalarial compounds. Quinine, quinidine and mefloquine are shown to have a three-point binding mode to Fe(III)PPIX, which comprises direct coordination of the drug to the Fe(III) centre through its benzylic alcohol functionality, π-stacking between the drug and porphyrin aromatic systems, and intramolecular hydrogen bond formation between the porphyrin propionate group and the protonated quinuclidine nitrogen atom of the drug in the case of quinine and quinidine, and formation of an intramolecular hydrogen bonding network in the case of mefloquine. Extended X-ray absorption fine structure spectroscopy (EXAFS) was use to elucidate structural information of Fe(III)PPIX-drug complexes in solution, and indicates that coordination persists in solution.

The protocol for lipid-mediated formation of β-haematin, where monopalmitic glycerol was used as a model lipid, was successfully modified to incorporate antimalarial drugs into the aqueous layer in order to investigate drug activity under biologically-relevant conditions. Four compounds were chosen, namely chloroquine and amodiaquine, both 4-aminoquinolines and quinine and quinidine. IC_{50} values for the inhibition of β-haematin formation show good correlation with biological activities determined against a chloroquine-sensitive *Plasmodium falciparum* strain. The lipid-water interface system was further used to investigate the effects of quinine, quinidine chloroquine and amodiaquine on the kinetics of β-haematin formation. The results led to the development of a kinetic model based on the Avrami equation and the Langmuir isotherm. The data strongly support a mechanism of antimalarial drug action by adsorption to the growing face of haemozoin, with precipitation of Fe(III)PPIX at high drug concentrations accounting for decreased yields. Adsorptions constants (log K_{ads}) determined for each drug show a strong correlation with biological activity. Finally, the first SCD structure of the μ-propionato dimer of Fe(III)PPIX, the structural unit of haemozoin, has been determined as its DMSO solvate. EXAFS suggests that this species is only formed upon nucleation, with the π-π dimer species being favoured in solution.

Opsomming

Die werk in die dissertasie verleen struktuur en kinetiese insig in the meganisme van aktiwiteit vir kinolien antimalariamiddels wat kan bydra tot die ontwikkeling van nuwe medisyne. Kinolien antimalariamiddel-ferriheem (Fe(III)PPIX) komplekse was ondersoek. Navorsing is gedoen op die enkelkristal X-straaldiffraksie strukture van die komplekse gevorm tussen Fe(III)PPIX en die kinolien metanol antimalaria middels kinien, kinidien en mefloquine. Die strukture is die eerste komplekse wat waargeneem is tussen vrye Fe(III)PPIX en kinolien antimalariamiddels. Kinien, kinidien en mefloquine het 'n drie-punt bindingsvorm, direkte koördinasie met die Fe(III) deur die bensielalkohol groep, 'n π-stapel tussen die middel en die porfirien aromatiese sisteem, 'n intramolekulêre waterstofbinding tussen the porfirienpropionaat funksie en die geprotoneerde kinuklidien stikstofatoom (kinien en kinidien) en 'n netwerk van intramolekulêre waterstof bindings (mefloquine) insluit. Uitgebreide X-straal absorpsie fyn struktuur spektroskopie (EXAFS) is gebruik om inligting oor Fe(III)PPIX-middel komplekse in oplossing te verkry en het aangedui dat die koördinasie in oplossing voorkom.

Deur gebruik te maak van monopalmitiengliserol as die lipid in the lipid-water interfase sisteem, waar antimalariamiddels suksesvol in die buffer geïnkorporeer was, was die middel se aktiwiteit onder biologiese kondisies geondersoek. Vier middels was gekies naamlik, chloroquine en amodiaquine, albei 4-aminokinoliene en kinien en kinidien om die IC_{50}-waarde vir inhibisie van β-hematien vorming te bepaal. Die IC_{50} waardes het 'n goeie korrelasie met biologiese aktiwiteite teen die chloroquine-sensitiewe *Plasmodium falciparum* stam gewys. Die lipid-water interfase-sisteem was ook gebruik om die effek van kinien, kinidien, chloroquine en amodiaquine op die kineties effek op die vorming van β-hematien te ondersoek. Die resultate het gelei to die ontwikkeling van die kinetiese model gebaseer op die Avrami vergelyking en die Langmuir isoterm. Die data ondersteun 'n meganisme van middel aksie waar die middel teen die groeiende vlak van hemosoïen kristal adsorbeer. Die neerslag van Fe(III)PPIX wat vorm by hoë konsentrasies, het gelei tot laer opbrengste. Die adsorpsiekonstante (log K_{ads}) bepaal vir elke middel, het goeie korrelasie met biologiese aktiwiteit getoon. Enkelkristal X-straaldiffraksie strukture van μ-propionatodimeer van Fe(III)PPIX, die struktuur eenheid van hemosoïen, was bepaal as 'n DMSO solvaat. EXAFS het aangedui dat die spesie slegs by kernvorming ontstaan en dat die π-π dimeerspesie in oplossing voorkom.

Dedication

To my Family

Michael

Karin

Kaboelie

Kazibi

Kabelo

"A scientist in his laboratory is not a mere technician: he is also a child confronting

natural phenomena that impress him as though they were fairy tales."

-Marie Curie-

Acknowledgements

- First and foremost, I would like to thank my supervisor Dr Katherine de Villiers-Chen for being an exceptional mentor. Your positive outlook, kind words and passion for chemistry has been inspiring. Thank you for your guidance, endless support and encouragement throughout the years. I have grown so much and feel very privileged to have worked with you.

- My co-supervisor Dr Tanya le Roex, thank you so much for your input and guidance in the field of crystallography and for contributing to my growth as a scientist.

- When one is sometimes sitting in the box it's difficult to look in from the outside, therefore I would like to thank Professor Tim Egan from the University of Cape Town for his input on several aspects of this work.

- Dr Victor Streltsov (CSIRO Materials Science and Engineering, Melbourne, Australia) for introducing me to the synchrotron and helping me collect and interpret the data of the EXAFS experiments.

- I would like to thank Dr Vincent Smith for his patience with me on the X-ray diffraction machine.

- Me Peta Steyn for always allowing me to use the UV-vis spectrophotometer.

- The technical staff of the de Beers building for their assistance.

- Debbie Isaacs for always maintaining a friendly working environment.

- To the friends in the de Beers building I made through the years, thank you for making research fun and a pleasant "home" to come to.

- Life as a student would have been very difficult without the love and support from my family, Michael, Karin, Kaboelie, Kazibi, Kabelo, Alexis and Ouma Doepie. Thank you for loving me. You know I would be lost without you and I thank God for you every day.

- The National Research Foundation for financial support throughout my post-graduate studies and also the Chemistry Department at Stellenbosch University.

- Hannes for making my last few weeks at Stellenbosch magical.

- My   Heavenly   Father   for   giving   met   the   ability   to   complete   this.

Publications and Conference Proceedings

Publications:

1. de Villiers, K. A., <u>Gildenhuys, J.</u> and le Roex T., Iron(III) Protoporphyrin IX Complexes of the Antimalarial *Cinchona* Alkaloids Quinine and Quinidine, *Acs Chem. Biol*. **2012**, 7, 666-671.

2. <u>Gildenhuys, J.</u>, le Roex, T., Egan, T. J. and de Villiers, K. A., The Single Crystal X-ray Structure of β-Haematin DMSO Solvate Grown in the Presence of Chloroquine, a β-Haematin Growth-Rate Inhibitor, *J. Am. Chem. Soc*., **2013**, 135, 1037-1047.

Conference Proceedings:

1. ICBIC 15, **2011**, Vancouver, Canada

   Poster: <u>Johandie Gildenhuys</u>, Katherine A. de Villiers and Tanya le Roex, Insight into the Mode of Action of Quinoline Antimalarial Drugs: The Crystal Structure of Quinidine-ferriprotoporphyrin.

2. SACI Young Chemists' Meeting, **2011**, UWC, RSA

   Oral: <u>Johandie Gildenhuys</u>, Katherine A. de Villiers and Tanya le Roex, Iron(III) Protoporphyrin IX Complexes of the Antimalarial *Cinchona* Alkaloids Quinine and Quinidine.

3. SACI Inorganic Chemistry Conference, **2013**, Durban, RSA

   Poster: <u>Johandie Gildenhuys</u>, Victor A. Streltsov and Katherine A. de Villiers, An EXAFS Investigation of Iron(III) Protoporphyrin IX Species and their Complexes with Antimalarial Drugs.

Table of Contents

1 Literature Review

1.1 Introduction

Malaria, a mosquito-borne infectious disease, has cursed humanity from its primate ancestry until the present, affecting the daily lives of millions of people around the globe.[1] Based on data presented in the World Malaria Report (2011), it is clear that malaria has no boundaries. Half of the world's population remains at risk, and the disease is having dramatic effects, cutting economic growth rates and taking the lives of 0.5 - 1 million people annually - young children and pregnant women living in sub-Saharan Africa are most at risk.[2] Malaria is a significant global health problem, and the reality is that parasitic resistance towards the majority of quinoline - containing antimalarial drugs - most notably chloroquine (CQ), is increasing.[2] This means that there is an urgent need to develop new, effective, and inexpensive antimalarial drugs. In order to achieve this goal, a better understanding of the molecular mechanisms of action of current antimalarial drugs is imperative.[3]

1.2 Malaria History and Discovery

The word malaria arises from the Italian translation of bad air, "mal'aria", due to the believed connection between the disease and marshes. Writings corresponding to malaria symptoms date back 4000 years, thus it is evident that this disease has influenced the lives of human populations for centuries.[4] Today the symptoms of chills, headaches and periodic fever are recognised and connected to malaria infection.

The characteristic brown-black pigment observed in the blood of victims suffering from malaria was first reported in 1717 by the noted Italian physician Giovanni Maria Lancisi.[5] In 1880, with the research done by French army doctor Charles Louis Alphones Laveran, the parasite itself was observed within the red blood cells of soldiers suffering from malaria.[6] Seventeen years later, in 1897, Sir Ronald Ross made the connection that the vector for the malaria parasite was the mosquito.[7] In the same year, the Italian physician Giovanni Battista Grassi proved that the *Anopheles* mosquito was the vector for human malaria, and Robert Koch showed that quinine could be used effectively against the malaria parasite.[1] A cure for malaria, quinine, was discovered more than 300 years ago, up in the mountains of the Andes in South America, where it was extracted from the bark of

the *Cinchona* tree.[1] In addition, the antifever properties of the Qinghao plants were described in 340 BC, and the antimalarial endoperoxide drug artemisinin was isolated from this plant in 1971.[8]

1.3   Lifecycle of the Malaria Parasite

Malaria in humans is caused by parasites of the genus *Plasmodium,* of which 5 species (*P. falciparum, P. malariae, P. ovale, P. vivax and P. knowlesi*) are known. *P. falciparum* is the most virulent species, and is responsible for 90% of malaria deaths.[1]

The lifecycle of the malaria parasite is complex (Figure 1.1).[9] When the female *Anopheles* mosquito (primary host) takes a blood meal from an infected human (secondary host), it ingests gametocytes, which undergo sexual reproduction in the mosquito gut to mature sex cells called gametes. Fused male and female gametes (zygotes) develop further to form ookinetes, and later oocysts in the midgut wall. The oocysts grow and burst releasing sporozoites into the body cavity of the mosquito, which then travel and invade the mosquito salivary glands. Transmission occurs when the infected female mosquito injects the parasite, in the form of sporozoites, into the uninfected human host while taking a blood meal in order to develop her eggs. [10]

As the sporozoites enter the blood stream, they travel to and invade the liver cells first; here they may remain dormant for an extended period of time, and often this is the cause of relapses months and even years after initial infection. The time spent in the liver allows the sporozoites to multiply into merozoites.[10] The merozoites then re-enter the host's red blood cells (RBCs) upon exiting the liver cells, beginning the erythrocytic cycle. This stage of the parasite's development is associated with the symptoms of malaria infection. While resident inside RBCs, merozoites undergo asexual reproduction, developing through the ring stage, and later the trophozoite stage, which is the most active period in terms of parasite growth. During the latter stage the parasite also develops the digestive vacuole (DV) where host haemoglobin is digested. The schizont stage follows, releasing merozoites back into the host's bloodstream. This erythrocytic cycle repeats every 48 hours in the case of *P. falciparum*, and the rupture of merozoites causes the periodic fevers and chills associated with malaria infection. Some of the merozoites develop into the sexual form of the parasite, called the male and female gametocytes (Figure 1.1). These

gametocytes circulate in the blood stream, and when the mosquito takes another blood meal, the cycle of infection begins afresh (Figure 1.1).[11,12,13]
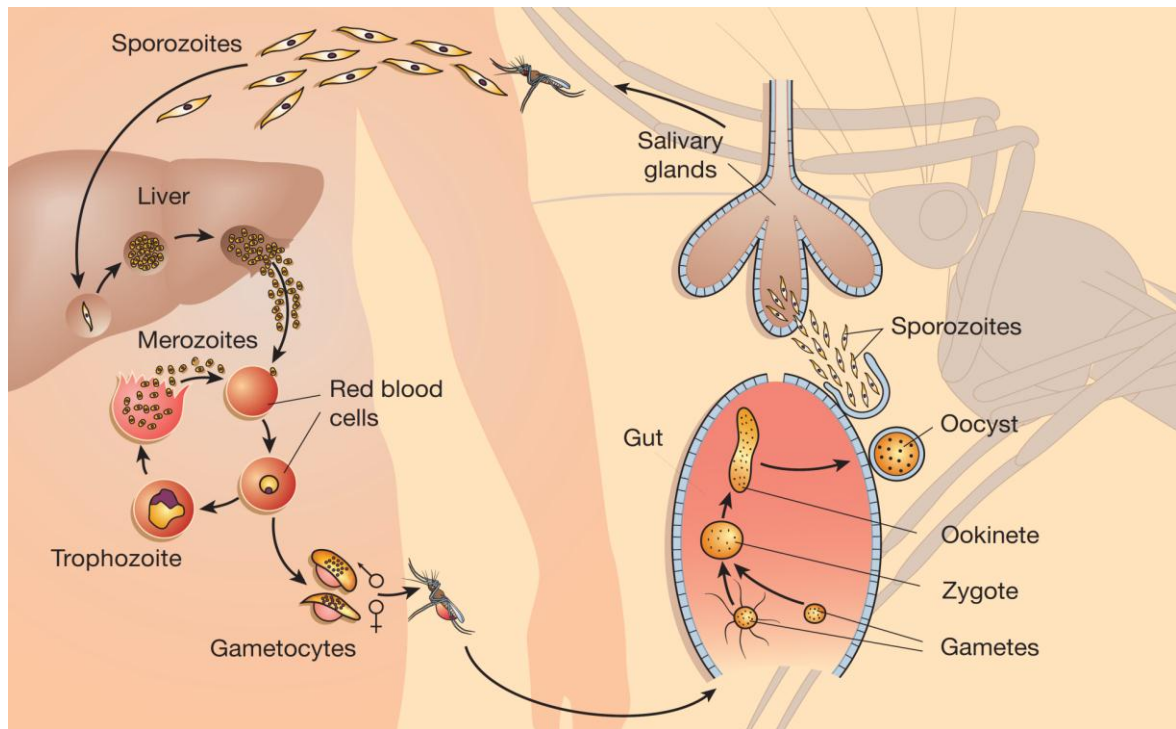
Figure 1.1 The life cycle of the malaria parasite. Reproduced from reference.[9]

Following infection, an incubation period of 7-30 days can pass before any symptoms of malaria are observed. A malaria attack is exemplified by a cold stage, a hot stage and a sweating stage that comes and goes periodically. Symptoms include fever, chills, headaches, nausea and in severe cases kidney failure and cerebral malaria. The female mosquito, unlike humans, does not suffer from the presence of the parasite.[1]

1.4   The Blood Stage

During the residency of the malaria parasite inside red blood cells of the human host, large quantities of haemoglobin are digested by a series of protease enzymes, which include the aspartic, cysteine and zinc metallo-proteases,[14-16] providing a source of amino acids as well as space for the growing parasite.[15] The haemoglobin is being efficiently transported to the parasite's acidic DV, also known as the food vacuole (FV), in endocytotic vesicles which are pinched off from the cytostome formed by invagination of the parasite plasma membrane.[17] The acidic environment of the DV has an estimated pH of 4.8.[18] The four

equivalents of haem iron(II) protoporphyrin IX (Fe(II)PPIX) released per unit of haemoglobin during digestion are readily oxidized to Fe(III)PPIX (Figure 1.2), which is potentially toxic to the parasite owing to the redox-active iron centre which may be involved in generating reactive oxygen species, and thus catalysing membrane damage *via* lipid peroxidation.[19] The features of the Fe(III)PPIX molecule include a five-coordinate Fe(III) centre with the axial ligand being either hydroxide (HO⁻) or aqua (H_2O) depending on pH, and an aromatic tetrapyrrole macrocycle with two propionic acid, two vinyl and four methyl groups as side chains.
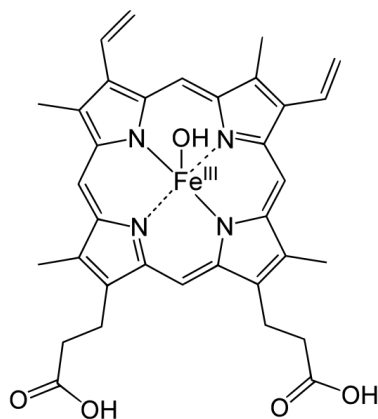
Figure 1.2 The molecular structure of iron(III) protoporphyrin IX (Fe(III)PPIX). Features include a five-coordinate Fe(III) centre with either HO⁻ or H_2O as the axial ligand, and an aromatic tetrapyrrole macrocycle. Substituents include two propionic acid, two vinyl, and four methyl side chains.

The parasite circumvents this imminent threat by detoxifying Fe(III)PPIX *via* biocrystallisation, whereby the potentially harmful Fe(III)PPIX is converted into an insoluble, inert crystal of Fe(III)PPIX called haemozoin (Figure 1.3).[20,21]
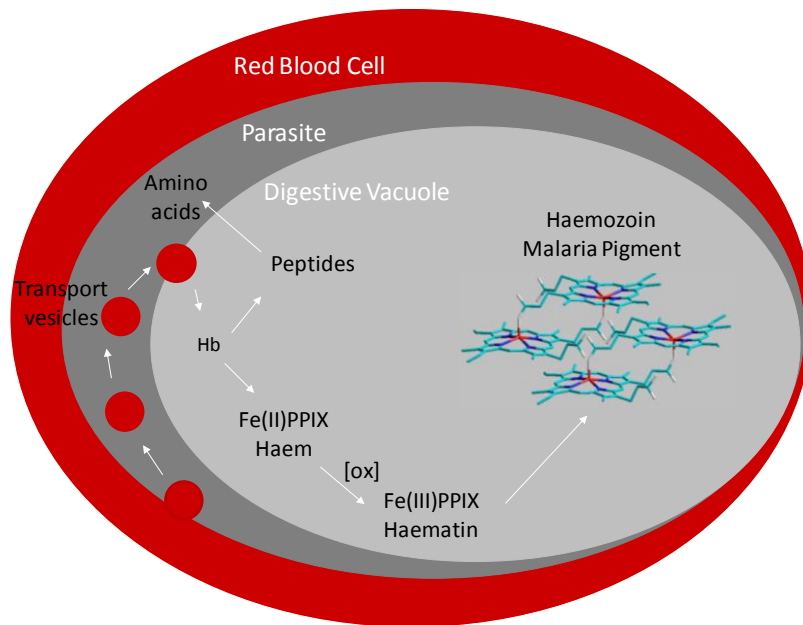
Figure 1.3 Schematic representation of the pathway for haemozoin formation. Haemoglobin (Hb) is efficiently ingested and transported to the parasite's acidic digestive vacuole by transport vesicles, after which Hb undergoes degradation into amino acids and haem, (Fe(II)PPIX). Subsequent oxidation ([ox]) of haem yields haematin (Fe(III)PPIX) which is detoxified into malaria pigment (haemozoin).

An electron microscopy study by Egan *et al.*[20] has shown that at least 95% of all Fe(III)PPIX released during haemoglobin digestion is incorporated into haemozoin. Transmission electron microscopy (TEM) and electron spectroscopic imaging (ESI) of the parasite were used, showing for the first time that haemozoin formation is the overwhelming fate of Fe(III)PPIX iron released in the malaria parasite (Figure 1.4).
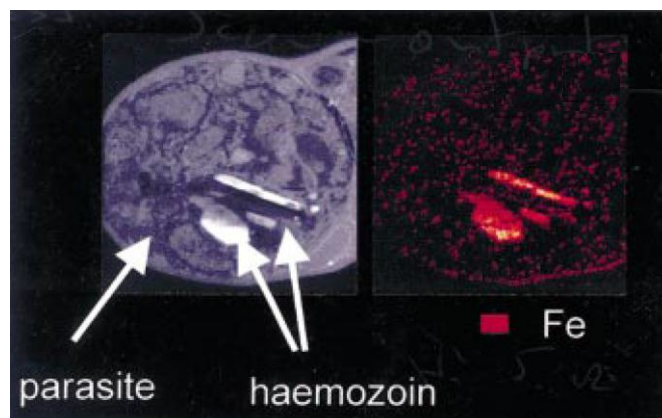
Figure 1.4 The TEM image (left) and ESI (right) of an infected red blood cell, showing that iron distribution coincides with haemozoin crystals. Reproduced from reference.[20]

The erythrocytic stage of the malaria parasite's lifecycle is very important from a chemotherapy perspective, since quinoline containing antimalarials exhibit their antiplasmodial activity at this stage. During its residency inside host RBCs, the parasite is vulnerable at various points to drug action, however, interruption of haemoglobin degradation or Fe(III)PPPIX detoxification, have been widely considered.[22] Understanding haemozoin formation in particular has been a focus in the literature during the last three decades given its important implications for the design of new therapeutic agents.

1.5 Haemozoin

It is known today that haemozoin is the pigment observed and reported by Lancisi.[5] With the discovery of haemozoin in other blood-feeding organisms such as the insect *Rhodnius prolixus,*[23] helmith worms including *Schistosoma mansoni,*[24,25] *Echinostoma trivolvis,*[26] and *Haemoproteus columbae,*[24] (Figure 1.5) research interest in haemozoin has increased significantly in recent years. Though unrelated to the malaria parasite, these organisms also detoxify Fe(III)PPIX by converting it into haemozoin.
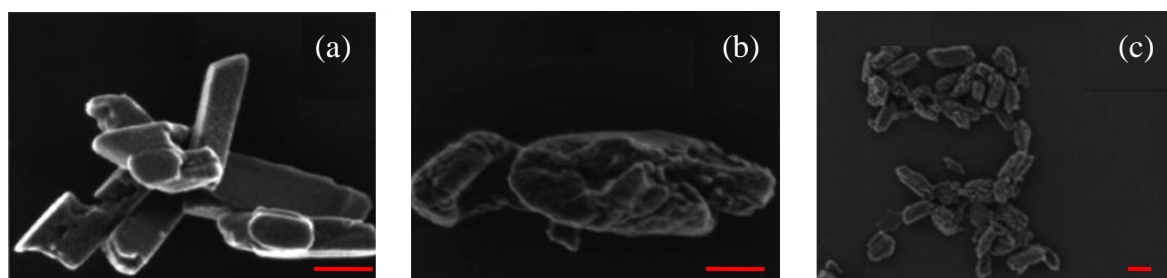
Figure 1.5 Samples of haemozoin purified from (a) *P. falciparum*, (b) *S. mansoni* and (c) *H. columbea*. The scale bar in each represents 200 nm. Reproduced from reference.[24]

1.5.1 Structure of Haemozoin

The discovery of a synthetic aggregate of Fe(III)PPIX called β-haematin, first described by Hamsik in 1936,[27] opened the door to the study of the unique formation of haemozoin *in vitro*. Since then, it has been show that β-haematin is chemically and spectroscopically identical to haemozoin.[28,29,30] Haemozoin and β-haematin give rise to identical Fourier transform infrared (FT-IR) spectra, powder X-ray diffraction patterns (PXRD), synchrotron PXRD patterns and Raman spectra.[28,30,31]

1.5.1.1   Interpretation from Haemozoin and β-Haematin

Malaria pigment was first described as a melanotic pigment, due to its presumed association with melanins.[1] This idea was contested in 1911 by Brown on the basis of comparison studies between well-known melanins and malaria pigment. Through bleach reactions and solubility studies he showed that there was marked dissimilarity between them. Using spectroscopic examination, Brown also showed that the chromophore (precursor) of malaria pigment is haematin.[32]

Early characterisations of haemozoin suggested it to be a haemoprotein complex,[33] however the pioneering work of Fitch and Kanjananggulpan dismissed this notion. By using *P. berghei* infected erythrocytes, the material extracted was washed to remove protein by proteolytic digestion as well as lipid by chloroform/methanol extraction to yield high purity material. They showed for the first time that purified haemozoin consists only of ferriprotoporphyrin IX (Fe(III)PPIX) and suggested that haemozoin and β-haematin (synthetic haemozoin) are most likely identical.[29]

Early structural interpretations by Slater *et al*.[28,30] led to the conclusion that haemozoin was a bio-polymer comprising Fe(III)PPIX units sequentially linked *via* propionate coordination to the Fe(III) centre between adjacent monomers (Figure 1.6 (a)). They assigned the strong absorbance bands at 1211 cm^{-1} and 1664 cm^{-1} in the FT-IR spectrum of haemozoin to the C-O and C=O stretching frequencies of the coordinated propionate group to the Fe(III) centre (Figure 1.6 (b and c)). It was also Slater *et al*.[30] who showed that haemozoin and its synthetic counterpart β-haematin give rise to identical PXRD patterns and FT-IR spectra.
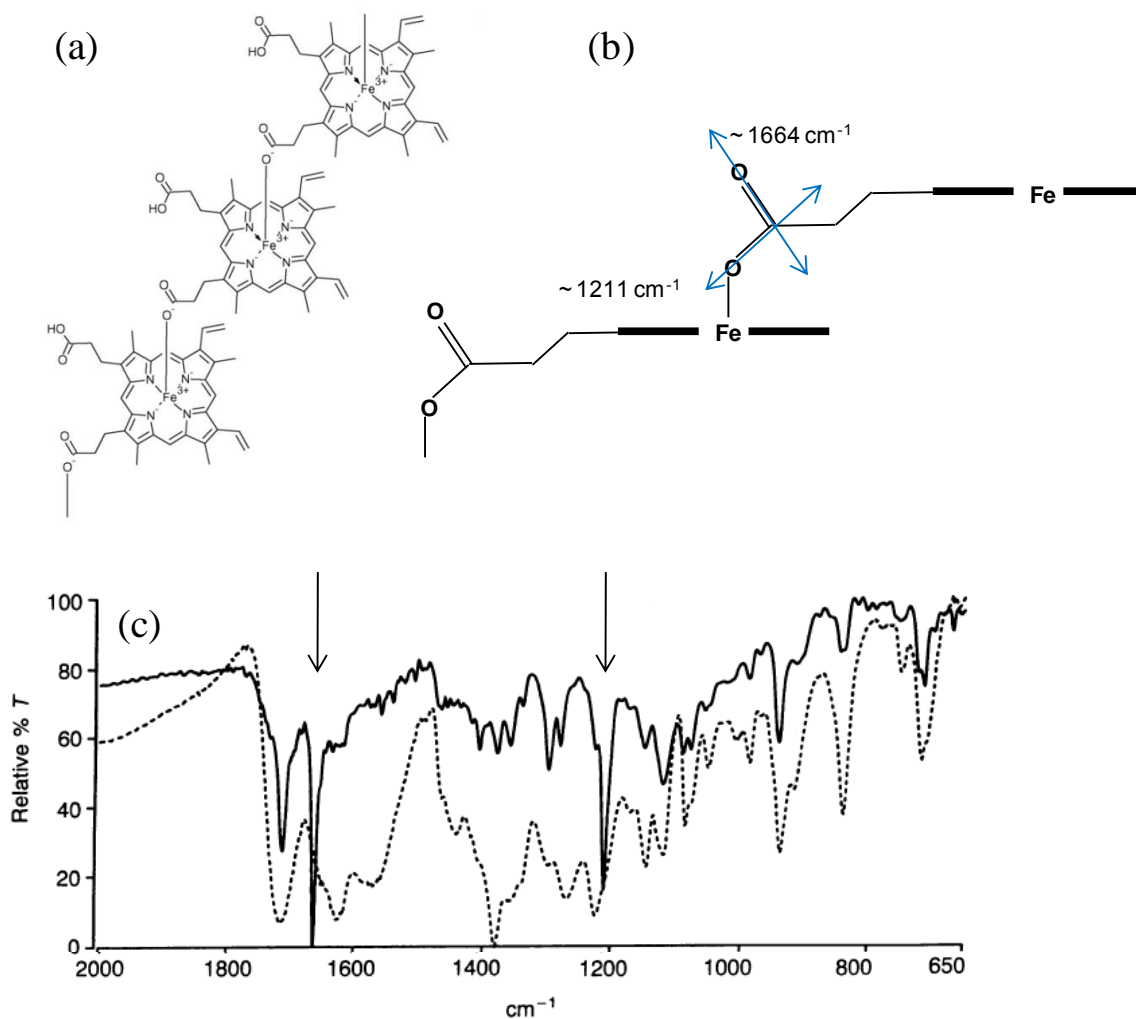
Figure 1.6 The structure of haemozoin proposed by Slater *et al.*[30] (a) They suggested that haemozoin was a linear polymer linked *via* Fe(III)-propionate coordination bonds. (b) A schematic representation of the then-believed structure of haemozoin viewed side on. C-O and C=O stretching frequencies responsible for the strong absorbance bands at 1211 cm^{-1} and 1664 cm^{-1} in the UV-visible spectrum are indicated. The thicker black lines represent the mean porphyrin plane. (c) The FT-IR spectrum of haemozoin (─) and Fe(III)PPIX (---). Characteristic peaks at 1211 cm^{-1} and 1664 cm^{-1} in the spectrum of haemozoin are indicated with arrows, and are absent in the spectrum of Fe(III)PPIX. Reproduced from reference.[30]

Making use of synchrotron powder X-ray diffraction (PXRD), Bohle *et al.*[34] conclusively demonstrated that β-haematin is identical to haemozoin. Furthermore, their results revealed that the structure comprised a centrosymmetric unit cell, and they therefore proposed a revised structure for haemozoin (β-haematin) consisting of antiparallel polymer chains, as shown in Figure 1.7.

8
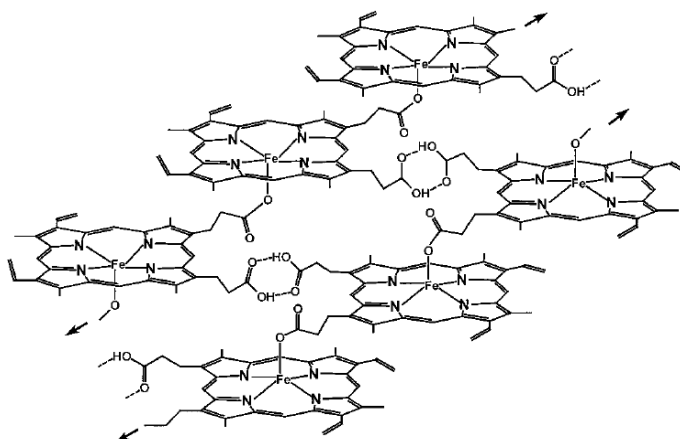
Figure 1.7 The proposed structure of haemozoin/β-haematin by Bohle *et al.*[34] consists of antiparallel polymer chains stabilised *via* intermolecular hydrogen bonding. Reproduced from reference.[34]

The true structure of β-haematin was only determined by Pagola *et al.*[35] in 2000. After careful analysis of synchrotron powder X-ray diffraction data, the authors were able to determine that the repeating unit in the crystal structure of β-haematin is a cyclic dimer of Fe(III)PPIX in which a deprotonated propionic acid group (propionate side chain) of one protoporphyrin unit coordinates to the Fe(III) centre of the second and *vice versa* to form a discrete centrosymmetric unit, and not a polymer as predicted years before.[28,30] Hydrogen bonding between dimers occurs *via* the second propionic acid group of each protoporphyrin unit, and serves to link these dimers together, forming chains in the crystal structure (Figure 1.8).[35]
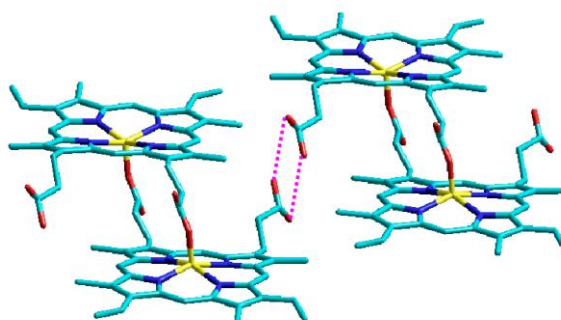
Figure 1.8 The structure of β-haematin. Formation of the cyclic dimers occurs through Fe(III)-propionate coordination bonds, with dimers linked by intermolecular hydrogen bonds between propionic acid groups (represented as pink dashed lines). Reproduced from reference.[35]

The centrosymmetric haemozoin dimer comes about as a result of the coordination of one propionate side chain of one Fe(III)PPIX coordinating to the Fe(III) centre of a second Fe(III)PPIX and *vice versa* (Figure 1.9). In agreement with early structural interpretations put forward by Slater *et al.*,[30] the strong absorbance bands at 1211 cm^{-1} and 1664 cm^{-1} in the FT-IR spectrum of haemozoin are attributed to the C-O and C=O stretching frequencies of the coordinated propionate ligand (Figure 1.6 (c)). Today haemozoin or β-haematin can be readily characterised by their FT-IR spectra. Having solved the structure of β-haematin, and confirmed the same for haemozoin, had great implications for probing the mechanism of the biomineralisation process, whereby potentially harmful Fe(III)PPIX is converted into haemozoin.
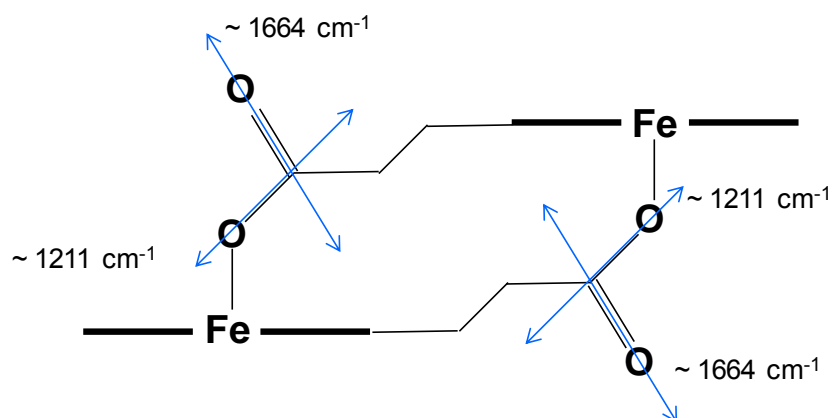
Figure 1.9 A schematic representation of the haemozoin centrosymmetric dimer (μ-propionato dimer) viewed side on. C-O and C=O stretching frequencies responsible for the strong absorbance bands at 1211 cm^{-1} and 1664 cm^{-1} in the UV-visible spectrum are indicated. The thicker black lines represent the mean porphyrin plane.

One theory recently put forward by Klonis *et al.*[36] suggested that the structure of haemozoin is composed of π-π dimers stabilised by μ-propionate coordination (Figure 1.10). This conclusion was based on their solution of the structure of haemozoin by synchrotron PXRD, using maximum entropy-based pattern fitting.[36] They proposed that nucleation of haemozoin crystals is initiated by π-π dimers, contradicting the idea that haemozoin and β-haematin nucleation is initiated from cyclic dimers of Fe(III)PPIX.[37] The latter interpretation was based on the original structure determination of β-haematin. However, and it must be pointed out that the crystal structure is not sufficient to infer the nucleating species.
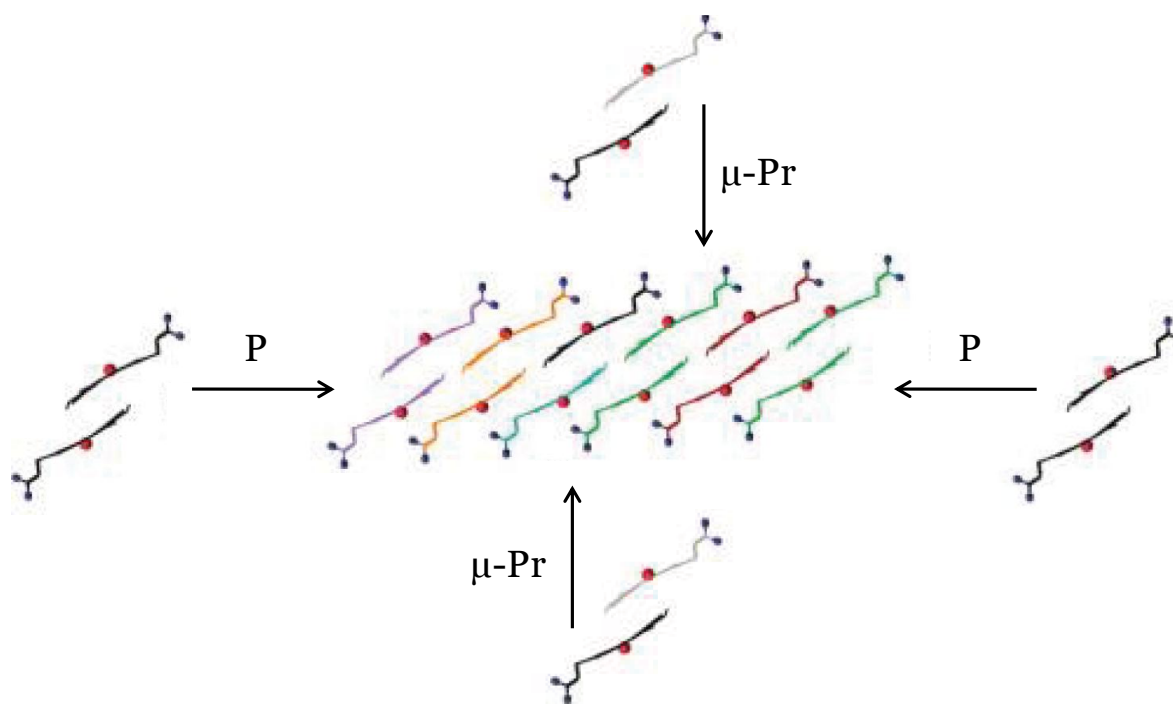
Figure 1.10 A proposed model for the formation of haemozoin: π-π dimers form columns which are extended in length *via* antiparallel non-covalent polymer (P-type) interactions and linked to adjacent columns *via* μ-propionate (μ-Pr) coordination. Reproduced from reference.[36]

1.5.1.2   Local Fe(III) Environment of Haemozoin and β-Haematin

To fortify the similarities, Walczak *et al.*[38] set out to investigate haemozoin and its synthetic homologue, β-haematin, utilizing extended X-ray absorption fine structure (EXAFS) spectroscopy. They showed the usefulness of EXAFS to analyse and compare the distributions of atoms surrounding the absorbing Fe atom in β-haematin and haemozoin. Using the PXRD structure of β-haematin as a model, the scattering properties $f(k)$ and $\delta(k)$ were calculated for EXAFS analysis.[35] Due to the fact that Fe(III)PPIX is a complex system, and scattering of photo-electrons is possible from many atoms surrounding the Fe centre, atoms were grouped into four coordination shells (Figure 1.11). The first shell contains the oxygen atom of the axial ligand, while the four nitrogen atoms of the porphyrin macrocycle, which coordinate to Fe in the equatorial plane, comprise the second shell. The third and fourth shells contain the eight α carbon and the four *meso* carbon atoms, respectively.
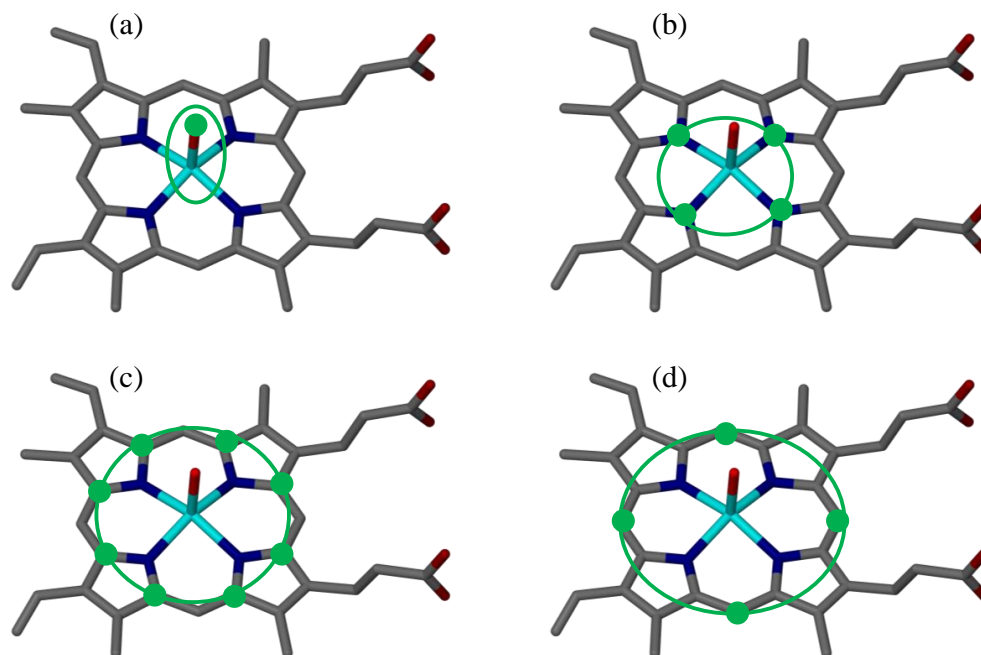
Figure 1.11 A model of Fe(III)PPIX showing the four coordination shells surrounding the absorbing Fe centre. (a) The first shell contains the oxygen atom of the axial ligand. (b) The four nitrogen atoms of the porphyrin macrocycle, which coordinate to Fe in the equatorial plane, comprise the second shell. (c) The third shell contains the eight α carbon atoms, and (d) the four *meso* carbon atoms make up the fourth shell. These shells were used as a starting model for EXAFS analysis to investigate the distribution of atoms around the Fe centre in haemozoin and β-haematin. Redrawn based on reference.[38]

The model was refined to include multi-scattering paths. There was very good agreement between the experimental data and the model, with R-factors of 0.005 and 0.007 obtained for β-haematin and haemozoin respectively (Figure 1.12).
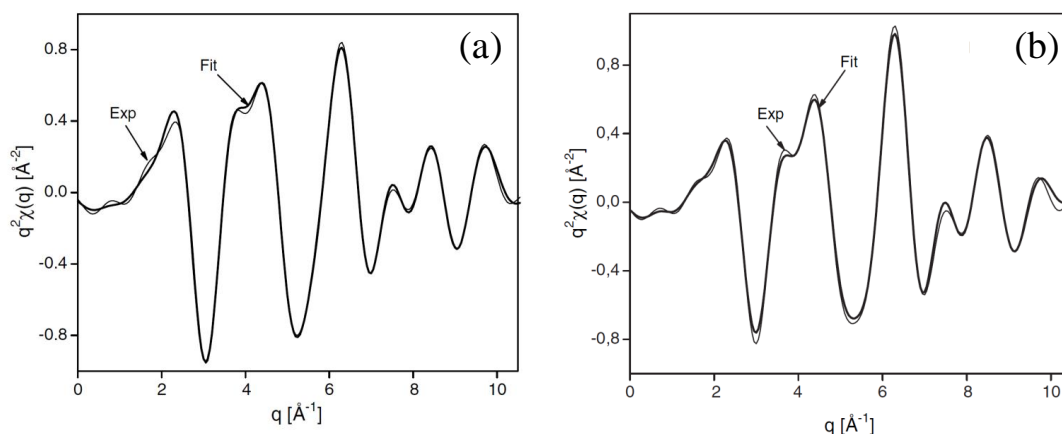
Figure 1.12 Fe K_α-edge X-ray absorption spectra. The best fit of experimental data (labelled Exp) for (a) β-haematin and (b) haemozoin to a model generated from the coordinates of β-haematin determined by PXRD.[35] R-factors are 0.005 and 0.007 respectively. Reproduced from reference.[38]

Comparison of the EXAFS data for β-haematin and haemozoin highlighted a difference in the position of the axial oxygen atom. In the case of haemozoin, the Fe─O bond length was found to have a larger statistical error compared to the same parameter in β-haematin. The authors reasoned that not all of the oxygen bridges that bond Fe(III)PPIX can be formed in the natural pigment, due to the large error and large value of the Debye-Waller factor, indicating large disorder in the position and occupancy of the oxygen site. The X-ray absorption near edge structure (XANES) results for β-haematin and haemozoin confirmed that the oxidation state of Fe is close to three.[38]

1.5.1.3   Crystal Morphology of Haemozoin

Crystal morphology is unique to every crystal structure and is sculptured by the relative growth rate of the various faces of the crystal. According to Hartman and Perdok,[39] the morphology of a crystal is dependent on the growth rates of its various faces, which in turn depend on the layer energy, E_1 (a measures of the stability of the layer), and the attachment energy, E_{att} (which controls the growth rate perpendicular to the layer). These energies can be calculated for various low-index faces of a crystal, and can in turn be used to determine the theoretical crystal form.[35] Using this approach, the theoretical growth form of β-haematin has been investigated (Figure 1.13 A and B).[40] Buller *et al.*[40] determined a needle-like crystal morphology which is extended along the c-axis. Expressed in the

morphology are the dominant (100) and (010) faces, a lesser developed (011) face and a minor (001) face. The theoretical morphology of haemozoin shows a strong resemblance to purified haemozoin crystals (Figure 1.13 C, D and E).[40] An average crystal width-to-thickness ratio of w/t = 1.3 ±0.5 was determined, and most of the crystals were seen to lie on their wide (100) face.
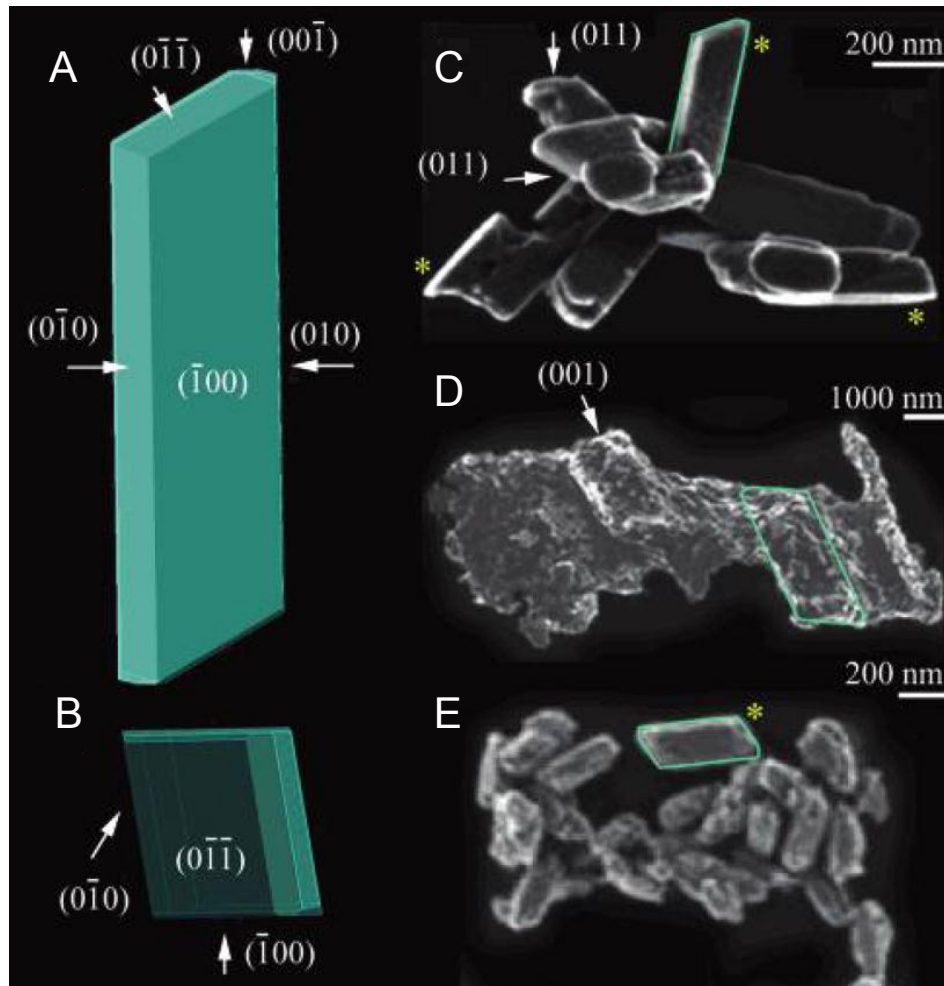
Figure 1.13 The theoretical growth form of β-haematin (A and B) indicating the dominant (100) and (010) faces, a lesser developed (011) face and a minor (011) face. The external morphology of haemozoin (C, D and E) purified from *P. falciparum, S. mansoni and H. columbae* respectively. Reproduced from reference.[40]

The authors identified the fastest growing crystal face, (001), of β-haematin, and showed that quinoline antimalarial drugs are able to bind remarkably well into the crevices created at this face. They reasoned that this could represent a possible mode of inhibition by quinoline antimalarial drugs. As such, their proposal is discussed in more detail later (section 1.6.4).

1.5.1.3.1 *Stereoisomers of β-Haematin*

The molecule of Fe(III)PPIX has enantio-facial symmetry, therefore isomers of the dimer of β-haematin can form. Straaso *et al.*[41] identified four possible stereoisomers in the dimer structure of β-haematin crystals after analysing the powder X-ray diffraction data of β-haematin crystals. These possible isomers consisted of two centrosymmetric and two chiral enantiomers, which they named $cd\bar{1}_1$, $cd\bar{1}_2$ and $cd2(+)$, $cd2(-)$ respectively (Figure 1.14). Only the $cd\bar{1}_1$ centrosymmetric cyclic dimer was described in the initial elucidation of the β-haematin structure.[35]

| (a) | (b) | (c) | (d) |

$cd\bar{1}_1$ $cd\bar{1}_2$ $cd2(-)$ $cd2(+)$
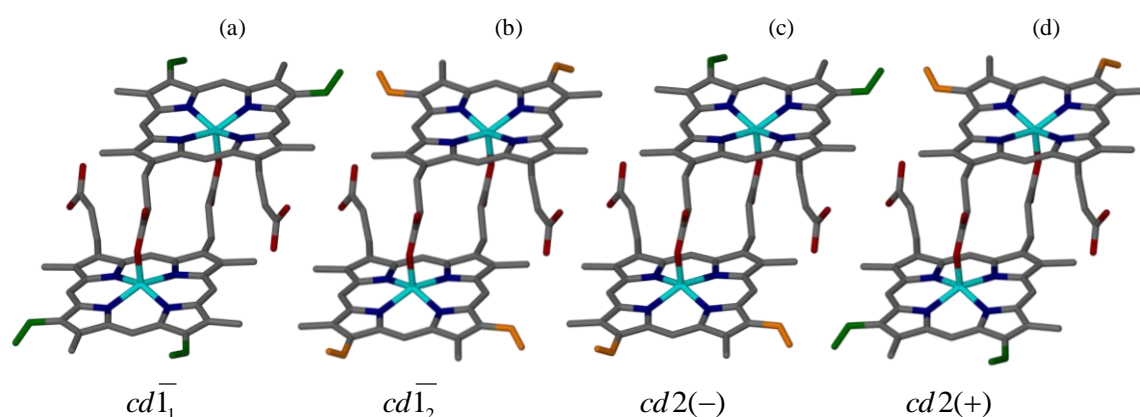
Figure 1.14 A schematic representation of the four isomers of the β-haematin μ-propionato dimer.[41] The two achiral centrosymmetric dimers, (a) and (b), have been termed cd$\bar{1}_1$, and cd$\bar{1}_2$, respectively, while the two chiral non-centrosymmetric dimers, (c) and (d), have been termed cd2(+) and cd2(-), respectively. The vinyl substituents shown in green occupy α (top porphyrin) and γ (bottom porphyrin) sites, while those shown in orange occupy the β (top porphyrin) and δ (bottom porphyrin) sites. Atom colour coding: C – grey; N – blue; O – red; Fe – cyan and vinyl groups – green and orange. Redrawn based on reference.[41]

In these four isomers, the vinyl substituents are located at the α/γ, β/γ, α/δ and β/γ positions, respectively. The authors proposed that β-haematin consists of a major ($cd\bar{1}_{1,}$) and a minor ($cd\bar{1}_2$) phase, and reasoned that adsorption of the chiral stereoisomers onto various faces of the growing crystal could result in blocking further growth. They suggested that this could be the reason why only micrometre-sized crystals are observed in β-haematin formation, and could explain why a suitable crystal for single crystal X-ray diffraction has not been obtained. Alternative interpretations propose that there is only a single phase, and that disorder in the structure, particularly with regard to the methyl and

vinyl substituents is caused by the presence of all four isomers.[42] The authors acknowledge that powder X-ray diffraction is limited, and that it cannot distinguish between the observed vinyl/methyl disorder. They explained that SCD would provide insight into resolving the problem. Besides the reference system for the four stereoisomers used above, different nomenclature systems are also referred to in the literature; these are outlined in Table 1.1.

Table 1.1 The different nomenclature systems used to describe the stereoisomers of the μ-propionato dimer.[#]

Straaso[a]	CPI[b]	IUPAC[c]	Vinyl sites[d]
cd$\bar{1}_1$	(R/S)	2,2	α/γ
cd$\bar{1}_2$	(S/R)	18,18	β/δ
cd2(-)	(S/S)	2,18	α/δ
cd2(+)	(R/R)	18,2	β/γ

[#] Reproduced from reference.[42]
[a] Straaso *et al.*[41]
[b] Cahn, Prelog, and Ingold system for Fe-O coordination to *Re* or *Si* face of Fe(III)PPIX.
[c] IUPAC [43] The numbering (2 and 18) refer to the propanoate bearing C-atoms from which the Fe-O bond.
[d] Reproduced from reference.[42]

In order to understand the mechanism of haemozoin crystallisation and the involvement of the different stereoisomers, Marom *et al.*[44] conducted van der Waals-corrected density functional theory (DFT) studies of β-haematin. Based on computational modelling of the different stereoisomers, they proposed a mechanism whereby the formation of cyclic dimers of Fe(III)PPIX is the first stage of nucleation.

1.5.1.3.2 *β-Haematin Crystal Properties*

In 2003 Bohle *et al.*[45] showed that β-haematin is able to absorb up to 14% of its mass in water, corresponding to a mol ratio of 4.78 water molecules per molecule of Fe(III)PPIX. Samples of hydrated β-haematin were heated to temperatures exceeding 150 ^{o}C, after which reabsorption of water took place at room temperature. Depending on the experimental method used to make β-haematin, more crystalline samples have been shown to have a greater capacity for reabsorbing water when compared to more amorphous samples. They also showed, by comparing synchrotron PXRD patterns, that samples become more ordered as they are allowed to rehydrate. The authors could not account for

16

where the water is adsorbing and simply stated that it may be possible for the water to either intercalate between layers or attach to the surface of crystals.

1.5.1.3.3 *Single Crystal Analoque of β-Haematin*

Due to the essential role that β-haematin studies have contributed to our understanding of haemozoin, much effort has gone into growing a malaria pigment analogue large enough for single crystal X-ray diffraction. The structure of β-haematin was solved using Rietveld refinement of data collected from synchrotron X-ray powder diffraction.[35] Only as recently as 2012, Bohle and Dodd[46] presented the first single crystal X-ray diffraction structure of a propionate-linked dimer similar to that found in haemozoin. The haemozoin model compound, [gallium(III) protoporphyrin IX]$_2$ (Figure 1.15), was crystallised from a solution of Ga(PPIX)-OH in 2,6-lutidine in the presence of one equivalent of pyridine.
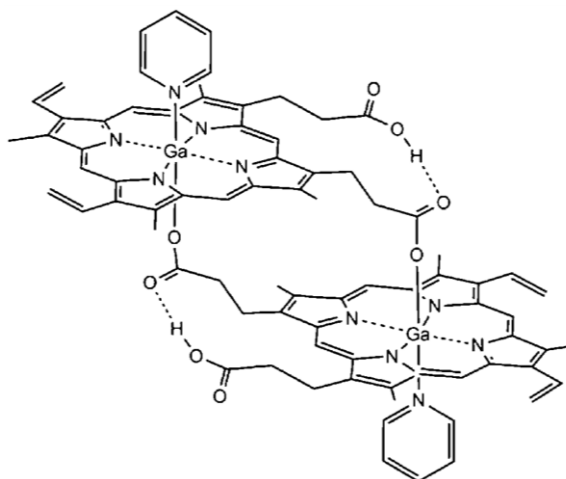
Figure 1.15 The crystal structure of [gallium(III) protoporphyrin IX]$_2$. The dimeric propionate-bridged dimer has a six-coordinated metal atom with a pyridine ligand bound trans to the propionate group. An intraporphyrin hydrogen bond is observed between the gallium-bound propionate and the free propionic acid group from the same porphyrin unit. Reproduced from reference.[46]

The crystal structure shows a cyclic dimer of Ga(III)PPIX, in which the propionate side chain of one protoporphyrin unit coordinates to the Ga(III) centre of the second and *vice versa* to form a centrosymmetric cyclic dimer, as observed in β-haematin and haemozoin structures. However, the Ga(III) centre is six-coordinate with a pyridine ligand bound trans to the coordinated propionate group, therefore the Ga(III) centre resides in the plane of the

phorphyrin. Furthermore, the free propionic acid forms an intramolecular hydrogen bond with the propionate group of the same porphyrin molecule. Owing to the coordination of the pyridine and the absence of intermolecular hydrogen bonding, [gallium(III) protoporphyrin IX]$_2$ is more soluble in methanol (MeOH) and other organic solvents compared to β-haematin, therefore allowing for the characterisation of solution structures using ^{1}H NMR spectroscopy. Solution ^{1}H NMR spectra of [gallium(III) protoporphyrin IX]$_2$ in methanol-d_4 by 1D NOESY indicates that pyridine promotes dimerisation: an increase in intensity of the methane-20-propionate 2β, 18β NOE peak is observed as pyridine is added (Figure 1.16). Comparatively, in the haemozoin dimer, the Fe centre is five-coordinate such that the Fe(III) centre resides outside of the porphyrin plane and no intramolecular hydrogen bonding is observed.
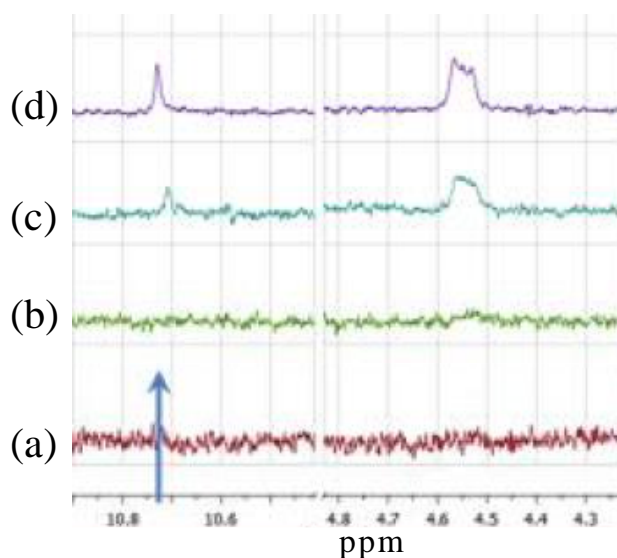
Figure 1.16 The [1]D NOESY ^{1}H NMR spectra of [gallium(III) protoporphyrin IX]$_2$ in methanol-d_4 indicate that pyridine promotes dimerisation, due to the increase in intensity observed for the methane-20-propionate 2β, 18β NOE peak (indicated with blue arrow) as (a) 0 equiv, (b) 3 equiv, (c) 14 equiv, and (d) 27 equiv of pyridine are added. Reproduced from reference.[46]

1.5.1.4   Analogues of β-Haematin

In 2011 Bohle *et al.*[47] published the structure of the μ-propionate coordination dimer of Fe(III) mesoporphyrin IX, a species which is isostructural to the β-haematin dimer and which they referred to as mesohaematin anhydride. In the mesoporphyrin, the vinyl groups are substituted for ethyl groups, leading to a compound more soluble in dichloromethane (DCM). Solved by X-ray powder diffraction, the structure of this dimer was shown to be

similar to the Fe(III)PPIX dimer observed in malaria pigment, however unlike β-haematin in which dimers hydrogen bond to one another through their free propionic acid groups, the free propionic acid side chains of the mesohaematin anhydride dimer are hydrogen bonded to solvent dimethyl sulfoxide (DMSO) molecules. (Figure 1.17 (a)).[47] The authors subsequently investigated the interaction between chloroquine (CQ) and deuterohaematin anhydride (where the vinyl groups are substituted for hydrogen atoms) in solution (DCM) using UV-visible spectroscopy. Following the addition of up to 37 equivalents of CQ, only very small shifts in the soret band (1-2 nm) were observed, with no change in the Q band region, (Figure 1.17 (b)). The authors suggested that the UV spectrum shows direct evidence for noncovalent interactions between CQ and deuterohaematin anhydride, since there are no changes in the Q bands.[48] Furthermore they reasoned that there is minimal self-aggregation at low concentration of deuterohaematin anhydride due to no broadening observed in the Soret band. They also state that π-π complex formation between CQ and deuterohaematin anhydride would be expected to lead to hypochromism in the Soret band.[49]
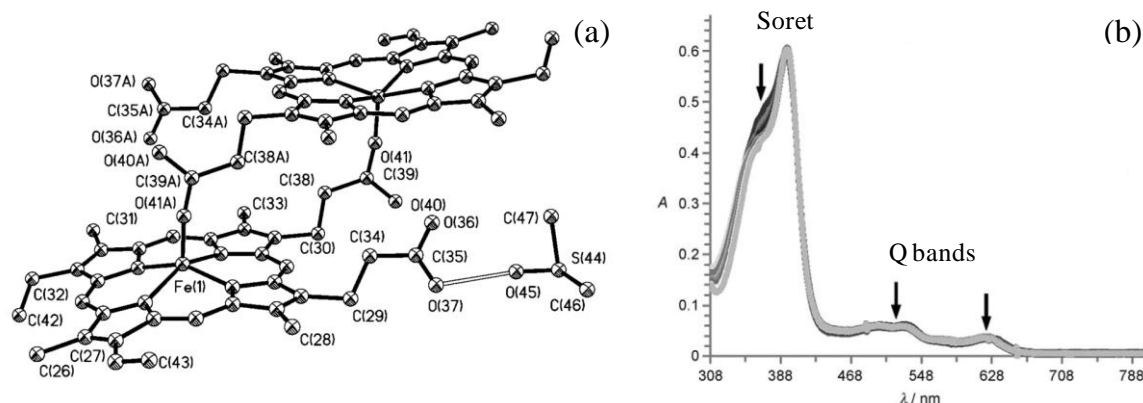
Figure 1.17 (a) The mesohaematin anhydride dimer, showing the hydrogen bond between the free propionic acid side chain of the porphyrin dimer, O37, and the DMSO solvent molecule O(45). (b) The UV-visible spectrum of CQ and deuterohaematin anhydride in solution (DCM) shows the changes observed on addition of CQ (up to 37 equivalents) in DCM to deuterohaematin anhydride. Reproduced from reference.[47]

EXAFS spectroscopy was used to compare the similarities between haemozoin and the newly synthesised synthetic analogues, namely mesohaematin- and deuterohaematin anhydrides.[37] Using crystallographic powder diffraction data for mesohaematin anhydride and β-haematin, scattering properties $f(k)$ and $\delta(k)$ could be calculated as a starting

model for the EXAFS analysis to model the structure around the Fe atom of these structures. Following careful analysis of the experimental EXAFS spectra of haematin, β-haematin, mesohaematin anhydride and deuterohaematin anhydride, and the refined EXAFS parameters, the authors concluded that there was a greater similarity between the synthetic anhydrides and β-haematin compared to haematin (Figure 1.18).
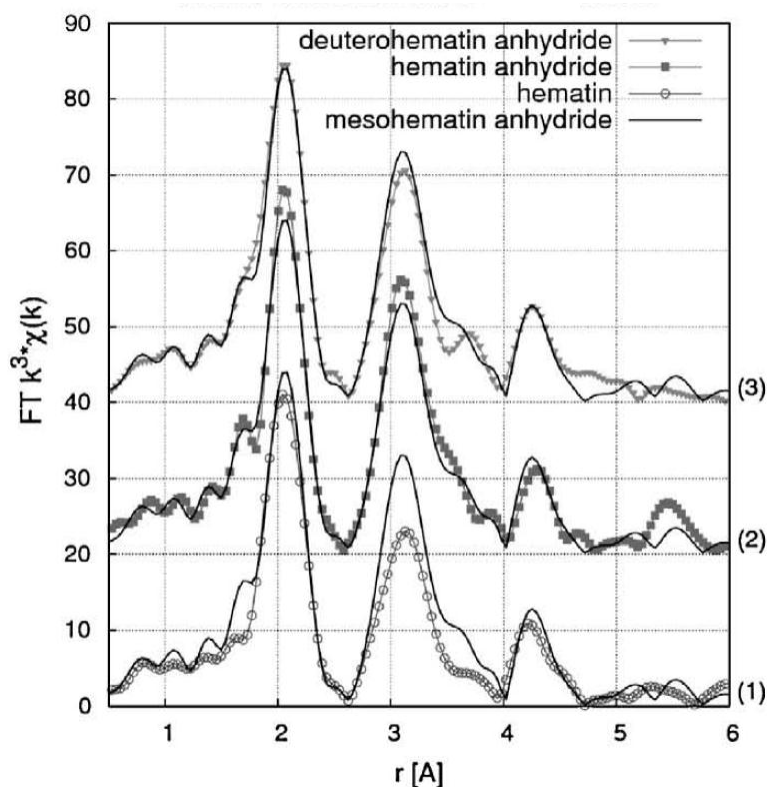
Figure 1.18 The experimental EXAFS spectra of (1) haematin, (2) β-haematin (haematin anhydride) and (3) deuterohaematin anhydride compared to the EXAFS spectrum of mesohaematin anhydride (solid line) in each case. Reproduced from reference.[37]

This study also showed that it is possible to distinguish between the dimer in β-haematin (μ-propionato) and the monomer conformation of haematin using EXAFS.

In a subsequent study, EXAFS spectroscopy was again used to study the iron environment of mesohaematin anhydride dissolved in DMSO. Using the mesohaematin anhydride PXRD structure as a starting model for the analysis, the study showed that in the presence or absence of freebase CQ, the dimer character of the mesohaematin anhydride persists in the aprotic solvent system (Figure 1.19).[50] This conclusion was reached based on the fact that the oxygen coordinating to the Fe centre remained in position within structural disorder parameters in the different environments. Interestingly, EXAFS analysis of CQ in

20

the presence of the dissolution of mesohaematin anhydride showed a strong influence at a distance of 2.5 and 3.8 Å from the absorbing Fe (Figure 1.19, green circles). Based on the EXAFS refinement, the authors proposed that a CQ-ferrimesoporphyrin IX complex may be present, however, none of the atoms form ionic or covalent bonds to the central Fe(III) atom.
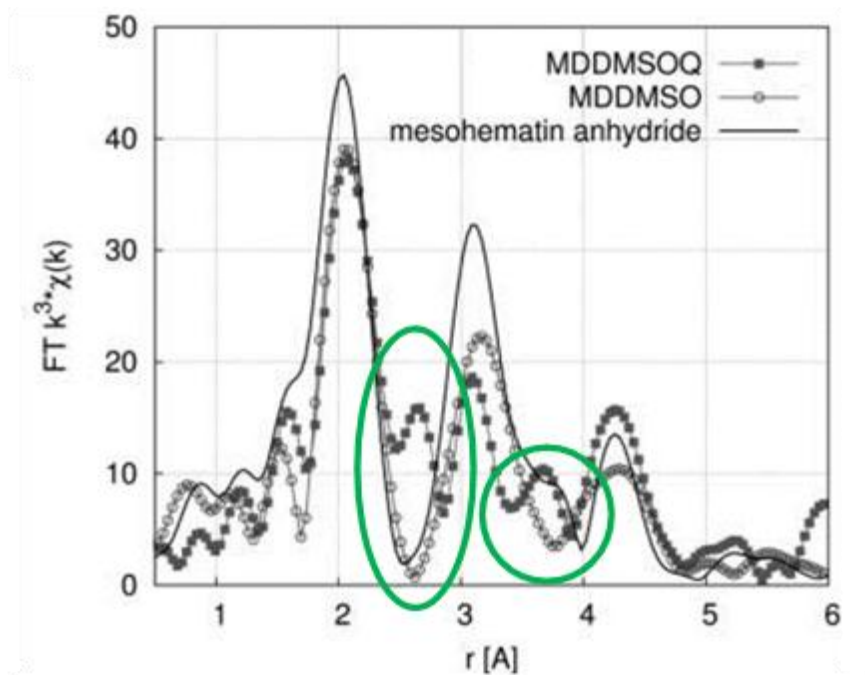
Figure 1.19 The experimental EXAFS spectra of mesohaematin anhydride microcrystalline powder phase (solid line), mesohaematin anhydride dissolved in DMSO (MDDMSO, open circles) and mesohaematin anhydride and free base CQ dissolved in DMSO (MDDMSOQ, black squares). The additional features in the EXAFS spectrum of MDDMSOQ due to the CQ are circled in green. Reproduced from reference.[50]

In a related study, changing the solvent conditions from aprotic (DMSO) to protic (acetic acid) in the absence or presence of water, and with or without the addition of free base CQ, was investigated. The EXAFS spectra indicate disruption of the μ-propionate dimer, resulting in the propionate groups dissociating from the iron centre.[51] When comparing the Fourier transformed spectra of crystalline mesohaematin anhydride to mesohaematin anhydride dissolved in acetic acid and water (15:1 *v/v*, MDAA15), there is a narrowing and shift in the first peak (at 1.5-2.5 Å) and a reduction in the amplitude and change in the shape of the second peak (at 2.7-3.8 Å), Figure 1.20 (1). Similar changes are observed in the remainder of the spectra for mesohaematin anhydride in the presence or absence of free

base CQ, shown in Figure 1.20. Between the distances from 2.85 to 3.75 Å, oxygen and carbon atoms were detected, most probably from the acetic acid. The different results obtained from these related studies emphasise that the solution conditions may significantly influence Fe(III)PPIX speciation.
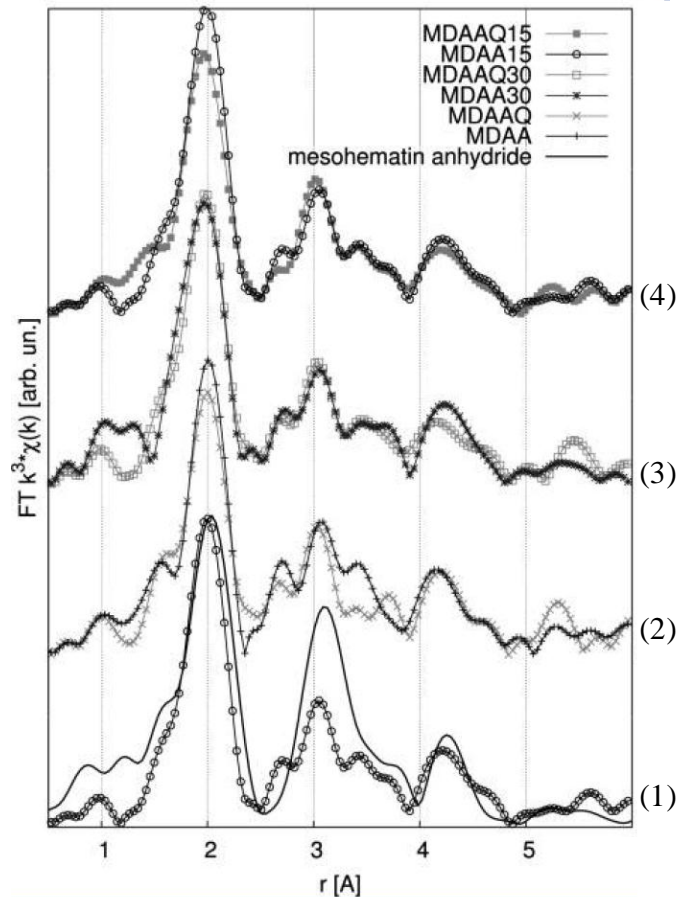
Figure 1.20 Experimental EXAFS spectra of mesohaematin anhydride dissolved in acetic acid, MDAA. The inclusion of CQ in a solution is indicated by a Q in the species key, while the inclusion of water is indicated numerically, the percentage ranging from 15-30 % (*v/v*). (1) EXAFS spectra of mesohaematin anhydride microcrystalline powder phase (solid line) and compared to MDAAQ30. (2) EXAFS spectrum of MDAA compared to that of MDAAQ. (3) EXAFS spectrum of MDAA30 compared to that of MDAAQ30. (4) EXAFS spectrum of MDAA15 compared to that of MDAAQ15. Reproduced from reference.[51]

1.5.2   Haemozoin Formation *In Vivo*

It is suspected that haemozoin is formed *via* biocrystallisation, a process in which living organisms form crystalline materials from organic macromolecules.[52] While not completely understood, the formation of haemozoin is a highly efficient manner of detoxifying the Fe(III)PPIX released during haemoglobin degradation inside the host's red blood cell, and involves transformation between different Fe(III)PPIX species.

1.5.2.1   The Role of Proteins in Haemozoin Formation

The role that different proteins may play in haemozoin nucleation and formation has been studied for some time. Sullivan *et al.*[53] put forward the idea that histidine-rich proteins (HRP), especially HRP-2 and HRP-3, are capable of catalysing haemozoin formation. Papalexis *et al.*[54] showed that the concentration of HRP-2 in the parasite's food vacuole (FV) is too low to support catalytic activity. The idea that HRP are required to catalyse haemozoin formation was eventually dismissed when it was shown that haemozoin crystals are still able to form in the absence of HRP-2 and HRP-3.[55] The involvement of a haem detoxification protein (HDP) has been questioned more recently.[56] This protein was shown to be extremely potent in converting haem into haemozoin, and is transported to the FV *via* endocytosis of host cytosol in the same way in which haemoglobin is deliverd to the FV. It was hypothesised that HDP can mediate the formation of haemozoin dimers and then deliver these dimers to lipid nonospheres where stacking can lead to haemozoin crystal growth.[56]

1.5.2.2   The Role of Lipids in Haemozoin Formation

When Fitch *et al.*[57] investigated purified lipids, they found that arachidonic, linoleic, oleic, palmitoleic acids, mono- and di-oleoylglycerol were able to promote β-haematin formation. Tri-oleoylglycerol, cholesterol, di-oleoylphosphatidylethanolamin, and both stearic and palmitic acids were inactive in promoting β-haematin formation. Based on the results the authors suggested that lipids co-precipitate with monomeric Fe(III)PPIX in the acidic FV, allowing Fe(III)PPIX to dissolve in the lipid and be converted into haemozoin. Recent studies have shown that the formation of haemozoin most likely takes place inside neutral lipid bodies. Jackson *et al.*[58] first characterised the lipid environment using Nile

Red (a fluorescent hydrophobic probe), electron microscopy and spectral imaging confocal microscopy. A population of neutral lipids closely associated with the DV of the parasite was identified, and analysis of these lipids indicated that these neutral lipid bodies are composed predominantly of mono- and di-acylglycerols. Mono-, di- and triacylglycerol were subsequently found to promote β-haematin formation.[58] In a subsequent review published by Coppens and Vielemeyer,[59] haemozoin crystals were observed within a lipid body for the first time (Figure 1.21 (a)). Pisciotta *et al.*[60] set out to investigate the role of neutral lipid nanospheres in haem crystallisation by *P. falciparum,* and demonstrated that neutral lipid nanospheres present within the digestive vacuole are the most likely *in vivo* site of haemozoin formation (Figure 1.21 (b)). Upon analysis, significant amounts of the saturated lipids monostearic glycerol (MSG) and monopalmitic glycerol (MPG) were found in association with haemozoin.
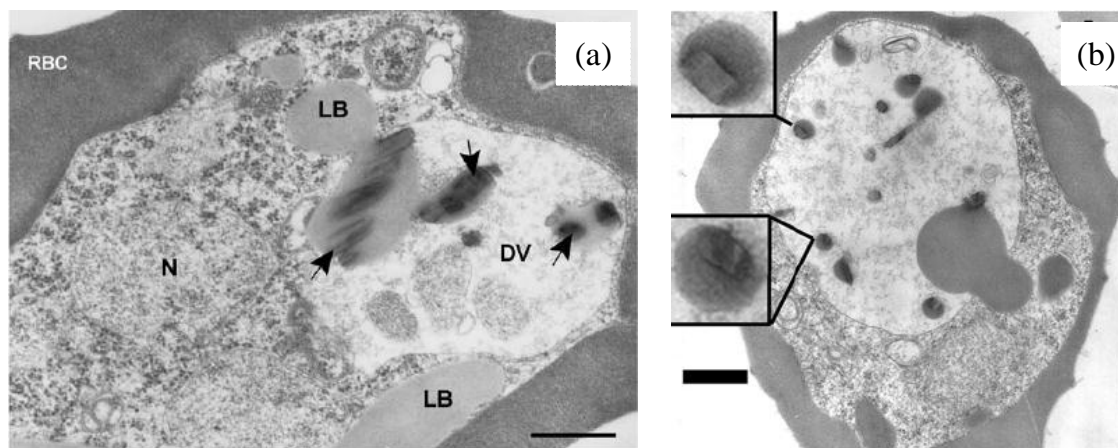
Figure 1.21 (a) Within a parasitised red blood cell (RBC), haemozoin crystals are observed in association with neutral lipid bodies (LB) inside the digestive vacuole (DV). The arrows indicate a close association of haemozoin crystals within the lipid body. N indicates the parasite nucleus. Scale bar 0.5 µm. Reproduced from reference.[59] (b) TEM image of an early trophozoite stage during the life cycle of *P. falciparum*. Haemozoin crystals are surrounded by the neutral lipid sphere inside the digestive vacuole of the malaria parasite. The inset shows no sign of a bilayer membrane surrounding the lipid. Scale bare 1.0 µm. Reproduced from reference.[60]

Oliveira *et al.*[61] have also shown that haemozoin formation occurs inside lipid droplet-like particles in both *Schistosoma mansoni* and *Rhodnius prolixus*. These two organisms also detoxify Fe(III)PPIX in the same manner as the malaria parasite, and TEM images of these organisms show haemozoin crystals inside lipid droplets and membrane bound vesicles respectively (Figure 1.22).
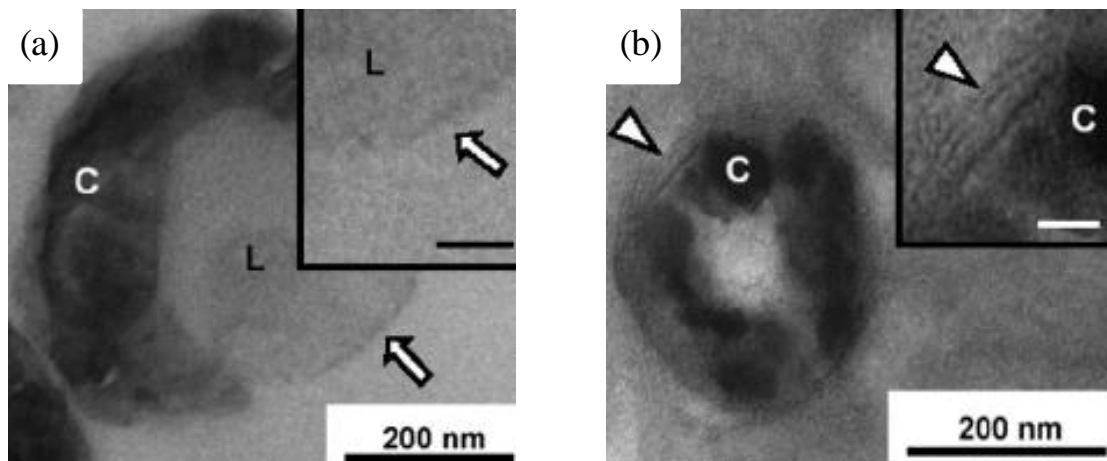
Figure 1.22 TEM images of haemozoin crystals (C) in (a) *S. Mansoni* inside lipid droplets (L) and (b) *R. Prolixus* inside membrane-bound vesicles. Inset shows higher magnification with scale bar 25 nm. Reproduced from reference.[61]

More recently an alternatively proposal has been put forward that haemozoin nucleation may occur at the DV inner membrane, rather than at the surface of lipid droplets. Kapishnikov *et al*.[62,63] set out to investigate the location and orientation of haemozoin using cryogenic soft X-ray tomography and 3D electron microscopy, to better understand the nucleation process involved in haemozoin formation. They proposed that a thin layer of lipid is coating the DV membrane from within, possibly serving as the active site for haemozoin nucleation, and that crystal growth take place in the aqueous environment in the DV. The role that membrane fragments may play in the formation of haemozoin was put forward by Hempelmann *et al*.,[64] after they showed TEM images of a membrane fragment in close association with haemozoin crystals.

During the parasite's residency inside host RBCs (Figure 1.23), the formation of haemozoin in the parasite's DV is supposed to take place at various locations, including the bulk aqueous phase (1), the bulk lipid phase (2), or at any of the three interfaces: (3) aqueous-lipid, (4) lipid-membrane and (5) aqueous-membrane.
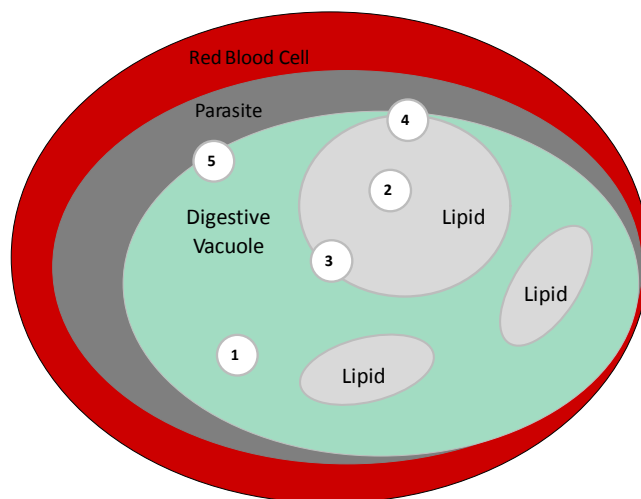
Figure 1.23 Schematic indicating the possible location for haemozoin nucleation inside the DV. 1 – The bulk aqueous phase. 2 – Inside lipid nanospheres. 3 – At the lipid-water interface. 4 – At the interface between the DV membrane and lipid phase, and 5 – at the interface between the DV membrane and the aqueous phase. Redrawn from reference.[65]

Although there are ongoing efforts to firmly establish where the haemozoin crystals are located once formed and what direction crystal growth takes place in, the overall body of data emanating from recent studies support the involvement of lipids and strongly suggest that crystal nucleation is associated with a lipid-water interface. This cumulative body of evidence shifts the intracellular microenvironment of Fe(III)PPIX crystallisation from a polar aqueous environment to a non-polar neutral lipid environment.

1.5.3 Formation of Synthethic Haemozoin (β-Haematin)

1.5.3.1 Non-Biological Methods for β-Haematin Synthesis

The process of β-haematin formation can be followed in the laboratory, however, the majority of methods used to date have relied on non-biological conditions.[66,67] Bohle and Helms described the synthesis of β-haematin by dehydrohalogenation of haemin, where β-haematin was formed in 12 hours at 22 ^{o}C from a solution of haemin (Cl-Fe(III)PPIX) dissolved in methanol and 2,6-lutidine under anhydrous conditions.[66] Slater et $al.$[30] synthesised β-haematin from haematin dissolved in 0.1 M NaOH and precipitated Fe(III)PPIX by adding acetic acid; the reaction was run over night at 70 ^{o}C, and the precipitate was washed multiple times with water.

Egan *et al.*[68] reported a method by which β-haematin was formed in just one hour in acetate buffer (4.5 mM), although the procedure still called for elevated temperatures (60 ^{o}C). The authors went on to study the kinetics of β-haematin formation under these conditions and showed that the time dependence could be accounted for by fitting the data to the Avrami equation. The Avrami equation (eq. 1.1) describes how solids transform from one phase into another at a constant temperature, and it specifically describes the kinetics involved in crystallisation processes.[69,70]

$$\frac{m_R}{m_0} = e^{-zt^n} \tag{1.1}$$

In the above equation, m_R is the mass of Fe(III)PPIX remaining at time *t* compared to the initial mass m_0, *z* is an empirical rate constant, and *n* is a constant known as the Avrami constant, which is usually an integer ranging between 1 and 4. The best fit of the data to the Avrami model was when n = 4 (Figure 1.24).[68] An Avrami constant equal to 4 indicates spontaneous nucleation and crystal growth in three dimensions. On the other hand, when n = 1, the model assumes random nucleation and that crystal growth takes place in one dimension, that is crystal growth is linear. When the constant takes on intermediate values 2 or 3, random or instantaneous nucleation occur and crystal growth is rod-like or disc-like. The sigmoidal dose response curve was explained on the basis of the reaction process (β-haematin formation) taking place in three stages: induction, during which β-haematin crystal nucleation takes place, growth/propagation, during which Fe(III)PPIX is readily converted to β-haematin and termination, where available Fe(III)PPIX is fully converted to β-haematin.[71]
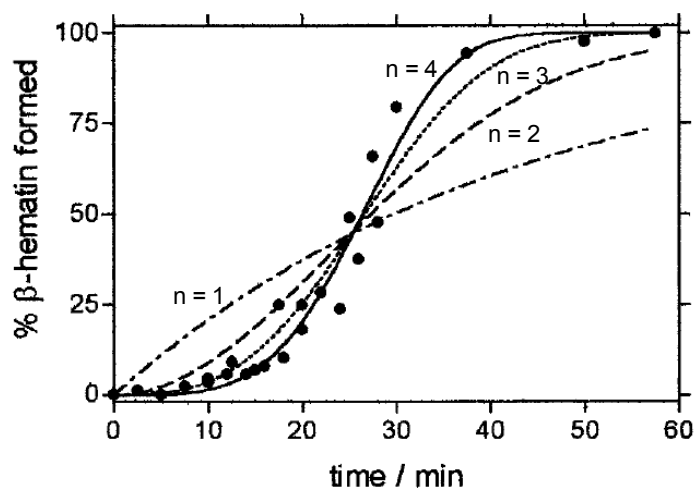
Figure 1.24 β-haematin formation in 4.5 M acetate buffer (60 $^{\circ}$C) monitored by IR spectroscopy. The best fit through the experimental data (●) was attained when n = 4 (─) in the Avrami equation. The other lines are the best fit to the data when n = 1 (– · –), 2 (– –) and 3 ($\cdots$) respectively in the Avrami equation. When the value of n is 4, this indicates spontaneous nucleation and three dimensional crystal growth. Reproduced from reference.[68]

In 2006, Egan and Tshivhase[72] described a method of β-haematin synthesis in 0.05 M benzoic acid (pH 4.5, 60 $^{\circ}$C). This method was more active in promoting β-haematin formation with the reaction completed within 100 minutes, compared to acetic acid, which at the same temperature, but at a concentration of 2.0 M would take up to 4 h to reach completion.[68] The kinetic data from this study was also fitted to the Avrami equation with n = 4, indicating that β-haematin formation involved sporadic nucleation and growth in three dimensions. It was proposed that the role of the carboxylic acid in mediating β-haematin formation was to disrupt the hydrogen bonding network between the propionate groups, the axial water molecule ligated to the Fe(III) centre of Fe(III)PPIX, as well as solvent water molecules, assisting the reorganisation of new hydrogen bonds which would facilitate β-haematin formation. The greater activity of benzoic acid compared to acetic acid was explained on the basis of the ability of benzoic acid to form π-π interactions with haematin as a result of the benzene ring. It was suggested that these π-π interactions disrupt the π-stacking between porphyrins, therefore promoting the rearrangement of the haematin aggregate to form β-haematin.[72]

1.5.3.2   Lipid-Mediated β-Haematin Formation

Given the close association of lipids with haemozoin *in vivo*, Egan *et al.*[73] set out to investigate the role played by lipids in the formation of β-haematin. Their results showed that β-haematin forms rapidly under biomimetic conditions (pH 4.8, 37 $^{\circ}$C) near octanol/water, pentanol/water and lipid/water interfaces. The half life of 5.3 min observed in the kinetics of β-haematin formation brought about at the monoglyceride lipid MMG-water interface demonstrated that the lipid-water interface may play an important role during Fe(III)PPIX crystallisation, Figure 1.25.[73] Notably, the observed kinetic profile differs from the sigmoidal profile observed in acetate, however, the data were not analysed according to the Avrami model.
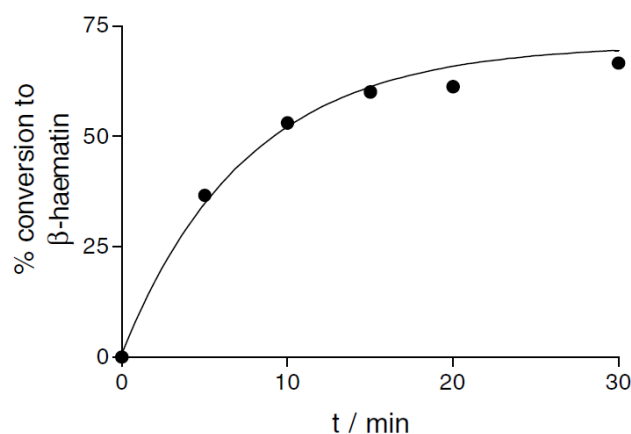
Figure 1.25 The kinetics of β-haematin formation brought about at the monoglyceride lipid MMG-water interface. The data were fitted to a first–order equation with $k = 0.13 \pm 0.02$ min^{-1}, corresponding to a half-life of 5.3 min. Reproduced from reference.[73]

Studying the abilities of different lipids, including monoglycerides (*rac*-1-monopalmitoylglycerol (MPG), *rac*-1-monostearoylglycerol (MSG) and *rac*-1-monooleoylglycerol (MOG)); diglycerides (1,3-dioleoylglycerol (DOG), 1,3-dipalmitoylglycerol (DPG) and 1,3-dilinoleoylglycerol (DLG)), triglycerides (trioleoylglycerol (TOG) and trimyristoylglycerol (TMG)) and cholesterol (CHL), to promote β-haematin formation under biologically relevant conditions (37 $^{\circ}$C, pH 4.8), Hoang *et al.*[74] showed that on average, the mono-*acyl* glycerols are 60-80% efficient in their conversion (Figure 1.26 (a)). Furthermore, they found that the rate at which β-haematin formation occurs in this lipid-water interface system is physiologically relevant

and is able to account for haemozoin formation *in vivo*,[74] with kinetic studies performed showing biologically relevant half-life values in the order of minutes for the formation of β-haematin. Using the lipid-water interface model system, they performed studies on the rate of β-haematin formation under biomimetic conditions. The reaction was shown to be complete within five minutes, with a significant amount of β-haematin formed in less than one min (Figure 1.26 (b)).
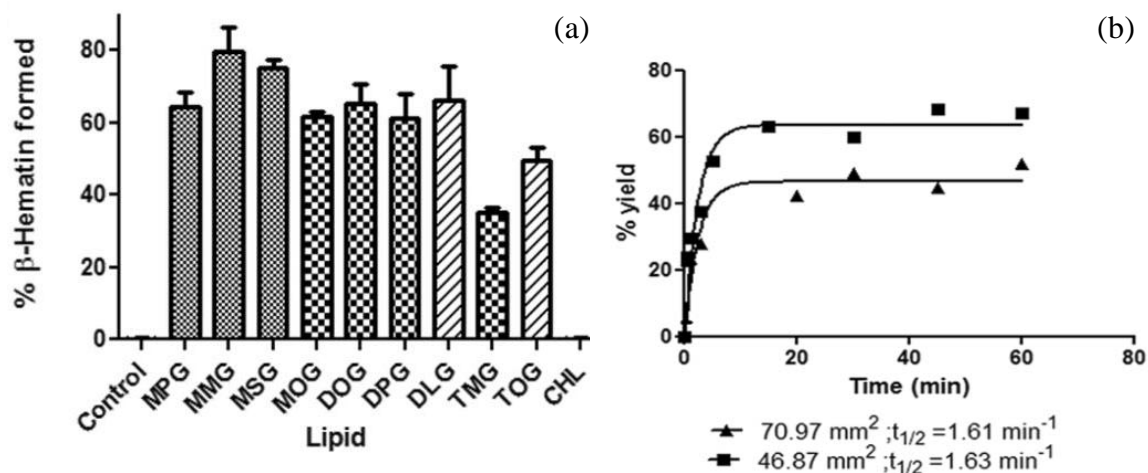
Figure 1.26 (a) The efficiency of different lipids, monoglycerides MPG, MSG and MOG; diglycerides DOG, DPG, DLG, triglycerides TOG and TMG and cholesterol (CHL), in promoting the formation of β-haematin. The percentage yield of β-haematin formation was compared after 60 minutes incubation time. The mono- and diglycerides show similar yields, while less product is formed using triglycerides. The control reaction in which Fe(III)PPIX was incubated in aqueous medium alone shows no yield. (b) The % β-haematin formed depending on the surface area of the vessel used during the reaction, demonstrates that the reaction is complete in less than 5 minutes. Reproduced from reference.[74]

TEM and fluorescence imaging data of samples recovered from just beneath the interface indicate that lipids spontaneously organise into a lipid emulsion. Following 10 minutes of incubation, Fe(III)PPIX can be seen localised near the lipid-water interface. The presence of β-haematin crystals was confirmed by infrared spectroscopy and powder X-ray diffraction. TEM imaging of Fe(III)PPIX-lipid samples (using both MPG and MSG) indicates that β-haematin forms at the interface (Figure 1.27), in keeping with observations of haemozoin crystals *in vivo*.
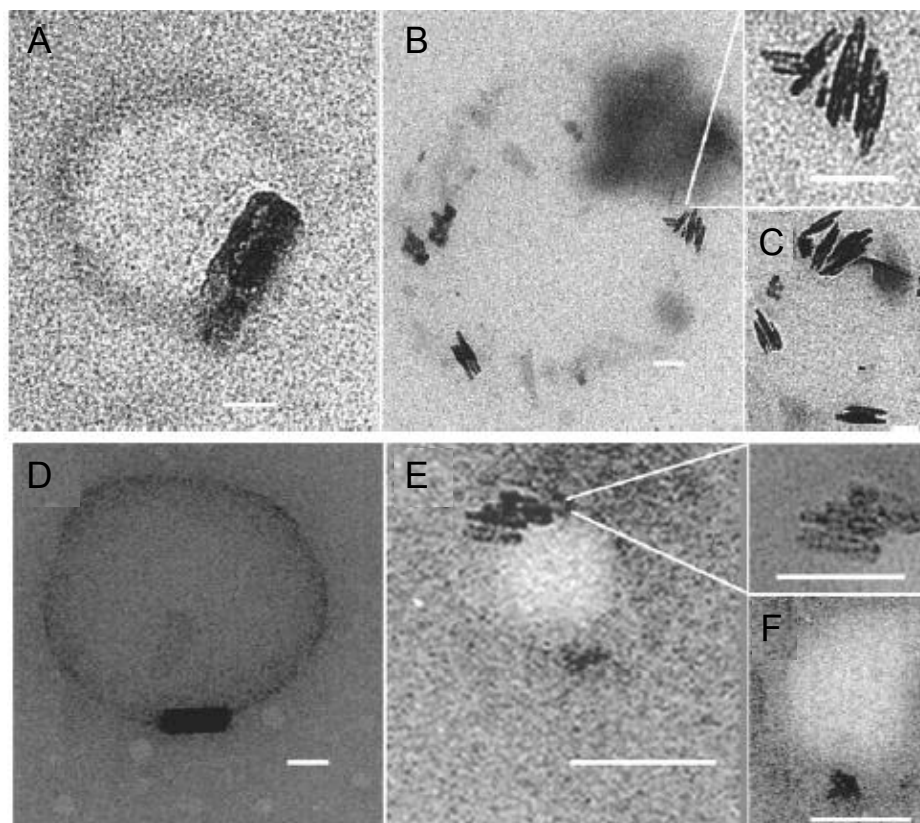
Figure 1.27 TEM images of β-haematin formed between the MPG-water (A-C) and MSG-water (D-F) interface. Samples were analysed following 10 min of incubation. In both cases β-haematin crystals were observed along the lipid-water interface (A and D) with clusters of β-haematin crystals oriented parallel to each other at the interface (B, C, E and F). Reproduced from reference.[74]

More recently, Ketchum *et al.*[65] investigated the crystallisation of β-haematin from aqueous buffer (pH 4.8) and water-saturated octanol to mimic the environment of the lipid nanosphere. Based on the observed crystal morphologies from the aqueous and water-saturated octanol environments respectively (Figure 1.28), only the morphology of the β-haematin crystals grown at the water-saturated octanol interface resembles the morphology of haemozoin crystals as they are formed *in vivo*. They also showed that haematin solubility in the pure aqueous solution (pH 4.8) is almost four times lower than at the water-saturated octanol interface, suggesting therefore that crystallisation from the water-saturated octanol interface would be faster.
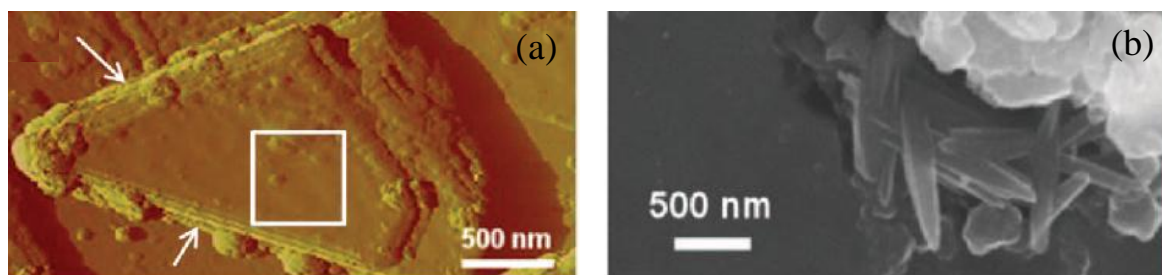
Figure 1.28 β-haematin crystal morphology. (a) AFM image of the crystalline material grown from aqueous solution at pH = 4.8 in 0.1 M acetate buffer. (b) SEM image of a cluster of crystals grown at the interface of aqueous citrate buffer (pH 4.8) and water-saturated octanol. The morphology of the crystals obtained from the aqueous solution is distinctly different to haemozoin crystal extracted from malaria-infected red blood cells. Reproduced from reference.[65]

Huy *et al.*[75] recently investigated the association of phospholipid with synthetic haemozoin (β-haematin), since the lipid membrane of the digestive vacuole has recently been implicated in haemozoin formation *in vivo*.[60] β-haematin crystals grown from haem solutions incubated with phospholipid in an acetate buffer (pH 4.8) were investigated by cryo-TEM, and indeed showed evidence of being surrounded by a lipid membrane (Figure 1.29).
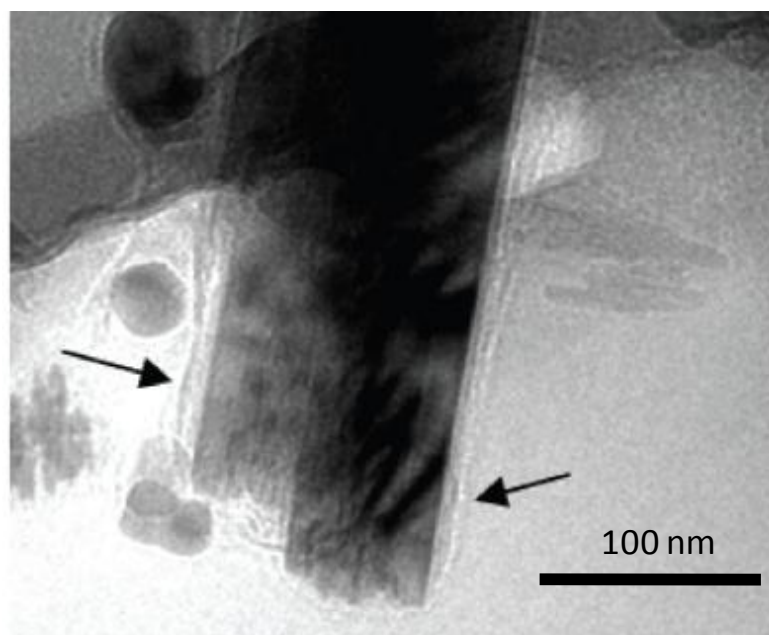
Figure 1.29 β-Haematin crystals grown from haem (Fe(III)PPIX) incubated with phospholipid in an acetate buffer (pH 4.8). The arrows indicate the monolayers of phospholipids that surround the β-haematin crystals. Reproduced from reference.[75]

1.5.3.3   Detergent-Mediated Formation of β-Haematin

Owing to cost considerations, detergents have been investigated as substitutes for the lipid environment in which both haemozoin and β-haematin formation takes place. In 1999 Fitch *et al.*[57] showed that detergents such at Tween 80, n-octyl-glucopyranoside and sodium dodecyl sulfate (SDS) were active in promoting β-haematin formation, presumably by helping dissolve monomeric Fe(III)PPIX. Recently, the detergent nonyl phenoxypolyethoxylethanol (NP-40) has been found to be a good candidate to develop an assay to search for new inhibitors of β-haematin formation.[76] Most recently, Sandlin *et al.*[77] have made use of this lipophilic detergent NP-40 based assay to promote β-haematin formation as part of a screen to identify inhibitors of β-haematin formation.

1.5.4   Theoretical Investigations of Haemozoin Formation

1.5.4.1   Fe(III)PPIX in Aqueous Solution

The varied speciation of Fe(III)PPIX in solution has made it difficult to rationalise which species is more relevant in haemozoin formation and which species is more relevant to drug action. Therefore, due consideration of this complexity is required before undertaking any investigation. On the basis of the IR spectrum of the green material precipitated from aqueous solution under basic conditions, Brown *et al.*[78] put forward the idea that Fe(III)PPIX exists in aqueous solution as a μ-oxo dimer (whereby the iron centres are linked *via* an oxo (Fe–O–Fe) bridge). Having been widely accepted in the literature for more than 30 years, this idea was recently overturned. A model of aqueous Fe(III)PPIX whereby molecules interact through π-π or stacking interactions, more specifically *via* non covalent interaction of the unligated faces to form a π-π dimer with the axial ligands pointing outwards, was proposed.[79] This conclusion was based on the UV-visible spectrum of aqueous Fe(III)PPIX, showing the typically broad and weak Soret band, which has been attributed to dimerisation. These observations were not consistent with the spectrum of the μ-oxo dimer, induced in 0.1 M NaOH containing 10% (*v/v*) pyridine (Figure 1.30).[80]
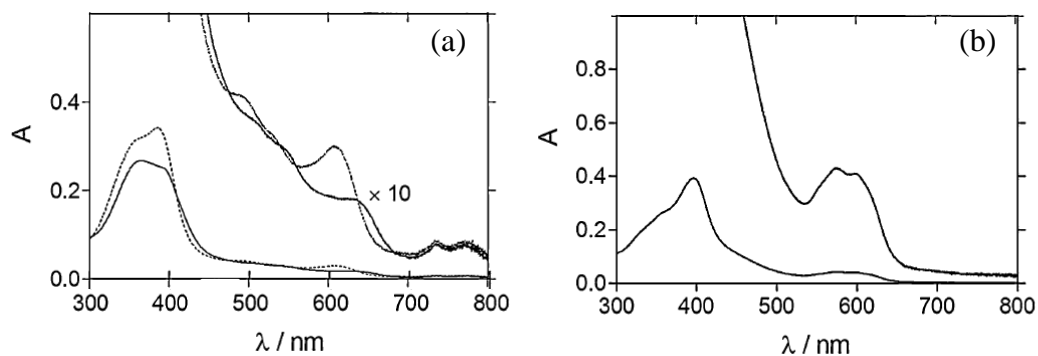
Figure 1.30 The speciation of Fe(III)PPIX in solution. (a) The UV-visible spectrum of 7 μM Fe(III)PPIX in aqueous solution at pH 6.029 (solid line) and at pH 9.669 (dotted line). The weak and broad Soret band has been attributed to dimerisation and does not reflect the characteristics of the μ-oxo dimer species. (b) The UV-visible spectrum of the μ-oxo dimer of Fe(III)PPIX, induced in 0.1 M NaOH containing 10% (*v/v*) pyridine. Reproduced from reference.[79]

The ^{1}H NMR spectrum of aqueous Fe(III)PPIX was shown to be characteristic of a five-coordinate, high-spin Fe(III)PPIX species, with broad peaks as far downfield as 50-60 ppm due to the paramagnetic iron centre. It is quite dissimilar to that of either the six-coordinate species formed spontaneously in DMSO or the μ-oxo dimer (Figure 1.31). Due to antiferromagnetic coupling *via* the oxo-bridge, the ^{1}H NMR spectrum of the latter species falls within the normal 0-10 ppm range. Magnetic susceptibility measurements indicated that there is no antiferromagnetic coupling in the aqueous (π-π) dimer, with an average magnetic moment, μ, per Fe(III) centre of 4.21 compared to 1.04 for the μ-oxo dimer.
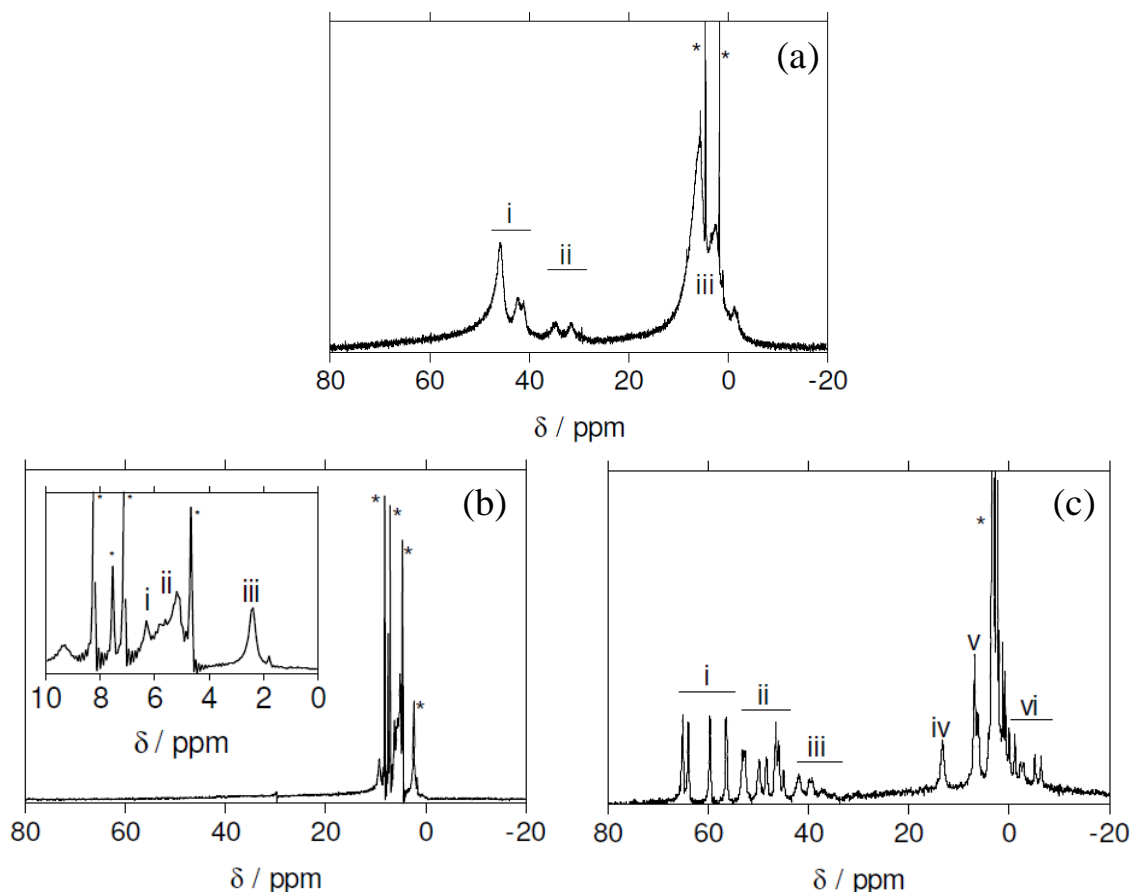
Figure 1.31 (a) The ^{1}H NMR spectrum of aqueous Fe(III)PPIX. The peaks were assigned based on the design by Budd *et al*:[81] *i* methyl groups, *ii* vinyl α-CH and α-CH$_2$ and *iii cis* and *trans* vinyl β-CH$_2$ and propionyl β-CH$_2$ peaks. (b) The ^{1}H NMR spectrum of μ-oxo dimer of Fe(III)PPIX, induced in 10% (*v/v*) aqueous pyridine-*d$_6$* in 0.1 M NaOD/D$_2$O. Peaks are assigned as *i* propionyl α-CH$_2$, *ii* methyl groups and *iii* propionyl β-CH$_2$. (c) The ^{1}H NMR spectrum of Fe(III)PPIX in DMSO-*d$_6$*. Peaks are assigned as *i* methyl groups, *ii* vinyl α-CH, *iii* porphyrin *meso* H, *iv* propionic acid COOH group, *v* propionyl β-CH$_2$ and *vi cis* and *trans* vinyl β-CH$_2$. Asterisks indicate solvent signals. Reproduced from reference.[79]

The proposed π-π dimer structure was supported by X-ray crystal structures of haemin (Cl-Fe(III)PPIX)[82] and aqua-iron(III)octaethylporphyrin perchlorate [Fe(OEP)(H$_2$O)]ClO$_4$,[83] (Figure 1.32).

35
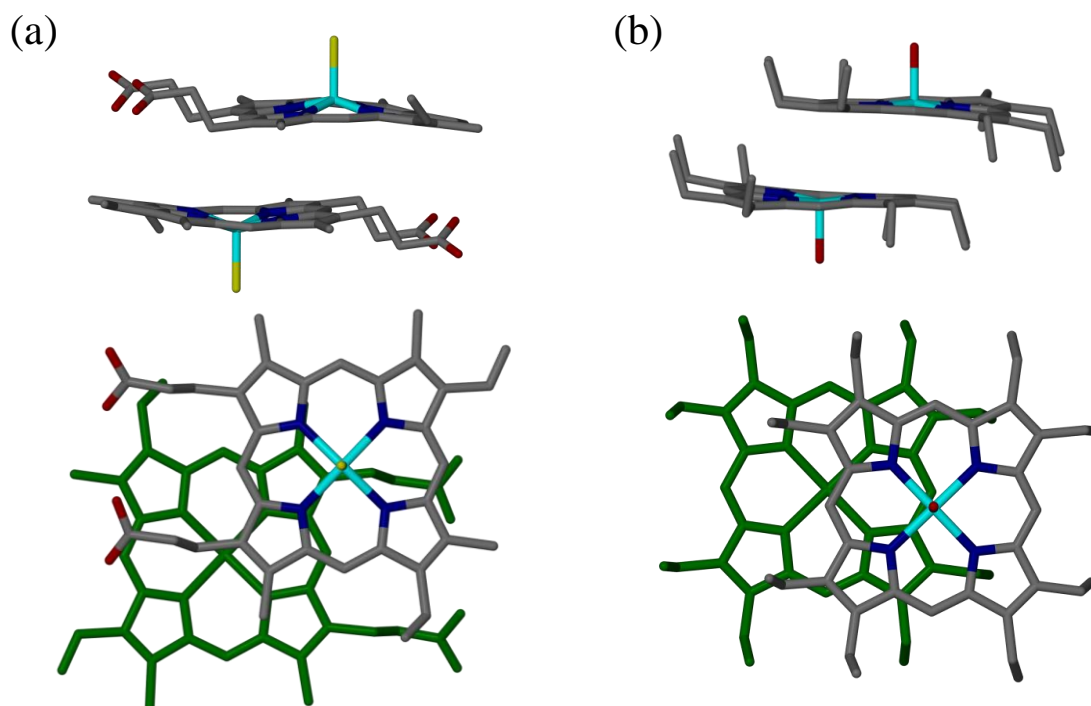
Figure 1.32 A model of the aqueous π-π dimer is supported by the single crystal X-ray structures of (a) haemin (Cl-Fe(III)PPIX),[82] and (b) aqua-iron(III)octaethylporphyrin perchlorate [Fe(OEP)(H$_2$O)]ClO$_4$,[83] viewed from the side (top), and top (bottom) in each case. The structures were accessed from the Cambridge structural database,[84] using reference codes CHEMIN and HECZUK respectively, and show significant lateral displacement between the two porphyrin molecules relative to one another.

1.5.4.2 Theoretical Modelling of β-Haematin Formation

The new insight into the speciation of aqueous Fe(III)PPIX, namely a π-π dimer, had direct implications for understanding the mechanism of haemozoin formation, since haemozoin formation from a μ-oxo dimer species, where the propionate coordination sites are blocked, is difficult to comprehend. The π-π dimer species provides a rational pathway to propose how aqueous Fe(III)PPIX may be incorporated into haemozoin.

Using molecular dynamics simulations, Egan *et al.*[73] provided insight into the mechanism by which haemozoin may form, and the role that lipids may play in the process (Figure 1.33). The authors explain that the competitive hydrogen bonding of the water molecules weakens as the hydrophobic Fe(III)PPIX π-π dimer enters the lipid layer. The negatively charged propionate group is then attracted to the positively charged Fe(III) centre to form the β-haematin precursor (Figure 1.33 (b)). Subsequent bond formation between the Fe(III)

centre and the propionate group, together with the release of the axial water ligands, is all that is needed in order for the precursor to convert to the β-haematin (haemozoin) dimer.[73]
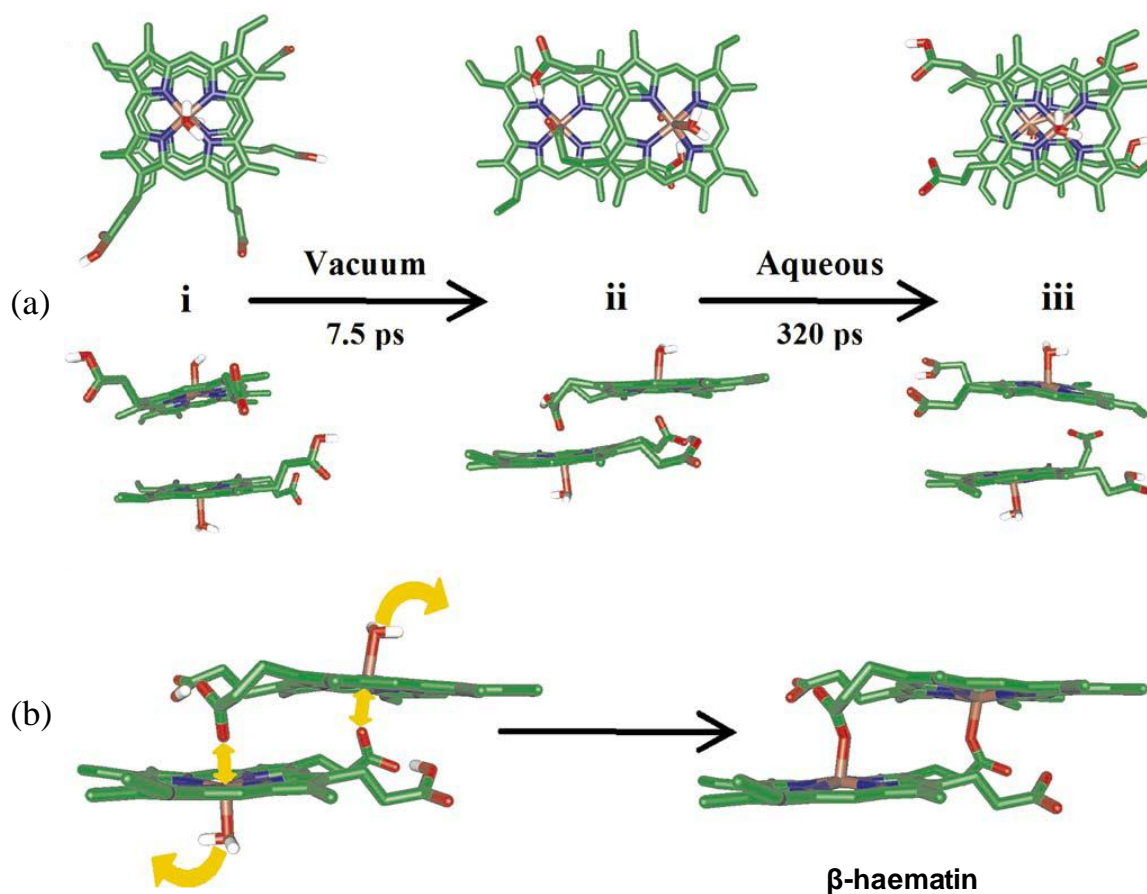
Figure 1.33 Molecular dynamics simulation of the interaction of two H_2O-Fe(III)PPIX molecules. Solvent water molecules are not shown for clarity. (a) The simulation was started with the molecules placed in a back-to-back arrangement (as expected for a π-π dimer), with the propionate and propionic acid groups extended from the porphyrin core and far away from each other (i). The β-haematin precursor is rapidly formed *in vacuo* (ii). In a simulated aqueous environment, the β-haematin precursor very quickly breaks down, and the propionate groups again interact with the solvent molecules (iii). Enlarged in (b), the simulation suggests the coordination of the propionate groups with the Fe(III) centre and loss of axial H_2O ligand that needs to take place in order for the precursor dimer to convert over to the β-haematin dimer. Reproduced from reference.[73]

Hempelmann explained that in order to form the iron-propionate bond under aqueous conditions, non-physiological temperatures or ionic strength would be required to grow β-haematin crystals *in vitro*.[64] In the lipid environment, however, the iron-propionate bond is likely to be more stable owing to a low water concentration. Furthermore, hydrogen

bonding between propionic acid side chains is more likely, whereas in aqueous solutions, the high concentration of water would have a higher probability of interacting with the propionic acid group.

1.5.4.3 Fe(III)PPIX in Non-Aqueous Solution

The π-π dimer species provides a rational pathway to propose how aqueous Fe(III)PPIX may be incorporated into haemozoin (Figure 1.34, 1). Molecular dynamics simulations *in vacuo* have shown that as Fe(III)PPIX enters a low dielectric medium such as a lipid environment,[73] it most likely forms an intermolecular precursor to haemozoin (Figure 1.34, 2) which then converts to the haemozoin dimer by coordination of the propionate groups with the Fe(III) and displacement of H_2O ligands (Figure 1.34, 3). The haemozoin crystal is formed upon hydrogen bonding between these dimers (Figure 1.34, 4).[85]
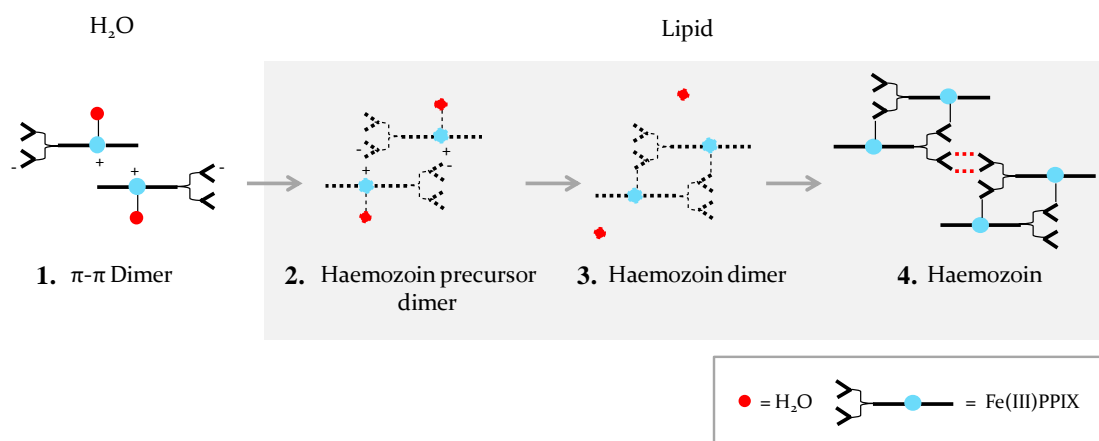
Figure 1.34 A schematic representation showing the proposed route of haemozoin formation (1-4). (1) As the aqueous π-π dimer enters the lipid environment (2) the haemozoin precursor dimer is formed. (3) Coordination of the propionate groups with the Fe(III) centre and displacement of H_2O ligands forms the haemozoin dimer. (4) The haemozoin crystal is formed upon hydrogen bonding between these dimers. Redrawn from reference.[85]

In a recent publication by Asher *et al.*,[86] the speciation of Fe(III)PPIX in aqueous and mixed aqueous solutions was investigated. In different solvent environments, and depending on temperature, concentration, pH, the presence of salts and the solvent used, Fe(III)PPIX was shown to exist as a monomer, π-π dimer, μ-oxo dimer or π-stacked aggregate of μ-oxo dimers (Figure 1.35). It was also shown that conversion between the μ-oxo dimer and π-π dimer is fully reversible in mixed aqueous solution. A 10-fold dilution

of a 3×10^{-4} M solution of the µ-oxo dimer of Fe(III)PPIX in aqueous DMSO (5.64 M, pH 10) into the same concentration of aqueous methanol gave rise to spectral changes which were consistent with the π-π dimer (Figure 1.35 II and III) and *visa versa*. Furthermore, aprotic solvents such as 5.64 M DMSO, acetone, dimethylformamide (DMF), tetrahydrofuran (THF) and 2,6 lutidine at pH 10 were shown to promote µ-oxo dimer formation while protic solvents such as methanol, ethanol, propanol, ethylene glycol, diethylene glycol and formamide, at the same concentration and under the same conditions, gave rise to π-π dimer formation.
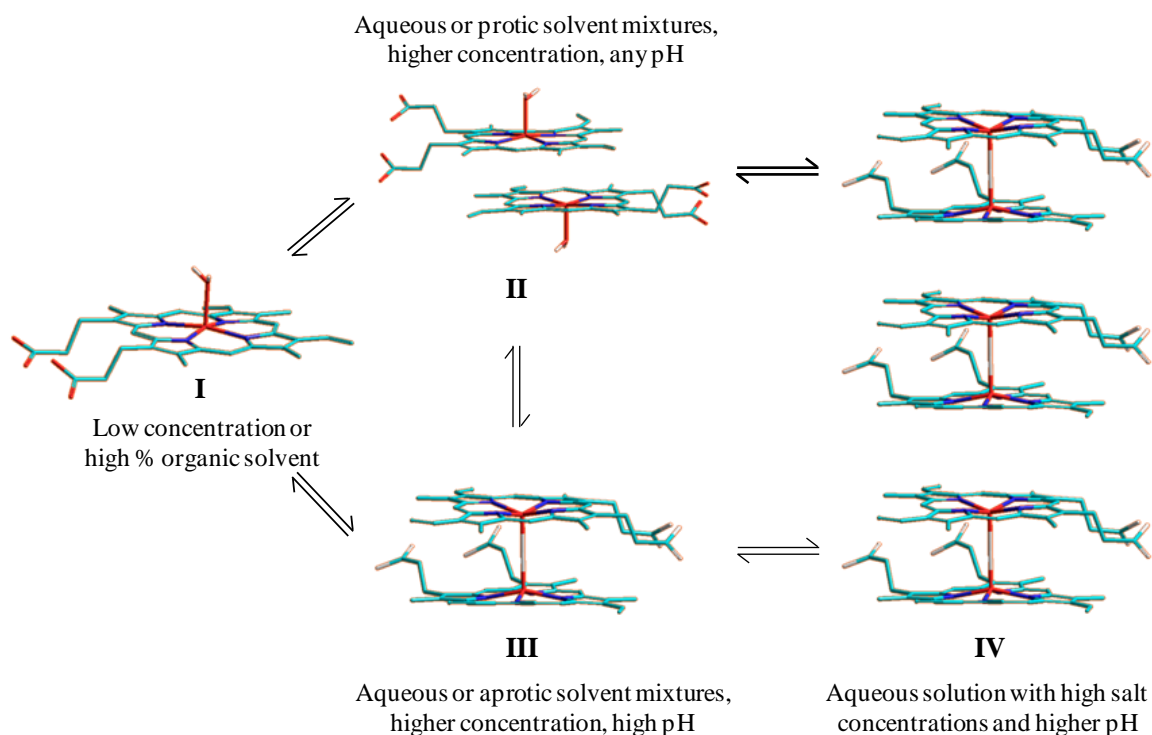
Figure 1.35 The speciation of Fe(III)PPIX species in aqueous and mixed aqueous solution. The following species are shown in equilibrium: (I) monomer, (II) π-π dimer, (III) µ-oxo dimer and (IV) larger aggregate of µ-oxo dimers. Redrawn from reference.[86]

Despite the structure of β-haematin (haemozoin) having been determined from powder X-ray diffraction, the mechanism by which the parasite crystallises Fe(III)PPIX remains poorly understood.

All these methods for synthesising β-haematin have come a far way in order to improve our understanding of haemozoin formation *in vitro*. The recent studies in particular indicate the significant role of lipid involvement in haemozoin formation. The kinetic studies performed in lipid-water interface model systems have returned biologically-relevant half-life values in the order of minutes for the formation of β-haematin.[73, 74,87] Interestingly, the activity of drugs has not been studied in detail in this system; given that biologically-relevant kinetics of β-haematin formation have been demonstrated, it would seem an ideal system to investigate in order to probe Fe(III)PPIX-drug interactions, which may aid in understanding the antimalarial mechanism of action.

1.6   Quinoline Antimalarial Drugs

1.6.1   History of Discovery

Extracted from the bark of the South American *Cinchona* tree, quinine was the first antimalarial drug used in western medicine and has since been in use for more than 300 years.[1] Quinine and related quinoline antimalarial drugs (Figure 1.36) have been the most successful class of antimalarial drugs to date.
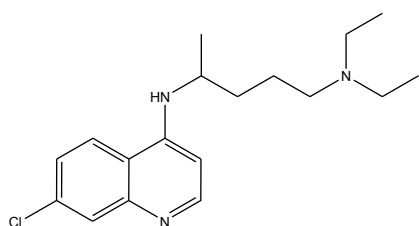
Chloroquine (CQ)
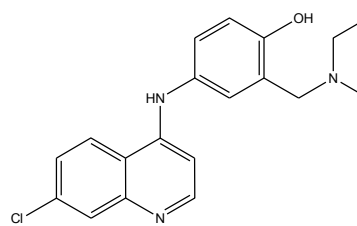
Amodiaquine (AQ)
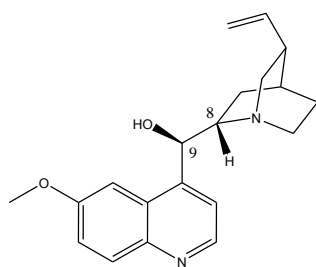
Quinine (QN): 8S, 9R
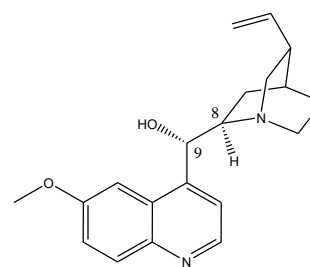
Quinidine (QD): 8R, 9S
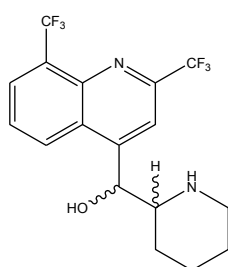
Mefloquine (MQ)
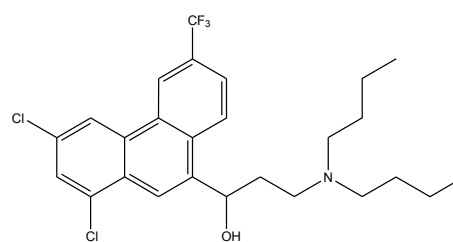
Halofantrine (Hf)

Figure 1.36 Molecular structures of a selection of important quinoline (CQ, AQ, QN, QD and MQ) and phenanthrene (Hf) antimalarial drugs.

1.6.1.1   Quinoline Methanol Antimalarial Drugs

Medicinal properties of the *Chinchona* bark date back to the 1560s. The *Cinchona* alkaloids (Figure 1.37 (a)) are a group of naturally occurring quinoline methanol stereoisomers. Quinine (QN, 8*S*, 9*R*) and quinidine (QD 8R, 9S) are active antimalarials with a *erythro* orientation (diastereomers with identical substituents on the same side), while 9-epiquinine (EQN, 8S, 9S) and 9-epiquinidine (EQD, 8R, 9R) are inactive with a *threo* orientation (diastereomers with identical substituents on opposite sides).[88] This difference in activity between the alkaloids is also reflected in their abilities to inhibit the formation of β-haematin (Figure 1.37 (b)).[89,90]

(a)

(b)

	Log $K_{association}$	IC$_{50}$ (nM)	BHIA/%
QN	4.10	29.3	84 ± 1
QD	5.02	13.4	85 ± 9
EQN	4.04	3471	2 ± 13
EQD	4.37	2700	12 ± 12
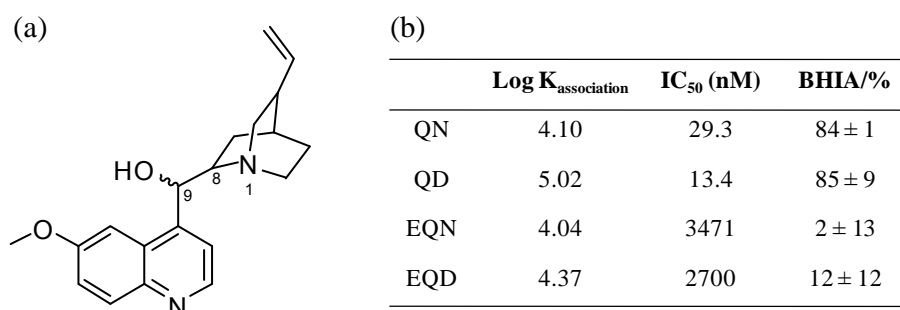
Figure 1.37 The *Cinchona* alkaloids. (a) Molecular structures of the *Cinchona* alkaloids quinine (QN, 8*S*, 9*R*), quinidine (QD, 8*R*, 9*S*), 9-epiquinine (EQN, 8*S*, 9*S*) and 9-epiquinidine (EQD, 8*R*, 9*R*). (b) Table of relative strengths of association in solution (Log K),[91,92] biological activity (IC$_{50}$) values against the CQ-sensitive strain (D-6),[88] and β-haematin inhibitory activity (BHIA).[89]

Compounds shown to inhibit β-haematin formation are able to form association complexes in solution,[90,92-94] however, not all compounds that form complexes with Fe(III)PPIX in solution are able to inhibit β-haematin formation.[95,96] As shown in Figure 1.37 (b), all the *Cinchona* alkaloids have comparable association constants, but when comparing the IC$_{50}$ and β-haematin inhibitory activity (BHIA) values, it is apparent that only QN and QD are active antimalarials and are able to inhibit β-haematin formation effectively.

Mefloquine (MQ), a synthetic analogue of QN, was synthesised in the 1970's and sold under the trade name Lariam. The drug had a promising future, due to it having a longer half-life and being safe to use during pregnancy.[97] However, MQ is now known for its neuropsychiatric side effects, and resistance to this drug has limited its accessibility. Today, MQ is most commonly prescribed in combination with artesunate, an example of

an artemisinin-based combination therapy (ACT), and is recommended by the World Health Organisation for the treatment of malaria in areas of low transmission.[2,98]

1.6.1.2   4-Aminoquinoline Antimalarial Drugs

Chloroquine (Resochin), a synthetic analogue of the oldest known antimalarial quinine, has been the drug of choice since its development towards the end of World War II.[1] The development of CQ was motivated due to the high demand for QN which could not be met during World War II owing to the Japanese invasion of Java where *Cinchona* plantations which supplied 90% of the world's demand were located. CQ is considered the most successful antimalarial drug to date as a result of its relatively low toxicity, its ability to be used during pregnancy, and its affordability. However, with widespread chloroquine-resistant *P. falciparum,* novel antimalarial drugs are urgently needed as replacements for this and other mainstay chemotherapeutics.[3,99] Amodiaquine (AQ), similar to chloroquine was used since the 1970's and is still in use today for treatment of uncomplicated malaria.[2]

1.6.2   Site of Action

As mentioned before, the parasite is vulnerable to drug action at several points during its residency inside host RBCs.[22] Currently it is known that CQ and other quinoline anitmalarial drugs are active against the growing (trophozoite) stage of the parasite life cycle during which haemoglobin is actively digested.[100] Yayon *et al*.[101] demonstrated using fluoromicroscopic examination that antimalarial drugs accumulate in malaria infected erythrocytes. This site of action is further supported by the fact that CQ-resistant (CQR) strains show a decrease in CQ accumulation compared to CQ-sensitive (CQS) parasite.[102]

The quinoline antimalarial drugs are diprotic weak bases.[103] They find their way into the FV by a mechanism known as pH trapping.[55] In the form of a neutral weak base, CQ is able to cross membranes and enter into the FV. In the acidic environment of the FV however, the drug becomes protonated and therefore membrane-impermeable, leading to a 20 000 fold higher concentration inside the FV compared to the outside, based on the Henderson-Hasselbach equation.[104]

During the parasite's residency inside host RBCs, the parasite is vulnerable at various points to drug action, however interruption of haemoglobin degradation or Fe(III)PPPIX detoxification, have been widely considered.[22]

1.6.3   Resistance to Quinoline Antimalarial Drugs

Antimalarial drug resistance has been defined as the "ability of a parasite strain to survive and/or multiply despite the administration and absorption of drugs given in doses equal to or higher than those usually recommended but in tolerance of the subject".[105] Since the appearance of drug resistance to historically successful antimalarials, research has focused on the development of new and effective antimalarials.[106]

Chloroquine, a diprotic weak base with two proton-binding groups, the quinoline nitrogen atom (pK_{a1} = 8.1) and the side chain terminal amine (pK_{a2} = 10.2), can be driven by the pH gradient across the parasite's food vacuole membranes in its unprotonated form, to accumulate in the acidic food vacuole (FV). Resistance occurs due to an overall reduced uptake of the drug, most probably as a result of efflux out of the FV.[107] Krogstad and co-workers have shown that CQR parasites release CQ 40- to 50-fold faster than CQS parasites,[107] which leads to lower accumulation of CQ in the FV, such that the concentration is no longer sufficient to inhibit Fe(III)PPIX crystallisation. Since the pH of the FV shows no significant difference between CQS and CQR parasites,[18] the rapid efflux of CQ out of the FV of CQR parasites suggests that they have an elevated permeation pathway for CQ across the FV membrane.

It has been established that CQ resistance is associated with mutation in the pfcrt gene on chromosome 7, which encodes the *P. falciparum* CQ-resistance transporter (PfCRT). PfCRT is a 424-amino acid transmembrane protein on the surface of the food vacuole, and a mutation at position 76 in the amino acid sequence of this protein (K76T), in which the neutral, hydrophilic threonine α-amino acid (T) replace the positively charge lysine α-amino acid (K), is associated with the resistant strain.[108] A second food vacuole transporter protein associated with drug resistance, namely *P. falciparum* multidrug resistance gene 1 (Pfmdr1), is located on chromosome 5 and encodes P-glycoprotein homologue (Pgh1).[109] An over-expression of Pgh1 is associated with resistance to QN, MQ and Hf.[110] QN resistance is also connected to *P. falciparum* sodium proton exchanger (pfnhe-1),[111] however the mechanism for QN resistance is not altogether clear.

To date the mechanism by which mutated PfCRT brings about CQ resistance has not been solved. Two schools of thought exist, however, the first being that PfCRT can act as a channel (enabling protonated CQ to flow out of the FV *via* an electrochemical gradient). An alternative explanation is that PfCRT can act as a transporter (where CQ are displaced out of the FV *via* an active efflux transporter) of CQ.[104] In both of these mechanisms, the accumulation of CQ in the food vacuole is reduced below the amount needed for inhibition of haemozoin formation.

Since resistance to quinoline antimalarials does not appear to influence the formation of haemozoin, and since this crucial survival process is not under the genetic control of the parasite, haemozoin still remains a valid drug target. Furthermore, there is no equivalent process in the human host. Thus understanding the process of haemozoin formation, as well as the mechanism of action at the molecular level of the antimalarial drugs which have been and remain clinically relevant today, are important research foci if we intend to develop novel antimalarial haemozoin inhibitors.

1.6.4   Mechanisms of Action of Quinoline Antimalarial Drugs

The quinoline antimalarial drugs CQ, AQ, QN, QD and MQ are known to inhibit the formation of β-haematin under different conditions.[53,90,93,112,113] With knowledge of the crystal morphology of β-haematin, the possible role played by antimalarials in inhibiting crystal nucleation and crystal growth could be addressed. To date, the lack of any crystal structures of either Fe(III)PPIX or haemozoin/β-haematin complexed to a quinoline antimalarial has meant that Fe(III)PPIX-drug interactions have only been studied through the use of spectroscopic methods and computational analyses.

1.6.4.1   Haemozoin Crystal Capping

Regarding the inhibition of β-haematin formation, it has been hypothesised that drug compounds adhere directly to the growing surface of β-haematin crystals, thus preventing further crystal growth.[35,40,114] At the time when haemozoin was still believed to be a polymer, Sullivan *et al.*[114,115] suggested that Fe(III)PPIX-quinoline complexes were directly responsible for termination. By capping onto the growing polymer at its elongated site, the Fe(III)PPIX-drug complex would inhibit further polymer growth (Figure 1.38).
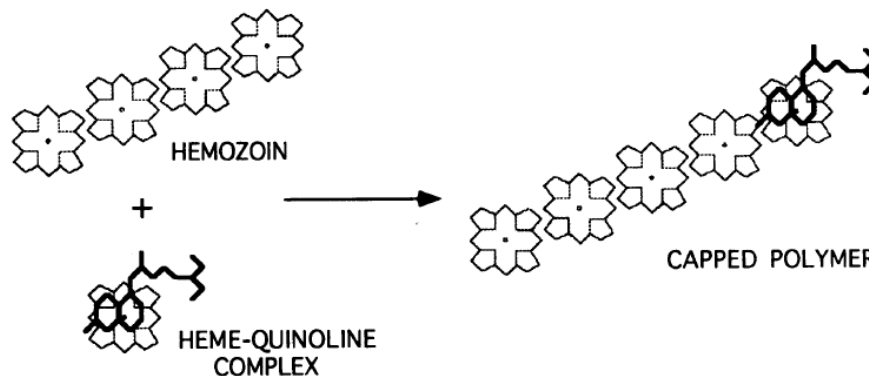
Figure 1.38 Proposed model for quinoline inhibition of haemozoin formation. The Fe(III)PPIX-drug complex at the end of the elongation site of the growing polymer prevents further addition of Fe(III)PPIX. Reproduced from reference.[114]

In a later study, and first having identified the fastest growing (001) crystal face, Buller *et al.*[40] used computational approaches to show that quinoline antimalarial drugs are able to bind remarkably well into crevices created at this face, being stabilised by exposed functional groups of Fe(III)PPIX (Figure 1.39 (a)), which include the propionic acid, methyl and vinyl groups, as well as aromatic surfaces which run parallel to the *a*-axis. In the case of CQ (monoprotonated) bound to the (001) face of the β-haematin crystal, the energetically-favourable hydrogen bonding interactions include (**1**) $N_{drug}\cdots HC=C_{porphyrin}$ 2.4 Å, (**2**) $Cl_{drug}\cdots H_3C_{porphyrin}$ 3.0 Å, (**3**) $NH_{drug}\cdots O2_{porphyrin}$ 2.7 Å and (**4**) $NH_{drug}\cdots C=C_{porphyrin}$ 2.7 Å (Figure 1.39 (b)). Due to the exocyclic amine chain of CQ being longer and more flexibile compared to the quinuclidine side chain of QN, it was reasoned that this allows for a stronger intercalation of the quinoline, such that CQ is more tightly bound within the crevices. Interestingly, the authors were able to demonstrate a correlation between the antimalarial activity of various quinolines and their theoretical binding characteristics to the (001) face of β-haematin. However, they were not able to support their results by experiment. It is important to point out that CQ, AQ, QN and MQ were only shown to be able to cap onto the (001) surface of β-haematin when only the nonprimary exocyclic amine is protonated. The authors reasoned that if CQ was also protonated at the aromatic nitrogen atom, the drug would not be able to dock effectively into the crevice. This is interesting since the drug is expected to be doubly protonated in the FV.

46

(a) (b)
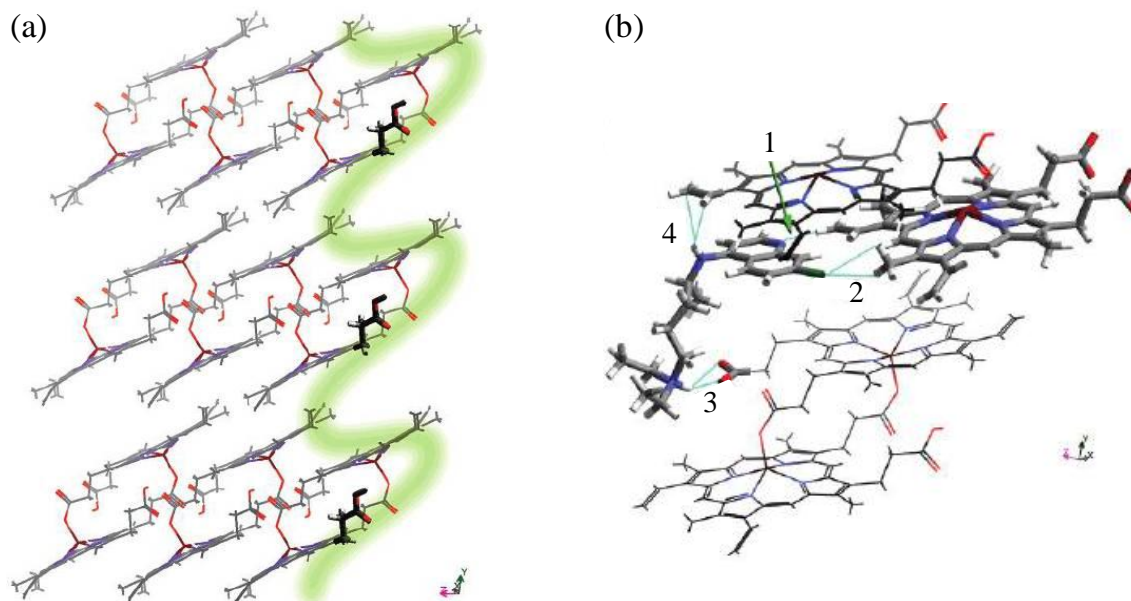
Figure 1.39 β-haematin crystal capping. (a) β-haematin, viewed along the *a*-axis, showing exposed propionic acid, methyl and vinyl groups as well as aromatic surfaces at the (001) side face, with the available crevices outlined in green. (b) Chloroquine bound to the (001) face of the β-haematin crystal, highlighting the energetically favourable hydrogen bonding interactions: (**1**) $N_{drug}\cdots HC=C_{porphyrin}$ 2.4 Å, (**2**) $Cl_{drug}\cdots H_3C_{porphyrin}$ 3.0 Å, (**3**) $NH_{drug}\cdots O2_{porphyrin}$ 2.7 Å and (**4**) $NH_{drug}\cdots C=C_{porphyrin}$ 2.7 Å. Also shown is the intercalation of the quinoline rings in between the surface of the aromatic groups of β-haematin. Reproduced from reference.[40]

1.6.4.2 Fe(III)PPIX-Drug Complexes in Solution

An alternative hypothesis is that drug compounds form complexes with free Fe(III)PPIX in the aqueous medium of the FV, either through π-stacking or coordination, therefore preventing its incorporation into β-haematin.[116,117,118] As mentioned before, with the ability of Fe(III)PPIX to exist as a precursor in the form of monomer, π-π dimer, μ-oxo dimer or even the cyclic dimer required for formation of haemozoin, there are multiple Fe(III)PPIX-drug interactions which could be of relevance in antimalarial drug activity, and investigating these would be valuable in furthering our understanding of the mode of action of quinoline antimalarials.

Using NMR inversion recovery experiments, and exploiting the paramagnetic influence of the Fe centre on drug proton resonances to map the geometries of Fe(III)PPIX-drug complexes, Leed *et al*.[119] showed that depending on the protonation state of the drug,

significant differences are observed for the Fe – H distances. Using these distances as constraints in molecular modelling, it was shown that CQ, QN and QD form non-covalent complexes in solution, irrespective of whether they are neutral, mono- or diprotonated. At the time, the μ-oxo dimer form of Fe(III)PPIX was considered to be present under aqueous conditions, and thus was modelled in the calculated structures. Interestingly, there is no evidence of QN or QD complexing directly with Fe(III)PPIX in the predicted structures. In the case of CQ, π-π interactions between the aromatic rings of the drug and the tetrapyrrole region of Fe(III)PPIX played an important role in stabilising the CQ-Fe(III)PPIX complex. In subsequent NMR experiments, de Dios *et al.*[120] proposed that CQ forms a covalent complex with monomeric Fe(III)PPIX in the solid state *via* coordination between the Fe centre of Fe(III)PPIX and the quinolinyl N atom of the drug. Using a similar method, AQ has also been shown to form π-π complex with the μ-oxo dimer form of Fe(III)PPIX, with the complex being significantly stabilised by the aromatic side chains of AQ.[121] The stoichiometry for the CQ, QN, QD and the AQ complex was determined to be 1:2 drug:Fe(III)PPIX.

By re-examining the nature of Fe(III)PPIX in aqueous solution, Casabianca *et al.*[122,123] have shown that the way in which CQ interacts with Fe(III)PPIX monomer–*μ*-oxo dimer equilibrium is quite distinct from that of QN. Their data suggests that CQ is more likely to promote *μ*-oxo dimer formation, indicating a preference to bind to the dimeric form of Fe(III)PPIX. On the other hand, QN prefers binding to the monomeric form of Fe(III)PPIX. Given that the Fe(III) centre of the *μ*-oxo dimer is five-coordinate, Behere and Goff further suggested the unlikelihood for QN to be able to coordinate to the metal of a *μ*-oxo dimeric Fe(III)PPIX.[48] In the five-coordinate Fe(III) centres in the μ-oxo dimer structure the Fe–O–Fe bonds are stronger than the monomeric five-coordinated Fe(III)PPIX species, therefore QN would not be able to coordinate to the metal of the *μ*-oxo dimeric Fe(III)PPIX.

In the 1980's, Warhurst[124] conducted spectrophotometric studies to examine the complexes of QN, QD, EQN and MQ with haemin in benzene. The results indicated direct coordination of the drug to the Fe centre of Fe(III)PPIX *via* the nitrogen atom of the quinuclidine (QN and QD) and piperidine (MQ) rings. Interestingly, no evidence of coordination was observed for the inactive drug EQN. Later on, Behere *et al.*[48] showed that QN forms a complex with Fe(III)PPIX, facilitated by coordination of the Fe centre to the deprotonated benzylic alcohol functional group of the drug in non-aqueous solutions,

generating a neutral complex in a low-dielectric medium. The hyperfine-shifted porphyrin signals in the ^{1}H NMR were distinctive for alkoxide complexes, and the authors reasoned that the strong Lewis acid and oxophilic character of the Fe(III) centre promotes alkoxide formation. The results indicated a Fe(III)PPIX-drug stoichiometry of 1:1 and no binding of QN to the μ-oxo dimer form of Fe(III)PPIX was detected.

As recently as 2011, Alumasa *et al*.[125] studied the biological activity of QN analogues lacking various functional groups. The loss of either of the quinuclidine ring or hydroxyl functional group was found to almost completely destroy activity, indicating that these groups are essential in the inhibition of haemozoin formation. They also investigated the QN-Fe(III)PPIX adduct formed under aqueous conditions (pH 6-8.5), where 2 mM haemin in 0.1 M NaOH was slowly titrated with increasing volumes of 100 mM QN stock, while monitoring the pH. After analysing the adduct by mass spectrometry and fluorescence, as well as vibrational and solid-state NMR spectroscopy, they reasoned that the resulting adduct consists of QN free base complexed with Fe(III)PPIX (Figure 1.40 (a)). It was argued that both propionic acid side chains of Fe(III)PPIX are deprotonated, given the absence of a carboxylic acid stretch in the IR spectrum of the material (Figure 1.40 (b)). Furthermore, it was proposed that a strong hydrogen bond between the quinuclidyl nitrogen and the QN hydroxyl (–OH) proton, is essential in stabilising such a complex.

(a)   (b)
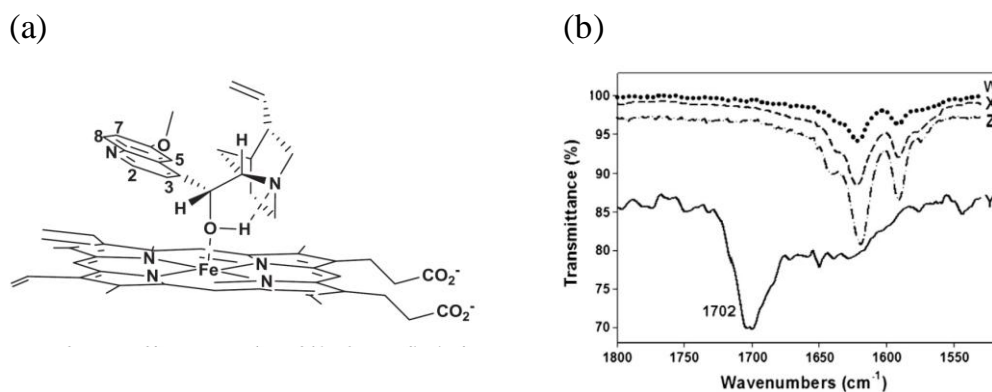
Figure 1.40 (a) The structure of the proposed QN-Fe(III)PPIX adduct. (b) IR spectra of the QN-Fe(III)PPIX adduct precipitated from aqueous solution (W, dotted line), QN free base (X, dashed line), Fe(III)PPIX (Y, continuous line), and QN hydrochloride salt (Z, dash-dot line). The strong peak at 1702 cm^{-1} in the spectrum of Fe(III)PPIX represents the carbonyl stretch of the Fe(III)PPIX propionic acid groups and is absent in the spectrum of the Fe(III)PPIX-drug adduct, reportedly indicating that the Fe(III)PPIX species has two propionate groups. Reproduced from reference.[125]

Making use of IR and Raman spectroscopy, Asghari-Khiavi *et al.*[126] provided evidence that in the solid state, CQ does not form a complex with the μ-oxo dimer. This was based on the presence of the absorption band at 878 cm^{-1} (assigned to the asymmetric stretching frequency (ν_{as}) Fe–O–Fe in the IR spectra of air dried samples of aqueous haematin and the μ-oxo dimer. The results suggest that Fe(III)PPIX samples dried from aqueous solution convert to the μ-oxo dimer form, however the basic conditions used in preparing both samples may also play a role. Nevertheless, this absorption band was absent in the case of CQ-haematin and CQ-μ-oxo dimer mixed samples (Figure 1.41).
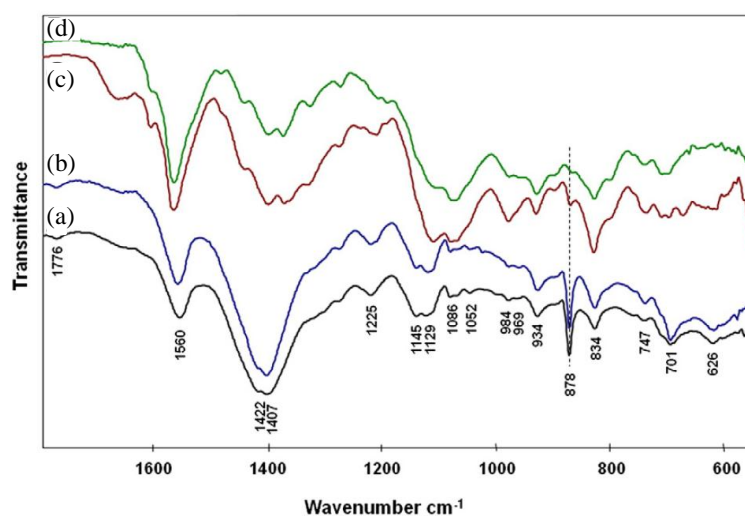
Figure 1.41 The ATR-IR spectra of (a) haematin, (b) μ-oxo dimer, (c) CQ-haematin mix and (d) CQ-μ-oxo dimer mix. Samples were air dried from aqueous solutions. The absorption band at 878 cm^{-1} observed in haematin and μ-oxo dimer is dramatically decreased in the spectra of drug-Fe(III)PPIX complexes. Reproduced from reference.[126]

Based on their Raman spectroscopy results, the band at 397 cm^{-1} in the Raman spectra of CQ-haematin mix (Figure 1.42 (c)) was attributed to the formation of an hydrogen bond between a propionate group of Fe(III)PPIX and the tertiary amino nitrogen atom of CQ.[126] No evidence was found to support the formation of hydrogen bonding between the carboxylate group and the quinuclidine (QN) or piperidine (MQ) nitrogen atom of drug compounds QN and MQ, since there was no band present at 397 cm^{-1} in the Raman spectra.[126]
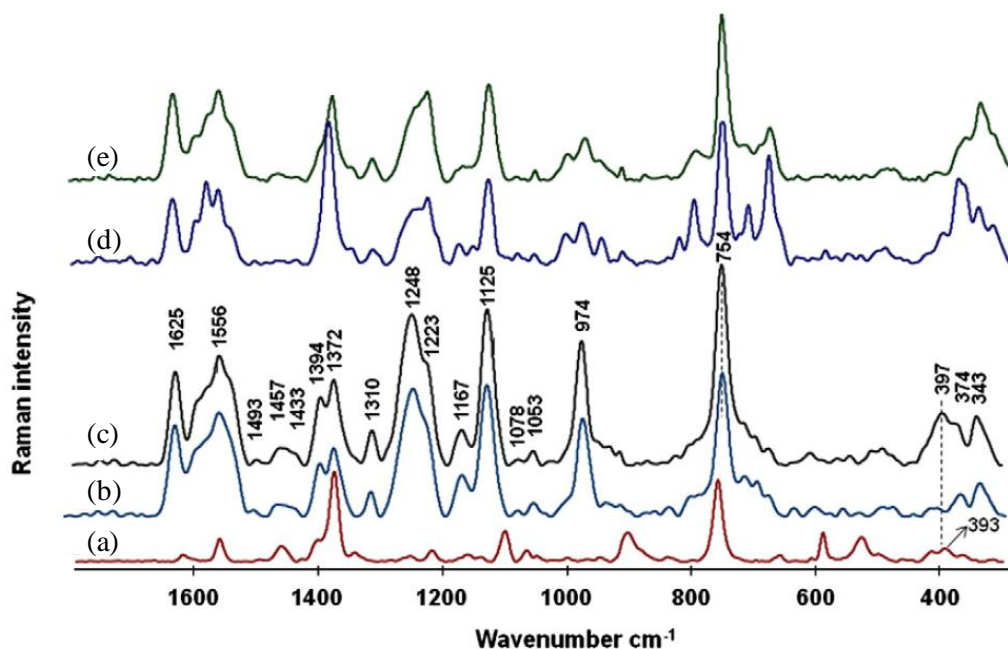
Figure 1.42 The Raman spectra of (a) CQ, (b) haematin, (c) CQ-haematin mix, (d) β-haematin and (e) crystalline haematin. The band at 397 cm^{-1} was attributed to the vibrational mode of the drug which is sensitive to hydrogen bonding around N1 and enhances due to coupling to a strong propionate band. Reproduced from reference.[126]

1.6.4.3   Structure-Activity Studies of 4-Aminoquinolines

In order to understand the inhibition activity of drug compounds, the influence of the functional groups needs to be appreciated. Egan *et al.*[95] proposed a detailed model of the structure-function relationships for chloroquine. They showed that the 4-aminoquinoline nucleus is efficient for complexing Fe(III)PPIX, but not sufficient for inhibiting haemozoin formation. The weakly basic quinoline and terminal amine nitrogen atoms are necessary for drug accumulation *via* pH trapping. Introduction of the 7-chloro group has proven to be most effective for the inhibition of haemozoin formation (Figure 1.43).

The 4-aminoquinoline nucleus is responsible for complexing Fe(III)PPIX

The 7-chloro group is required for inhibition of β-haematin formation

The weak bases are required for vacuolar accumulation *via* pH trapping
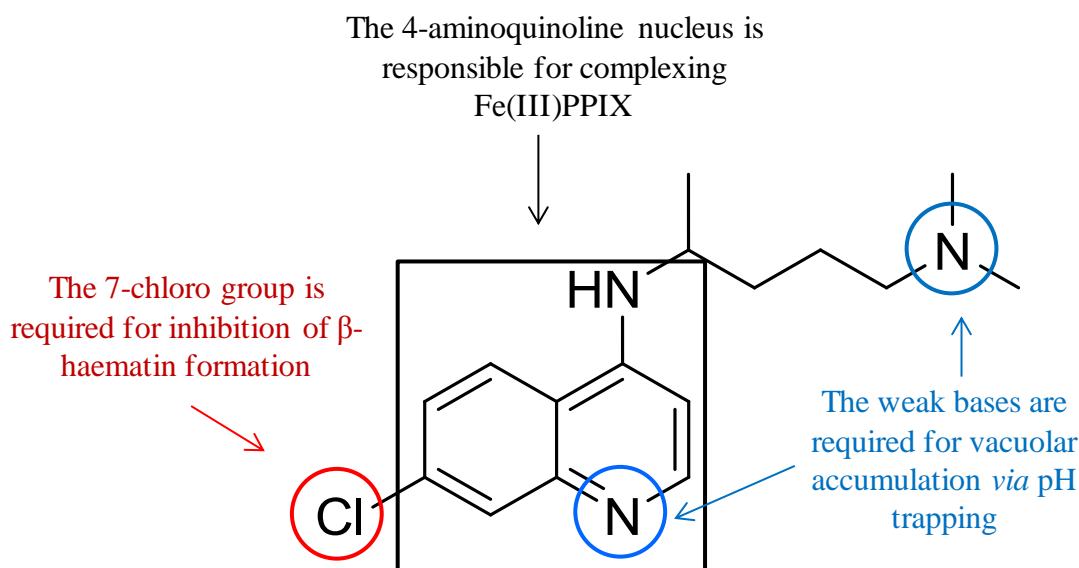
Figure 1.43 The proposed structure-activity relationships in 4-aminoquinoline antimalarials (chloroquine). Reproduced from reference.[95]

1.6.4.4   The Crystal Structure of Halofantrine-Fe(III)PPIX

The first crystal structure of a complex formed between an antimalarial drug and Fe(III)PPIX was only recently published. Using single crystal X-ray diffraction (SCD), the structure of the coordination complex formed between halofantrine (Hf) and Fe(III)PPIX was determined (Figure 1.44).[85] Haematin and Hf had been incubated together at a monomyristoylglycerol (MMG) – aqueous (citrate, pH 4.8) interface. Following centrifugation, the pellet was redissolved in a small volume of a solution containing acetone and pyridine. The resultant solution was left to stand at room temperature, and crystals were observed after 10 days.[85]
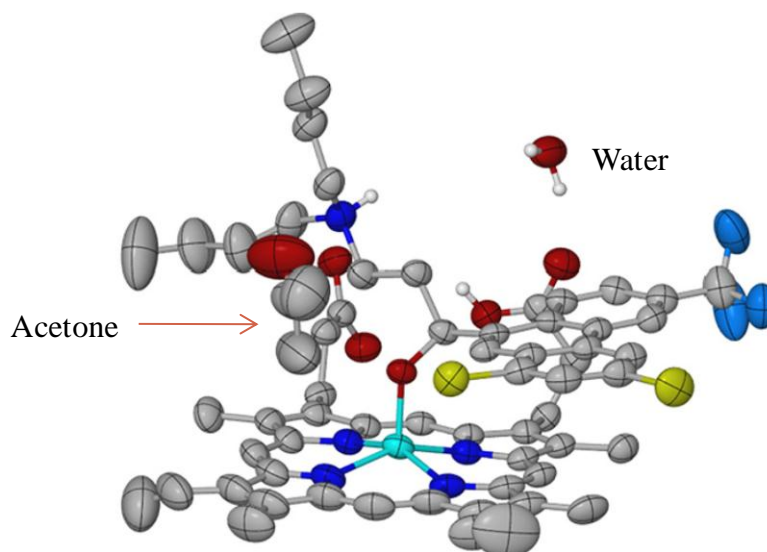
Figure 1.44 The crystal structure of Hf-Fe(III)PPIX. Thermal ellipsoids are drawn at 50% probability. Solvent molecules acetone and water are included. Atom colour labelling: grey ─ C, white ─ H, lime green ─ Cl, prussian blue ─ F, cyan ─ Fe, dark blue ─ N and red ─ O. Reproduced from reference.[85]

The structure shows that the drug interacts with Fe(III)PPIX as a monomer and not a μ-oxo dimer. Furthermore, Hf forms a 5-coordinate complex with Fe(III)PPIX *via* its deprotonated hydroxyl group. The Fe-O bond length (1.840(4) Å) was shown to be in agreement with the coordination of an alkoxide (1.816 – 1.867 Å),[127,128,129,130] rather than an alcohol (2.112 – 2.160 Å).[131,132] Intermolecular hydrogen bonding between the protonated N atom of Hf and the propionate of Fe(III)PPIX was observed as well as hydrogen bonding between the propionic acid and propionate group of adjacent Fe(III)PPIX molecules.

1.6.4.5 Rationalising Activities of the *Cinchona* Alkaloids

In the past, various hypotheses have been put forward in an attempt to relate the structural features of the active and inactive *Cinchona* alkaloids to their observed biological and β-haematin inhibitory activities. By comparing the crystal structures of QN and QD to those of their inactive epimers, EQN and EQD, Karle *et al.*[88] showed that the formation of an intermolecular hydrogen bond between the hydroxyl and amine groups was possible for all four compounds. However, there was a distinct difference in the "torsion angle" in the case

of QN and QD, compared to EQN and EQD, upon formation of these intermolecular hydrogen bonds (Figure 1.45). The N—H and the O—H bonds are positioned 13° relative to each other in the QN structure, in comparison to 67° in the case of EQN. The authors proposed that these structural differences may account for the difference in antimalarial activity profile of the alkaloid compounds.
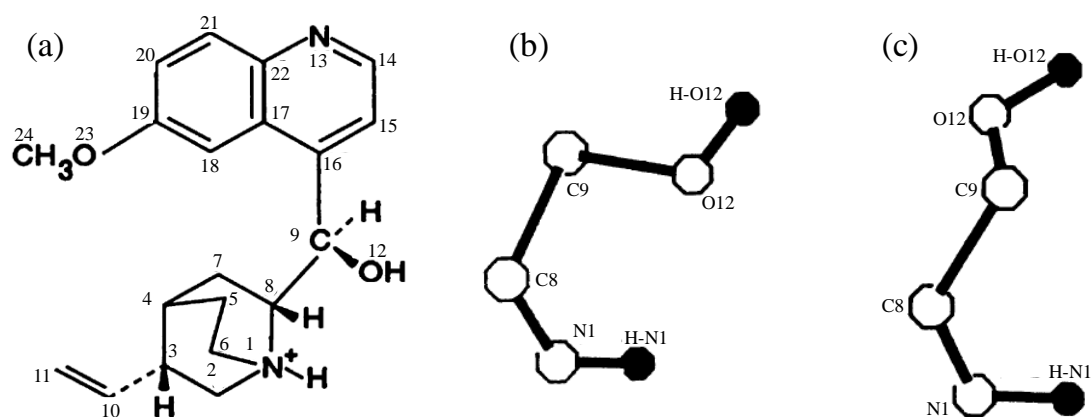
Figure 1.45 (a) The numbering scheme for EQD adopted by Karle *et al*. (b) 9-epiquinidine hydrochloride monohydrate and (c) quinidine sulfate dihydrate, both viewed down the right angles of the HN1–N1–C8–C9–O12–HO12 segment. Reproduced from reference.[88]

Warhurst *et al*.[89] reported that active *erythro* alkaloids can be transferred into the lipid phase with a distribution ratio of 55:1, compared to the decreased ratio of 4.5:1 for the inactive *threo* alkaloids. The authors examined the possible influence of the dipole orientation of the protonated quinuclidine nitrogen atom when modelling solvated structures of the complexes of QN and EQN with Fe(III)PPIX, and showed that the positive electric field of the protonated quinuclidine nitrogen atom in EQN is directed to the solvent, therefore increasing solvation, but in the case of QN it is directed towards the quinoline ring (Figure 1.46).[89] They therefore reasoned that the cumulative effect of lipid-water distribution and Fe(III)PPIX-drug interaction could contribute to the difference in antiplasmodial activity of the active and inactive alkaloids.

(a)   (b)
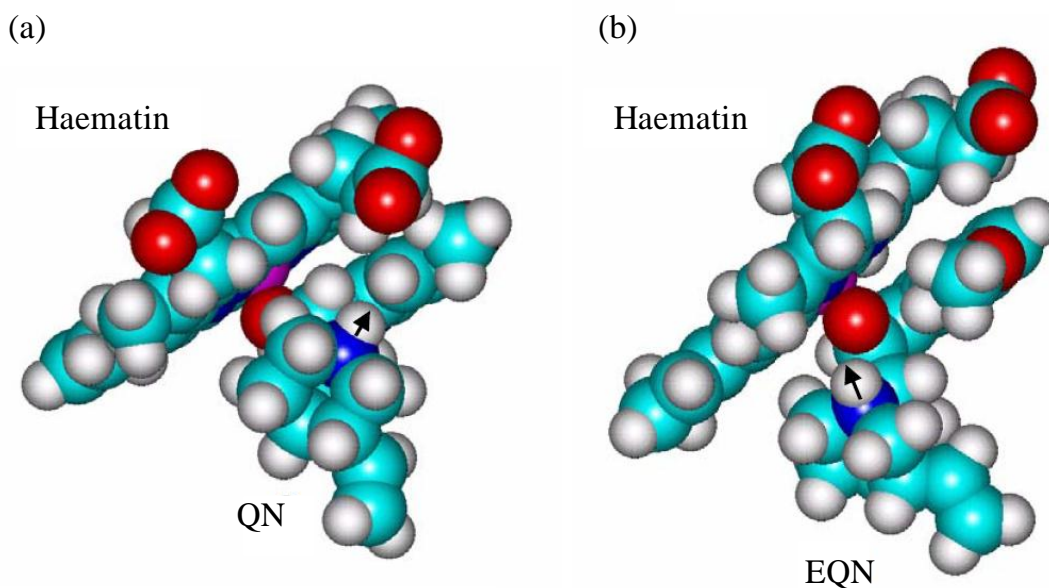
Figure 1.46 The space filling models of (a) quinine (QN) and (b) 9-epiquinine (EQN) complexing with Fe(III)PPIX (haematin) respectively. The black arrow indicates the electric field of the alkaloid N1-H1, which is towards the quinoline ring in QN and towards solvent in EQN. Reproduced from reference.[89]

All attempts by de Villiers *et al.*[85] to crystallise Fe(III)PPIX in complex with any other antimalarial compounds having the benzylic hydroxyl group were unsuccessful. However, due to structural resemblances between the *Cinchona* alkaloids and Hf, they undertook an *in vacuo* molecular mechanics investigation of the complexes of QN, QD, EQN and EQD with Fe(III)PPIX.[85] Their reasoning to do so was supported by comparable changes observed in the UV-visible spectra of Fe(III)PPIX following spectrophotometric titration with both Hf and QD free bases in acetonitrile.

In vacuo conditions were chosen as a model of a low dielectric lipid environment in order to explore the relationship between the structures of the four alkaloids (QN, QD, EQN and EQD), which differ only in their stereochemistry at two centres, and their notable differences in antimalarial and β-haematin inhibitory activities.[85] Aside from the methyl, vinyl and propionate groups on the porphyrin and the methoxy and vinyl groups on the alkaloid periphery, only two torsion angles were identified as being significantly flexible, namely N2-Fe(III)-O10-C9 (φ) and C4-C9-C8-N1 (ψ), (Figure 1.47). When considering rotation about these bonds in the strain free complexes (i.e. when no constraints are put on the complexes and they are free to adopt their lowest energy conformation), no significant

difference between the four Fe(III)PPIX-drug complexes was observed (Figure 1.48, white circles).[85]
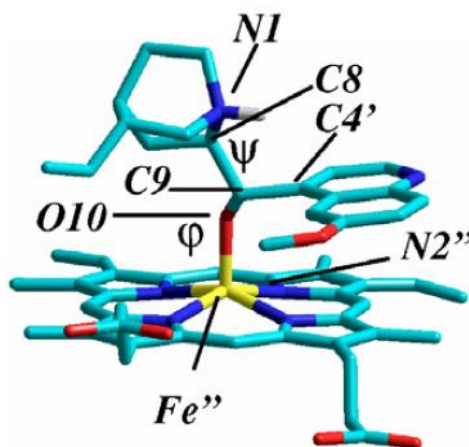
Figure 1.47 Model structure of Fe(III)PPIX-alkaloid complex showing the two dihedral angles N2-Fe(III)-O10-C9 (φ) and C4-C9-C8-N1 (ψ) about which the most free rotation is expected in the strain free complexes. Reproduced from reference.[85]

The hydrogen bonds in the Hf-Fe(III)PPIX crystal structure exist between neighbouring complexes. However, in the aprotic lipid environment where haemozoin formation is thought to occur, this hydrogen bonding potential is more likely to be satisfied by forming intramolecular hydrogen bonds. It was concluded that an intramolecular hydrogen bond (salt bridge) between the protonated quinuclidine N-atom of the alkaloid and the negatively charged Fe(III)PPIX propionate side chain could be formed. A notable effect of the intramolecular hydrogen bond within each complex is the reduction in free rotation about the Fe(III)―O10 and C9―C8 bonds compared to the strain free complexes. The relative strain energy surfaces, generated by rotating ψ and φ relative to one another and determining the free energy at each step are shown in Figure 1.48. The position of the global energy minimum is indicated with a white circle and the conformation required for the salt-bridge formation is indicated with a black circle, for each complex. It is evident that the active alkaloids (QN and QD) are able to form the intramolecular hydrogen bond relatively easily compared to the inactive epimers.
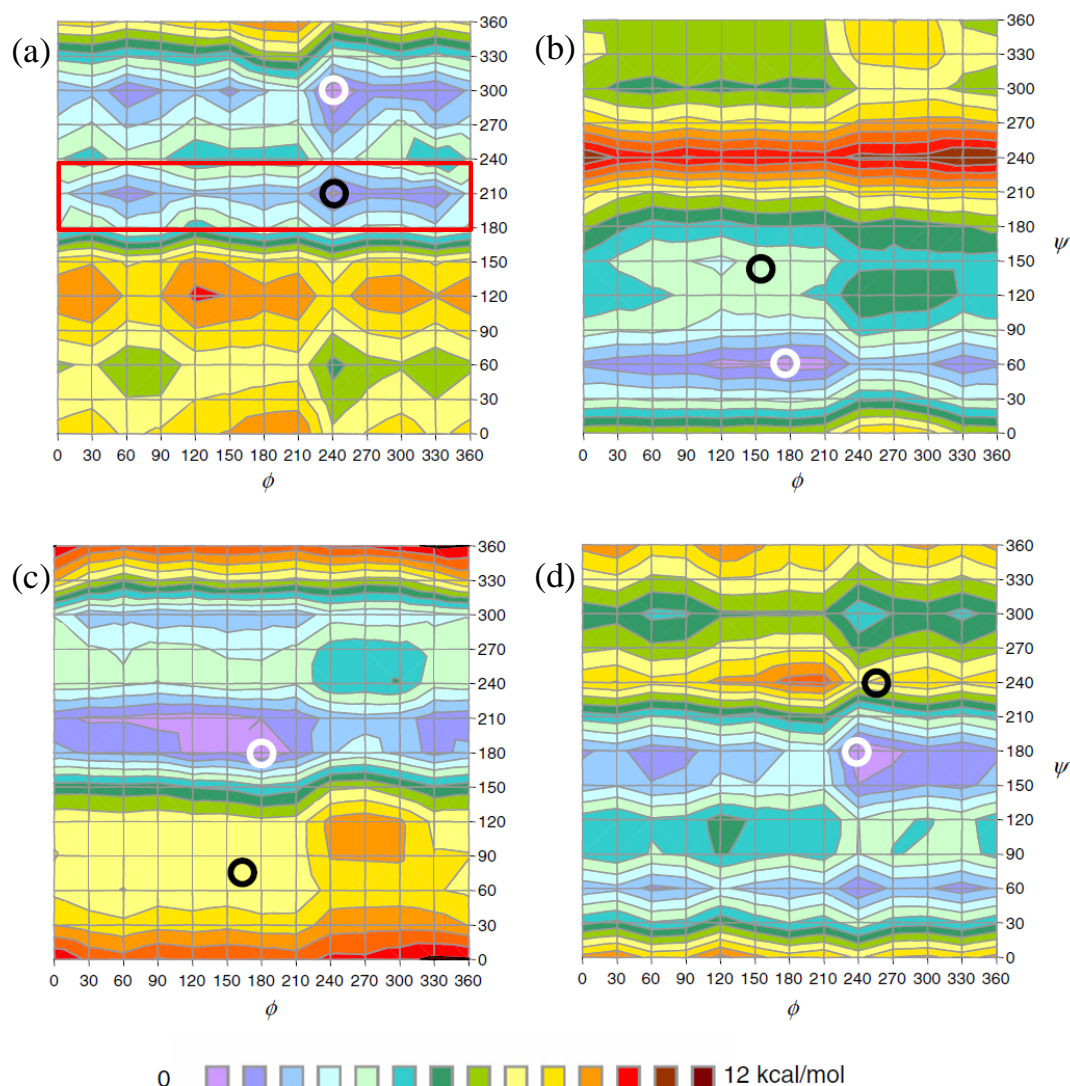
Figure 1.48 The relative strain energy surface for the rotation around the torsion angles φ and ψ for (a) QD- , (b) QN- , (c) EQD- and (d) EQN-Fe(III)PPIX. The positions of the global energy minimum (white circle) and the conformation required for salt-bridge formation (black circle) are indicated for each complex. The low energy furrow observed in the QD-Fe(III)PPIX complex is indicated in the red box at the point where ψ is fixed at 210°. Reproduced from reference.[85]

A feature of the calculated relative strain energy surface for QD-Fe(III)PPIX is the low energy furrow at the point that ψ is fixed at ± 210° (Figure 1.48 (a)). It would seem that the barrier to rotation about the Fe(III)-O10 bond is minimal in this region, and that φ could therefore adopt any value. A direct correlation was observed between the difference in strain energy required for salt bridge formation and the minimum energy obtained from the strain-free complex and the biological activity of the four stereoisomers (Figure 1.49).
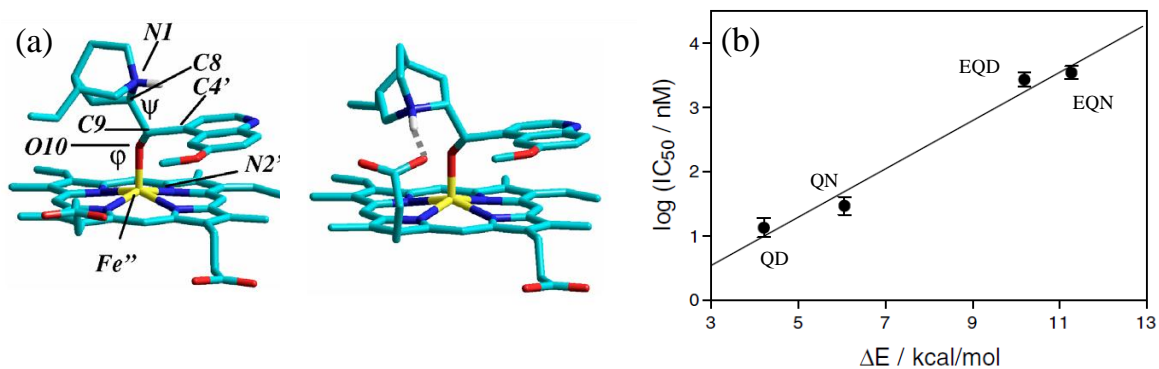
Figure 1.49 (a) Modelled complex of Fe(III)PPIX and the *Cinchona* alkaloid QN. The strain free complex is shown on the left together with the conformation induced by the formation of an intramolecular salt bridge at the right. (b) Correlation between the biological activity and the strain energy required for salt-bridge formation (ΔE) are shown for each complex. Reproduced from reference.[85]

Based on the theoretical studies, it was proposed that the formation of the haemozoin precursor dimer may be inhibited by salt bridge formation, thus accounting for the strong activity of the two active isomers QN and QD.[85] In aqueous medium, Fe(III)PPIX has been shown to exist as a π-π dimer in which the unligated faces of the two porphyrins interact with each other while the axial ligands are directed outwards.[79] Both the active and inactive *Cinchona* alkaloids have been shown to associate with Fe(III)PPIX to a similar degree in an aqueous environment (Figure 1.50, 1 and 5),[118] still allowing Fe(III)PPIX to exist as a π-π dimer. As the complexes of the inactive isomers enter the lipid environment, formation of the haemozoin precursor dimer dominates complex formation (Figure 1.50, 2), allowing the formation of haemozoin to proceed as normal.[85] However, when complexes of the active isomers enter the lipid environment, it was hypothesised that the strong salt bridge formed makes the propionate group unavailable for the formation of the haemozoin precursor dimer and subsequently haemozoin formation does not proceed (Figure 1.50, 6). According to this model, the *Cinchona* alkaloids inhibit the formation of haemozoin through interaction with monomeric Fe(III)PPIX, which is in agreement with the findings of Casabianca *et al*.[122,123]
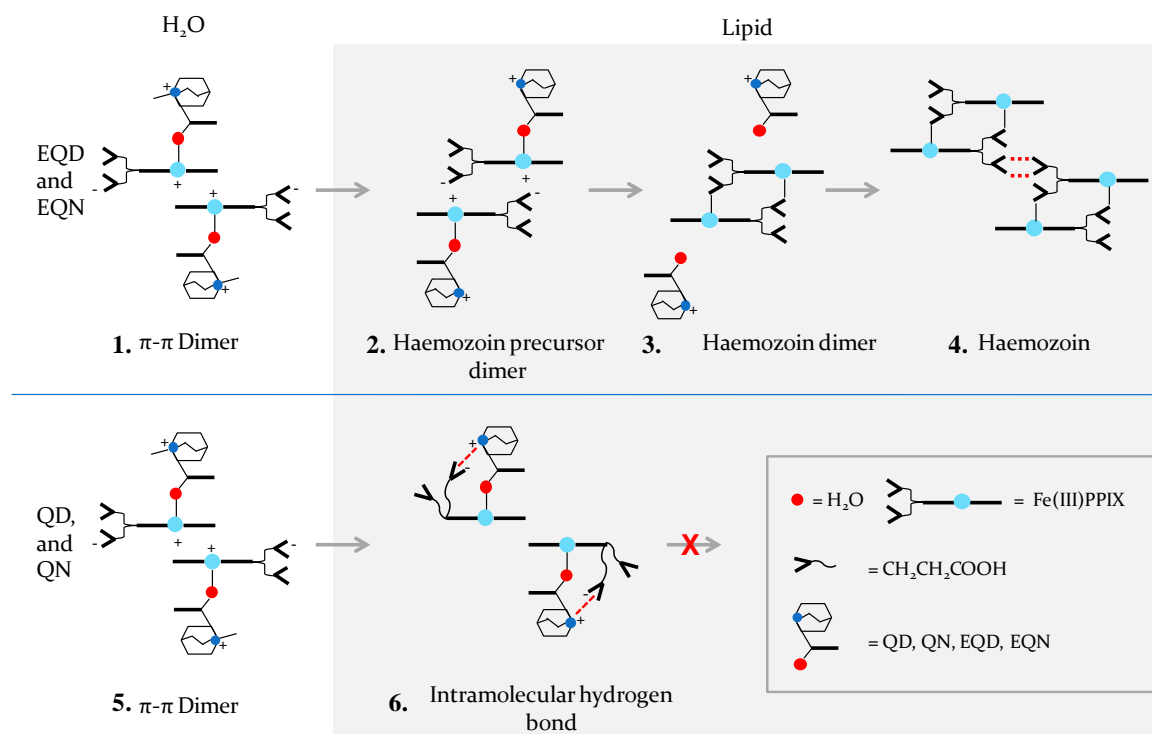
Figure 1.50 Proposed rationalisation of activity profile of the *Cinchona* alkaloids. The inactive *Cinchona* alkaloids (EQD and EQN) associate with Fe(III)PPIX in aqueous solution (1), but are not able to inhibit haemozoin formation (2, 4) Following association with Fe(III)PPIX in aqueous solution (5), the active compounds, QN and QD, are able to form stabilised coordination complexes with Fe(III)PPIX (6), which do not allow haemozoin formation to proceed. Redrawn from reference.[85]

It was observed that the active alkaloids (QN and QD) were able to form the intramolecular hydrogen bonds more easily in comparison to the inactive alkaloids, and suggested that MQ and lumefantrine (Lf) could interact with Fe(III)PPIX in a similar manner through coordination to the Fe centre of Fe(III)PPIX.[85] However, the authors were unable to demonstrate coordination of any further compound, particularly the quinolines, to the Fe centre of Fe(III)PPIX experimentally.

The three-point binding mode observed theoretically between Fe(III)PPIX and the *Cinchona* alkaloids, namely π-stacking, coordination, and intramolecular hydrogen bond formation, could be exploited in the rational design of novel haemozoin inhibitors. However, while this model addressed certain questions in the literature, for example the disparate activity profiles of the four alkaloids given their very similar association constants in aqueous DMSO solutions,[118] the absence of crystal structure data has limited the support for this model. Furthermore, since the only crystal structure of a Fe(III)PPIX-

drug complex is that of the phenanthrene compound halofantrine,[85] the pharmacophore for quinoline antimalarials is for the most part unknown and the reason for why certain compounds inhibit haemozoin formation while others do not still requires explanation. Single crystal X-ray diffraction structures of Fe(III)PPIX complexing to quinoline antimalarial drugs will aid in the understanding of whether these compounds coordinate to the Fe(III) centre of Fe(III)PPIX *via* the quinoline, quinuclidine or piperidine nitrogen atoms or the hydroxyl oxygen atom of the drug. Furthermore, the complexes of active and inactive *Cinchona* alkaloids could help to explain the differences in activity. Obviously correct interpretation of Fe(III)PPIX-drug complexes in solution is also critical, since the solid state is not representative of the biological environment of the FV.

1.6.4.6 Inhibition of β-Haematin Formation

1.6.4.6.1 *Pyridine Hemichrome Inhibition of β-Haematin (Phiβ) Assay*

The quest to find a novel antimalarial compound is of wide interest given resistance, and two approaches can be followed in order to accomplish this goal.[22] The first approach is to screen libraries of compounds, both natural and combinatorial, for activity against a validated drug target. The formation of haemozoin is unique to the parasite and represents an attractive drug target for antimalarials,[133] though this unique crystallisation process still remains not fully understood. Nevertheless, compound screening may be of importance in the discovery of new antimalarials. Most recently, Sandlin *et al.*[77] have made use of a lipophilic detergent NP-40 based assay to screen and identify inhibitors of β-haematin formation. A second approach, namely rational drug design, relies upon a sound understanding of the biological target (haemozoin) as well as the mechanism by which drug activity is brought about. In the case of chloroquine (CQ), quinine (QN), quinidine (QD), amodiaquine (AQ) and mefloquine (MQ), these aspects have not been unequivocally established to date.

The inhibition of β-haematin formation has been studied using different methods. In 1994, Egan *et al.*[90] made use of acidic acetate solutions (4.5 M, pH 4.5 at 60 $^{\circ}$C) to promote the formation of β-haematin, and infrared spectroscopy to characterise the products obtained in the absence and presence of antimalarial drugs. It was observed that quinoline antimalarial drugs inhibit the spontaneous formation of β-haematin, while inactive compounds such as EQN had no effect on the reaction.[90]

The pyridine hemichrome inhibition of β-haematin (Phiβ) assay developed by Ncokazi *et al.* exploits the ability of 5% (*v/v*) aqueous pyridine pH 7.4 to solubilise free Fe(III)PPIX in the presence of β-haematin, resulting in a characteristic orange-pink *bis*-pyridyl complex in solution, which has a distinctive absorbance maximum at 405 nm.[134] With increasing pyridine concentration, the broad and relatively low intensity soret band attributed to the aqueous Fe(III)PPIX π-π dimer species exhibits a red shift (transitions are shifted to longer wavelengths) from 389 to 404 nm, with a sharper and more intense peak indicating the monomerisation of the iron porphyrin (Figure 1.51).[134] The changes in the spectra are consistent with the coordination of two pyridine ligands to the Fe(III) centre of the porphyrin.[135]
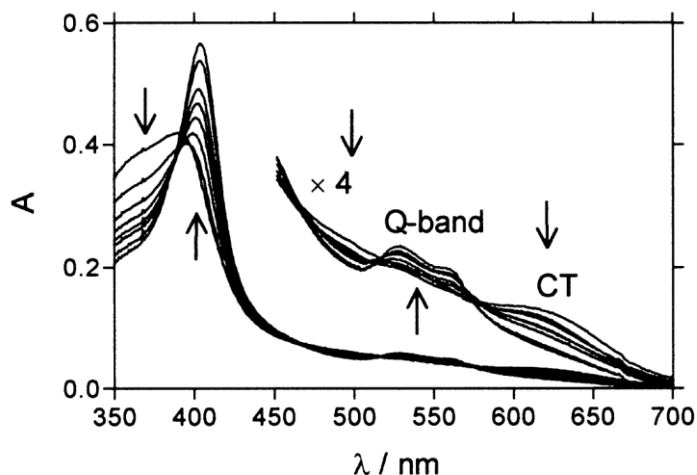
Figure 1.51 The effect of increasing pyridine concentration on the spectrum of Fe(III)PPIX in aqueous solution. The changes in the spectra are consistent with coordination of two pyridine ligands to the Fe(III) centre of Fe(III)PPIX. Arrows indicate the direction of change as the concentration of pyridine is increased. Reproduced from reference.[134]

In order for the assay to be useful, conditions under which the pyridine reacts exclusively with Fe(III)PPIX and not β-haematin were investigated. Under pH conditions close to neutral, the axial ligand of Fe(III)PPIX is likely to be water, which being a weak field ligand is easily replaced by the strong field pyridine ligand. β-Haematin, however, is a cyclic dimer of Fe(III)PPIX in which the propionate side chain of one protoporphyrin coordinates to the Fe(III) centre of the other.[35] Thus, the coordination of pyridine to the Fe(III) centre of this microcrystalline solid would be much more difficult, requiring the breakage of the Fe-O (propionate) bond and disruption of the crystal. Ncokazi *et al.*

explained that under basic conditions where β-haematin is less stable, and at high enough concentration of the pyridine to compete with the propionate groups, β-haematin decomposes to form Fe(III)PPIX-pyridine complexes. However, in aqueous solutions containing only 5-10% (*v/v*) pyridine, buffered at a pH value that is neutral or only mildly basic, the pyridine does not react with β-haematin (Figure 1.52).[134]
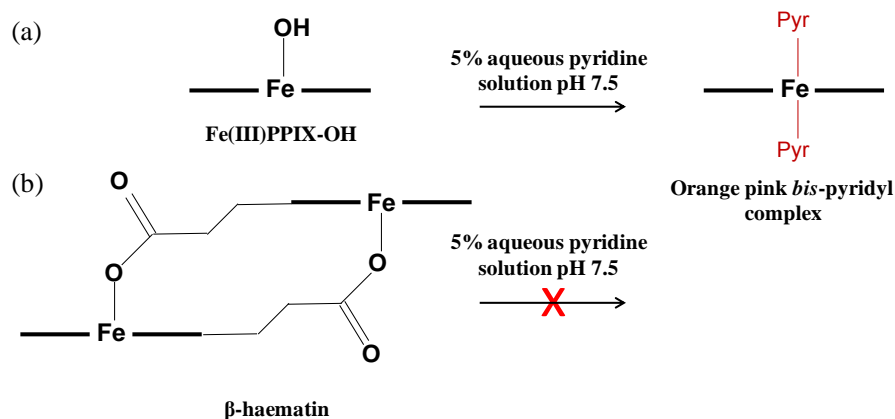
Figure 1.52 Interaction of aqueous pyridine with Fe(III)PPIX species. (a) Schematic of the *bis*-pyridyl complex formed after reacting 5% (*v/v*) aqueous pyridine with Fe(III)PPIX in solution. The orange-pink *bis*-pyridyl complex has a distinctive absorbance maximum, measurable at 405 nm. (b) The *bis*-pyridyl complex will not form in the presence of β-haematin. The thicker black lines represent the mean porphyrin plane, which is viewed from the side.

In 5-10% aqueous pyridine solutions, Ncokazi *et al.* showed that absorbance data can be used to directly quantify the percentage Fe(III)PPIX in a Fe(III)PPIX/β-haematin mixture (Figure 1.53).[134]
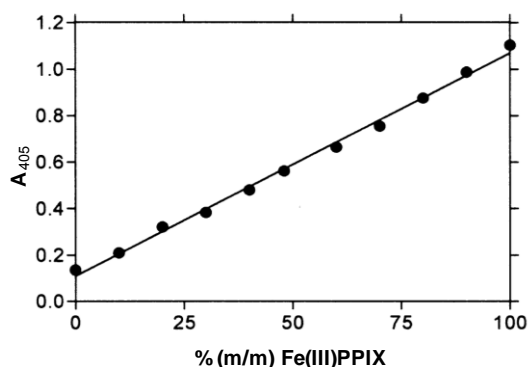
Figure 1.53 Linear dependence of Soret band intensity (A_{405}) on Fe(III)PPIX concentration. Reproduced from reference.[134]

In the so-called Phiβ assay, β-haematin formation was studied under the conditions used by Egan *et al.* in 1994,[90] specifically 4.5 M acetate solution (pH 4.5, 60 $^{\circ}$C). The Phiβ assay provided a means of quantifying the amount of Fe(III)PPIX remaining following the formation of β-haematin in the presence of potential inhibitors.[136] An example of the visual effect of pyridine can be seen in Figure 1.54, where the pyridine-based assay was conducted in a 96-well plate. β-Haematin inhibitors are readily identifiable, owing to the formation of the orange-pink colour in the well. The greater the activity of the test compounds, resulting in greater quantities of unreacted Fe(III)PPIX, the more intense the orange-pink colour.
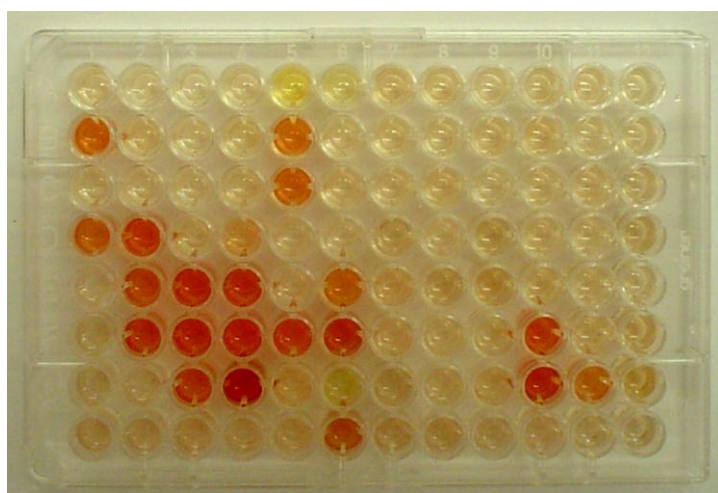
Figure 1.54 Example of the Phiβ assay used in a 96-well plate where 47 compounds were screened for their ability to inhibit β-haematin formation. After the reaction was completed, 5% (*v/v*) aqueous pyridine (pH 7.5) was added and inhibitors of β-haematin could be identified by direct visual inspection. Reproduced from reference.[134]

Overall, it was demonstrated that the Phiβ assay is an easy to use and reproducible method to study the inhibition of β-haematin formation.[134] Furthermore, absorbance data can be easily manipulated in order to reflect the % β-haematin formed.

1.6.4.6.2 *Effect of Quinoline Antimalarial Drugs on Kinetics of β-Haematin Formation.*

Chong and Sullivan[137] made used of a high throughput crystal growth determination assay to investigate the effect of quinoline antimalarials on the kinetics of crystal growth. They found that the 50% inhibitory concentration (IC$_{50}$) value is dependent on incubation time

and they further recognised that β-haematin formation eventually occurs in the presence of CQ and QD.[137] Subsequent studies by Egan *et al.*[71] supported these previous findings. An investigation of β-haematin formation, mediated by 4.5 M acetate, pH 4.5 at 60 °C, in the presence of quinoline antimalarials showed a sigmoidal dependence of β-haematin formation on drug concentration (Figure 1.55).[71] A decrease in the rate of β-haematin formation in the presence of CQ and QN was also observed. However, a much slower decrease in the rate for β-haematin formation was seen for QN, Figure 1.55 (b).[71] The reaction was monitored spectroscopically at 405 nm, employing 5% (*v/v*) aqueous pyridine (pH 7.5) for the reasons discussed above.
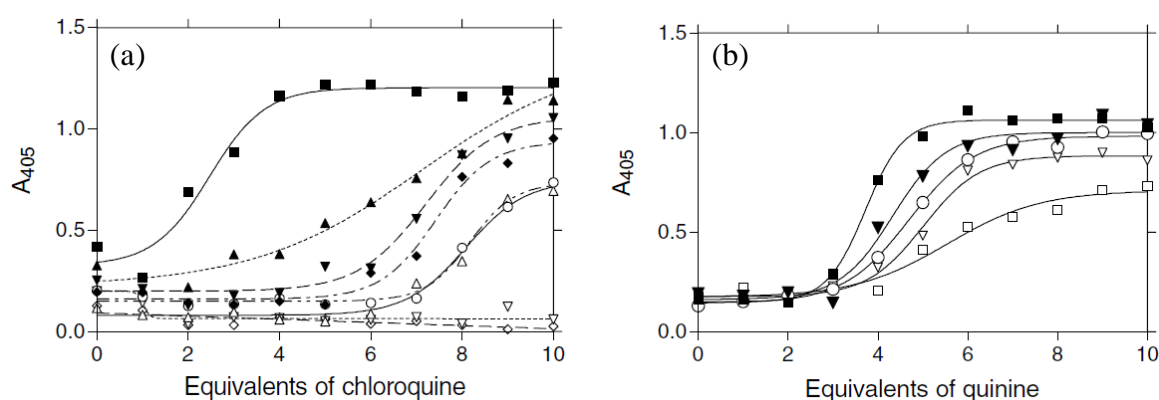
Figure 1.55 The effect of quinoline antimalarial drugs on β-haematin formation. Increasing molar equivalents of (a) CQ and (b) QN were observed to decrease the rate of β-haematin formation. The different incubation times in hours are 1(■), 2 (▲), 3 (▼), 4 (turned black square), 5 (○), 6, (Δ) 7, (upside down triangle), 8 (◊) and 24 h (□). Reproduced from reference.[71]

As discussed earlier, the sigmoidal dose response curve is based on the reaction process (β-haematin formation) taking place in three stages: induction, growth/propagation and termination.[71] At low drug equivalents, the reaction would be expected to reach its termination stage and little unreacted Fe(III)PPIX would remain to react with the pyridine, thus giving rise to a low absorbance value. Upon increasing the drug equivalents, the reaction only reaches its growth stage, resulting in increasing concentrations of unreacted Fe(III)PPIX to react with the pyridine. When the drug equivalents are sufficiently high, the reaction remains in the induction stage, (very little Fe(III)PPIX is converted into β-haematin) and the absorbance value is high.

The IC_{50} values of the 4-aminoquinolines for the inhibition of β-haematin formation were shown to depend strongly on incubation time (Figure 1.56). The authors showed that at 1 hour incubation time, CQ was a stronger inhibitor than QN, but at 2 hours the IC_{50} data indicate that QN was a stronger inhibitor than CQ, therefore incubation times must be considered carefully when investigating inhibitory activity. The authors demonstrated that the IC_{50} data following an incubation time of one hour correlate well with biological activity, suggesting that drug action may be more relevant at the early part of the inhibitory process.
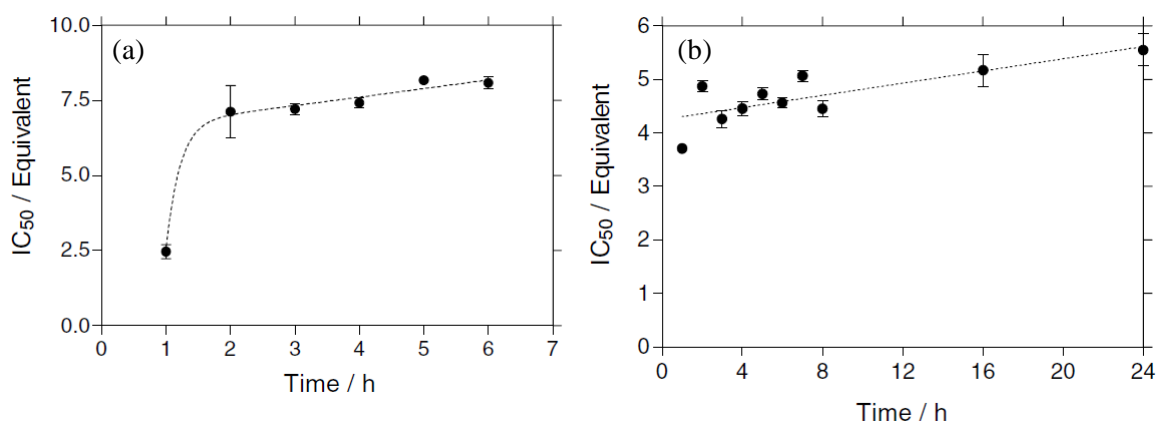
Figure 1.56 The effect of increasing incubation time on the IC_{50} values for inhibition of β-haematin formation by (a) CQ and (b) QN. Reproduced from reference.[71]

The mechanisms of action of antimalarial drugs were unknown for a long time, and there is still a long way to go to understanding how these drugs provide chemotherapy against the malaria parasite. In spite of the important role that CQ has played over the years, little is known about the molecular interaction of CQ and related antimalarials with the proposed drug target(s), haemozoin and its precursor Fe(III)PPIX. At the present we do not understand enough about the mode of action of these existing drugs; however, we need to focus on understanding their mode of action first in order to be able to design novel and more efficient drug candidates.

1.7   Aim and Objectives

After thoroughly reviewing the literature on Fe(III)PPIX, malaria pigment and the current understanding on the mechanisms of action of quinoline antimalarial drugs, three questions not fully answered in this field were identified. For this reason, the following aims were set as targets:

1. Determine the structural features of Fe(III)PPIX-quinoline drug complexes which could account for their activity. In doing so, probe the relationship between the solid-state structures and the structures present in solution.

2. Investigate the effect of quinoline antimalarial drugs on lipid-mediated β-haematin formation.

3. Gain deeper insight into the mechanism of formation of β-haematin (haemozoin) through structural analysis.

To achieve the aforementioned aims, the specific objectives of this research project were to:

1. Use various crystal growing techniques to grow single crystals of Fe(III)PPIX-drug complexes and study their molecular features using X-ray diffraction techniques and infrared spectroscopy.

2. Compare UV-visible spectra to rationalise species existing in solution.

3. Validate the biomimetic lipid-water interface system as a means of assaying antimalarial drug activity.

4. Investigate the effect of quinoline antimalarial drugs on the kinetics of β-haematin formation, making use of the lipid-water interface system.

5. Investigate crystals of β-haematin using single crystal X-ray diffraction.

6. Use extended X-ray absorption fine structure (EXAFS) spectroscopy to gain understanding about Fe(III)PPIX-drug complexes and Fe(III)PPIX in solution.

2   Experimental Techniques

The work presented in this dissertation has involved the use of several instrumental techniques. These techniques are briefly described in this chapter to outline their use in the field of antimalarial drug research.

2.1   X-ray Crystallography

X-ray crystallography is a technique used by crystallographers in which the closely spaced lattice of atoms in a crystal is recorded from the pattern produced by the diffraction of X-rays through the crystal. Analysing these results reveal the nature of the lattice. A crystal by definition is a solid containing an internal lattice of atoms, molecules, or ions that is regular, repeating and geometrically arranged.[138]

This non-destructive technique uses X-ray radiation to gain information about the internal lattice of a crystalline material. Each single crystal has a characteristic diffraction pattern. Using Miller indices (*hkl*) assigned to each reflection by measuring the directions of the diffraction and the corresponding intensities, refinements are performed in order to obtain the three-dimensional crystal structure. From this determination, information about bond lengths, angles and chemical formula can be ascertained for the crystal structure responsible for diffraction.

2.1.1   Single-Crystal X-Ray Diffraction

Single crystal X-ray diffraction (SCD) is currently the most accurate characterisation technique available by which to analyse crystalline materials.

The interaction of X-rays with a sample produces constructive interference when Bragg's Law is satisfied (eq. 2.1). Bragg considered crystals to be made up of parallel lattice planes of atoms. When X-rays are in-phase with one another they will leave the crystal at an angle equal to that of the incident beam. Bragg's law identifies the angles of the incident radiation relative to the lattice planes for which diffraction peaks occur. Constructive interference occurs when the path difference is an integral number of wavelengths (nλ). This is known as Bragg's law (eq. 2.1).

$$n\lambda = 2d\ sin\theta \qquad (2.1)$$

This describes the relationship between the wavelength of the incident X-ray, λ, angle of incidence θ, and the interplanar spacing d, between lattice planes with n the order of reflections.[139] The wavelength, λ, of the X-ray is typically 1 Å, comparable to the interatomic spacing. No diffraction occurs when the above condition is not satisfied.
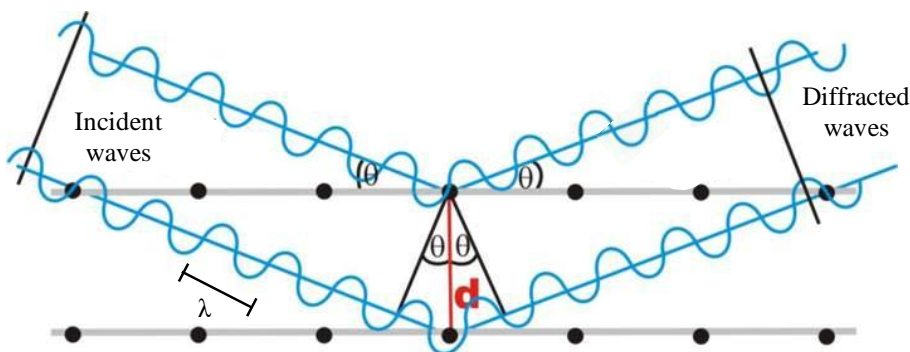
Figure 2.1 Bragg considered crystals to be made up of parallel planes of atoms (●). The incident waves are reflected specularly from the parallel planes. Bragg's law is satisfied when the distance between the two incident waves and the two diffracted waves differ by an integer d, the interplanar spacing. Reproduced from reference.[140]

To label the reflections, Miller indices of the planes are used (*hkl*). The diffracted X-rays are then detected by the CCD (Charge-Coupled Device) area-detector. By changing the position of the detector, sample and X-ray source, all possible diffractions of the lattice should be achieved and the detected data can be processed.

2.1.1.1   Data Collection

Data collections for the five SCD structures presented in this dissertation were carried out using a Bruker Apex Duo diffractometer fitted with either a cupper, Co-K_α (λ = 1.5418 Å) or molybdenum, Mo-K_α (λ= 0.71073 Å) incoatec IμS microsource and an Oxford Cryosystems Cryostat (700 Series Cryostream Plus). Data were captured with a CCD area-detector. Crystals were mounted on the MiTeGen mount in paratone oil, and data were collected at 100K. It should be noted that most crystals were found to be unstable, most likely the result of rapid desolvation when the crystals were removed from mother liquor. Therefore, it was necessary to mount the crystals and place the gonionmeter head directly in the cold stream as quickly as possible to avoid decomposition. APEX II software[141] was

used to determine a reliable unit cell and implement a suitable data collection strategy, as well as for subsequent data reduction and absorption corrections.

2.1.1.2   Structure Solution and Refinement

All structures were solved by direct methods and refined using the SHELX-97[142] package implemented through XSeed.[143] All diagrams were generated using POVRay[144], implemented through XSeed.[143] PLATON/SQUEEZE implemented in WinGX,[145] was used to analyse residual electron density present in the structure due to disordered solvent molecules, which could not be modelled during structure refinement. SQUEEZE calculations generate values for the void volume and the total number of electrons in the void.[146]

2.1.1.3   Application to Fe(III)PPIX Studies

SCD studies in the field of antimalarial drug research have been limited to date by the fact that one requires a single crystal which is stable and with dimensions in the order of $0.1 - 0.5$ mm for this method. To grow single crystals of Fe(III)PPIX-drug complexes, in order to study the interactions of antimalarials with Fe(III)PPIX, is very difficult, as evidenced by the limited number of structures published in the literature. On the other hand, if one is able to acquire such a crystal, this technique is the most precise method for structure determination, as was shown in the case of the first crystal structure of a Fe(III)PPIX-drug complex, the Fe(III)PPIX-halofantrine crystal structure.[85]

2.2   Powder X-ray Diffraction

Powder X-ray diffraction (PXRD) is a non-destructive technique and is mainly used to characterise solid materials. Homogeneity of crystal samples can be determined by comparing the PXRD data with the corresponding calculated powder pattern generated from a known structure.

2.2.1.1   Data Collection

Powder X-ray diffraction data were recorded on a PANalytical X'Pert PRO X-ray Powder Diffractometer from PANalytical, Netherlands with Bragg-Brentano geometry, and using a Cu-K_α radiation (λ = 1.5418 Å) source. Samples were ground to fine powders before being placed on a zero-background sample holder. Intensity data were collected using a X'Celerato detector and 2θ scans in the range of $5 - 30^o$.

2.2.1.2   Application to Fe(III)PPIX Studies

PXRD was used to confirm the formation of β-haematin as well as the extent of crystallinity of the samples, since it was not possible to obtain suitable crystals for analysis by SCD. Notably, this method has been used previously to solve the structure of synthetic malaria pigment, however, the high-resolution data was collected using a synchrotron light source rather than a standard laboratory diffractometer.[35]

2.3   Infrared Spectroscopy

Infrared Spectroscopy (IR) exploits the fact that molecules vibrate and rotate when the energy which they absorb is sufficient to excite them from the ground state into an excited state.[147] The specific frequencies which molecules absorb are characteristic of the chemical functional groups in the sample, and therefore IR spectroscopy can be used to identify structural features in compounds.

In order for a molecule to be IR active, at least one vibrational mode must be associated with a change in the dipole. The number of ways a molecule can vibrate is related to the number of atoms, therefore the number of bonds in molecule. If a molecule has n-atoms, the molecules has 3n-6 degrees of vibrational freedom (3n-5 if molecule is linear).[147] Vibrational modes include stretching, bending, scissoring, rocking and twisting. IR absorption data is presented in the form of a spectrum with wavenumber ($\tilde{v}$) on the x-axis, and percent transmission on the y-axis. The IR region is divided into three smaller areas, near IR (13 000-4 000 cm^{-1}), mid IR (4000-200 cm^{-1}) and far IR (200-10 cm^{-1}).

2.3.1   Detection Modes

2.3.1.1   Attenuated Total Reflectance-Infrared Spectroscopy

One advantage of using the attenuated total reflectance-infrared spectroscopy (ATR-IR) technique is that no sample preparation is required and both solid and liquid samples can be examined. The sample is placed in close contact with the ATR crystal normally zinc selenide (ZnSe) or germanium (Ge) crystal, which haves a high refractive index, by compressing it with a diamond tip (Figure 2.2). First, the IR light is directed to the ATR crystal at a specific angle so as to reflect the light several times within the ATR-crystal. These internal reflections generate an evanescent wave and in the regions where the sample absorbs energy, the wave will be attenuated (alter). Once the light exits the crystal, it passes through the detector which measures the absorbance by the sample from the damped signal of the output beam. The sample thickness will influence the quality of the transmission spectroscopy.
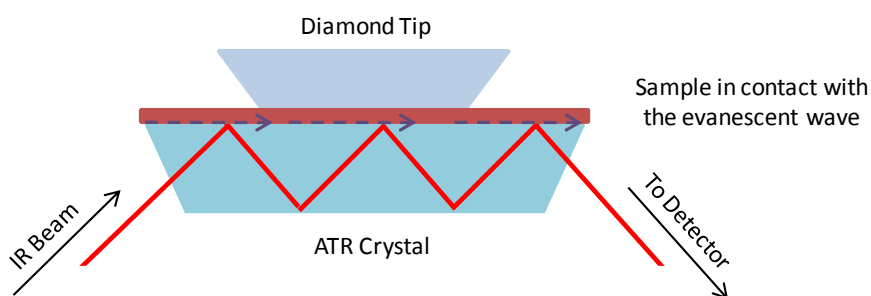
Figure 2.2 A schematic representation of the ATR-IR system. The sample is pressed into very close contact with a ZnSe or Ge crystal by a diamond tip. As the beam of IR light passes through the ATR crystal multiple times, an evanescent wave (dashed blue arrow) is produced. The evanescent wave interacts with the sample and results in a damped signal to the output beam of the infrared radiation. Reproduced from reference.[148]

2.3.1.2   Application to Haemozoin Studies

Fourier transform infrared (FT-IR) spectroscopy was used to characterise samples of β-haematin, prepared by various methods. As mentioned in the literature review, the strong absorbance bands at 1211 cm^{-1} and 1664 cm^{-1} in the FT-IR spectrum of β-haematin have been attributed to the C-O and C=O stretching frequencies, respectively of the coordinated propionate group. These strong bands are visible in the ATR-IR spectra of β-haematin and

haemozoin, but are absent in the spectrum of Fe(III)PPIX and are either absent or present to a lesser extent in samples of the material prepared in the presence of quinoline antimalarial drugs.[30]

2.4   UV-Visible Spectroscopy

UV-visible (UV-vis) spectroscopy involves the spectroscopy of photons in the UV-vis region (400-700 nM). When electromagnetic radiation of the correct frequency is absorbed by the material, molecules undergo electronic transitions from their normal ground state (where valence electrons can be found in σ, π or non-bonding orbitals (n)), to higher energy excited state (antibonding orbitals σ* or π*). Due to the fact that transitions from bonding orbitals require to high a frequency to be measured easily (too short a wavelength), allowed transitions include σ→ σ*, π →π*, n→ σ* and n→ π*.[149]

2.4.1   Data Collection

UV-vis single wavelength readings were recorded using a UNICAM Helios UV-vis spectrophotometer. UV-vis spectra readings were recorded using a SPECORD®210PLUS UV-vis spectrophotometer. Quartz cuvettes from SUPRASIL®, Hellma and 1 cm path lengths were used in the spectrophotometer.

2.4.2   UV-Visible Spectrum of Fe(III)PPIX

Due to the complexity of the speciation of Fe(III)PPIX in solution, UV-spectra have been studied in depth to characterise the species observed in solution.[86] The porphyrin of Fe(III)PPIX is a highly-conjugate molecule containing 22 π electrons. Due to this conjugated π-electron system, solution of porphyrins are able to absorb UV-vis light and typically have an intense colour.[150] The molecular orbital (MO) diagram for the Fe(III) centre and the conjugated porphyrin ring system of Fe(III)PPIX is shown in Figure 2.3. The Fe(III) centre in Fe(III)PPIX is high spin, therefore each of the five d-orbitals is singly occupied by an electron (spin state S = 5/2). The extensive aromatic porphyrin core is considered to have D_{4h} symmetry (refer back to Figure 1.2, section 1.4).[151] The absorption spectra of porphyrins were explained by Gouterman during the 1960's.[152,153] The characteristic bands in the UV-vis spectra arise from transitions between the two highest

occupied molecular orbitals (HOMO), a_{1u} and a_{2u} orbital, and the lowest unoccupied molecular orbitals (LUMO), doubly degenerate e_g orbitals. The nature of the metal centre of the porphyrin and the substituents on it affect the relative energies of these transitions. Due to orbital mixing these energy states are split creating a higher energy state giving rise to the Soret (or B) band, and a lower energy state creating the Q bands (Figure 2.4).
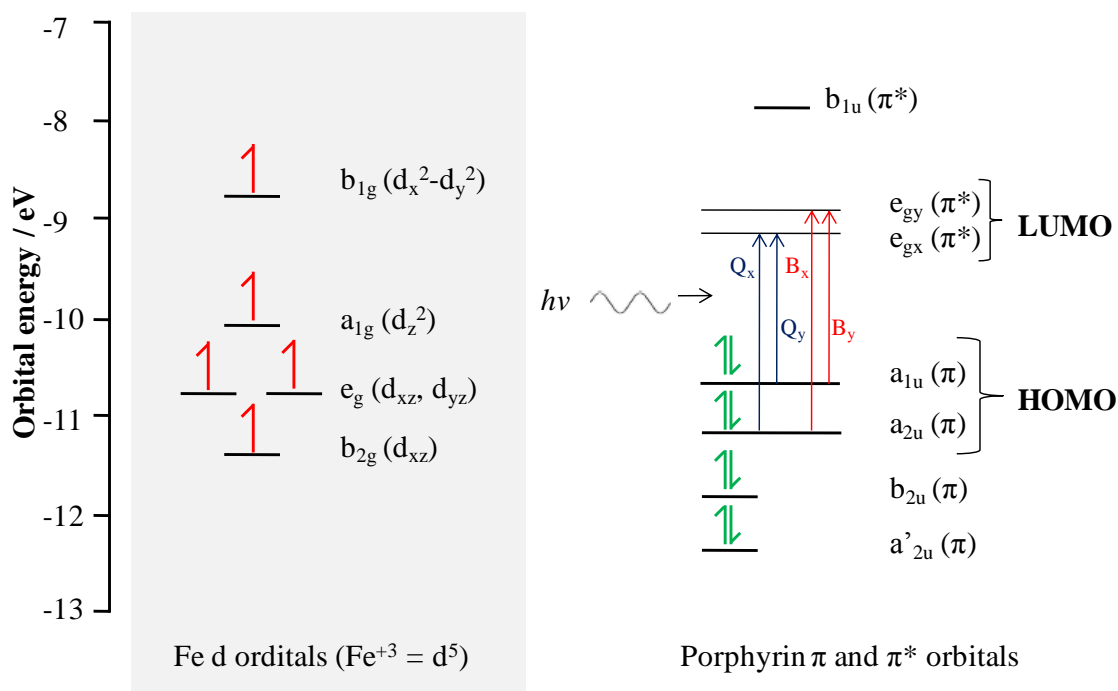
Figure 2.3 The molecular orbital (MO) diagram for the Fe(III) centre and the conjugated porphyrin ring system of Fe(III)PPIX. The characteristic bands (Q and Soret) in the absorption spectra arise from transitions between the two highest occupied molecular orbitals (HOMO), a_{1u} and a_{2u} orbital, and the lowest unoccupied molecular orbitals (LUMO), doubly degenerate e_g orbitals, in the conjugate porphyrin ring system.

The UV-vis spectrum of Fe(III)PPIX in methanol solution shows distinct bands due to the major electronic transition of the porphyrin core at the Soret band and the Q and Charge-Transfer (CT) bands (Figure 2.4 (a)). Comparing this spectra to the spectra of Fe(III)PPIX as μ-oxo dimer species where the Fe(III) centre is in a low spin state (Figure 2.4 (b)), there is clearly a difference in appearance. Therefore UV-vis can also be used to distinguish between different Fe(III)PPIX species.
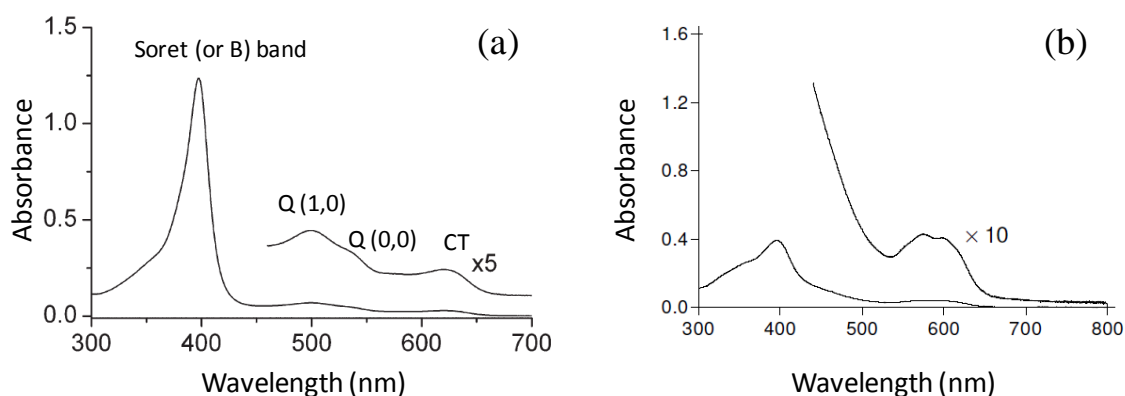
Figure 2.4 The UV spectra of haemin in (a) methanol solution and (b) Fe(III)PPIX dissolved in 0.1 M NaOH containing 10% (*v/v*) pyridine. Showing the absorption Soret (or B), Q and CT bands. Reproduced from reference.[154]

It has previously been shown in the pyridine hemichrome inhibition of β-haematin (Phiβ) assay that 5% (*v/v*) aqueous pyridine solution (pH 7.5), can selectively react with free Fe(III)PPIX, resulting in a characteristic orange-pink *bis*-pyridyl complex in solution with a distinctive absorbance maximum at 405 nm.[134] In the current work, we applied the principles of the Phiβ assay to the lipid-water interface model system (refer back to Figure 1.51, section 1.6).

Spectrophotometric titration of quinoline drugs against Fe(III)PPIX in solution has a hypochromic effect (absorbance band decreases) on the Soret band of Fe(III)PPIX, which quinoline drugs induce when binding to Fe(III)PPIX in solution. These binding isotherms is used to determine Fe(III)PPIX stoichiometries and association constants. The CT bands arise as a result of electronic transition from an ligand to the Fe centre of Fe(III)PPIX.[118,125,155]

2.5   Australian Synchrotron Light Source

2.5.1   Background

A synchrotron light source produces a high intensity beam of light as a result of accelerating electrons, which travel close to the speed of light in a ring-shaped chamber under ultra-high-vacuum conditions and have their path changed by powerful magnetic fields. A synchrotron light source includes 6 stages of operation (Figure 2.5). Starting with the electron gun (1), electrons are produced by thermionic emission from a heated tungsten matrix cathode. These electrons are then accelerated in the linear accelerator (2) to nearly the speed of light. The electrons then make their way into the booster synchrotron (3) where the energy stored in the electrons is increased to much higher energies. The storage ring (4) is the final destination for the accelerated electrons, where they circulate under ultra-high-vacuum conditions for many hours, before the electrons make their way into individual beamlines (5), positioned around the storage ring.

The synchrotron light can be filtered and directed down several beamlines located around the storage ring to be used in a wide range of high-resolution, in situ, real-time imaging and analysis techniques to examine the atomic and molecular detail of a wide range of materials, Figure 2.5.[156] At the beamlines, devices such as monochromators, filters and mirrors are used to select the appropriate wavelength of light for the experimental technique, and to focus the beam. The end station (6) is where the experiment is conducted, and the synchrotron light source is used to gather data in the form of images, chemical spectra, or scattered light.[156]
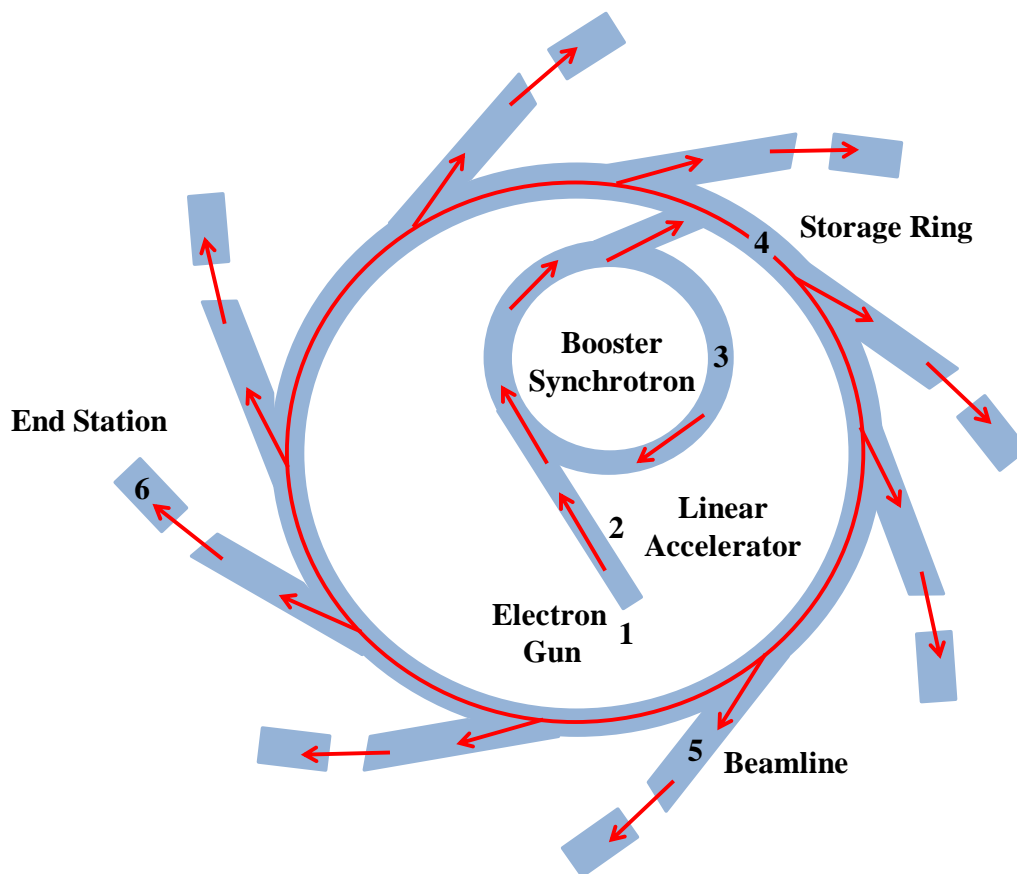
Figure 2.5 Schematic representation of synchrotron facility. Electrons emitted by an electron gun (1) are first accelerated in a linear accelerator (2), before entering a booster synchrotron (3), where they are further accelerated to higher energy levels. The electrons are then injected into the storage ring (4) where they travel close to the speed of light under ultra-high-vacuum conditions at a constant energy, having their paths changed by powerful magnetic fields. The light enter the different beamlines (5) located around the storage ring and make sure that the appropriate wavelengths is selected to utilise in the experiment at the end station (6). Redrawn based on reference.[156]

X-ray absorption spectroscopy (XAS) is one of many experimental techniques that rely on the intense radiation produced by a synchrotron light source. The measurements in this dissertation were carried out at the Australian synchrotron light source, in collaboration with Dr. Victor Streltsov from the Commonwealth Scientific and Industrial Research Organisation (CSIRO).

2.5.2   X-ray Absorption Spectroscopy

X-ray absorption spectroscopy (XAS) is a widely used method for investigating local atomic structure around an absorbing atom, for example Fe(III) in Fe(III)PPIX. The high energy X-rays generated by a synchrotron light source pass through the sample according to eq. 2.2.

$$I = I_0 e^{-\mu t} \tag{2.2}$$

where I_0 represents the intensity of the incident X-rays reaching the sample, I is the intensity of the X-rays that are transmitted through the sample, t is the sample thickness and μ is the absorption coefficient. The latter is a measure of the rate at which the intensity of an incident beam is reduced as it passes through a specific material.

An XAS spectrum consists of three regions. The absorption edges, which are labelled K, L or M, corresponding to the excitation of an electron from the n = 1, 2, 3 quantum levels of electron energy states.[157] The values for the absorption edge energies are well known and depend on the absorbing atom of interest. Therefore, K-edge chosen corresponds to the excitation of core level electrons (1s) in the K shell of the absorbing atom, and K_α and K_β emission lines result from electrons transferring to the K (n = 1) shell from the n = 2 orbitals (L shell) and n = 3 orbitals (M shell), respectively.

In the XAS spectrum oscillations are visible above the edge. These oscillations take place at a specific value of photon energy, when the photons have sufficient energy to excite a photon from an atom's core in the sample to create a photo-electron. This happens when the energy of the X-ray is higher than the energy level that is binding that electron to the core of the atom.[157] XAS therefore deals with measuring the energy dependence of μ at and above the binding energy of a known core level electron of a known atomic species (eq. 2.3).[157]

$$\mu \approx \frac{\rho Z^4}{A E^3} \tag{2.3}$$

According to the above equation, the value of μ depends on the sample density ρ, the atomic number Z, the atomic mass A, and the X-ray energy E. XAS is element-specific since the dependence on Z infers that μ for each absorbing atom is unique. Therefore, the

selected absorbing element can be examined by tuning the X-ray energy to an appropriate absorption edge corresponding to the binding energies of the electrons.

The other twee regions of the XAS spectrum relative to the edge are the X-ray absorption near edge structure, XANES and extended X-ray absorption fine-structure, EXAFS. The XANES region refers to absorption energies near the edge ($\pm$ 30-50 eV within the main absorption edge) and follows after the pre-edge and edge region in the spectrum (Figure 2.6). On the other hand, the EXAFS region refers to the oscillatory behaviour of the absorption coefficient above the absorption edge. Typically the EXAFS region starts anywhere from 50 to 100 eV above the absorption edge and can extend as far as 1000 eV past the edge (Figure 2.6).
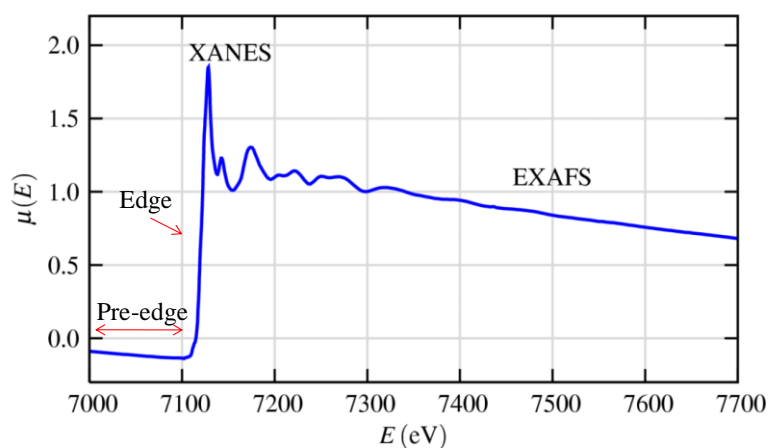
Figure 2.6 The Fe K_α-edge X-ray absorption spectroscopy (XAS) spectrum of FeO. The X-ray adsorption near edge structure (XANES) and extended X-ray absorption fine-structure (EXAFS) regions are indicated near to and above the absorption edge, respectively. Reproduced from reference.[157]

XANES and EXAFS contain related but different information about an element's local coordination and chemical state. XANES is sensitive to the formal oxidation state and geometry of the absorbing atom, while EXAFS provides information about the local structure around the absorbing atom, which includes bond lengths, thermal disorder and coordination numbers to neighbouring atoms. EXAFS data can be analysed in a more quantitative way than is currently possible for XANES,[158] therefore EXAFS was chosen in this work, since the local structure surrounding the absorbing Fe atom of Fe(III)PPIX are of interest.

2.5.3   Extended X-ray Absorption Fine Structure

2.5.3.1   Background

The oscillations in an extended X-ray absorption fine structure spectrum (EXAFS) can be thought of in a quantum mechanical manner, if the wave characteristics of the photo-electron are considered. As the spherical wave propagates away from the absorbing atom and interacts with the electronic potential of the neighbouring atoms (Figure 2.7), a part of this wave is back-scattered to the origin. The interference between the outgoing and scattered photo-electron waves gives rise to the oscillations visible in the EXAFS region.
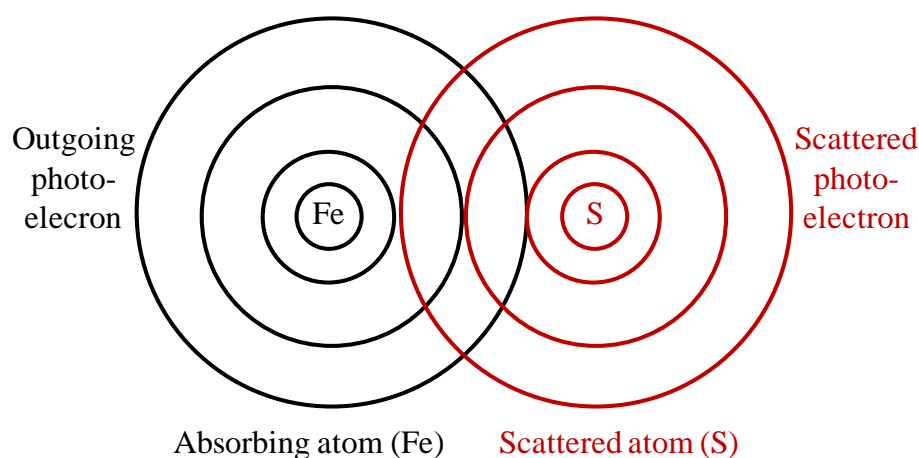
Figure 2.7 Consideration of the photo-electron as a spherical wave. Backscattering of the photo-electron from neighbouring atom (S) surrounding an absorbing atom (Fe) causes interference and leads to the oscillations visible in the EXAFS region of the spectrum. If there was no interference from neighbouring atoms, no oscillations would be visible, and the absorption coefficient would decrease smoothly with increasing energy. Redrawn from reference.[158]

The EXAFS function $\chi(E)$ is shown in eq. 2.4,

$$\chi(E) = \frac{\mu(E) - \mu_0(E)}{\Delta\mu_0(E)} \qquad (2.4)$$

where $\mu(E)$ is the measured absorption coefficient, $\mu_0(E)$ is the intrinsic absorption coefficient of an isolated atom which is expected to be a smooth function in the absence of interference from neighbouring atoms, and $\Delta\mu_0(E)$ is the measured oscillations in absorption coefficient $\mu(E)$ at a threshold energy E_0 (Figure 2.8).[157]
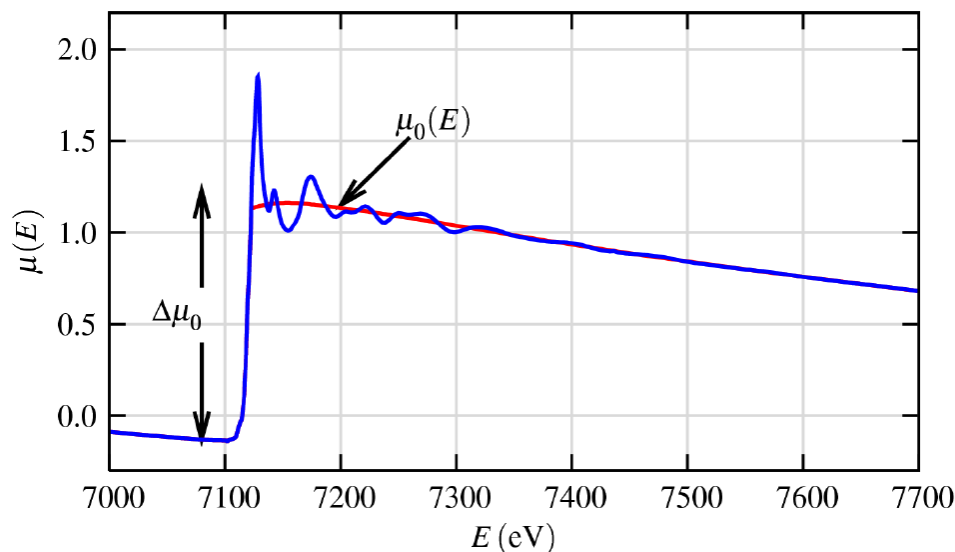
Figure 2.8 The Fe K$_\alpha$-edge XAS spectrum. The measured absorption coefficient, $\mu(E)$ is shown relative to a smooth background function $\mu_0(E)$ and edge-step $\Delta\mu_0(E_o)$ for FeO. Reproduced from reference.[157]

Since data collection is carried out on a 100-channel Ge detector, data reduction starts with merging of all the measured $\mu(E)$ spectra, using the AVERAGE program.[159] The EXAFS signals, which contain the information about the local structure around the absorbing atom, can then be extracted. In EXAFS spectroscopy, it is practice to convert the X-ray energy into the wave vector of the photo-electron (k) (Figure 2.9 (a)). In this form, the different frequencies of the oscillations of $\chi(k)$ are directly proportional to (bond) distances between the absorbing atom and its nearest neighbours. Therefore provides information about the location and distance between atoms within a molecule/material. The raw EXAFS spectrum is rapidly attenuated at high k values (Figure 2.9 (a)) and therefore, the oscillations of $\chi(k)$ are typically multiplied by a function of k (for example k^2 or k^3), to produce EXAFS data in which the intensity of the oscillations are similar over the entire k range (Figure 2.9 (b)).[157]
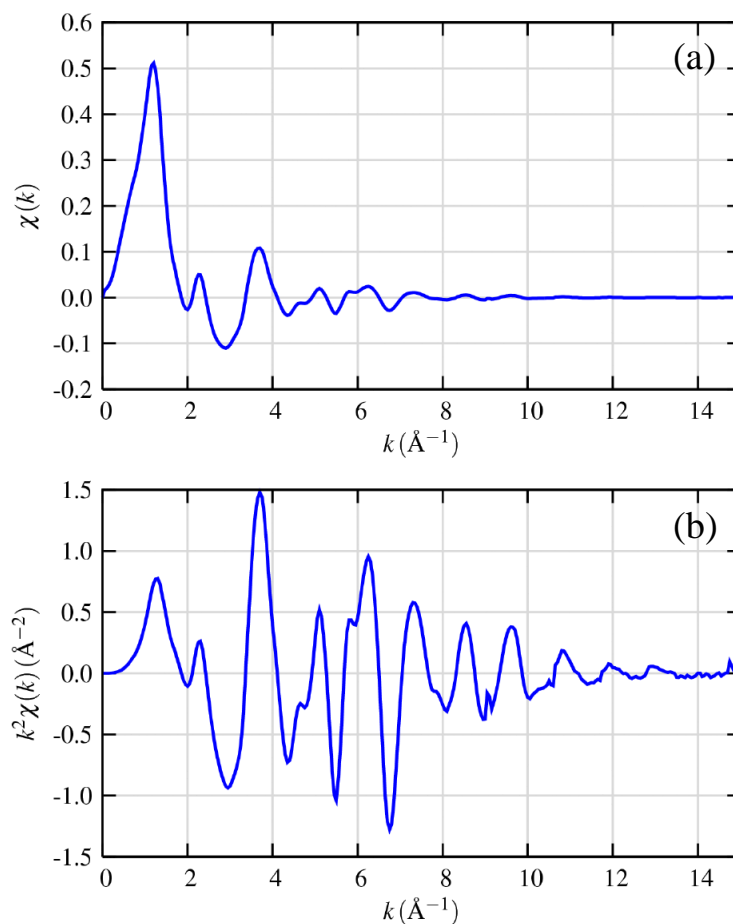
Figure 2.9 EXAFS spectrum for FeO. (a) The EXAFS signal as a function of photo-electron wave vector, $\chi(k)$. (b) To emphasise the oscillations, $\chi(k)$ is multiplied by a function of k (in this case k^2). Reproduced from reference.[157]

The k-weighted EXAFS data are used in fitting of the experimental EXAFS to the calculated EXAFS.[157] The next step is to Fourier transform the EXAFS signal $\chi(k)$ into $R(\text{Å})$-space (Figure 2.10) to obtain a radial distribution. In the Fourier transform spectrum, the different shells of atoms around the absorbing atom are represented as peaks. The interatomic distance does not automatically correspond to the x-axis since there is a phase shift in the peaks in $|\chi(R)|$ when compared to the actual distance.
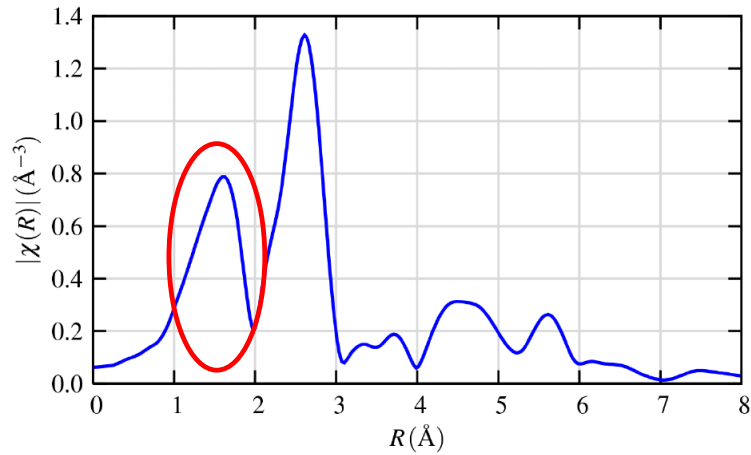
Figure 2.10 The Fourier transformed radial function, $\chi(R)$ in $R(\text{Å})$ space. The different shells of atoms around the absorbing atom are represented by the peaks in the spectrum. The first shell is denoted with a red circle. Reproduced from reference.[157]

The EXAFS equation is use to describe and model the relationship (distance and spatial coordinates) of neighbouring atoms to an absorbing atom using the different frequencies in the oscillations of $\chi(k)$, eq. 2.5:

$$\chi(k) = \sum_j \frac{N_j S_0^2 f_j(k) e^{-2k^2 \sigma_j^2}}{k R_j^2} sin\left[2kR_j + \delta_j(k)\right] \tag{2.5}$$

In the above equation, N is the number of neighbouring atoms around the absorbing atom in shell j, R is the distance of these neighbouring atoms to the absorbing atom, and σ^2 (the Debye-Wallers factor) is the mean-square disorder in R. Scattering properties of the neighbouring atoms include the amplitude reduction factor S_0^2, scattering amplitude $f(k)$, and the phase shift $\delta(k)$. The values of N, R and σ^2 can be determined, since structure determination is made on the basis of fitting the experimental data to a structural model which is known, and the values of $f(k)$ and $\delta(k)$ can be obtained to a good approximate by comparing the data to the known structure. EXAFS spectroscopy is sensitive to the chemical speciation of the neighbouring atoms, since $f(k)$ and $\delta(k)$ depend on atomic number (Z).[157]

2.5.3.2   EXAFS Analysis Programs

With the development of efficient analysis algorithms such as ATHENA,[160,161] EXAFS oscillations $\chi(k)$ can be extracted from the measured absorption coefficient function. The first step involves automated background subtraction; in ATHENA for example, the AUTOBK algorithm is implemented for this purpose. Using the data generated in ATHENA, the ARTEMIS program is later used to quantitatively analyse the EXAFS oscillations ($\chi(k)$).[160,161] ARTEMIS interfaces with FEFF, an automated algorithm for *ab initio* multiple scattering calculations generated according to a proposed input list of atom coordinates and distances from the absorbing atom (Figure 2.11). Using a model structure that is close to the expected structure (in solution or solid), a list of the x, y, and z coordinates is generated for all neighbouring atoms relative to a selected central atom, as well as the interatomic distances. This information is contained in the input file for FEFF, where the scattering amplitude $f(k)$ and phase shifts $\delta(k)$ are calculated theoretically.
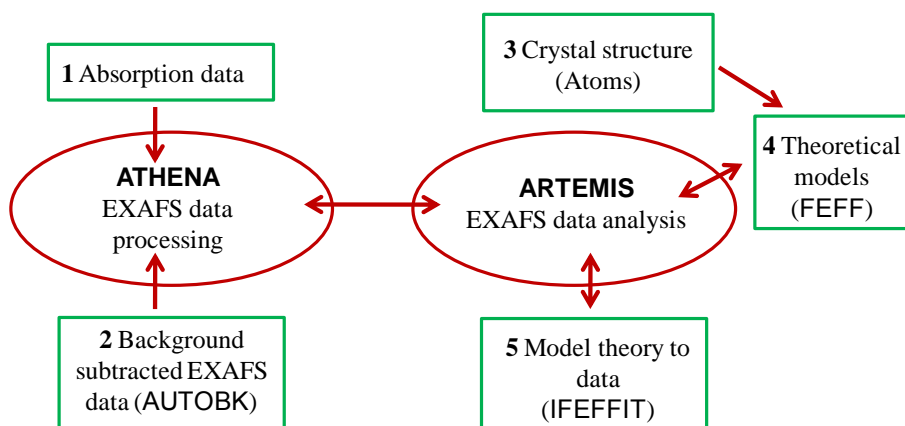
Figure 2.11 EXAFS data processing overview. The ATHENA program processes the absorption data (1) and interfaces with the automated background subtraction algorithm AUTOBK to remove instrumental background and absorption from other edges (2). Data analysis using ARTEMIS begins with inputting a suitable model for the most likely structure; this is often informed by SCD data (3). Theoretical models are processed through FEFF (4), and fitting of the model structure to the experimental data is enabled by IFEFFIT (5).

When considering the path that a photo-electron can travel, this path includes many atomic shells, from 1st neighbour shells, 2nd neighbour shells, 3rd neighbour shells and so on. A photo-electron can scatter from more than one atom before returning to the absorbing atom. Therefore multiple-scattering (MS) analysis of EXAFS data is important where the

backscatter of the photo-electrons is due to the contribution of two or more atoms, compare to single scattering (SS) (Figure 2.12). When multiple-scattering occurs at an angle greater than 150°, the contribution is strong. Angles can be determined from the strong dependence of the scattering, which could be use to assign a three-dimensional structure for the first few coordination shells from the absorbing atom.[158] ARTEMIS calculates these effects and includes them in the calculated $f(k)$ and $\delta(k)$ values in the EXAFS equation (eq. 2.4). The calculated $f(k)$ and $\delta(k)$ values can be used in the EXAFS equation to predict the structural parameters N, R and σ^2.
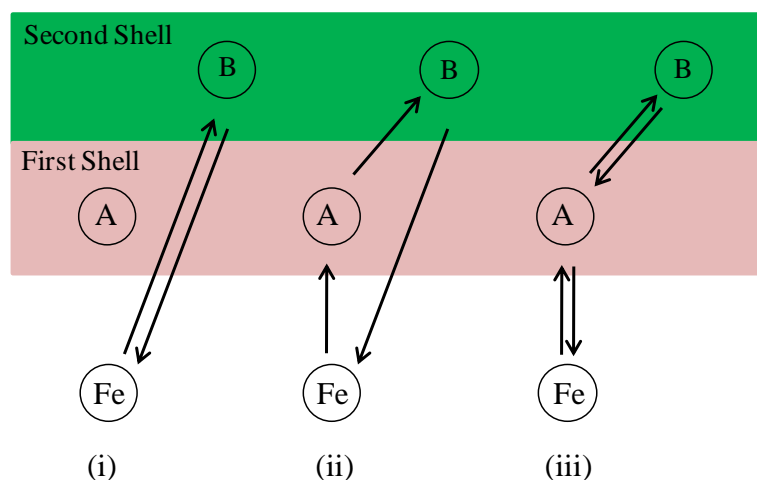
Figure 2.12 Back scattering contributions from neighbouring atoms. By considering Fe as the absorbing atom and A and B as its neighbouring atoms in the first and second shell respectively, there are three possible multiple-scattering pathways to consider when looking at atoms in the second shell. (i) The outgoing photo-electron to B, is only back-scattered by atom B. (ii) The outgoing photo-electron passes through A and B, is only back scattered by B. (iii) The outgoing photo-electron passes through A and B, is back scattered from B *via* A. Redrawn from reference.[158]

ARTEMIS also interfaces with IFEFFIT, which is used for fitting the EXAFS experimental data to the theoretical model of $\chi(k)$ built with FEFF (Figure 2.11). A fit is considered good if the R-value is less than 0.2, with S_0^2 equal to 0.9 ± 0.1 and σ^2 between 0.0005 and 0.02 Å^2.[158]

One advantage of EXAFS is that the sample can be in powder or solution form, although homogeneity is required. The disadvantage is that the structure determination is made on the basis of fitting the experimental data to a structural model. Hence it is imperative that you have a reasonable idea of the expected structure in order to generate a suitable

model.[158] Having SCD data is beneficial in order to generate a starting model together with theoretical parameters to be used in the EXAFS fitting. If the structure in solution is of interest while only the solid state structure is known by SCD, then the SCD structure provides a reasonable starting point to probe the solution speciation.

2.5.4   EXAFS Applied to Haemozoin Studies

EXAFS studies can be employed to investigate the local iron environment of Fe(III)PPIX, which allows both the type and the distance of each shell of atoms surrounding the absorbing metal atom to be identified.

As mentioned in the introduction (section 1.5.1), Walczak *et al.*[38] used EXAFS to confirmed that the oxidation state of Fe in haemozoin and β-haematin is the same for both structures, close to three, even though they found large disorder in the occupation and position of the oxygen site. In a subsequent study, EXAFS spectroscopy was used to compare the similarities between haemozoin and newly-synthesised synthetic substitutes for haemozoin, namely mesohaematin and deuterohaematin anhydrides (Figure 2.13).[37] The effect of CQ on the mesohaematin anhydride dimer when dissolved in DMSO and acetic acid respectively was also investigated.[162,163] Together, the body of literature relating to speciation studies of Fe(III)PPIX using EXAFS demonstrates the usefulness of the technique and its applicability to solution studies in particular.
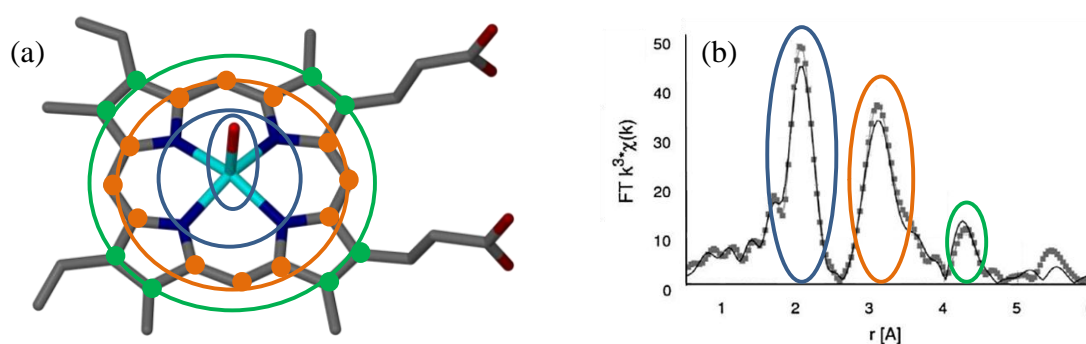
Figure 2.13 (a) The different shells of atoms surrounding the absorbing Fe centre of Fe(III)PPIX. This includes the four equatorial nitrogen and axial oxygen atoms (blue rings), the α and *meso* carbon atoms (orange rings) and the β carbon atoms (green rings). (b) These atoms give rise to the peaks observed in the Fourier transformed EXAFS spectra of *meso* β-haematin (solid line) and β-haematin (black squares). (b) was reproduced from reference.[37]

3   Materials, Instrumentation and General Methods

3.1   Materials

The materials used in this work were obtained from commercial suppliers and were analytical grade or of highest purity available commercially and used without further purification. The materials used are listed in Table 3.1.

Table 3.1 Materials used and their commercial source.

MATERIALS	COMMERCIAL SOURCE
Solids	
Bovin haematin (H$_2$O/HO—Fe(III)PPIX)	Sigma Aldrich
Bovin haemin (Cl- Fe(III)PPIX)	Sigma Aldrich
Soduim hydroxide pellets (NaOH)	Sigma Aldrich
Citric acid monohydrate (Citrate)	Sigma Aldrich
N-2-[hydroxyethyl]piperizine-N'-[2-ethanesulfonic acid] (HEPES)	Sigma Aldrich
rac-1-Monopalmitoylglycerol (MPG)	Sigma Aldrich
Liquids and Solvents	
Acetonitrile	Sigma Aldrich
Nitric acid (HNO$_3$)	Kimix Chemicals
Dimethyl Sulfoxide (DMSO)	Sigma Aldrich
Pyridine	Sigma Aldrich
Acetone	Kimix Chemicals
Methanol	Kimix Chemicals
Antimalarial drugs	
Chloroquine diphosphate (CQ)	Sigma Aldrich
Amodiaquine dihydrochloride dihydrate (AQ)	Sigma Aldrich
Quinine hemisulphate hydrate (QN)	Sigma Aldrich
Quinidine sulphate dihydrate (QD)	Sigma Aldrich
Mefloquine hydrochloride (MQ)	Sigme Aldrich
Halofantrine hydrochloride (Hf)	Sigma Aldrich

3.2   Instrumentation

3.2.1   pH Measurements

All pH measurements were performed using a METTER TOLEDO FE20/EL20 pH meter. Buffer solutions (pH 7 and pH 4) were obtained from CRISON and were used to calibrate the electrode before use.

3.2.2   Water Bath

A MEMMERT waterbath WNB 7-45 was used in this study at the temperature required for each experiment.

3.2.3   Centrifugation

Volumes of 5 – 15 mL were centrifuged in Greiner Falcon centrifuge tubes making use of a HERMLE LABORTECHNIK small centrifuge Z 206 A, with a maximum speed of 6 000 rpm.

3.2.4   UV-Visible Spectroscopy

UV-vis single wavelength readings were recorded using a UNICAM Helios UV-vis spectrophotometer. UV-vis spectra were recorded using a SPECORD®210PLUS UV-vis Spectrophotometer. Quartz cuvettes from SUPRASIL®, Hellma of 1 cm path length were used in the spectrophotometer. Cuvettes used over in the same experiments were washed according to the procedures described in section 3.4 and air dried.

3.2.5   Infrared Spectroscopy

ATR-IR spectra were recorded using the NEXUS^{TM} FT-IR spectrometer from THERMO NICOLET instruments fitted with a Golden Gate ATR accessory.

3.2.6   Electron Microscopy

Scanning electron microscopy was carried out using ZEISS EVO MA15VP scanning electron microscope.

3.2.7   Powder X-ray Diffraction

Powder X-ray diffraction data were recorded using the PANalytical X-ray Powder Diffractometer (XRD) from PANalytical, Netherlands.

3.2.8   Single Crystal X-ray Diffraction

Single crystal X-ray diffraction data were obtained using the Bruker Apex Duo single-crystal X-ray diffractometer from Bruker AXS, Germany.

3.2.9   Australian Synchrotron

Extended X-ray absorption fine structure (EXAFS) scans were recorded at the Australian synchrotron beamline for X-ray absorption spectroscopy.

3.3   Computer Software

The computer software used to analyse data is listed in Table 3.2.

Table 3.2 The computer software used in this dissertation.

PROGRAMME	VERSION	USE
GraphPad Prism[164]	5	Analysis and graphing
XSeed5[143]	2.05	Windows program for X-ray crystallography
POVRay[144]	3.6	Generate high quality molecular graphics
PLATON[165]/SQUEEZE[146]	-	Calculate the electron contribution of guest molecules
AVERAGE[159]	2.0	Merge EXAFS scans
ATHENA[160,161]	1.2.11	Data processing and background removal for EXAFS data.
ARTEMIS[160,161]	1.2.11	Model fitting to EXAFS experimental data
Endnote[166]	X2	Bibliography

3.4   General Preparation and Washing of Glassware and Plasticware

Where water was used to prepare solutions, glass distilled water was used unless otherwise stated. When small volumes needed to be used during preparation (100-500 μL) Eppendorf micro pipettes was used, and for even smaller volumes, 10 and 25 µL Hamilton syringes was used.

Fe(III)PPIX is known to adsorb onto glass and plastic surfaces and therefore precautions are required.[79,86] All glassware and cuvettes used to store solutions of Fe(III)PPIX in or during experiments were left to stand in 0.1 M NaOH for one hour, followed by extensive rinsing with water. The glassware and cuvettes were then washed with 1 M HNO_3 and again extensively washed with water. When washing the Greiner Falcon centrifuge tubes, the tubes were also left to stand in 0.1 M NaOH for one hour, followed by extensive rinsing with water to remove Fe(III)PPIX residues from the sides of the tubes.

4   Structural Characterisation of Fe(III)PPIX-Drug Complexes

4.1   Introduction

Due to mounting parasitic resistance towards current treatments, there is a need to develop new and effective antimalarials. In this regard, the lack of definitive structural evidence of antimalarial drug interactions with free Fe(III)PPIX, Fe(III)PPIX being the precursor to haemozoin formation, precludes rational design of new drug candidates. In particular, the lack of solid-state structures of Fe(III)PPIX complexes formed with both quinoline methanol and 4-aminoquinoline compounds has hindered our understanding of the mode of action of these clinically-relevant antimalarial drugs. The only known informative crystal structure of a Fe(III)PPIX-drug complex is that of Fe(III)PPIX-halofantrine (Hf), published in 2008.[85] Hence, the pharmacophore for quinoline antimalarials remains unidentified, and why certain compounds inhibit haemozoin formation while others do not, still remains ambiguous. At the present, one hypothesis is that drug compounds form complexes with free Fe(III)PPIX in solution, either through π-stacking or coordination, preventing its incorporation into β-haematin.[116,117,118] Questions regarding the nature of the interactions, for example whether they are covalent or non-covalent, and the structural features of quinolines that influence their binding to Fe(III)PPIX still remain unanswered.

In this chapter, single crystal X-ray diffraction (SCD) was used to determine the solid-state structure of the coordination complexes formed between Fe(III)PPIX and each of the quinoline methanol antimalarials quinine (QN), quinidine (QD) and mefloquine (MQ). Association studies of Fe(III)PPIX in solution with these antimalarials were undertaken to rationalise the existence of Fe(III)PPIX-drug species in non-aqueous solutions. Additionally, extended X-ray absorption fine structure (EXAFS) spectroscopy was used to confirm whether the species observed in the solid state also exists in solution, this being the medium that is more biologically relevant.

The Fe(III)PPIX-drug complexes determined in this study are the first known SCD examples of complexes formed between Fe(III)PPIX and quinoline antimalarial drugs. Specifically, analysis of the QD-Fe(III)PPIX, QN-Fe(III)PPIX and MQ-Fe(III)PPIX crystal structures has made known a pharmacophore which is central to our understanding the antimalarial activity of quinoline methanol antimalarial drugs. Since binding to free Fe(III)PPIX would certainly limit haemozoin formation, and given that these coordination complexes are also proposed to exist in solution, it seems reasonable to hypothesise that

the observed complexation may contribute to the antimalarial action of these compounds. Furthermore, through analysis of the crystal structures of the *Cinchona* alkaloid complexes, an explanation of the long-standing question regarding the greater activity of QD compared to QN is proposed.

4.2   Experimental Methods

This section describes the methods used to grow the single crystals of the Fe(III)PPIX-drug complexes and to fully characterise their structures. The materials used have been previously listed in Table 3.1.

4.2.1   Rationale for Growing Single Crystals of Fe(III)PPIX-Drug Complexes

Malariologists have been trying for decades to crystallise Fe(III)PPIX-drug complexes in order to better understand the mechanisms of action of antimalarial compounds. While the solid state is not representative of the biological environment in which inhibition of haemozoin formation takes place, X-ray crystallography can provide insight into structural features (inter- and intra-molecular interactions for example) which may be important for drug activity.

Owing to the fact that the speciation of Fe(III)PPIX varies from monomer to π-π dimer and even μ-oxo dimer depending on the solvent system,[86] crystallisation experiments in this field are not of a seemingly routine nature where an extensive variety of solvent systems can be investigated with little consideration. However, standard techniques for growing crystals, including solvothermal crystallisation, slow evaporation, slow cooling, vapour diffusion and solvent diffusion, could be used. Solvothermal crystallisation allows reactions to be performed in a closed vessel, where one has control over the reaction time as well as the temperature and pressure of the sample. Although all of these techniques were attempted, only slow evaporation yielded crystals suitable for SCD.

As a starting point, the same approach that was used to grow the crystals of Hf-Fe(III)PPIX was followed in order to try and grow crystals of other quinoline drug compounds complexing to Fe(III)PPIX.[85] After numerous attempts, none of the samples yielded crystals. The next step was to try and grow crystals from an aqueous medium at the pH of the food vacuole (roughly 4.8).[18] However, only amorphous material that

precipitated out of solution was recovered. With the discovery of haemozoin crystals in association with lipid droplets inside the parasite food vacuole,[60] the likely environment of haemozoin formation shifted from a aqueous environment to a neutral lipid environment. Therefore, it was reasoned that drug action could also take place in this environment. The strategy for subsequent crystallisation experiments was to make use of solvents such as dimethyl sulfoxide (DMSO), methanol, ethanol, acetonitrile and 1-propanol, which have been used previously to either grow or extract β-haematin crystals.[30,66,67,167]

The success in using the acetonitrile and DMSO-methanol solvent systems to grow suitable crystals for SCD is due to persistence in changing Fe(III)PPIX or drug concentration, crystal solution environment and utilising all of the crystallisation methods mentioned above, until suitable crystals were grown. The procedures that resulted in the complexes determined in this study are described in detail below.

4.2.2   X-Ray Crystallography

The Crystallographic Information Files (CIF) along with the final SHELX ".res" and ".hkl" files for all crystal structures presented in this chapter can be found on the attached CD.

4.2.2.1   The Crystal Structure of QN-Fe(III)PPIX

4.2.2.1.1   *Crystallisation of QN-Fe(III)PPIX*

The free base form of QN was prepared from an aqueous solution of the salt, using concentrated NaOH in order to yield a precipitate of the neutral species. The free base form of QN was recovered by drying the precipitate in the presence of phosphorus pentoxide for 3 to 7 days. A 3.08 mM stock solution of QN free base was prepared by dissolving 10.0 mg (30.82 μmol) in 10.0 mL acetonitrile. A 3.07 mM stock solution of Fe(III)PPIX was prepared by mixing Fe(III)PPIX (12.0 mg, 18.4 μmol) in 6.0 mL acetonitrile. The crystallisation medium was then prepared by adding 1.00 mL of the QN stock solution to 0.40 mL of the Fe(III)PPIX stock solution. Fe(III)PPIX is only sparingly soluble in acetonitrile and therefore exists as a suspension, only dissolving upon addition of the QN free base. The mixture was stirred for 30 min after which it was filtered through a PTFE filter disk (0.45 μm pore size) to remove excess Fe(III)PPIX. The glass vial

containing the filtrate was covered with parafilm, which was punctured with 2 needle-sized holes to allow for slow evaporation of solvent. The sample was left to stand at room temperature, and small needle shaped crystals were observed on the sides of the vial after 3 days. A crystal of dimensions $0.26 \times 0.13 \times 0.10$ mm was selected for X-ray diffraction.

4.2.2.1.2 *Structure Solution and Refinement*

Apart from the disordered methyl and vinyl groups and the included acetonitrile solvent molecule, all non-hydrogen atoms of the complex were refined with anisotropic temperature factors. The absolute stereochemistry of the complex was confirmed by the value of the Flack parameter [0.024(7)].[168] Using simple bond length constraints, the hydrogen atom located on the quinuclidine nitrogen atom was located in the difference map and refined independently with its own displacement parameters. The hydrogen atom located on one of the propionic acid groups was also located in the difference map and refined independently. There is disorder displayed on the porphyrin pyrrole rings by the vinyl and methyl substituents. The vinyl groups are disordered over 2 positions with site occupancy factors (s.o.f's) of 0.50 in each position, and the methyl groups are located in the alternate positions, also with s.o.f's of 0.50 in each position. The QN-Fe(III)PPIX moieties pack in layers in the *bc* plane with acetonitrile solvent molecules located within the layers. Located in pockets within and between the layers, the presence of additional solvent and/or water molecules is suspected, however, the electron density could not be unambiguously modelled. This structure was therefore analysed using SQUEEZE,[165] which showed a total void volume of 972 Å^3 and an electron count of 268 electrons.

4.2.2.2   The Crystal Structure of QD-Fe(III)PPIX

4.2.2.2.1 *Crystallisation of QD-Fe(III)PPIX*

A 1.53 mM stock solution of Fe(III)PPIX was prepared by dissolving Fe(III)PPIX (10.0 mg, 15.3 μmol) in 10.0 mL dimethyl sulfoxide. A 25.5 mM stock solution of QD sulphate dihydrate was prepared by mixing 100.0 mg (0.255 mmol) in 10.0 mL methanol. The crystallisation medium was prepared by adding 0.50 mL of the QD stock solution to 0.20 mL of the Fe(III)PPIX stock solution in a small 10 mL glass vial. The mixture was stirred for 30 min, after which the vial was covered with parafilm. The parafilm was punctured

with 2 needle-sized holes to allow for slow evaporation of solvent. The sample was left in the fridge for 4 to 5 weeks after which it was noted that small crystals had formed on the bottom of the vial. A single crystal of dimensions $0.30 \times 0.18 \times 0.13$ mm was selected for X-ray diffraction.

4.2.2.2.2 *Structure Solution and Refinement*

All non-hydrogen atoms of the complex were refined with anisotropic temperature factors. The absolute stereochemistry of the complex was confirmed by the value of the Flack parameter [0.020(5)].[168] As for QN-Fe(III)PPIX, the hydrogen atom located on the quinuclidine nitrogen atom was located in the difference map and refined independently with its own displacement parameters, using simple bond length constraints. The hydrogen atom located on one of the propionic acid groups was also located in the difference map and refined independently as before. There is disorder displayed on the porphyrin pyrrole rings by the vinyl and methyl substituents. As before, the vinyl groups are disordered over 2 positions with s.o.f's of 0.50 in each position and the methyl groups are located in the alternate position, also with s.o.f's of 0.50 in each position. The QD-Fe(III)PPIX structure packs to form channels in which disordered solvent molecules are included. The highly disordered solvent molecules could not be successfy modelled and instead, the structure was analysed using SQUEEZE,[165] the results of which showed a total void volume of 3696 Å^3 and an electron count of 1192 electrons.

4.2.2.3   The Crystal Structure of MQ-Fe(III)PPIX

4.2.2.3.1 *Crystallisation of MQ-Fe(III)PPIX*

Using concentrated NaOH in order to yield a precipitate of the neutral species, the free base of CQ was prepared from an aqueous solution of the salt. The free base form of CQ is hygroscopic, and was recovered by freeze drying the "sticky" precipitate. A solution containing 3.13 mM CQ free base and 2.42 mM MQ hydrochloride was prepared by dissolving CQ free base (5.0 mg, 15.6 μmol) and MQ (5.0 mg, 0.012 mmol) in 5.0 mL acetonitrile. It is important to note that MQ is obtained from Sigma-Aldrich as a racemate. After stirring the solution until all species had completely dissolved, haemin (4.0 mg, 6.14 μmol) was added. The resultant solution was stirred at 50 °C for a further 20 min, after

which it was filtered through a PTFE filter disc (0.45 µm pore size) to remove excess Fe(III)PPIX. The glass vial containing the filtrate was then capped and placed in a water bath at 37 $^{\circ}$C for 24 hours. Small plate-shaped crystals were observed on the bottom of the vial after 24 hours. A single crystal of dimensions $0.2 \times 0.1 \times 0.05$ mm was selected for X-ray diffraction.

4.2.2.3.2 *Structure Solution and Refinement*

Since two enantiomers of MQ were present in solution, it was not unexpected that two MQ-Fe(III)PPIX moieties were found in the asymmetric unit. For clarity, one is referred to as MQ-Fe(III)PPIX (I) and the other one as MQ-Fe(III)PPIX (II). Apart from some of the atoms on the disordered acetonitrile solvent molecules, all non-hydrogen atoms were refined with anisotropic temperature factors. The hydrogen atoms located on the propionic acid groups and the piperidine nitrogen atoms were located in the difference map and refined independently, with a simple bond length constraint for the H atoms on the nitrogens. There is disorder displayed on the porphyrin pyrrole rings by the vinyl and methyl substituents in both moieties. In MQ-Fe(III)PPIX (I), the vinyl groups are disordered over two positions with s.o.f's of 0.74 and 0.26. The vinyl group with an occupancy of 0.74 is disordered further over two positions with s.o.f's of 0.42 and 0.32. In MQ-Fe(III)PPIX (II), the vinyl groups are disordered over two positions with s.o.f's of 0.52 and 0.48, with the group with occupancy 0.52 being further disordered over two positions (s.o.f's of 0.21 and 0.31). One of the trifluoromethyl groups on the MQ-Fe(III)PPIX (II) moiety is disordered over two positions with s.o.f's of 0.47 and 0.53 respectively. Simple bond length constraints were applied to this disordered group. In the MQ-Fe(III)PPIX (I) propionate group, both oxygen atoms are disordered over two positions, with s.o.f's. of 0.81 and 0.19. The disordered acetonitrile molecules were modelled isotropically and simple bond length constraints were applied. One of the acetonitrile solvent molecules is disordered over two positions, which were modeled with s.o.f's of 0.65 and 0.35. The remaining disordered acetonitrile molecule was modeled with partial occupancy, and over two positions with s.o.f.'s of 0.30 and 0.52. The water molecule was also modeled with a partial occupancy of 0.29.

4.2.3   The Association of QD and QN with Fe(III)PPIX in Solution

4.2.3.1   Preparation of Solutions

4.2.3.1.1   *Fe(III)PPIX Stock Solution*

A 1.23 mM solution of Fe(III)PPIX was prepared by dissolving haemin (8.00 mg, 12.27 µmol) in 10.0 mL DMSO.

4.2.3.1.2   *QD Stock Solutions*

A: A 10.0 mM stock solution of QD sulphate dihydrate was prepared by dissolving the solid (6.10 mg, 15.0 µmol) in 1.50 mL methanol.

B: A 10.0 mM stock solution of free base QD was prepared by dissolving the solid (4.80 mg, 14.80 µmol) in 1.50 mL acetonitrile. The free base form of QD was prepared from an aqueous solution of the salt using concentrated NaOH in order to yield a precipitate of the neutral species. The free base form of QD was recovered by drying the precipitate in the presence of phosphorus pentoxide for 3 to 7 days.

C: A 2.5 mM stock solution of QD sulphate dihydrate was prepared by dissolving the solid (1.5 mg, 3.8 µmol) in 1.50 mL 1-pentanol.

D: A 10.0 mM stock solution of QD sulphate dihydrate was prepared by dissolving the solid (6.10 mg, 15.0 µmol) in 0.15 mL HEPES (2 M, pH 7.5) and 1.35 mL H_2O.

4.2.3.2   Experimental Procedures

4.2.3.2.1   *The Association of QD with Fe(III)PPIX in DMSO-Methanol*

The sample cuvette contained 20.0 µL Fe(III)PPIX stock solution, 580.0 µL DMSO and 1400.0 µL methanol, while the reference cuvette contained 600.0 µL DMSO and 1400.0 µL methanol. Spectrophotometric titrations of Fe(III)PPIX were performed by the addition (to both sample and reference) of 4×5.0 µL aliquots followed by 6×10.0 µL and 1×20.0 µL aliquots of drug stock solution **A**. The UV-vis spectra of the solutions were recorded between 300-800 nm after each addition of the QD stock solution and corrected for

dilution. The final drug concentration in the cuvette was approximately 0.476 mM, compared to 0.012 mM Fe(III)PPIX.

4.2.3.2.2 *The Association of QD with Fe(III)PPIX in Acetonitrile*

The sample cuvette contained 20.0 µL Fe(III)PPIX stock solution and 1980.0 µL acetonitrile, while the reference cuvette contained 20.0 µL DMSO and 1980.0 µL acetonitrile. Spectrophotometric titrations of Fe(III)PPIX were performed by the addition (to both sample and reference) of 4×5.0 µL aliquots followed by 6×10.0 µL and 1×20.0 µL aliquots of drug stock solution **B**. The UV-vis spectra of the solutions were recorded between 300-800 nm after each addition of the QD stock solution and corrected for dilution. The final drug concentration in the cuvette was approximately 0.476 mM, compared to 0.012 mM Fe(III)PPIX.

4.2.3.2.3 *The Association of QD with Fe(III)PPIX in 1-Pentanol*

The sample cuvette contained 20.0 µL Fe(III)PPIX stock solution and 1980.0 µL 1-pentanol, while the reference cuvette contained 20.0 µL DMSO and 1980.0 µL 1-pentanol. Spectrophotometric titrations of Fe(III)PPIX were performed by the addition (to both sample and reference) of 4×5.0 µL aliquots followed by 6×10.0 µL and 1×20.0 µL aliquots of drug stock solution **C**. The UV-vis spectra of the solutions were recorded between 300-800 nm after each addition of the QD stock solution and corrected for dilution. The final drug concentration in the cuvette was approximately 0.119 mM compared to 0.012 mM Fe(III)PPIX.

4.2.3.2.4 *The Association of QD with Fe(III)PPIX in Aqueous Solution*

The sample cuvette contained 40.0 µL Fe(III)PPIX stock solution, 200.0 µL HEPES (2 M,. pH 7.5) and 1760.0 µL H_2O while the reference cuvette contained 40.0 µL DMSO, 200 µL HEPES (2 M, pH 7.5) and 1760.0 µL H_2O. Spectrophotometric titrations of Fe(III)PPIX were performed by the addition (to both sample and reference) of 4×5.0 µL aliquots followed by 6×10.0 µL and 1×20.0 µL aliquots of drug stock solution **D**. The UV-vis spectra of the solutions were recorded between 300-800 nm after each addition of the QD

stock solution and corrected for dilution. The final drug concentration in the cuvette was approximately 0.476 mM compared to 0.024 mM Fe(III)PPIX.

The association of QN with Fe(III)PPIX in the DMSO-methanol and acetonitrile solvent systems was investigated using the same experimental procedures as described above for QD except that QD was replaced with QN, either as a salt or free base as required.

4.2.4   EXAFS Studies of Fe(III)PPIX-Drug Species

4.2.4.1   Sample Preparation

The Fe K_α-edge EXAFS spectra were collected at the X-ray absorption spectroscopy (XAS) beamline at the Australian synchrotron. The crystals investigated, namely those of QD-Fe(III)PPIX, QN-Fe(III)PPIX and MQ-Fe(III)PPIX were grown as described in section 4.2.2 above. The crystals were placed in the sample holder with as much of the mother liquor removed as physically possible. In the case of the crystallisation solutions, the amount of haemin and drug was increased to yield a final Fe(III)PPIX concentration of 10 mM in order to obtain the best data possible. However, in the crystallisation solutions of QN-Fe(III)PPIX and MQ-Fe(III)PPIX, the actual concentration was lower owing to the poor solubility of haemin in acetonitrile. All liquid samples were filtered through a PTFE filter disk (0.45 μm pore size) to obtain homogeneous solutions and were prepared immediately before the EXAFS experiment was conducted.

All samples were flash frozen in liquid nitrogen, and the cryogenic temperature of ~ 18K was maintained for the duration of the measurement of the sample to limit thermal disorder and avoid sample degradation. Spectra were collected from several locations within the sample to ensure the sample was homogenous and to limit sample damage due to continuous exposure to the X-ray beam.

4.2.4.2   Data Analyses

The raw EXAFS scans collected by the 100-channel Ge detector were merged using the AVERAGE program.[159] Data processing and background removal were achieved with ATHENA and AUTOBK respectively, while fitting of experimental data to the corresponding model was done with ARTEMIS.[160,161]

4.3 Results

4.3.1 The Crystal Structure of QN-Fe(III)PPIX

QN-Fe(III)PPIX was crystallised by slow evaporation from an acetonitrile solution of Fe(III)PPIX and QN in its free base form and small needle-like crystals were recovered from the side of the glass vial after three days. A single crystal of dimensions $0.26 \times 0.13 \times 0.10$ mm was selected for single crystal X-ray diffraction. Structural analysis revealed that QN-Fe(III)PPIX crystallises in the orthorhombic space group $C222_1$. The asymmetric unit is show in Figure 4.1 and the crystal and structural refinement parameters are summarised in Table 4.1.
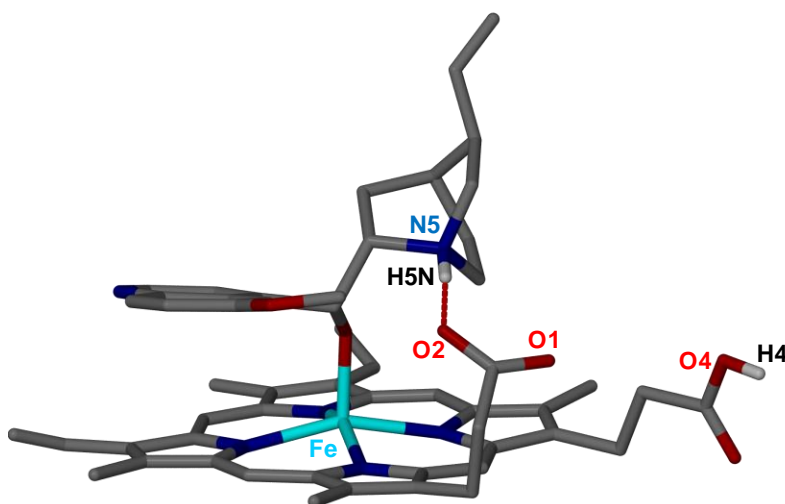
Figure 4.1 The asymmetric unit of the QN-Fe(III)PPIX complex. An intramolecular hydrogen bond between the propionate side chain of Fe(III)PPIX and the protonated quinuclidine nitrogen atom of the drug is shown as a red dashed line, with atoms involved in hydrogen bonding and the Fe(III) centre labelled. Solvent molecules and non-relevant H atoms have been removed for clarity. Atom colour coding: grey – C, cyan – Fe, dark blue – N, red – O and white – H.

Table 4.1 Crystal data, experimental and refinement parameters for QN-Fe(III)PPIX.

Molecular formula	$C_{54}H_{55}N_6O_6Fe_1.C_2H_3N$	
Stoichiometry	1:1	
Formula weight / g mol^{-1}	985.98	
Crystal system	orthorhombic	
Space group	$C222_1$	
Unit cell dimensions (Å, °)	a = 22.4947(9)	α = 90.00
	b = 24.785(1)	β = 90.00
	c = 18.0929(6)	γ = 90.00
Z	8	
Crystal size (mm^3)	$0.26 \times 0.13 \times 0.10$	
Temperature (K)	100(2)	
μ (mm^{-1})	2.864	
Independent reflections	6918	
R_{int}	0.0751	
Goodness of fit, S	0.868	
Final R indices [$I>2\sigma(I)$]	$R_1 = 0.0754$, $wR_2 = 0.2046$	

An intramolecular hydrogen bond between the propionate side chain of Fe(III)PPIX and the protonated quinuclidine nitrogen atom of the drug is observed in the asymmetric unit, while intermolecular hydrogen bonding occurs between the Fe(III)PPIX propionate group of one complex and the propionic acid side chain of a neighbouring complex. The intermolecular hydrogen bond results in pairs of hydrogen bonded QN-Fe(III)PPIX moieties. The various hydrogen bonds in the crystal structure are shown in Figure 4.2, while the hydrogen bond geometries are reported in Table 4.2.
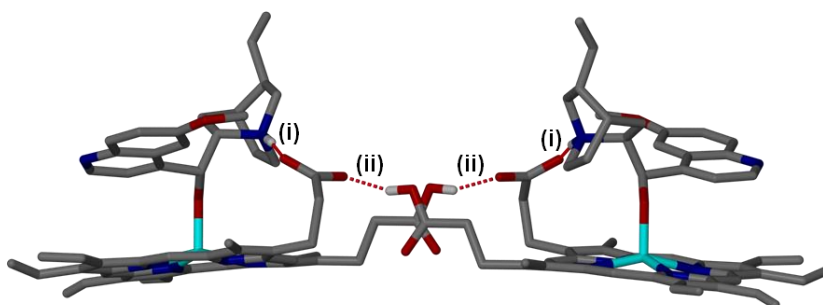
Figure 4.2 Hydrogen bonds (red dashed lines) observed in the crystal packing of QN-Fe(III)PPIX are (i) N5―H5N····O2 (intramolecular hydrogen bond) and (ii) O4―H4····O1 (intermolecular hydrogen bond). Solvent molecules and non-relevant H atoms have been removed for clarity. Atom colour coding: grey – C, cyan – Fe, dark blue – N, red – O and white – H.

Table 4.2 Hydrogen bond geometry in the QN-Fe(III)PPIX crystal structure.

Complex	D—H⋯A	D—H (Å)	H⋯A (Å)	D⋯A (Å)	D—H⋯A (°)
QN-Fe(III)PPIX	N5—H5N⋯O2	0.99(1)	1.69(1)	2.677(8)	174(14)
	O4—H4⋯O1*	0.88(3)	1.74(2)	2.578(7)	159(4)

*Symmetry code: −x+1, y, -z+2

In the crystal packing, the spaces in between the QN-Fe(III)PPIX moieties result in voids (with a total volume of 972 Å^3) which are filled with disordered solvent molecules. Figure 4.3 shows the packing in the crystal structure viewed along the crystallographic *a*-axis, with the disordered solvent molecules shown in space-filled mode.
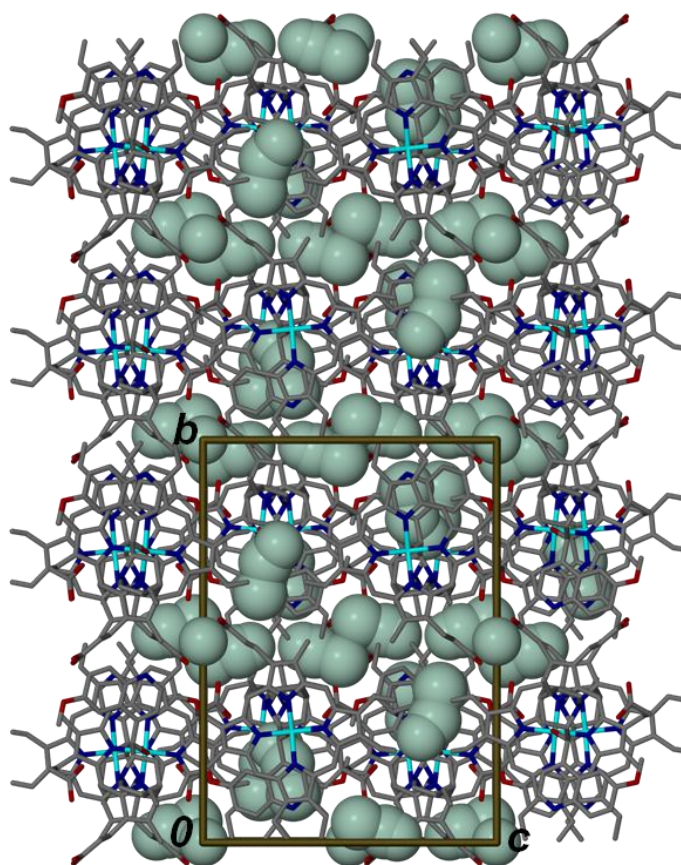
Figure 4.3 Crystal packing of QN-Fe(III)PPIX viewed along the crystallographic *a*-axis as indicated by the unit cell. Disordered acetonitrile molecules are shown in light blue (space-filling). Atom colour coding: grey – C, cyan – Fe, dark blue – N, red – O and white – H.

4.3.2   The Crystal Structure of QD-Fe(III)PPIX

Crystals of QD-Fe(III)PPIX were obtained by slow evaporation from a 3:7 (*v/v*) solution of DMSO-methanol, with drug added in excess in its acid form as a hemisulfate salt. Small crystals were recovered from the side of the glass vial after six weeks. A single crystal of dimensions $0.30 \times 0.18 \times 0.13$ mm was selected for X-ray diffraction. Structural analysis revealed that QD-Fe(III)PPIX crystallises in the orthorhombic space group I222. The asymmetric unit is shown in Figure 4.4 and the crystal and structural refinement parameters are summarised in Table 4.3.
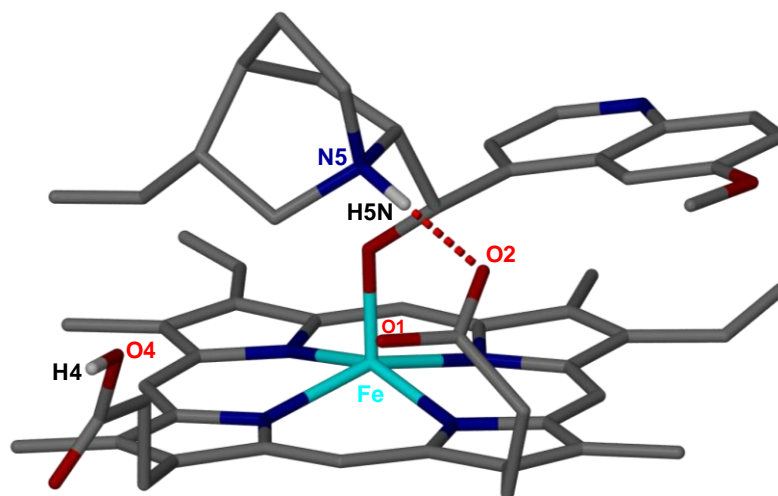
Figure 4.4 The asymmetric unit of the QD-Fe(III)PPIX complex. An intramolecular hydrogen bond between the propionate side chain of Fe(III)PPIX and the protonated quinuclidine nitrogen atom of the drug is shown as a red dashed line, with atoms involved in hydrogen bonding and the Fe(III) centre labelled. Solvent molecules and non-relevant H atoms have been removed for clarity. Atom colour coding: grey – C, cyan – Fe, dark blue – N, red – O and white – H.

Table 4.3 Crystal data, experimental and refinement parameters for QD-Fe(III)PPIX.

Molecular formula	$C_{54}H_{55}N_6O_6Fe_1$	
Stoichiometry	1:1	
Formula weight / g mol^{-1}	939.89	
Crystal system	orthorhombic	
Space group	I222	
Unit cell dimensions (Å, °)	a = 16.9423(6)	α = 90.00
	b = 20.4999(6)	β = 90.00
	c = 34.755(1)	γ = 90.00
Z	8	
Crystal size (mm^3)	$0.30 \times 0.18 \times 0.13$	
Temperature (K)	100(2)	
μ (mm^{-1})	2.369	
Independent reflections	10073	
R_{int}	0.0508	
Goodness of fit, S	0.878	
Final R indices [$I>2\sigma(I)$]	R_1 = 0.0605, wR_2 = 0.1931	

An intramolecular hydrogen bond between the propionate side chain of Fe(III)PPIX and the protonated quinuclidine nitrogen atom of the drug is observed in the asymmetric unit, while the intermolecular hydrogen bonding between the Fe(III)PPIX propionate and propionic acid side chain of a neighbouring complex results in pairs of hydrogen bonded QD-Fe(III)PPIX moieties. The various hydrogen bonds in the crystal structure are shown in Figure 4.5, while specific details of hydrogen bond geometries are reported in Table 4.4.
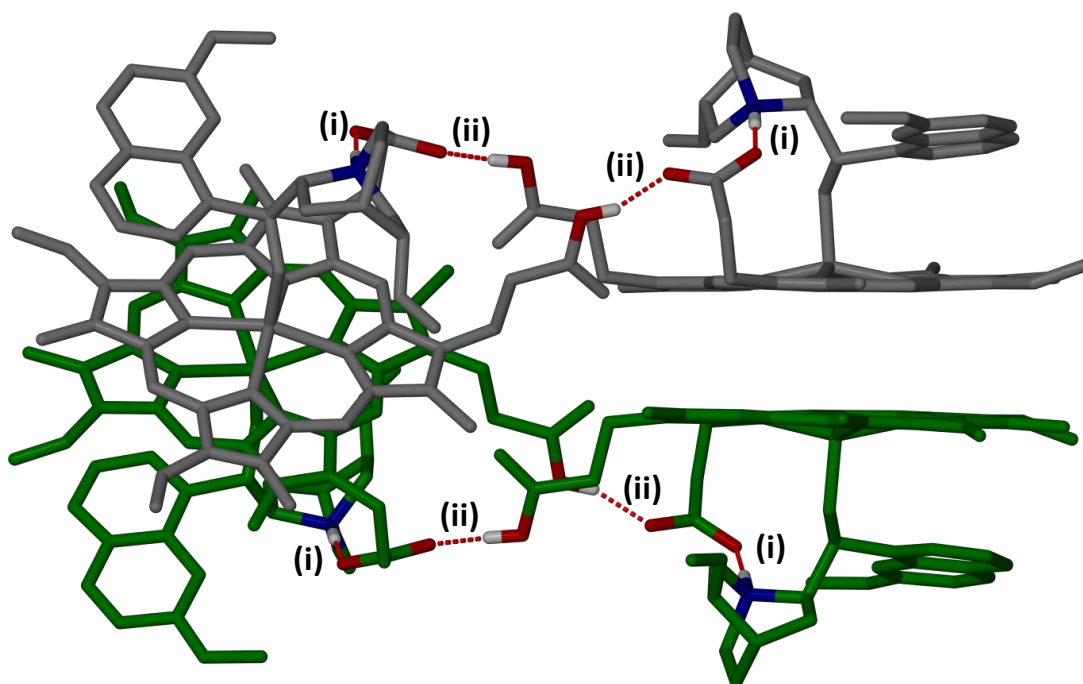
Figure 4.5 Hydrogen bonds (red dashed lines) observed in the crystal packing of QD-Fe(III)PPIX are (i) N5―H5N····O2 (intramolecular hydrogen bond) and (ii) O4―H4····O1 (intermolecular hydrogen bond). Solvent molecules and non-relevant H atoms have been removed for clarity. The two hydrogen-bonded pairs of QD-Fe(III)PPIX moieties shown are coloured grey and green respectively. Atom colour coding: blue – N, red – O and white – H.

Table 4.4 Hydrogen bond geometry in the QD-Fe(III)PPIX crystal structure.

Complex	D—H····A	D—H (Å)	H····A (Å)	D····A (Å)	D—H····A (°)
QD-Fe(III)PPIX	N5—H5N····O2	0.99(1)	1.66(1)	2.669(4)	175(6)
	O4—H4····O1[*]	0.84	1.76	2.525(5)	154(6)

[*]Symmetry code: −x+1, y, -z+2

The intermolecular hydrogen bonding between the Fe(III)PPIX propionate and propionic acid side chain of the neighbouring complex is supported by an observed vibration at approximately 1702 cm^{-1} in the infrared spectrum of QD-Fe(III)PPIX, shifted almost 10 cm^{-1} relative to the starting material (Fe(III)PPIX), confirming the presence of at least one propionic acid group in the product (Figure 4.6).
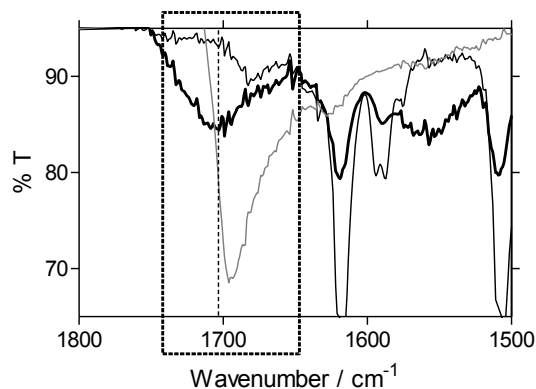
Figure 4.6 Infrared spectra of the QD-Fe(III)PPIX complex (thick black line) as well as the starting materials QD.HSO$_4$ (thin black line) and Fe(III)PPIX (thin grey line). The vertical dashed line indicates the carbonyl stretch assigned to a carboxylic acid functional group. This corresponds to the propionic acid side chain of Fe(III)PPIX.

The QD-Fe(III)PPIX moieties pack in the crystal structure forming rather large channels filled with disordered solvent molecules: SQUEEZE analysis indicated a total void volume of 3696 Å^3. The channels are best appreciated when viewing the unit cell along the crystallographic *b*-axis (Figure 4.7).
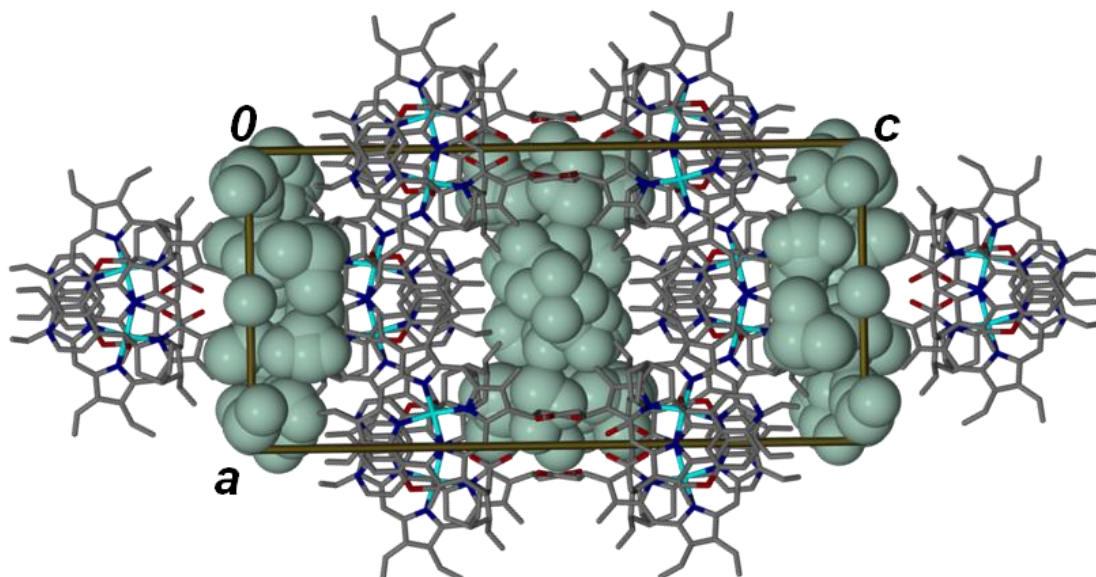
Figure 4.7 Crystal packing of QD-Fe(III)PPIX viewed along the crystallographic *b*-axis, as indicated by the unit cell. Disordered DMSO and methanol molecules are shown in light blue (space-filling). Atom colour coding: grey – C, cyan – Fe, dark blue – N, red – O and white – H.

105

4.3.3   Similarities Between QN-Fe(III)PPIX and QD-(III)PPIX

In addition to the hydrogen bonding features described above, the crystal structures of the QN-Fe(III)PPIX and QD-Fe(III)PPIX complexes share a number of structural features which may be important for the interaction of the drug with its proposed target, Fe(III)PPIX. First, analysis of the crystal structures confirms that the benzylic alcohol functional group of the drug is deprotonated in both complexes, facilitating coordination to the Fe(III) centre of Fe(III)PPIX. Second, the Fe-O bond lengths of 1.866 and 1.862 Å respectively, are in agreement with the coordination of an alkoxide (1.816 – 1.867 Å),[127,128,129,130] rather than an alcohol (2.112 – 2.160 Å).[131,132]

In the QN-Fe(III)PPIX and QD-Fe(III)PPIX complexes, we observed that the quinoline ring is tilted at an angle of approximately 12.7° and 10.1° relative to the mean porphyrin plane and furthermore is located towards the edge of the porphyrin. One of the aromatic porphyrin pyrrole rings and the drug quinoline ring make their closest contact with one another at a distance of approximate 3.3 Å in both structures. The mean interplanar distance between the two aromatic systems is approximately 3.3 Å, which is consistent with π-stacking (Figure 4.8).[169]

3.3-3.8 Å

Stacked   Offset
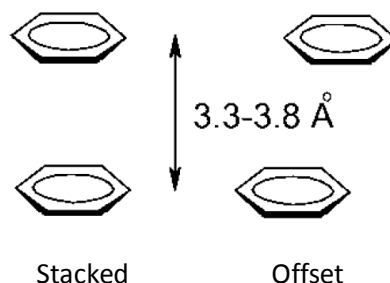
Figure 4.8 The π-π interaction found between aromatic rings. Reproduced from reference.[169]

An interesting feature observed in the crystal packing in both structures is that there is additional π-stacking between the unligated faces of Fe(III)PPIX of adjacent alkaloid-Fe(III)PPIX moieties, which may be a direct consequence of the crystal packing (Figure 4.9 (a) and (b)). However, the geometry of the porphyrins relative to one another is reminiscent of that reported for the so called π-π dimer.[79,83] The Fe(III) centres are offset relative to one another with a distance of 3.4 Å between the mean porphyrin planes.
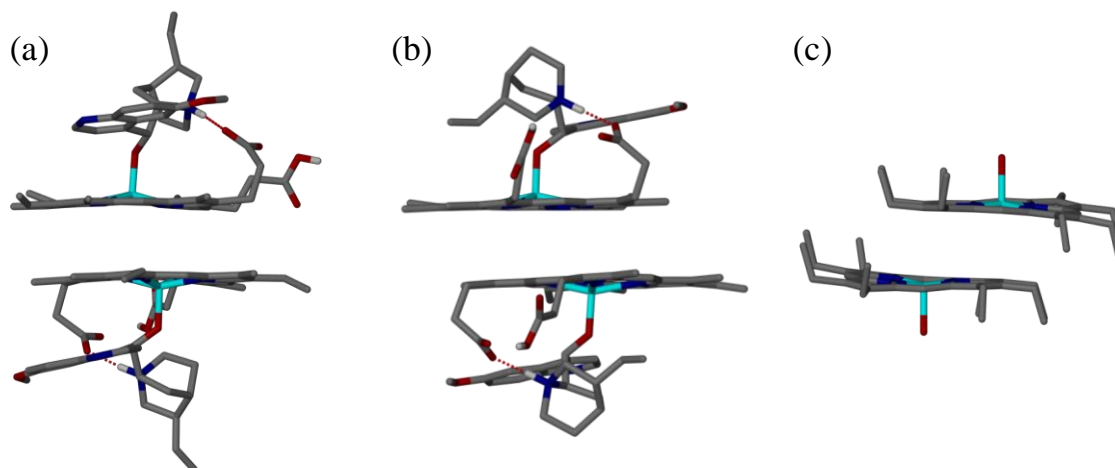
Figure 4.9 The offset π-π dimerisation observed between (a) QN-Fe(III)PPIX, and (b) QD-Fe(III)PPIX moieties in the crystal packing. (c) This "dimer" resembles the π-π dimer predicted in aqueous solution which was supported by the SCD structure of Cheng *et al*.[83] for aqua-iron(III) octaethylporphyrin perchlorate.[83] Picture (c) is reproduced from reference.[83] Hydrogen bonds are shown as red dashed lines.

Due to the highly disordered solvent molecules, which could not be successfully modelled in either structure, the structures were analysed using SQUEEZE.[146] The results showed a total void volume of 972 $Å^3$ and 3696 $Å^3$ and an electron count of 268 and 1192 electrons for QN-Fe(III)PPIX and QD-Fe(III)PPIX, respectively. It is clear that the packing in each crystal structure is unique. This interesting result is unexpected at first given that QN-Fe(III)PPIX and QD-Fe(III)PPIX complexes share so many structural similarities. An interesting observation in the crystal packing of QD-Fe(III)PPIX is the presence of rather large channels filled with disordered solvent molecules. Since porous materials are of increasing interest for gas storage and other applications, preliminary attempts were made to exchange the solvent in the crystals with other solvents, however, all attempts were unsuccessful. We suspect that this may be due to the fact that these crystals are seemingly very fragile when removed from their mother liquor.

4.3.4   The Crystal Structure of MQ-Fe(III)PPIX

Crystals of MQ-Fe(III)PPIX were obtained from an acetonitrile solution of Fe(III)PPIX, MQ hydrochloride and CQ free base. Small needle-like crystals were recovered from the side of the glass vial after one day. A single crystal of dimensions $0.05 \times 0.1 \times 0.2$ mm was selected for X-ray diffraction and structural analysis revealed that the MQ-Fe(III)PPIX complex crystallises in the triclinic space group $P\bar{1}$. The asymmetric unit is shown in Figure 4.10 and the crystal and structural refinement parameters are summarised in Table 4.5.
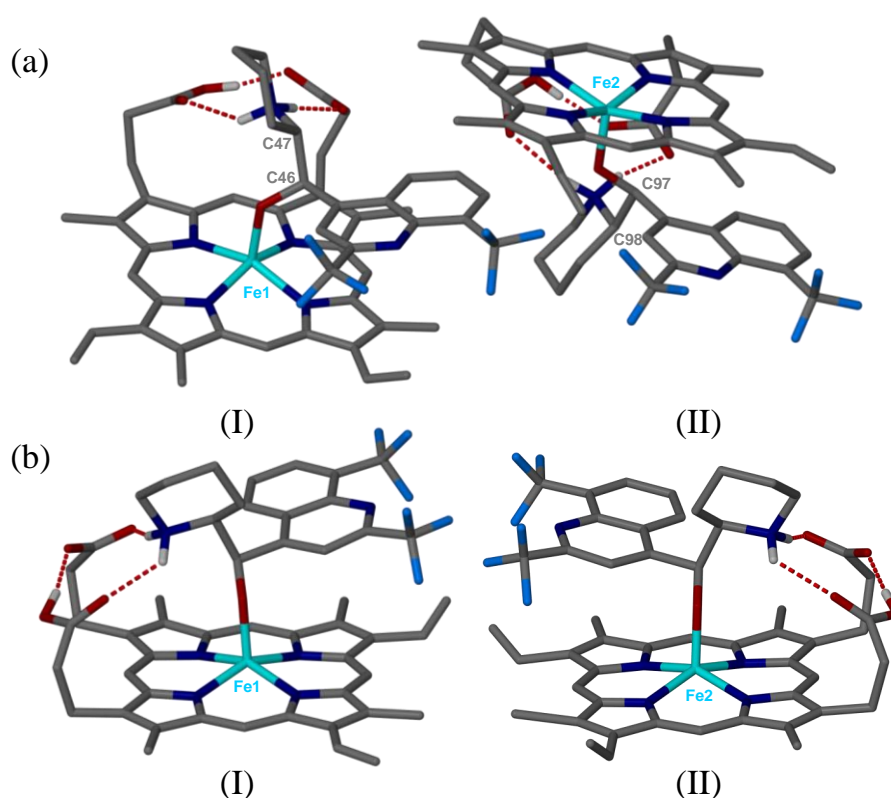
Figure 4.10 (a) The asymmetric unit of the MQ-Fe(III)PPIX complex contains both of the erythro enantiomers of MQ, labelled (I) and (II) respectively. (b) The display of I and II above does not reflect the asymmetric unit; rather the two moieties in the asymmetric unit of MQ-Fe(III)PPIX (I and II), determined by SCD, were separated to make viewing of the atoms more visible with the two MQ-Fe(III)PPIX moieties in the asymmetric unit having a (I) $C_{46}R$, $C_{47}S$ configuration and (II) $C_{97}S$, $C_{98}R$ configuration respectively. Intramolecular hydrogen bonds are shown with red dashed lines with chiral centres and the Fe(III) centres labelled. Solvent molecules and non-relevant H atoms have been removed for clarity. Atom colour labelling: grey – C, cyan – Fe, dark blue – N, light blue – F, red – O and white – H.

108

In chapter 6 it will be shown that in the presence of haemin and CQ free base, the formation of β-haematin (DMSO solvate) crystals occurs. Therefore, the rationale in adding CQ free base and MQ together with haemin in solution was to see if MQ would block the formation of β-haematin DMSO solvate crystals. Indeed, this was found to be the case, as the MQ-Fe(III)PPIX complex was formed preferentially.

Table 4.5 Crystal data, experimental and refinement parameters for MQ-Fe(III)PPIX.

Molecular formula	$C_{108}H_{101}O_{11}Fe_2N_{15}F_{12}$	
Stoichiometry	1:1	
Formula weight / g mol^{-1}	2155.81	
Crystal system	Triclinic	
Space group	$P\bar{1}$	
Unit cell dimensions (Å, °)	a = 13.655(1)	α = 90.523(1)
	b = 18.596(2)	β = 108.490(1)
	c = 20.269(2)	γ = 96.048(2)
Z	2	
Crystal size (mm^3)	$0.20 \times 0.10 \times 0.05$	
Temperature (K)	100(2)	
μ (mm^{-1})	0.395	
Independent reflections	24809	
R_{int}	0.0522	
Goodness of fit, S	1.029	
Final R indices [I>2σ(I)]	$R_1 = 0.0597$, $wR_2 = 0.1479$	

MQ exists as a mixture of four diastereomers, which are divided into (+)- and (-)-*erythro* enantiomers having (11R,12S) and (11S,12R) configurations respectively, and the (+)- and (-)-*threo* enantiomers having (11R,12R) and (11S,12S) configurations respectively (Figure 4.11). The MQ used in this study was obtained from Sigma-Aldrich as a racemate. Therefore, the MQ-Fe(III)PPIX crystal structure contains a mixture of the *erythro* enantiomers of MQ with the two MQ-Fe(III)PPIX moieties in the asymmetric unit having $C_{46}R$, $C_{47}S$ configuration (Figure 4.10 (I)) and $C_{97}S$, $C_{98}R$ configuration (Figure 4.10 (II)) respectively, which is expected. A racemic mixture of *erythro* enantiomers is most commonly used in clinical practice. However, the neurological side effects of MQ seem to be associated with the (-)-*erythro* enantiomer of MQ and therefore, enantiopure MQ is ideal.[170]
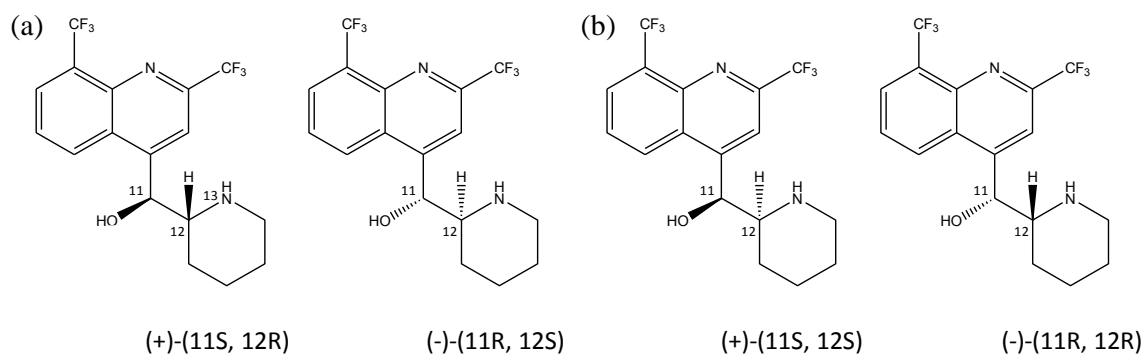
Figure 4.11 Optical isomers of MQ include (a) *erythro* enantiomers and (b) the *threo* enantiomers.

In the crystal structure of MQ-Fe(III)PPIX, coordination to the Fe(III) centre of Fe(III)PPIX *via* the deprotonated benzylic alcohol functional group of the drug is also observed. The Fe1-O5 and Fe2-O10 bond lengths are 1.899 and 1.891 Å respectively, which again is consistent with the coordination of an alkoxide species.[127,128,129,130] Three intramolecular hydrogen bonds are observed in each complex (I and II); the first occurs between the propionate and propionic acid side chains of Fe(III)PPIX, while the other two occur between each of these groups and the piperidinium nitrogen atom of the drug. This network of intramolecular hydrogen bonds is shown in Figure 4.12, while the hydrogen bond geometries are reported in Table 4.6. An interesting observation is the absence of the intermolecular hydrogen bonds through Fe(III)PPIX propionate and propionic acid side chains of neighbouring complexes that were present in the QN and QD complexes.

(I)   (II)
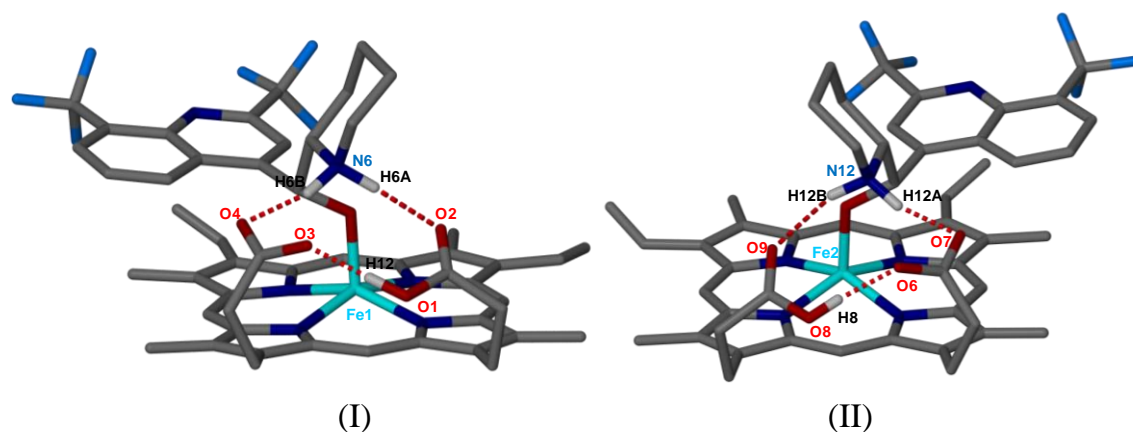
Figure 4.12 The hydrogen bonding network in the MQ-Fe(III)PPIX structure for the two MQ-Fe(III)PPIX moieties in the asymmetric unit having a (I) $C_{46}R$, $C_{47}S$ and (II) $C_{97}S$, $C_{98}R$ configuration respectively. The display of I and II above does not reflect the asymmetric unit; rather the two moieties in the asymmetric unit of MQ-Fe(III)PPIX (I and II), determined by SCD, were separated to make numbering of the atoms more visible.

Table 4.6 Hydrogen bond geometry in the MQ-Fe(III)PPIX crystal structure.

Complex	D—H⋯A	D—H (Å)	H⋯A (Å)	D⋯A (Å)	D—H⋯A (°)
MQ-Fe(III)PPIX ($C_{46}R$, $C_{47}S$)*	N6—H6A⋯O2	0.99	2.21	3.003(4)	136.0
	N6—H6B⋯O4	1.00	1.75	2.712(5)	161.5
	O1—H12⋯O3	0.95	1.63	2.577(4)	170.6
MQ-Fe(III)PPIX ($C_{92}S$, $C_{98}R$)*	N12—H12A⋯O7	1.00	1.72	2.698(3)	162.8
	N12—H12B⋯O9	0.99	2.30	3.083(3)	134.8
	O8—H8⋯O6	0.84	1.70	2.536(3)	173.8

* Labelling as in the crystal structure of MQ-Fe(III)PPIX

The crystal packing of MQ-Fe(III)PPIX is best appreciated when viewing the unit cell along the crystallographic *b*-axis as shown in Figure 4.13. The MQ-Fe(III)PPIX moieties pack in the crystal to form layers along the crystallographic *c*-axis. The empty spaces within the layers are filled with disordered acetonitrile solvent and water molecules.

As before, some π-π stacking between the unligated faces of Fe(III)PPIX of adjacent alkaloid-Fe(III)PPIX moieties is observed. The distance between the mean porphyrin planes are 3.38 and 3.69 Å, respectively with the Fe(III) centres offset relative to one another (Figure 4.13).
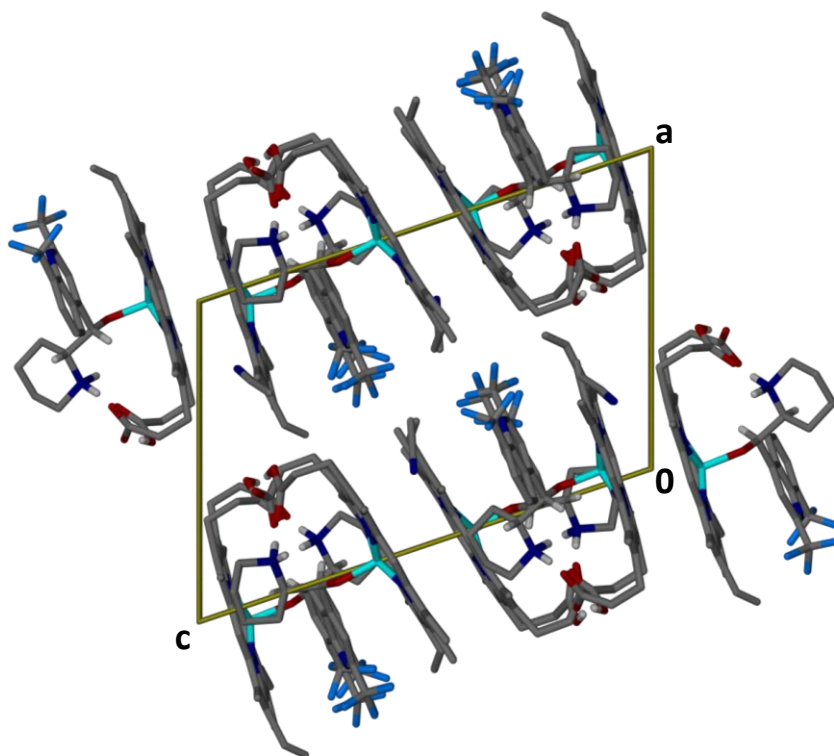

Figure 4.13 Crystal packing of MQ-Fe(III)PPIX viewed along the crystallographic *b*-axis as indicated by the unit cell. The offset π-π dimerisation is also observed between adjacent MQ-Fe(III)PPIX moieties in the crystal packing. Disordered solvent molecules have been removed for clarity.

4.3.5   The Association of QD and QN with Fe(III)PPIX in Solution

While the crystal structures of the quinoline methanols complexing with Fe(III)PPIX provide insight into the key interaction in the solid state, the question of whether the same interactions (effectively the same species) are observed in solution needed to be addressed. Asher *et al.*[86] showed that Fe(III)PPIX exhibits complex speciation equilibria in mixed aqueous solutions. Comparing the UV-vis spectra of Fe(III)PPIX in various solvent systems, it was found that in 40% (*v/v*) aqueous DMSO, pH 7.5, Fe(III)PPIX exists as a

monomer, although in the same concentration of methanol, Fe(III)PPIX exists as a π-π dimer which is independent of pH.[86]

In the present study, crystals of QD-Fe(III)PPIX and QN-Fe(III)PPIX were obtained under non-biological conditions: 3:7 (*v/v*) DMSO-methanol solution in the case of the QD-Fe(III)PPIX, and acetonitrile in the case of the QN-Fe(III)PPIX. However, as neither of the solvents were anhydrous, trace amounts of water could therefore be expected.

The speciation of Fe(III)PPIX in 3:7 (*v/v*) DMSO-methanol solution was determined before and after spectrophotometric titration with both QD and QN hemisulfate salts (Figure 4.14 (a) and Figure 4.15 (a)). Similarly, both QD free base and QN free base were titrated against Fe(III)PPIX in acetonitrile (Figure 4.14 (b) and Figure 4.15 (b)), since these solutions represent the crystallisation media of the QD-Fe(III)PPIX and QN-Fe(III)PPIX crystals respectively. The initial spectra are shown in red and the final spectra are shown with light blue dashed lines in Figure 4.14. In Figure 4.15 only the initial and final spectra after all the titrations are shown in the graphs for clarity.

Since the proposed location of drug activity has shifted from an aqueous environment to a neutral lipid environment,[60] the speciation of Fe(III)PPIX in 1-pentanol, which is used as a simple model for a lipid in β-haematin formation studies at the lipid-water interface system,[73] was investigated before and after spectrophotometric titration with QD hemisulfate salt (Figure 4.14 (c)). For comparison, the titration was repeated in aqueous solution and the results are shown in Figure 4.14 (b).

The UV-vis spectrum of monomeric Fe(III)PPIX in 40% aqueous DMSO shows a distinctive Soret band at approximately 400 nm due to the major electronic transition of the porphyrin core. In the absence of either of the *Cinchona* alkaloids, the speciation of Fe(III)PPIX in 3:7 (*v/v*) DMSO-methanol is consistent with a monomeric species. Little change is observed in the UV-vis spectrum in this medium upon titration of Fe(III)PPIX with QD or QN (Figure 4.14 (a) and Figure 4.15 (a)). Following titration with QD free base or QN free base in acetonitrile (Figure 4.14 (b) and Figure 4.15 (b)), a very similar final spectrum to that seen in 3:7 (*v/v*) DMSO-methanol solutions was observed, though this is quite different to the broadly domed Soret peak at 387 nm observed in the absence of either QN or QD. Direct observation of the Fe(III)PPIX speciation in a lipid solution was not possible due to light scattering. However, as 1-pentanol has been used as a simple model for a lipid, we investigated the speciation of Fe(III)PPIX in this alcohol (Figure 4.14

(c)). The final spectrum is again similar to the spectra recorded in both DMSO-methanol and acetonitrile solutions. However, compared to the spectrum recorded in aqueous solution, the final spectra recorded in organic solutions are different. In aqueous solution, the Soret band is broad and flat indicating a dimeric Fe(III)PPIX species. The charge-transfer band observed at ~603 nm in the spectra of Fe(III)PPIX in organic solvents differ from that in aqueous solution, suggesting different ligand interactions at the Fe(III) centre.
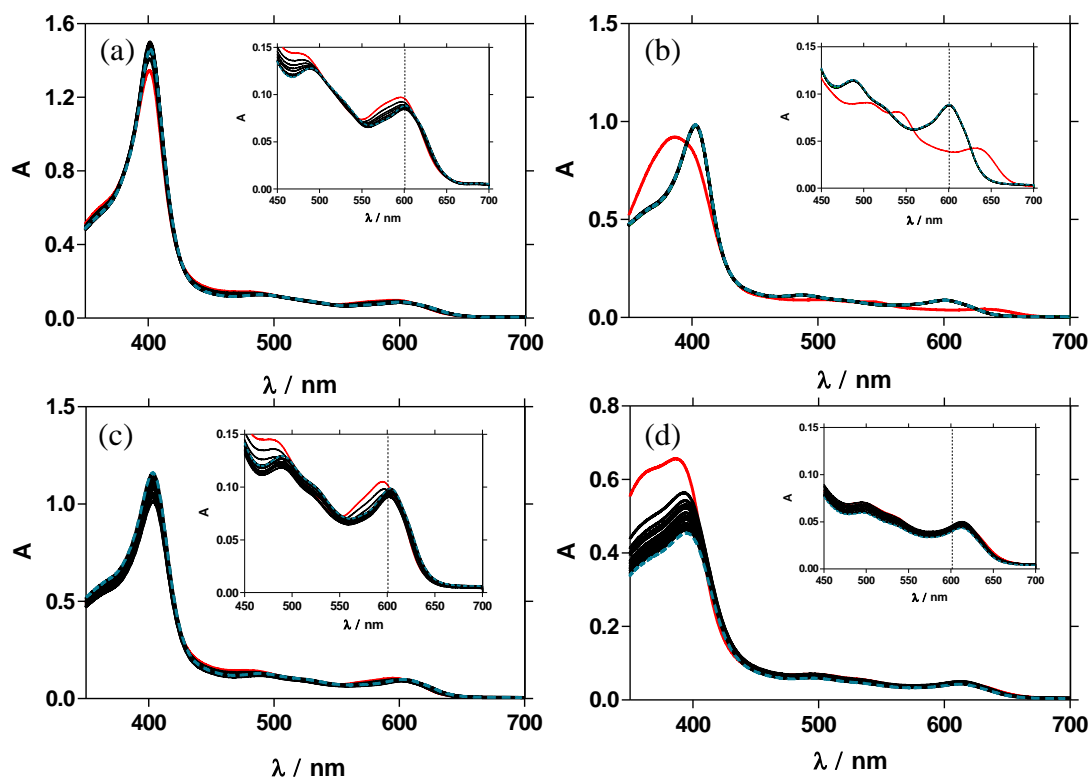
Figure 4.14 The UV-vis spectra of Fe(III)PPIX in solution before (—) and after spectrophotometric titration with QD hemisulphate (---). Conditions are (a) 3:7 (*v/v*) DMSO-methanol, (b) acetonitrile (titration with QD free base for solubility reasons), (c) 1-pentanol and (d) aqueous solution (0.2 M HEPES, pH 7.4). The position of the charge transfer band at 603 nm is marked by dotted vertical lines shown in the inset. As shown in the inset, the dotted line at 603 nm coincides with the charge transfer band in spectra (a-c) but not in aqueous solution (d).
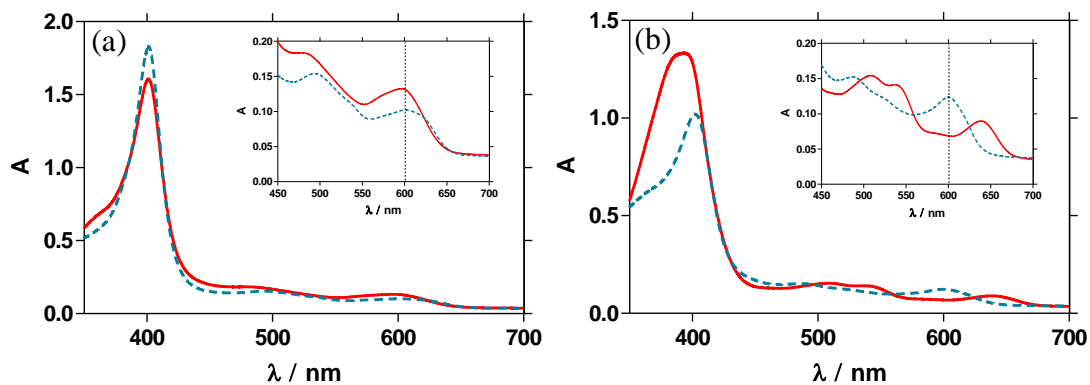
Figure 4.15 The UV-vis spectra of Fe(III)PPIX in solution before (—) and after spectrophotometric titration with QN hemisulphate (---). Conditions are (a) 3:7 (*v/v*) DMSO-methanol and (b) titration with QN free base in acetonitrile. The position of the charge transfer band at 603 nm is marked by dotted vertical lines shown in the inset.

4.3.6 EXAFS Studies

To further investigate whether the drug-Fe(III)PPIX complexes persist in solution, EXAFS spectroscopy was carried out. Spectra of crystalline samples of QD-Fe(III)PPIX, QN-Fe(III)PPIX and MQ-Fe(III)PPIX were collected together with spectra of the crystallisation medium of each.

In order to analyse the EXAFS data, a reasonable starting model of the neighbouring atoms around the absorbing Fe atom was needed as these atoms could be involved in photo-electron back scattering. In all three cases, having access to the single crystal diffraction data was particularly useful. This data was used to generate coordinates for all non-hydrogen atoms in a sphere of ≤ 5.0 Å around the central Fe atom of the porphyrin. Contributions from the porphyrin include the four nitrogen atoms directly bonded to the Fe centre, the α and *meso* carbon atoms, and the β-carbon atoms (Figure 4.16). Atoms involved in coordination to the Fe centre, for example the oxygen atom of the deprotonated alcohol functional group of quinoline methanol antimalarial drugs and all drug atoms used in the refinement, are referred to as axial atoms (a.a.), while atoms from a second Fe(III)PPIX molecule that could attribute to the backscattering as a result of π-π interactions or stacking between Fe(III)PPIX-drug moieties in the crystal packing, are labelled as atoms outside the ring (a.o.). The positions of the above mentioned atoms in the model were compared to the corresponding atomic positions determined from the EXAFS

refinement. The resulting R-factor, which indicates the goodness of fit, as well as best fit values of bond lengths, were used to rationalize whether species observed in the solid-state persist in solution or not.
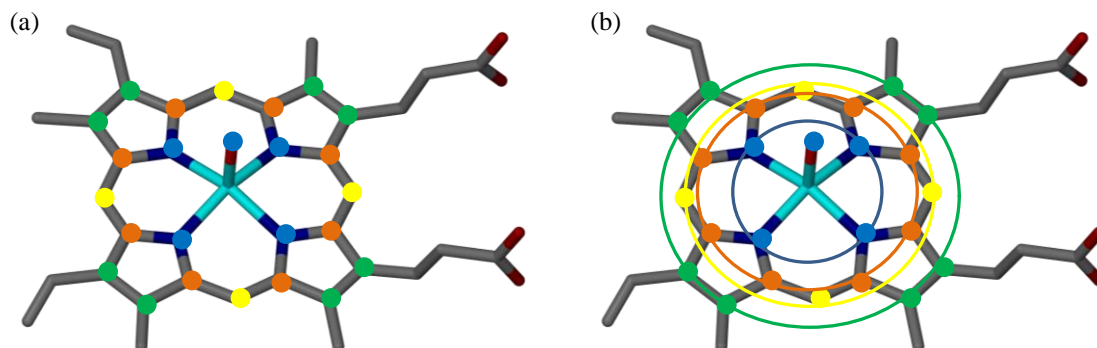
Figure 4.16 The atoms of Fe(III)PPIX included in the model used in the EXAFS refinement. (a) This includes the four nitrogen atoms and axial oxygen atom in blue, the α carbon atoms in orange, the β carbon atoms in green and the *meso* carbon atoms coloured yellow. (b) When connecting the atoms of the same colour with a circle, the circle represents all the atoms that contribute to any one shell in the EXAFS refinement.

In the fitting process, N(X) is the average number of atoms considered to be in a particular shell, r is the distance (Å) from the absorbing atom (Fe) to the atoms in a particular shell, and σ^2 (Å^2) is the Debye-Waller factor accounting for the dynamic (and partial static) disorder of the atoms in any shell. Further refinement parameters for all spectra include ΔE_0 (in eV) which is the shift in the photo-electron energy threshold (from $E_0 \sim 7122$eV for the Fe K_α-edge), S_0^2 which is the amplitude reduction factor, n_{ind} which is the number of independent points examined and n_{var} which is the number of refined parameters. Finally, R and χ^2 are the statistical parameters which give an indication of the quality of the fit.

During the iterative fitting process, if an experimental spectrum is found to disagree with a proposed model, the model for the local environment around the Fe centre must be modified assuming the absence or existence of additional atoms.

4.3.6.1   EXAFS Studies of QD-Fe(III)PPIX

The EXAFS spectra recorded for the QD-Fe(III)PPIX crystallisation solution and the crystals of QD-Fe(III)PPIX were first fitted to a model which was based on the SCD structure of the QD-Fe(III)PPIX complex. Atoms involved in the EXAFS refinement are shown in Figure 4.17. The raw EXAFS oscillations $\chi(q)$ and the corresponding Fourier transforms (direct and phase corrected) that were obtained for the crystals of QD-Fe(III)PPIX and their crystallisation solution are shown in Figure 4.18. When phase correction is applied, the distances of atoms to the central Fe atom, reported on the x-axis of the radial distribution function, increase by approximately 0.5 Å; this is due to the scattering phase-shift.[157] Phase shift is only applied to get a better visual interpretation of the data, and even though it appears that there are slightly different corrections in the spectra, the distances are not significantly affected.
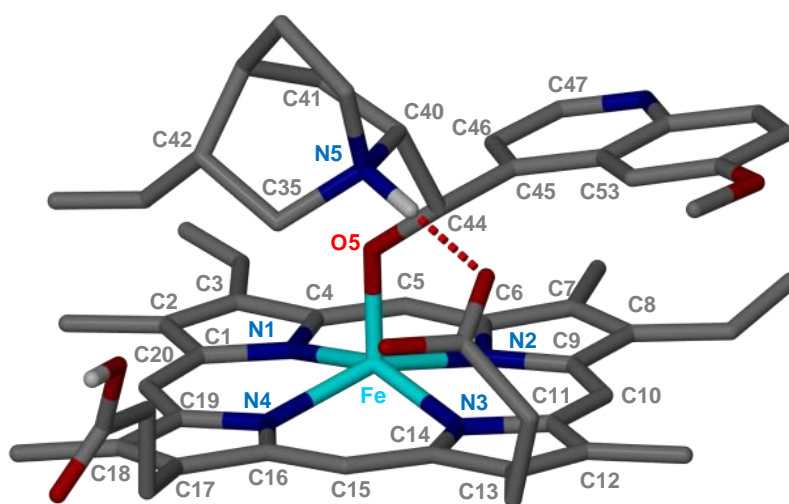
Figure 4.17 The asymmetric unit of QD-Fe(III)PPIX determined by SCD. The atoms considered in the EXAFS model refinement are labelled, while the intramolecular hydrogen bond observed in the solid-state is shown with a red dashed line. Atom colour labelling: grey – C, cyan – Fe, dark blue – N, red – O and white – H.
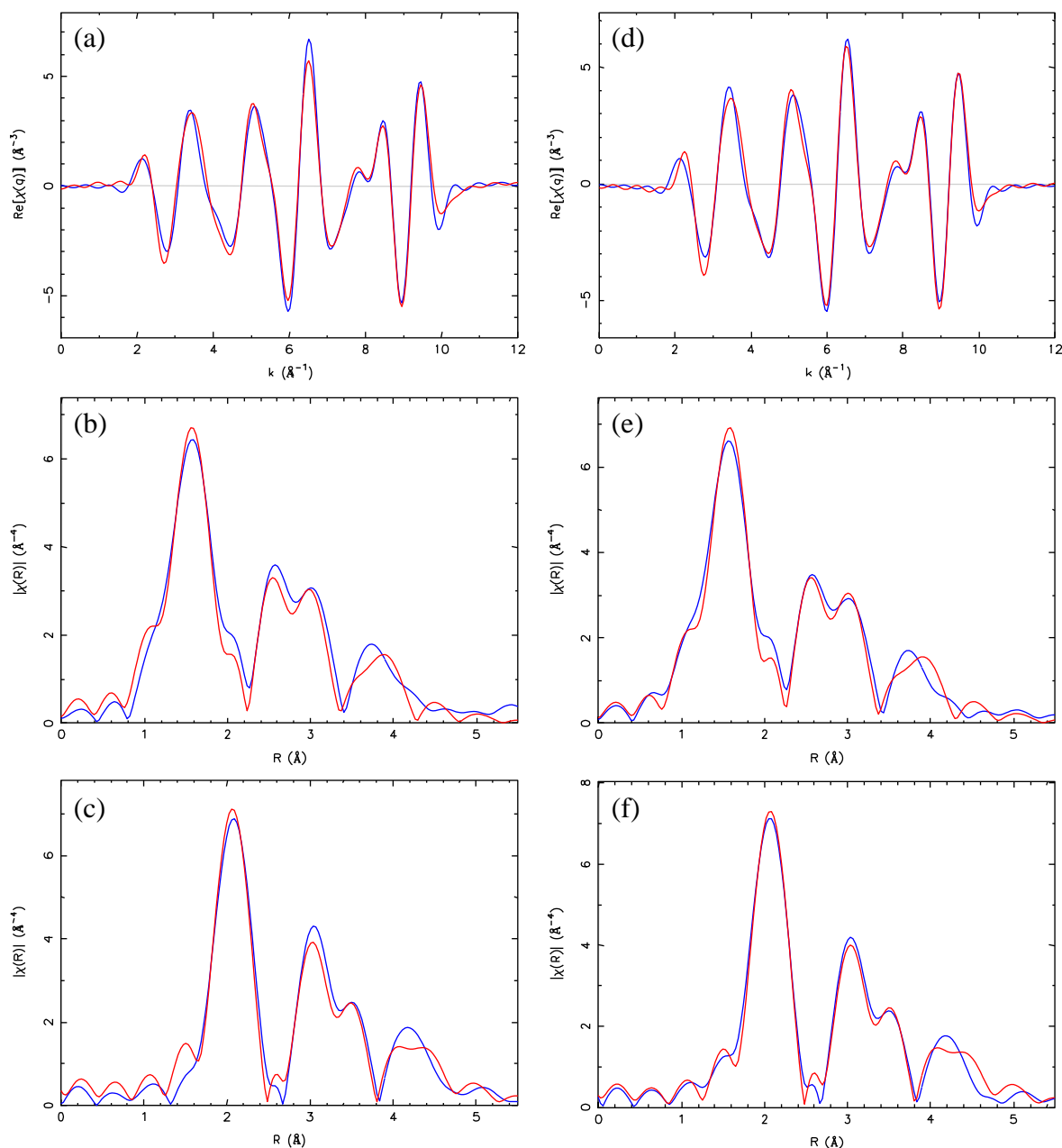
Figure 4.18 Experimental EXAFS spectra of QD-Fe(III)PPIX crystals (a, b, c) and the corresponding crystallisation solution (d, e, f). (a, d) The Fe K_α-edge k^3-weighted experimental (blue) and the best fit (red) EXAFS oscillations; (b, e) the corresponding Fourier transforms and (c, f) Fourier transforms with phase corrections applied.

The raw EXAFS oscillations $\chi(q)$ show no significant differences between the EXAFS model and the experimental spectra. In the corresponding Fourier transforms shown in Figure 4.18, similarities between the crystal and corresponding crystallisation solution medium are observed with the only deviation from the model in the region after 4.0 Å in the phase corrected spectra. The slight deviations observed in both the crystals and the

crystallisation solution EXAFS, when compared to the model, could be a result of the mother liquor present in the crystal data collection and, since the molecules are able to move more freely in solution, slight deviation from the model is expected in the spectra of the crystallisation solution.

The results of the detailed EXAFS analysis are presented in Table 4.7. The atomic positions of the model obtained from SCD data are also shown. The results indicate, given R factors for the best fit to the model of 0.033 and 0.029 for the QD-Fe(III)PPIX crystals and crystallisation solution respectively, and a χ^2 value of 1.37 for both, that there is a good fit between the crystal structure of QD-Fe(III)PPIX and crystallisation solution. There is a correlation between the distances of the atoms from the absorbing atom (Table 4.7, distance from Fe (Å)) and the observed peaks (coordination shell) in the phase corrected spectra in Figure 4.18. For example, the first broad peak in the spectra, observed at 1.7-2.4 Å when phase correction is applied, corresponds to the axial oxygen coordinating to the Fe centre through the alcohol functional group of the drug and the four nitrogen atoms from the Fe(III)PPIX ring. The average distance of these atoms from Fe in the crystal structure is 2.03 Å. When comparing the distances from the Fe absorber of the individual atoms in the crystal EXAFS to the crystallisation solution EXAFS, the atoms refined to identical distances from the Fe absorber. Therefore the local Fe environment in the crystallisation solution and in the crystal structure are essentially the same and this strongly suggests that the species shown to exist in the solid state is represented in solution as well.

Table 4.7 Refined EXAFS parameters of the crystals of QD-Fe(III)PPIX and the QD-Fe(III)PPIX crystallisation solution.

	QD-Fe(III)PPIX (SCD)[#]			QD-Fe(III)PPIX Crystals EXAFS				QD-Fe(III)PPIX Crystallisation Medium EXAFS			
ΔE_0(eV)	-			-0.7(1.4)				0.85(1.3)			
S_o^2	-			0.91(8)				0.91(8)			
n_{ind}	-			45.03				45.03			
n_{var}	-			19				19			
R	-			0.033				0.029			
χ^2	-			1.37				1.37			
EXAFS labelling[##]	Atom in SCD	Distance from Fe (Å)	Average	Atom (X)	N(X)	Distance from Fe (Å)	σ^2 (Å^2)	Atom (X)	N(X)	Distance from Fe (Å)	σ^2 (Å^2)
N1	N1	2.064		N1	1	2.03(2)	0.0004(9)	N1	1	2.03(2)	0.0004(9)
N2	N2	2.073		N2	1	2.07(2)	0.0004(9)	N2	1	2.07(2)	0.0004(9)
N3	N3	2.066		N3	1	2.06(2)	0.0004(9)	N3	1	2.06(2)	0.0004(9)
N4	N4	2.064		N4	1	2.05(2)	0.0004(9)	N4	1	2.05(2)	0.0004(9)
C2	**C1α**	**3.088**	**3.089**	**C2**	**4**	**3.06(2)**	**0.001(1)**	**C2**	**4**	**3.06(2)**	**0.001(1)**
C2	**C4 α**	**3.092**									
C2	**C6 α**	**3.09**									
C2	**C9 α**	**3.087**									
C3	C11 α	3.075	3.068	C3	4	3.02(2)	0.001(1)	C3	4	3.02(2)	0.001(1)
C3	C14 α	3.063									
C3	C16 α	3.070									
C3	C19 α	3.065									
C5	**C2 β**	**4.328**	**4.320**	**C5**	**4**	**4.28(5)**	**0.004(2)**	**C5**	**4**	**4.28(5)**	**0.004(2)**
C5	**C3 β**	**4.323**									
C5	**C7 β**	**4.318**									
C5	**C8 β**	**4.312**									
C4	C12 β	4.291	4.295	C4	4	4.27(5)	0.004(2)	C4	4	4.27(5)	0.004(2)
C4	C13 β	4.295									
C4	C17 β	4.291									
C4	C18 β	4.306									
C6	**C5 *meso***	**3.457**	**3.440**	**C6**	**4**	**3.4(1)**	**0.004(2)**	**C6**	**4**	**3.4(1)**	**0.004(2)**
C6	**C10 *meso***	**3.444**									

Table 4.7 Continued from previous page.

EXAFS labelling[##]	Atom in SCD	Distance from Fe (Å)	Average	Atom (X)	N(X)	Distance from Fe (Å)	σ^2 (Å^2)	Atom (X)	N(X)	Distance from Fe (Å)	σ^2 (Å^2)
C6	**C15 meso**	**3.414**									
C6	**C20 *meso***	**3.446**									
O1	O2 a.a.	1.862		O1	1	1.86(-0.07)	0.0004(9)	O1	1	1.86(-0.07)	0.0004(9)
C7	C44 a.a.	2.928		C7	1	2.8(-0.2)	0.001(1)	C7	1	2.8(-0.2)	0.001(1)
O2	C40 a.a.	4.222		O2	1	4.3(3)	0.004(2)	O2	1	4.3(3)	0.004(2)
C8	C45 a.a.	3.603		C8	1	3.69(9)	0.004(2)	C8	1	3.69(9)	0.004(2)
Cp1	C46 a.a.	3.749	3.765	Cp1	3	3.9(5)	0.004(2)	Cp1	3	3.9(5)	0.004(2)
Cp2	C35 a.a.	4.378	4.394	Cp2	2	4.4(1)	0.004(2)	Cp2	2	4.4(1)	0.004(2)
Cp3	C47 a.a.	4.877	4.736	Cp3	9	4.57(-0.08)	0.004(2)	Cp3	9	4.57(-0.08)	0.004(2)
Cp3	C41 a.a.	4.68									
Cp3	C42 a.a.	4.667									
Cp3	C53 a.a.	4.68									
Cp3	N5 a.a.	4.72									
	Fe o.r.	4.796		Fe	1	4.76(7)	0.004(5)	Fe	1	4.76(7)	0.004(5)
Cp1	N3 o.r.	3.756									
Cp3	N2 o.r.	4.659									
Cp3	C15 o.r.	4.799									
Cn1	C14 o.r.	4.14	4.17	Cn1	3	3.8(-0.2)	0.004(2)	Cn1	3	3.8(-0.22)	0.004(2)
Cp2	C13 o.r.	4.41									
Cn1	C12 o.r.	4.209									
Cp1	C11 o.r.	3.792									
Cn1	C10 o.r.	4.161									
Cp3	C9 o.r.	4.564									
Cp3	C27 o.r.	4.981									

[#]The model was built from the SCD data of QD-Fe(III)PPIX. The atoms uses to model distances from the Fe centre of the porphyrin are included to compare with the distances refined in the EXAFS data.

[##]If atoms have the same EXAFS labelling, it indicates that the atoms were refined at the same distance from the absorbing atom.

*Abbreviations: atoms marked a.a. - axial atoms belong to the drug molecule coordinated to Fe(III)PPIX *via* the deprotonated alcohol functional group, and the atoms marked o.r. – atoms outside the Fe(III)PPIX ring belong to the partner porphyrin which is involved in π-π stacking in the crystal structure. α, β and *meso* indicates the atoms in the Fe(III)PPIX ring.

4.3.6.2 EXAFS Studies of QN-Fe(III)PPIX

The EXAFS spectra recorded of the crystals of QN-Fe(III)PPIX as well as the solution from which the crystal was grown were first fitted to a model which was based on the SCD structure of the QN-Fe(III)PPIX complex. Atoms involved in the EXAFS refinement are shown in Figure 4.19. The raw EXAFS oscillations $\chi(q)$ and the corresponding Fourier transforms (direct and following phase corrected) that were obtained for the crystals of QN-Fe(III)PPIX and their crystallisation solution are shown in Figure 4.20.
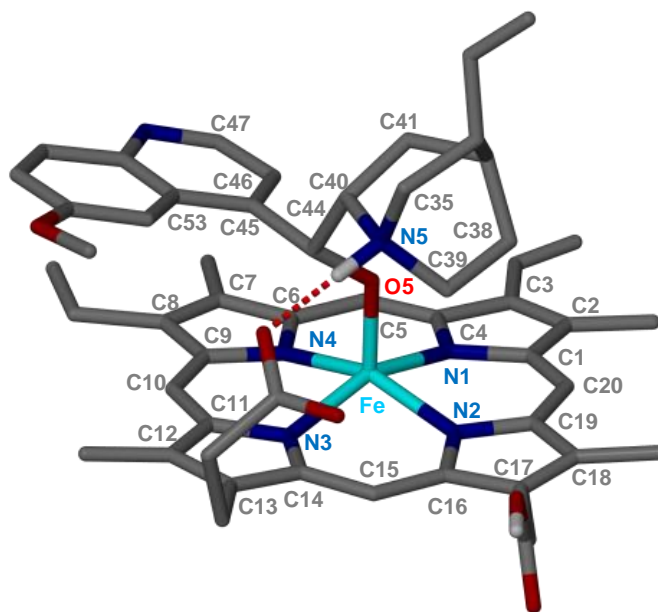
Figure 4.19 The asymmetric unit of QN-Fe(III)PPIX determined by SCD. The atoms considered in the EXAFS model refinement are labelled, while the intramolecular hydrogen bond observed in the solid-state is shown with a red dashed line. Atom colour labelling: grey – C, cyan – Fe, dark blue – N, red – O and white – H.
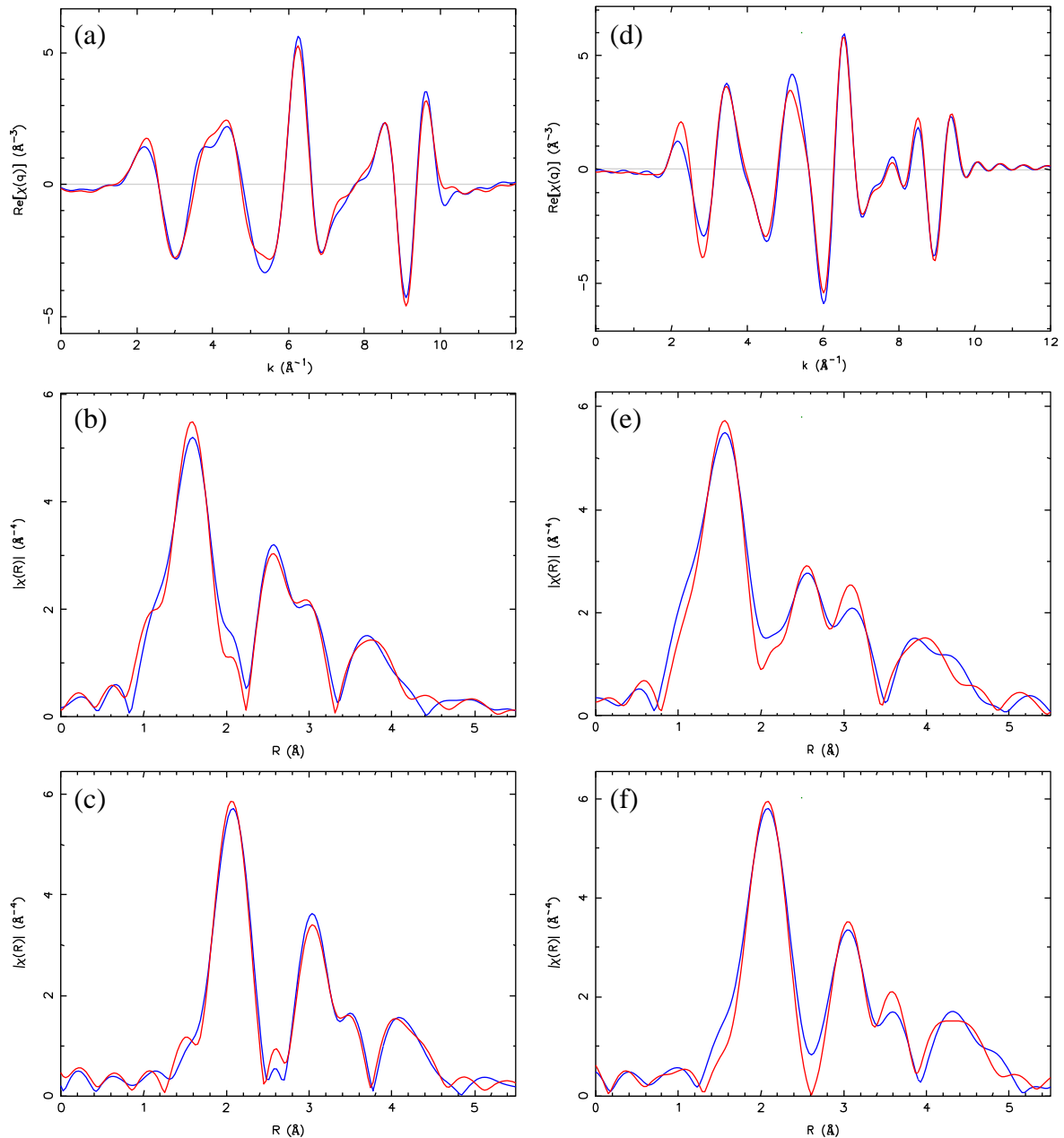
Figure 4.20 Experimental EXAFS spectra of QN-Fe(III)PPIX crystals (a, b, c) and the corresponding crystallisation solution (d, e, f). (a, d) The Fe K_α-edge k^3-weighted experimental (blue) and the best fit (red) EXAFS oscillations; (b, e) the corresponding Fourier transforms and (c, f) Fourier transforms with phase corrections applied.

The raw EXAFS oscillations $\chi(q)$ show slight differences between the EXAFS model and the experimental spectra which can be observed in the range of 2-8 Å^{-1} for the crystals and in the range of 2-6 Å^{-1} for the crystallisation solution (Figure 4.20 a and d). In the corresponding Fourier transform radial distribution functions shown in Figure 4.20, similarities between the crystal and corresponding crystallisation medium are observed

with deviation from the model in the region after 2.0 - 4.0 Å in the phase corrected spectra. It is worth remembering that the concentration of Fe(III)PPIX in the crystallisation solution was much lower than 10 mM due to the low solubility of Fe(III)PPIX in acetonitrile. This together with the fact that molecules are able to move more freely in solution as well as "breaking" or dissolving of the crystals during EXAFS collection, could account for the observed differences in the spectra when comparing the crystal spectrum to the crystallisation solution spectrum.

The results of the detailed EXAFS analysis are presented in Table 4.8 together with the atomic positions of the model obtained from SCD data. The results indicate that there is a good fit between the crystal structure of QN-Fe(III)PPIX and crystallisation solution when comparing the R factors for the best fit to the model, of 0.021 and 0.029, and a χ^2 value of 1.162 and 1.587 for the crystals and crystallisation solution respectively. When comparing the distances from the Fe absorber of the individual atoms in the crystal EXAFS to the crystallisation solution EXAFS, the atoms refined to almost identical distances from the Fe absorber. Therefore the results indicate that the local Fe environment in the crystallisation solution and in the crystal structure of QN-Fe(III)PPIX are the same and that the species shown to exist in the solid state by SCD persists in solution.

Table 4.8 Refined EXAFS parameters of the crystals of QN-Fe(III)PPIX and the QN-Fe(III)PPIX crystallisation solution.

	QN-Fe(III)PPIX (SCD)[#]			QN-Fe(III)PPIX Crystals EXAFS				QN-Fe(III)PPIX Crystallisation Medium EXAFS			
ΔE_0(eV)	-			1.4(5)				0.86(1.9)			
S_o^2	-			0.80(8)				1.0(1)			
n_{ind}	-			20.0				23.11			
n_{var}	-			14				19			
R	-			0.021				0.029			
χ^2	-			1.162				1.587			
EXAFS labelling[##]	Atom in SCD	Distance from Fe (Å)	Average	Atom (X)	N(X)	Distance from Fe (Å)	σ^2 (Å²)	Atom (X)	N(X)	Distance from Fe (Å)	σ^2 (Å²)
N1	N1	2.042		N1	1	2.03(2)	0.001(1)	N1	1	2.021(8)	0.002(1)
N2	N2	2.059		N2	1	2.07(2)	0.001(1)	N2	1	2.062(8)	0.002(1)
N3	N3	2.069		N3	1	2.06(2)	0.001(1)	N3	1	2.047(8)	0.002(1)
N4	N4	2.059		N4	1	2.05(2)	0.001(1)	N4	1	2.036(8)	0.002(1)
C2	**C1α**	**3.089**	**3.084**	**C2**	**4**	**3.03(3)**	**0.002(1)**	**C2**	**4**	**3.05(1)**	**0.003(2)**
C2	**C4 α**	**3.097**									
C2	**C6 α**	**3.082**									
C2	**C9 α**	**3.071**									
C3	C11 α	3.064	3.073	C3	4	3.03(3)	0.002(1)	C3	4	3.01(1)	0.003(2)
C3	C14 α	3.083									
C3	C16 α	3.076									
C3	C19 α	3.073									
C5	**C2 β**	**4.309**	**4.273**	**C5**	**4**	**4.29(6)**	**0.001(2)**	**C5**	**4**	**4.29(6)**	**0.003(3)**
C5	**C3 β**	**4.340**									
C5	**C7 β**	**4.300**									
C5	**C8 β**	**4.273**									
C4	C12 β	4.284	4.284	C4	4	4.28(6)	0.001(2)	C4	4	4.28(6)	0.003(3)
C4	C13 β	4.272									
C4	C17 β	4.278									
C4	C18 β	4.302									
C6	**C5 meso**	**3.445**	**3.421**	**C6**	**4**	**3.5(1)**	**0.001(2)**	**C6**	**4**	**3.5(1)**	**0.003(3)**
C6	**C10 meso**	**3.392**									

Table 4.8 Continued from previous page

EXAFS labelling[##]	Atom in SCD	Distance from Fe (Å)	Average	Atom (X)	N(X)	Distance from Fe (Å)	σ^2 (Å^2)	Atom (X)	N(X)	Distance from Fe (Å)	σ^2 (Å^2)
C6	**C15** *meso*	**3.441**									
C6	**C20** *meso*	**3.406**									
O1	O2 a.a.	1.866		O1	1	1.859(-.08)	0.001(2)	O1	1	1.8(-0.1)	0.002(1)
C7	C44 a.a.	2.939		C7	1	3.113	0.002(1)	C7	1	2.9(-0.09)	0.003(3)
O2	C40 a.a.	4.188		O2	1	4.2(2)	0.001(1)	O2	1	4.2(2)	0.003(3)
C8	C45 a.a.	3.622		C8	1	4.3(7)	0.001(1)	C8	1	3.55(-0.05)	0.003(3)
Cp1	C46 a.a.	3.752	3.959	Cp1	6	3.85(5)	0.005(3)	Cp1	5	3.87(7)	0.002(2)
Cp2	C38 a.a.	4.429	4.392	Cp2	6	4.5(2)	0.006(0.01)	Cp2	2	4.5(2)	0.007(.01)
Cp3	C47 a.a.	4.868	4.708	Cp3	6	4.648(-.005)	0.007(5)	Cp3	11	4.68(3)	0.01(2)
Cp3	C41 a.a.	4.706									
Cp1	C39 a.a.	4.147									
Cp3	C53 a.a.	4.729									
Cp3	N5 a.a.	4.638									
Fe	Fe o.r.	4.353		Fe	1	4.4(-.02)	0.001(3)	Fe	1	4.5(-0.2)	0.002(7)
Cp1	N3 o.r.	3.678									
Cp3	N2 o.r.	4.406									
Cp2	C15 o.r.	4.342									
Cp1	C14 o.r.	4.034									
Cp3	C13 o.r.	4.696									
Cp3	C12 o.r.	4.801									
Cp1	C11 o.r.	4.182									
Cp3	C10 o.r.	4.627									
Cp3	C9 o.r.	4.789									
Cp3	C16 o.r	4.524									

[#]The model was built from the SCD data of QN-Fe(III)PPIX. The atoms used to model distances from the Fe centre of the porphyrin are included to compare with the distances refined in the EXAFS data.

[##]If atoms have the same EXAFS labelling, it indicates that the atoms were refined at the same distance from the absorbing atom.

*Abbreviations: atoms marked a.a. - axial atoms belong to the drug molecule coordinated to Fe(III)PPIX *via* the deprotonated alcohol functional group, and the atoms marked o.r. – atoms outside the Fe(III)PPIX ring belong to the partner porphyrin which is involved in π-π stacking in the crystal structure. α, β and *meso* indicates the atoms place in the Fe(III)PPIX ring.

4.3.6.3   EXAFS Studies of MQ-Fe(III)PPIX

The EXAFS spectra recorded of the MQ-Fe(III)PPIX crystallisation solution as well as the crystals were first fitted to a model which was based on the SCD structure of the MQ-Fe(III)PPIX complex. Atoms involved in the EXAFS refinement are shown in Figure 4.21. The raw EXAFS oscillations $\chi(k)$ and the corresponding Fourier transforms obtained for the MQ-Fe(III)PPIX crystallisation solution and the crystals are shown in Figure 4.22.

(I)   (II)
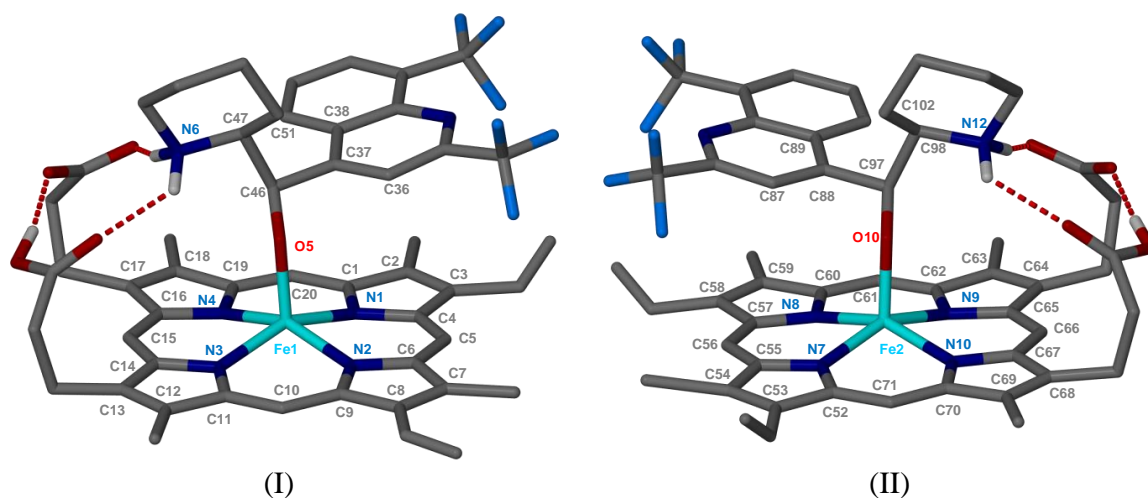
Figure 4.21 The two moieties in the asymmetric unit of MQ-Fe(III)PPIX (I and II), determined by SCD, are displayed separately above to make numbering of the atoms involved in the EXAFS refinements more visible. The atoms considered in the EXAFS model refinement are labelled, while the intramolecular hydrogen bonds observed in the solid-state are shown with red dashed lines. Atom colour labelling: grey – C, cyan – Fe, dark blue – N, light blue – F, red – O and white – H.

The EXAFS data obtained for the spectra of the MQ-Fe(III)PPIX crystallisation solution cannot be used as a representative of the bulk solution. This is due to the fact that, out of the triplicate data sets that were collected, only one was used as the experimental data to fit to the model since the other two sets deviated from the model. This deviation from the model was attributed to the lower concentration of Fe(III)PPIX in the solution (much lower than 10 mM) since Fe(III)PPIX is only sparingly soluble in acetonitrile.
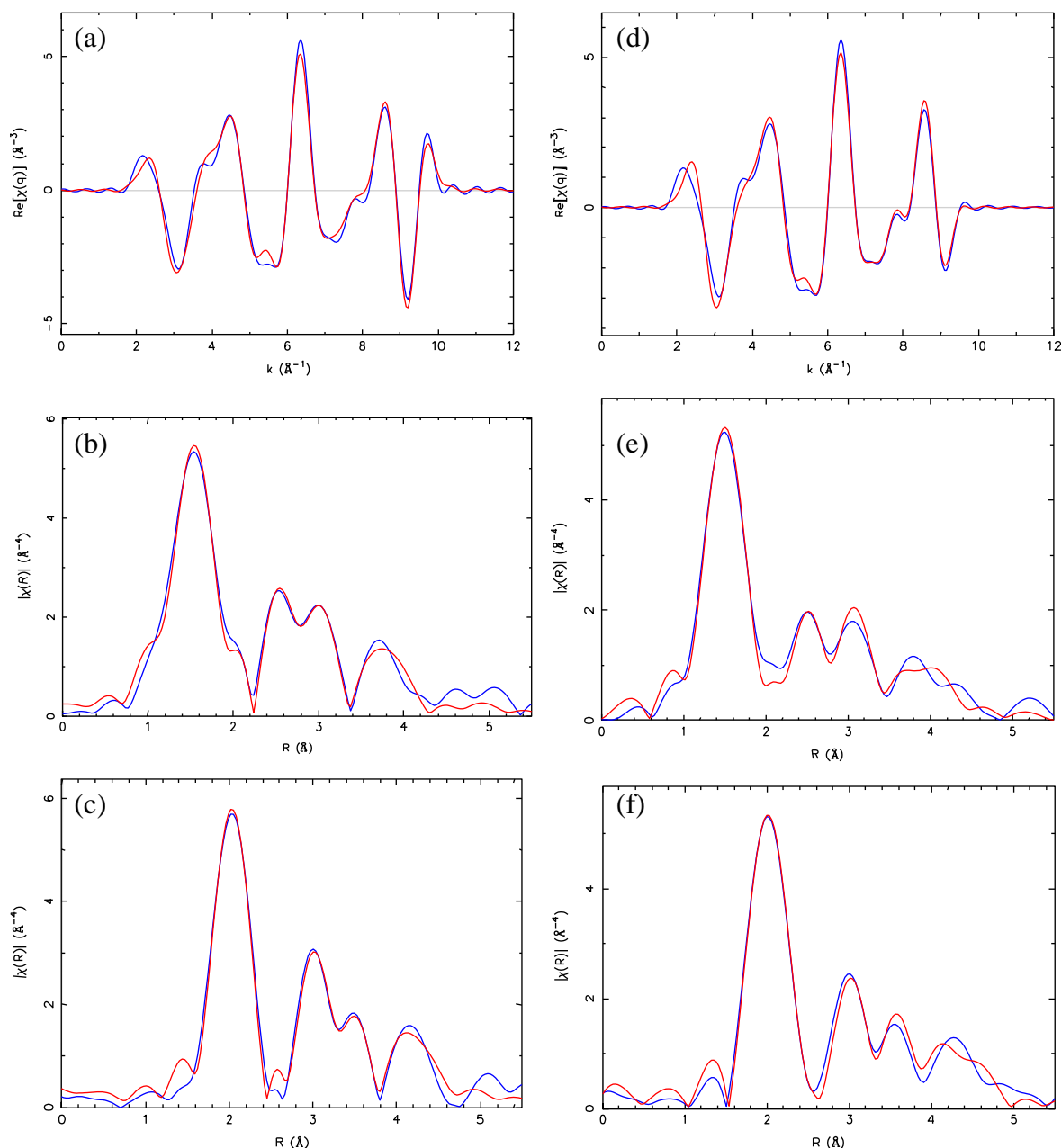
Figure 4.22 Experimental EXAFS spectra of MQ-Fe(III)PPIX crystals (a, b, c) and the corresponding crystallisation solution (d, e, f). (a, d) The Fe K_α-edge k^3-weighted experimental (blue) and the best fit (red) EXAFS oscillations; (b, e) the corresponding Fourier transforms and (c, f) Fourier transforms with phase corrections applied.

The raw EXAFS oscillations $\chi(q)$ show no significant differences between the EXAFS model and the experimental spectra from the one data set. In the corresponding Fourier transforms EXAFS shown in Figure 4.22, similarities between the crystal and corresponding crystallisation solution are observed, with the only deviation from the model in the region after 2.5 - 4.0 Å in the phase corrected spectra for the crystallisation solution.

The slight increases and decreases observed in both the crystals and the crystallisation solution EXAFS when compared to the model could be due to traces of mother liquor present in the crystal sample during data collection and the fact that molecules are able to move more freely in solution. Furthermore, the very low concentration of Fe(III)PPPIX in solution may have also been a contributing factor. Therefore, deviation from the model is expected in the spectra of the crystallisation solution.

When comparing the R factors for the best fit to the model, 0.021 and 0.022 and a χ^2 value of 1.63 and 2.46 for the crystals and crystallisation solution respectively, the results of the detailed EXAFS analysis presented in Table 4.9 indicate that there is a reasonable fit between the crystal structure of MQ-Fe(III)PPIX and the crystallisation solution.

Furthermore, when comparing the distances from the Fe absorber of the individual atoms in the crystal EXAFS to the crystallisation solution EXAFS, the atoms refined to almost identical distances from the Fe absorber. Therefore, the results indicate that the local Fe environment in the crystallisation solution (despite being from one data set) and the crystal structures are comparable. Even though there is a good fit between the experimental and the model, the data cannot be assumed to be representative of the bulk solution. Therefore it only suggests that the first shell of atoms surrounding the absorbing Fe atom are the same, which could indicate that the species observed in the crystal and crystallisation medium of MQ-Fe(III)PPIX are the same.

Table 4.9 Refined EXAFS parameters of the crystals of MQ-Fe(III)PPIX and the MQ-Fe(III)PPIX crystallisation solution.

	MQ-Fe(III)PPIX (SCD)[#]				MQ-Fe(III)PPIX Crystal EXAFS				MQ-Fe(III)PPIX Crystallisation Medium EXAFS			
ΔE_0(eV)	-				0.70(1.7)				1.27(1.25)			
S_o^2	-				0.65(6)				0.89(9)			
n_{ind}	-				24.99				22.48			
n_{var}	-				16				18			
R	-				0.021				0.022			
χ^2					1.63				2.46			
EXAFS labelling[##]	Atom in SCD	Distance from Fe(1)(Å)	Atom	Distance from Fe(2)(Å)	Average	Atom (X)	N(X)	Distance from Fe (Å)	σ^2 (Å²)	Atom (X)	N(X)	Distance from Fe (Å)	σ^2 (Å²)
N1	N1	2.071	N7	2.069		N1	1	2.008(5)	0.0001(9)	N1	1	2.008(-5)	0.0003(9)
N2	N2	2.071	N8	2.068		N2	1	2.048(5)	0.0001(9)	N2	1	2.048(-5)	0.0003(9)
N3	N3	2.061	N9	2.054		N3	1	2.034(5)	0.0001(9)	N3	1	2.034(-5)	0.0003(9)
N4	N4	2.058	N10	2.060		N4	1	2.023(5)	0.0001(9)	N4	1	2.023(-5)	0.0003(9)
C2	**C1α**	**3.093**	**C52 α**	**3.101**	**3.094**	**C2**	**4**	**3.0384(3)**	**0.002(1)**	**C2**	**4**	**3.0384(-3)**	**0.001(1)**
C2	**C4 α**	**3.091**	**C55 α**	**3.084**									
C2	**C6 α**	**3.092**	**C57 α**	**3.095**									
C2	**C9 α**	**3.103**	**C60 α**	**3.096**									
C3	C11 α	3.098	C62 α	3.077	3.080	C3	4	3.002(2)	0.002(1)	C3	4	3.002(-2)	0.001
C3	C14 α	3.077	C65 α	3.063									
C3	C16 α	3.065	C67 α	3.070									
C3	C19 α	3.086	C70 α	3.106									
C5	**C2 β**	**4.315**	**C53 β**	**4.323**	**4.318**	**C5**	**4**	**4.28(5)**	**0.001(3)**	**C5**	**4**	**4.28(5)**	**0.004(2)**
C5	**C3 β**	**4.314**	**C54 β**	**4.311**									
C5	**C7 β**	**4.323**	**C58 β**	**4.310**									
C5	**C8 β**	**4.333**	**C59 β**	**4.316**									
C4	C12 β	4.311	C63 β	4.290	4.300	C4	4	4.27(5)	0.001(3)	C4	4	4.27(5)	0.004(2)
C4	C13 β	4.305	C64 β	4.289									
C4	C17 β	4.286	C68 β	4.306									

Table 4.9 Continued from previous page.

EXAFS labelling[##]	Atom SCD	Distance from Fe (Å)	Atom	Distance from Fe (Å)	Average	Atom (X)	N(X)	Distance from Fe (Å)	σ^2 (Å²)	Atom (X)	N(X)	Distance from Fe (Å)	σ^2 (Å²)
C4	C18 β	4.297	C69 β	4.316									
C6	**C5 *meso***	**3.447**	**C56*meso***	**3.444**	**3.44**	**C6**	**4**	**3.5(1)**	**0.001(3)**	**C6**	**4**	**3.5(1)**	**0.004(2)**
C6	**C10*meso***	**3.457**	**C61*meso***	**3.444**									
C6	**C15*meso***	**3.421**	**C66*meso***	**3.423**									
C6	**C20*meso***	**3.449**	**C71*meso***	**3.467**									
O1	O5 a.a.	1.899	O10 a.a.	1.891	1.895	O1	1	1.87(6)	0.0001(1)	O1	1	1.87(-6)	0.001
C7	C46 a.a.	2.904	C97 a.a.	2.905	2.905	C7	1	2.97(8)	0.002((1)	C7	1	2.97(-8)	0.001(1)
C8	C37 a.a.	3.605	C88 a.a.	3.604	3.605	O2	1	3.7(3)	0.001(3)	O2	1	3.7(-3)	0.0001(9)
Cp1	C36 a.a.	3.849	C87 a.a.	3.841	3.864	C8	1	3.53(6)	0.001(3)	C8	1	3.53(-6)	0.004(2)
Cp3	C38 a.a.	4.683	C102a.a.	4.848	4.659	Cp1	4	3.9(4)	0.007(1)	Cp1	3	3.9(4)	0.004(2)
Cn1	C47 a.a.	4.211	C98 a.a.	4.209	4.156	Cp2	8	4.6(4)	0.003(0.01)	Cp2	2	4.6(4)	0.004(2)
Cp3	C51 a.a.	4.866	C89 a.a.	4.682		Cp3	7	4.57(8)	0.004(5)	Cp3	7	4.57(-8)	0.004(2)
Cp2	N6 a.a.	4.448	N9 a.a.	4.389	4.428		2			Cp4			
Fe	Fe o.r.	4.566	Fe o.r.	4.463		Fe	1	4.4(2)	0.002(5)	Fe	1	4.4(-2)	0.04(5)
Cp1	N1 o.r.	3.744	N9 o.r.	3.712									
Cp3	N4 o.r.	4.532	N10 o.r.	4.555									
Cp3	C6 o.r.	4.898	N8 o.r.	4.526									
Cp3	C5 o.r.	4.617	C66 o.r.	4.558		Cn1	4	3.8(2)	0.004(6)	Cn1	2	3.8(-2)	0.004(2)
Cn1	C4 o.r.	4.1	C65 o.r.	4.106									
Cp3	C3 o.r.	4.583	C64 o.r.	4.676									
Cp3	C2 o.r.	4.533	C63 o.r.	4.634									
Cp1	C1 o.r.	3.994	C62 o.r.	4.047									
Cp2	C20 o.r.	4.385	C61 o.r.	4.491									
Cp3	C19 o.r.	4.64	C30 o.r.	4.713									

#The model was built from the SCD data of MQ-Fe(III)PPIX. The atoms used to model distances from the Fe centre of the porphyrin are included to compare with the distances refined in the EXAFS data.

##If atoms have the same EXAFS labelling, it indicates that the atoms were refined at the same distance from the absorbing atom.

*Abbreviations: atoms marked a.a. - axial atoms belong to the drug molecule coordinated to Fe(III)PPIX *via* the deprotonated alcohol functional group, and the atoms marked o.r. – atoms outside the Fe(III)PPIX ring belong to the partner porphyrin which is involved in π-π stacking in the crystal structure. α, β and meso indicates the atoms place in the Fe(III)PPIX ring.

4.4   Discussion

When considering the history of antimalarial drugs, it is interesting to note that the *Cinchona* alkaloids, particularly QN, have been effectively used for centuries. Taking into account that this drug along with CQ was used in high quantities and, for most part was the drug of choice, it took the parasite a long time to build resistance to these drugs compared to other drugs. Today QN is still used to treat cerebral malaria,[171] therefore it is still relevant and understanding the mode of action of this and related quinoline antimalarial drugs is crucial in our fight against malaria.

The possibility that the active *Cinchona* alkaloids (QN and QD) may form a dative covalent bond to the Fe(III) centre of Fe(III)PPIX through the benzylic alcohol functional group has been suggested by several authors.[48,49,172] The crystal structures of QN-, QD- and MQ-Fe(III)PPIX determined in this work are the only structures to date of Fe(III)PPIX complexes with quinoline antimalarial drugs. It is noteworthy that all of the drug compounds can be further classified as quinoline methanols owning to the alcohol functional group in the benzylic position relative to the quinoline ring. These structures provide direct evidence that the antimalarial-active *Cinchona* alkaloids and MQ form five-coordinate complexes with the porphyrin *via* their benzylic alcohol functional group and not through the quinuclidine, piperidine or quinoline nitrogen atoms as has been proposed. These findings provide direct evidence of coordination between the deprotonated alcohol functional group of the drug and the Fe centre of Fe(III)PPIX, which was proposed by various molecular research regarding the ability of the hydroxyl group of QN (and therefore QD) to interact with the Fe(III) centre of Fe(III)PPIX in some fashion.[48,85,88,89,172]

The Fe-O bond length in all three structures is consistent with the coordination of the benzylic hydroxyl group to the Fe(III) centre as an alkoxide (1.816 – 1.867 Å),[127,128,129,130] rather than an alcohol (2.112 – 2.160 Å).[131,132] The crystal structures confirm that the alcohol function is deprotonated in each case since no H-atoms were found to be present in the electron density map. When considering the pK_a of the benzylic alcohol functional group and comparing it to the pK_a of benzyl alcohol which is close to 15.2,[173] the presence of an alkoxide species in the acidic food vacuole of the parasite (*in vivo*) seems questionable. However, Behere and Goff[48] proposed that the deprotonation of the alcohol (to yield an alkoxide complex in a non-aqueous solution) is facilitated by the basic quinuclidine nitrogen atom, which is able to accept the proton. This is presumably how

complex formation was facilitated in the case of QN-Fe(III)PPIX, which was crystallised from an acetonitrile solution of Fe(III)PPIX and QN in its free base form (meaning that the quinuclidine N-atom was able to accept the proton transferred from the alcohol). In the crystallisation of QD-Fe(III)PPIX however, the drug was added to the 3:7 (*v/v*) DMSO-methanol solution in its acid form (as a hemisulfate salt). Therefore the quinuclidine nitrogen atom was unavailable from the start to accept further protons. Since no counterions were observed in the crystal structure, the complex is not expected to have a net charge and this was rationalised in the following way. Substituting the chloride ligand from the starting material (haemin, Cl-Fe(III)PPIX) with an alkoxide species (QD) does not influence the neutral state of the porphyrin core. Deprotonation of only one of the Fe(III)PPIX propionic acid groups is therefore necessary to balance the positive charge on the protonated quinuclidine nitrogen atom and maintain an overall uncharged species. The formation of a single propionate group (while the other remains as a propionic acid) is confirmed in the crystal structure. The absence of a peak in the carbonyl region was recently used to support the presence of a fully deprotonated Fe(III)PPIX species precipitated from aqueous solution by the addition of QN free base[125] and the infrared spectrum of the QD-Fe(III)PPIX complex (previously shown in Figure 4.6) supports this finding with a peak at approximately 1702 cm^{-1}. Complex formation is thus accompanied by the overall loss of two protons. These observations suggest that the pK_a of alcohols may be depressed below that of the propionic acid group (with a pK_a lower than 5 to 6, which is the estimated pK_a for the propionic acid group in free Fe(III)PPIX),[174] due to the strong coordination to the Fe centre. Further investigation of the free energy associated with coordination of the alcohol form of the alkaloid versus the alkoxide, possibly *via* computation, would be useful in explaining this observation further. The possible formation of H_2SO_4 and HCl *in situ* is highly unlikely. A more likely explanation is that the alkaloids, which were added in excess to the crystallisation media, could act as a buffer, making use of the second most basic site (the quinoline nitrogen atom) after the quinuclidine nitrogen atom to accept protons.

The crystal structures also confirm that within each complex, QN-Fe(III)PPIX and QD-Fe(III)PPIX, there is an intramolecular hydrogen bond present between the propionate side chain of Fe(III)PPIX and the protonated quinuclidine nitrogen atom of the drug. This confirms the prediction made by using computational methods of the likely interactions in an environment void of hydrogen bonding partners.[85] It was observed that QN and QD are

able to readily adopt a conformation which allows the formation of an intramolecular hydrogen bond at a much lower energy conformation than the inactive epimers. It is particularly interesting that the observed dihedral angles in the crystal structures of QD-Fe(III)PPIX and QN-Fe(III)PPIX (required for salt-bridge formation) correlate with the previously computed dihedral angles (Table 4.10).[85]

Table 4.10 Comparison of computed and experimental dihedral angles in the QD-Fe(III)PPIX and QN-Fe(III)PPIX complexes.

Complex	Dihedral angle	Computed[#]	Experimental
QD-Fe(III)PPIX	ψ	$+210^o$	$+209$
	φ	$+240^o$	$+300$
QN-Fe(III)PPIX	ψ	$+145^o$	$+158^o$
	φ	$+155^o$	$+156^o$

[#]Values reproduced from reference.[85]

The difference in the value for the dihedral angle (φ) of QD-Fe(III)PPIX, -60° for the experimental versus the computed value of $+240^o$, is due to the effect of the alternative propionate group having been used in the calculations compared to that selected in the crystal structure. When the experimental and computed dihedral angle (φ) are compared for QN-Fe(III)PPIX, they are very similar as a result of the same propionate group having been used in the computed structure as well as the crystal structure. It is worth remembering that in the molecular modelling of the complexes, the choice of propionate group for the formation of the intramolecular hydrogen bond was to a large extent random and either one of the porphyrin propionates could have been chosen. A feature of the calculated relative strain energy surface for QD-Fe(III)PPIX, generated by rotating ψ and φ relative to one another and determining the free energy at each step, is the low energy furrow at the point that ψ is fixed at $\pm 210^o$ (Figure 1.48), the value predicted by molecular modelling and observed in the current study. Thus, the barrier rotation about the Fe(III)-O5 bond is minimal in this region which means that φ could essentially adopt any magnitude (Table 4.10). Interestingly, the complex observed in the solid-state, where φ is 300°, is only 1 kcal/mol higher in energy than the predicted complex where φ attained a magnitude of 240° (Figure 1.48).

The persistence of the intramolecular hydrogen bond in the QD-Fe(III)PPIX complex, despite its growth in an environment rich with hydrogen bonding partners ($\sim$ 72% (*v/v*)

methanol), is highly significant. Its existence in this environment supports the idea that QD may be structurally preorganised to favour such an interaction, which may be the reason for its greater activity compared to QN. All attempts to grow a QN-Fe(III)PPIX complex in the same crystallisation solution as the QD-Fe(III)PPIX complex were unsuccessful.

It has previously been shown that the conformation of MQ is independent of the crystallisation environment and the starting form of MQ, be it as a salt, freebase, racemic or optically pure mixture.[175,176] One question that has not been answered is whether the conformation of MQ remains unchanged upon complexing to Fe(III)PPIX. The geometries of different forms of MQ and the geometries of MQ as observed in the complex are shown in Table 4.11. The torsion angle (C4-C11-C12-N13 labelling as per Figure 4.11(a)) is essentially identical for all mefloquine molecules. Therefore, the SCD structure of MQ-Fe(III)PPIX supports the proposal that some molecules are structurally preorganised to complex with Fe(III)PPIX owing to their stereochemical configuration.

Table 4.11 Comparison of the geometries of different MQ species.

Complex	Torsion angle (º) C4–C11–C12–N13[b]	Torsion angle (º) O1–C11–C12–N13[b]
MQ-Fe(III)PPIX (C_{46}S, C_{47}S)*	**C37–C46–C47–N6*** 169.3	**O5–C46–C47–N6*** -67.3
MQ-Fe(III)PPIX (C_{97}S, C_{98}R)*	**C88–C97–C98–N12*** -167.5	**O10–C97–C98–N12*** 68.4
MQ methylsulfonate monohydrate[a]	-176.2	-54.5
(±)-MQ hydrochloride	174.7	-62.8
(±)-MQ free base[a]	169.7, 175.6[#]	-61.4, -66.6
(−)-MQ hydrochloride hydrate[a]	168.5, 171.4, -176.8, -179.4[##]	-71.6 to -54.4

[a] Values reproduced from reference.[175]
[b] Labelling as per Figure 4.11 (a).
* Labelling as in the crystal structure of MQ-Fe(III)PPIX.
[#] The torsion angle represents one enantiomer and would be the opposite sign for the other one.
[##] Values of the 4 different conformations as found in the crystal structure.

Interestingly, only an intramolecular hydrogen bonding network is observed in the crystal structure of the MQ-Fe(III)PPIX complex. This network of intramolecular hydrogen

bonding is presumably also responsible for stabilising the complex when formed, therefore blocking β-haematin formation.

Together the three crystal structures determined in this work provide direct and important evidence for the key interactions between the drug molecule and Fe(III)PPIX. Namely, coordination of the deprotonated benzylic alcohol group of the drug to the Fe(III) centre of Fe(III)PPIX, π-stacking between the aromatic porphyrin pyrrole and the drug quinoline rings, and most importantly, the intramolecular hydrogen bond formation between the porphyrin propionate group and the protonated quinuclidine nitrogen atom of the drug in the case of QN-Fe(III)PPIX and QD-Fe(III)PPIX and the intramolecular hydrogen bond network observed in MQ-Fe(III)PPIX between the propionate and propionic acid side chains of Fe(III)PPIX, with a further two between each of these groups and the piperidinium nitrogen atom of the drug. These three key interactions are supported by the recent publication of Alumasa *et al.*[125] By investigating a series of QN analogues in order to define the structural features necessary for inhibition of Fe(III)PPIX and biological activity, they showed that the lack of either the benzylic alcohol function or the quinuclidine ring (and therefore the quinuclidine nitrogen atom) lowers Fe(III)PPIX affinity, haemozoin inhibition activity and antiplasmodial activity. This provides further circumstantial evidence for the importance of coordination of the benzylic alcohol group to the Fe(III) centre of Fe(III)PPIX and the intramolecular hydrogen bond formation between the porphyrin propionate group and the protonated quinuclidine nitrogen atom of the drug to the antimalarial activities of the quinoline methanols as they target Fe(III)PPIX.

According to the model proposed for the formation of haemozoin and inhibition by the *Cinchona* alkaloids,[85] the relative ease by which the intramolecular hydrogen bond can be formed by the active alkaloids would render Fe(III)PPIX incapable of forming the haemozoin precursor dimer by preventing the release of Fe(III)PPIX from the complex and, therefore, inhibiting haemozoin formation.[85] The results obtained in the current study provide the first experimental evidence to support these previous proposals.

Both QN and QD are active antimalarial compounds and the formation of the intramolecular hydrogen bond is proposed to be crucial to their activity. The 9-epiquinine (EQN) and 9-epiquinidine (EQD) are inactive, and therefore a crystal structure would have been complementary to understanding the greater activity of the active alkaloids (QN and QD) compared to the inactive alkaloids (EQN and EQD). Unfortunately, however, none of

the attempts to obtain single crystals of Fe(IIII)PPIX complexing with 9-epiquinine (EQN) have been successful to date. Attempts to crystallise Fe(III)PPIX and 4-aminoquinoline drug complexes were also unsuccessful. This could be due to the fact that 4-aminoquinoline drugs are thought to not act by direct coordination to Fe(III)PPIX which could make crystallisation either very difficult or impossible. Walczak *et al.*[163] showed in an EXAFS study of the mode of action of CQ at a molecular level with a soluble analogue of the β-haematin that a reduction in the oxygen coordination number rules out the possibility of CQ forming a stable complex in the same way that quinoline methanol antimalarials do.

From the observed spectra of Fe(III)PPIX recorded in the different solutions, it is evident that the speciation of Fe(III)PPIX is the same in 3:7 (*v/v*) DMSO-methanol, acetonitrile, and 1-pentanol following titration with either $QD.HSO_4$ or QD freebase, yet distinctly different to that observed in aqueous solution (Figure 4.14 (d)). The observed charge transfer band at 603 nm in each of the final spectra (Figure 4.14 a, b and c insert and Figure 4.15 a and b insert) resembles that of HO―Fe(III)PPIX when the hydroxide is coordinated to the metal centre.[79] This is consistent with the observation in both crystal structures that the alkoxide form of the alkaloid (RO―Fe(III)PPIX) coordinates to the metal centre rather than the alcohol form (R(H)O―Fe(III)PPIX). The alcohol form would be expected to result in spectral changes similar to those observed for H_2O―Fe(III)PPIX.

Warhurst *et al.*[124] defined characteristic peaks at 490 and 602 nm in the absorption spectra for QN-Fe(III)PPIX coordination complexes in benzene (Figure 4.23). He proposed that the atom coordinated to the Fe centre of Fe(III)PPIX is the quinuclidine nitrogen atom of QN. He also proposed that in the case of MQ, coordination takes place *via* the nitrogen atom of the piperidine ring. The results represented in this chapter concur with Warhurst in so far as a coordination complex exists. However, based on SCD evidence, the final spectrum in each of the spectrophotometric titrations is attributed to the complex in which the alkaloid compound coordinates to the porphyrin Fe(III) centre *via* its benzylic alcohol (alkoxide) functional group.
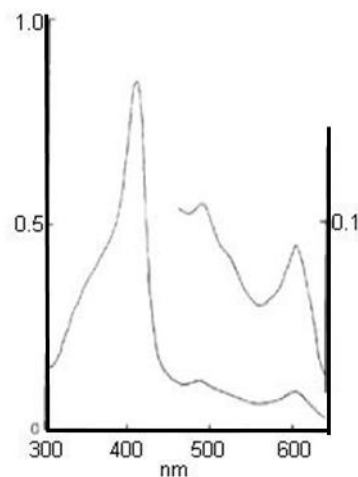
Figure 4.23 The absorption spectrum of QN-Fe(III)PPIX coordination complexes in benzene. The defined peaks at 490 and 602 nm were attributed to QN coordinating to the Fe centre of Fe(III)PPIX *via* the quinuclidine nitrogen atom. Reproduced from reference.[124]

Since the peak which represents the coordination of the drug molecule to Fe(III)PPPIX is absent in the spectrum recorded from aqueous solution, complex formation between Fe(III)PPIX and the *Cinchona* alkaloids is considered more likely to take place in a non-aqueous environment. Since the observation of haemozoin formation in association with lipids, the likely intracellular microenvironment of Fe(III)PPIX crystallisation shifted from a polar aqueous environment to a non-polar neutral lipid environment.[60] These findings support the most recent theories regarding the site of haemozoin formation and the likelihood that drug action takes place in a non-aqueous environment near the lipid-water interface inside the digestive vacuole of the malaria parasite.[177]

When taking the EXAFS data into account, which indicates that the species shown to exist in the solid state by SCD also exist in solution, the results suggest that coordination *via* the drugs deprotonated benzylic alcohol functional group to the Fe(III) centre of Fe(III)PPIX, is likely to occur in a non-aqueous solution environment. Since the EXAFS experiments do not provide sufficient resolution beyond ~4 Å from the Fe atom, it is not possible to comment on the presence or absence of the intramolecular hydrogen bond in solution.

4.5   Conclusion

The SCD data of QN-Fe(III)PPIX, QD-Fe(III)PPIX and MQ-Fe(III)PPIX complexes shown in this work confirm the long standing belief that the quinoline methanol antimalarials form 1:1 complexes with Fe(III)PPIX. These results provide the first experimental evidence for the activity of the drug compounds in the solid state. Due to new insight into the formation of haemozoin taking place at a lipid-water interface, the site of action of quinoline antimalarials has also shifted from an aqueous environment to a non-aqueous hydrophobic environment. The association studies presented in this chapter indicate that it is most probably the case that drug activity is taking place in a non-aqueous hydrophobic environment. Therefore, as observed in the SCD structures, activity involves three key interactions. These include direct coordination of the drug to the Fe(III) centre, π-stacking between the drug and porphyrin aromatic systems and, finally, intramolecular hydrogen bond formation. Whether these interactions are represented in the solution medium of the food vacuole of the parasite remains to be addressed. The EXAFS data certainly indicate that the species shown to exist in the solid state also exist in the crystallisation solution environment, which suggests that there is a good chance that the observed complexation mode would occur *in vivo*. Regardless, the SCD structures provide clear insight into the antimalarial interactions possible between quinoline methanol drugs and Fe(III)PPIX, and will be important to consider in designing new haemozoin inhibitors.

5   Inhibition of β-Haematin Formation at the Lipid-Water Interface

5.1   Introduction

To date, the inhibition of β-haematin formation by current antimalarial drugs has only been investigated under non-biological conditions.[66,67] Recent evidence by Pisciotta *et al.*[60] has provided insight into the mechanism of haemozoin formation through the observation of haemozoin crystals inside neutral lipid droplets in the aqueous digestive vacuole of the malaria parasite. On this basis, a novel biomimetic method for studying the formation of β-haematin at a lipid water interface was developed, with kinetic studies undertaken in this model system showing biologically relevant half-lives for β-haematin formation which are in the order of minutes.[73,74] Due to increasing interest in the lipid-mediated mechanism of β-haematin formation, and the fact that drug action is now thought to take place in this environment, the modified Phiβ assay (lipid-water interface system)[74] was chosen for measuring the inhibition of β-haematin formation by clinically-relevant antimalarials under biomimetic conditions. The kinetic effects of β-haematin formation in the presence of CQ, AQ, QD and QN were investigated as they represent the two different sub-classes within the quinoline family, namely 4-aminoquinoline and quinoline methanol antimalarial drugs, respectively. The study made use of monopalmitic glycerol (MPG) to model the lipid environment, since significant amounts of MPG have been detected in the digestive vacuole surrounding haemozoin.[60] This is the first systematic study of the effect of quinoline antimalarial drugs on β-haematin formation under biomimetic conditions, and has provided insight into the mechanism of action of this important class of antimalarial drugs.

5.2   Experimental Methods

The methods in this section describe how the MPG (lipid)-water interface system was used to investigate the formation of β-haematin in the presence of CQ, AQ, QD, QN and MQ. The effect of altering the concentrations of these quinoline methanol and 4-amino-quinoline drugs (incorporated into the aqueous buffer) was studied. The materials used have been previously listed in Table 3.1.

5.2.1   General Preparations: Lipid-Water Interface

5.2.1.1   0.10 M NaOH Solution

Solid pellets (4.00 g, 100.0 mmol) of NaOH were dissolved in distilled water to a total volume of 1000.0 mL in a volumetric flask.

5.2.1.2   0.20 M HEPES Buffer, pH 7.5

4.76 g of HEPES acid was dissolved in 80.0 mL distilled water. The pH was adjusted to 7.5 using a concentrated solution of sodium hydroxide (NaOH). The solution was transferred quantitatively and made to volume in a 100.0 mL volumetric flask.

5.2.1.3   2.0 M HEPES Buffer, pH 7.5

47.66 g of HEPES acid was dissolved in distilled water until a volume of 80.0 mL was reached in a beaker. The pH was adjusted to 7.5 using a concentrated solution of sodium hydroxide (NaOH). The solution was transferred quantitatively and made to volume in a 100.0 mL volumetric flask.

5.2.1.4   5:45:50 (*v/v*) Pyridine: Water: Acetone Solution

To 10.0 mL of 0.2 M HEPES buffer (pH 7.5), 5.0 mL pyridine and 50.0 mL acetone were added and thoroughly mixed together. The solution was made up to a final volume of 100.0 mL with distilled water in a volumetric flask. The mole ratio corresponding to the volumes used is 1:42:11 for pyridine, water and acetone respectively.

5.2.1.5   30:30:40 (*v/v*) Pyridine: Water: Acetone Solution

To 10.0 mL of 2.0 M HEPES buffer (pH 7.5), 30.0 mL pyridine and 40.0 mL acetone were added and thoroughly mixed together. The solution was made up to a final volume of 100.0 mL with distilled water. The mole ratio corresponding to the volumes used is 1:5:2 for pyridine, water and acetone respectively.

5.2.1.6   50 mM Citrate Buffer, pH 4.8

This buffer solution was prepared directly in a 1 litre Schott bottle. Citric acid monohydrate (10.51 g, 50.0 mmol) was dissolved in 950.0 mL distilled water. The pH was adjusted to 4.8 using a concentrated solution of sodium hydroxide (NaOH) after which the solution was made up to a final volume of 1000 mL. This buffer solution is referred to as "regular" citrate buffer in the remainder of the chapter to distinguish it from preparations in which antimalarial drugs are included.

5.2.1.7   1:9 (*v/v*) Acetone: Methanol Solution

10.0 mL of acetone was mixed together with methanol in a volumetric flask to a total volume of 100.0 mL.

5.2.1.8   Lipid Solution

18.0 mg MPG (1-monopalmitoyl-*rac*-glycerol, Figure 5.1) was dissolved in 18.0 mL of the 1:9 acetone: methanol solution to give a final concentration of 1.0 mg/mL. This solution was stored in a sealed glass vial below 0 °C and prepared fresh for each set of experiments.
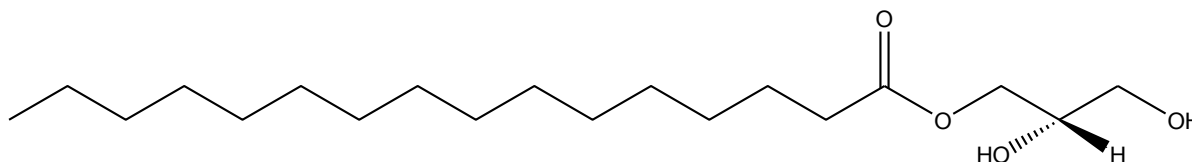
Figure 5.1 The chemical structure of 1-monopalmitoyl-*rac*-glycerol (MPG), the lipid used in this study as a model of the lipid environment associated with haemozoin.[60]

5.2.1.9 Fe(III)PPIX Solution

10.0 mg Fe(III)PPIX (haematin) was dissolved in 2.0 mL of 0.1 M NaOH in a Greiner Falcon centrifuge tube. After complete dissolution of the solid, 3.0 mL of the 1:9 (*v/v*) acetone: methanol solution was added and the new solution was thoroughly mixed to give a final concentration of 0.67 mg/mL. This solution was prepared fresh for each set of experiments.

5.2.2 Preparation of β-Haematin at the MPG-Water Interface

Experiments were carried out in Schott Duran crystallising dishes with an internal diameter of 9 cm. For the purpose of incubation, these glass vessels were partially immersed into a water bath set at 38 ^{o}C to ensure that the working temperature of the experiments remained close to biological temperature (37 ^{o}C) at all times. Aluminium foil was used to cover each vessel.

Regular citrate buffer (50.0 mL, 50.0 mM, pH 4.8) was measured into each glass vessel and pre-incubated at 37 ^{o}C for 45 minutes while the lipid and Fe(III)PPIX solutions were prepared. A solution of 1.0 mL of lipid solution and 0.5 mL of the Fe(III)PPIX solution was then prepared. This "premix" was added dropwise over the surface of the citrate buffer using a syringe with a needle diameter of 0.5 mm creating a lipid-water emulsion at the lipid-water interface. Once the Fe(III)PPIX had been delivered to the interface *via* the "premix", the vessels were left to incubate for a further 30 minutes.

At the end of the incubation period, the surface was agitated to release the product into the bulk aqueous medium. The total volume (∼ 51.5 mL) was then transferred to a centrifuge tube and centrifuged at 6000 revolutions per minute (rpm). The supernatant was discarded and the pellet kept for further analysis. 1.0 mL of the 5:45:50 (*v/v*) pyridine: water: acetone solution (pH 7.5) was added to "wash" the pellet. 5% (*v/v*) pyridine at pH 7.5 selectively dissolves unreacted Fe(III)PPIX in the presence of β-haematin, while 50% (*v/v*) acetone has proven useful in dissolving any co-pelleted lipid.[74] After a second centrifugation, the remaining product (pellet) was dried in a desiccator over phosphorus pentoxide for up to 52 hours before further analysis. The experimental procedures described above are shown in schematic form in Figure 5.2.
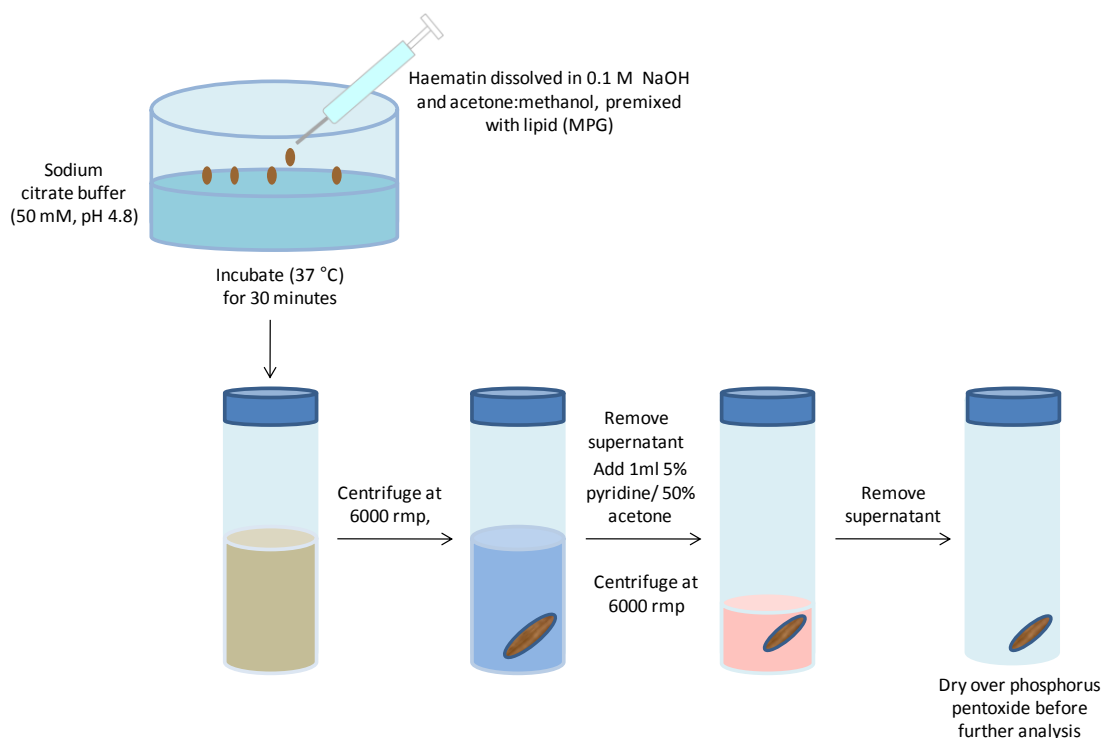
Figure 5.2 The experimental procedures for the formation of β-haematin at the lipid-water interface.

5.2.3   Modified Phiβ Assay for Measuring Inhibition of β-Haematin Formation.

The pyridine hemichrome inhibition of β-haematin (Phiβ) assay exploits the ability of a 5% (*v/v*) aqueous pyridine solution, pH 7.5, to selectively form a low-spin *bis*-pyridyl complex with free Fe(III)PPIX and not β-haematin.[134] The formation of the Fe(III)PPIX-pyridine complex yields an orange-pink coloured solution making it possible for the free Fe(III)PPIX concentration to be determined from the spectroscopic absorbance of the Soret band at 405 nm. In the current work, the principles of the Phiβ assay were applied when investigating the inhibition of β-haematin formation in the lipid-water interface model system.[74]

5.2.3.1 Inhibition of β-Haematin Formation at the MPG-Water Interface by Antimalarial Drugs

In order to investigate the effect of antimalarial drugs, the method of Hoang *et al.*[74] was modified to include aqueous-soluble antimalarial drugs in the citrate buffer. β-Haematin formation was then brought about in the same manner as before. The antimalarial drugs discussed in this work have been shown in Figure 1.36.

5.2.3.2 Citrate Buffer Solutions Containing Antimalarial Drugs

A stock solution of citric acid monohydrate was prepared by dissolving 10.51 g (50.0 mmol) in 950.0 mL distilled water together with the appropriate mass of antimalarial drug (Table 5.1). The pH was adjusted to 4.8 using a concentrated solution of sodium hydroxide (NaOH). The solution was made up to a final volume of 1000 mL. This approach is suitable for compounds that are soluble in aqueous solution and was used in this study to prepare buffer solutions containing CQ, AQ, QD and QN. MQ, which is not soluble in aqueous solution, was dissolved in a 1:9 (*v/v*) acetone:methanol solution and added together with the lipid premix as described later.

Table 5.1 Quantities of antimalarial salts required for the preparation of 0.1 mM solutions (volume = 1 000 mL) containing 50.0 mM citrate, pH 4.8.

COMPOUND	AVERAGE MOLECULAR MASS / Da	MASS/g
Chloroquine diphosphate (CQ)	515.86	0.0516
Amodiaquine dihydrochloride dihydrate (AQ)	464.8	0.0464
Quinine sulphate dihydrate (QN)	782.94 (391.45)*	0.0391
Quinidine sulphate dihydrate (QD)	782.94 (391.45)*	0.0391
Mefloquine hydrochloride (MQ)	414.077	0.0414[#]
Primaquine bisphosphate	455.35	0.0455

*The molecular mass of QD and QN is the value reported in brackets. These compounds are supplied as hemisulphate salts.

[#]Mefloquine hydrochloride is insoluble in the aqueous citrate buffer. The mass represents that needed to prepare 1000 mL of a 0.1 mM solution. However the mass incorporated into the lipid solution was equal to the amount that would be expected in the aqueous citrate buffer if the drug was soluble.

5.2.3.3   Determination of IC_{50} Values

5.2.3.3.1   *Aqueous Soluble Antimalarial Drugs*

All experiments were carried out in 15 mL Greiner Falcon centrifuge tubes with an internal diameter of 1.6 cm. For the purpose of incubation, these plastic tubes were partially immersed into a water bath set at 38 °C to ensure that the working temperature of the experiments remained 37 ± 1 °C at all times.

Serial dilutions of the respective drug-containing citrate buffer solution were prepared using calibrated micro-pipettes. Regular citrate buffer (50.0 mM, pH 4.8) was used to dilute the citrate/drug stock solutions to a series of different concentrations as required. Initially, the working concentration range was more-or-less determined by trial and error for each drug initially and subsequently refined in repeat measurements. Each tube contained a total volume of 5 mL of drug-containing citrate buffer. Each plastic tube was pre-incubated at 37 °C for approximately 45 minutes while the lipid and Fe(III)PPIX solutions were prepared.

A solution containing 0.2 mL (200 μL) of lipid solution and 0.005 mL (5 μL) of Fe(III)PPIX solution was prepared in a 2 mL Eppendorf tube for each experimental tube (i.e. 27 per triplicate set). The interface was prepared as before by adding the premix solution drop-wise to the pre-incubated interface using a syringe with a needle diameter of 0.5 mm. Once the premix solution had been delivered to the interface, the plastic tubes were capped and left to incubate for a further 30 minutes.

At the end of the incubation period, the interface was agitated to release the product into the bulk medium. 1.0 mL of an aqueous solution containing 30% pyridine solution, 10% HEPES buffer (2.0 M, pH 7.5) and 40% acetone (*v/v*) was added directly into the experimental solution to yield a solution which contained 5% (*v/v*) pyridine overall. After vigorous shaking of each tube to allow the pyridine to fully interact with the unreacted Fe(III)PPIX, the tubes were centrifuged at 6000 rpm for 10 minutes. At this point there was often the need to allow visible lipid precipitate to settle before transferring a 2.0 mL aliquot of the supernatant to a quartz cuvette. The absorbance value for each tube was measured at 405 nm to quantify the unreacted Fe(III)PPIX for each drug concentration. The experimental procedures described above are shown in schematic form in Figure 5.3.
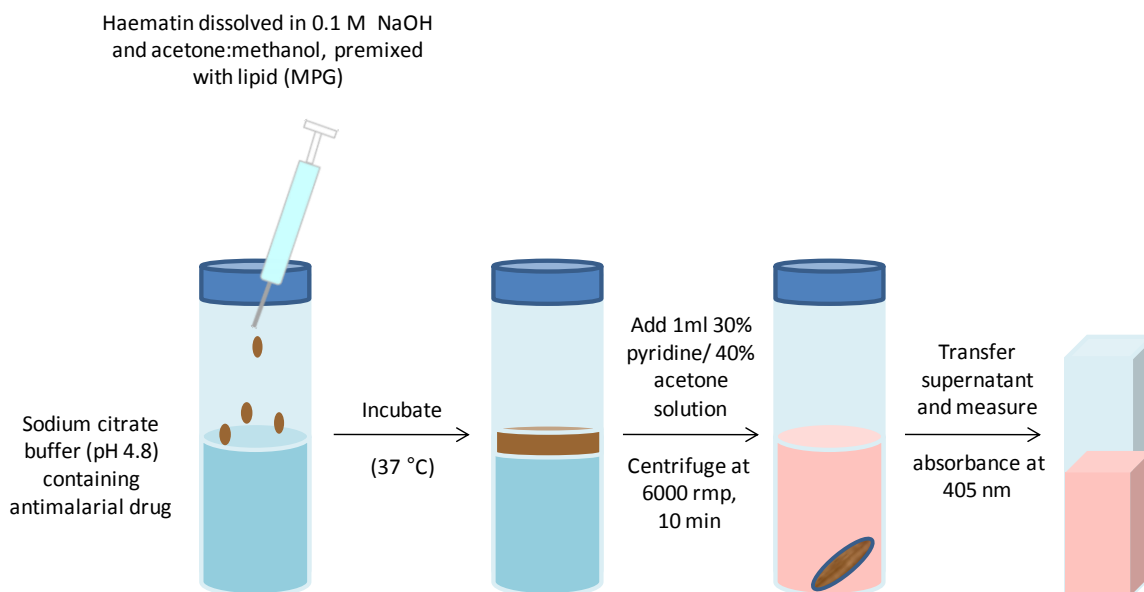
Figure 5.3 Experimental procedures for the inhibition of β-haematin formation at the lipid-water interface by antimalarial drugs.

Biological measurements are typically carried out in triplicate, however, due to the irreproducibility of the lipid emulsion formed at the interface, measurements at each time point, were performed nine times in order to increase certainty in the data (Figure 5.4).
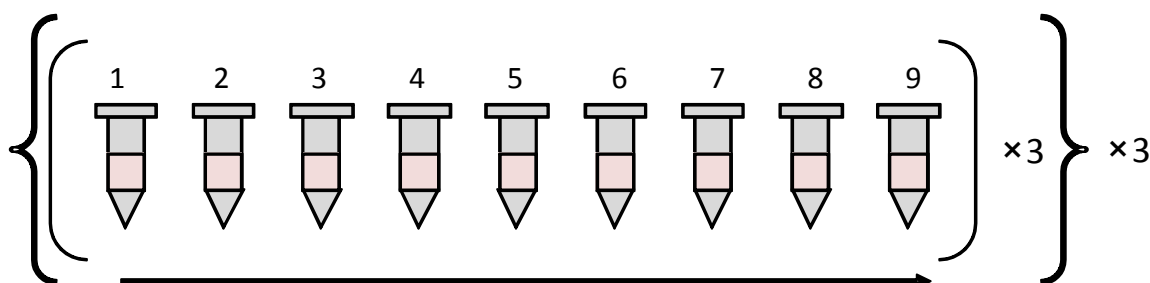
Figure 5.4 Schematic presentation of IC_{50} determination. For each tube (1 – 9) the incubation time was constant and the drug concentration varied. Measurements are routinely performed in triplicate. However, owing to poor reproducibility of the lipid-water interface, measurements were repeated nine times.

The absorbance values were plotted as a function of drug concentration and fitted to a simple sigmoidal or hyperbolic equation. Data were analysed by nonlinear least squares fitting using GraphPad Prism 5 software.[164] The drug concentration at 50% absorbance

change is a measure of the IC_{50} which is the drug concentration required to inhibit 50% β-haematin formation. A schematic of the data handling is shown in Figure 5.5.
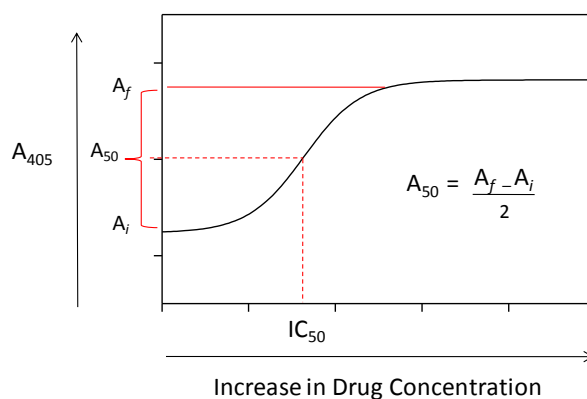
Figure 5.5 Schematic indicating how the absorbance data was used to calculate the drug concentration required to inhibit 50% of β-haematin formation (IC_{50}). The A_{50} is worked out by subtracting the initial absorbance (A_i) value, recorded for low drug concentrations, from the final absorbance value (A_f), at higher drug concentration and dividing the difference by two. The drug concentration corresponding to the 50% absorbance change value (A_{50}) is the drug concentration required to inhibit 50% of β-haematin formation (IC_{50}).

5.2.3.3.2 *Non-Aqueous Soluble Antimalarial Drugs*

Mefloquine hydrochloride (MQ) is insoluble in the citrate buffer solution. Therefore, the drug was incorporated into 100 μL of the lipid solution, while the remaining 100 μL of lipid solution plus Fe(III)PPIX solution was used to make up the premix. The drug-lipid solution was added drop wise first followed by the Fe(III)PPIX-lipid solution. The quantity of MQ incorporated into the lipid solution was equal to the amount that would be expected in the aqueous citrate buffer if the drug was soluble. Therefore, the concentrations were calculated relative to the total volume of the system.

5.2.3.4 The Effect of Time on Drug IC_{50} Values

Following the procedures outlined in section 5.2.3.3, the experiments to determine the IC_{50} value of a particular drug were repeated at different incubation times which were varied in turn between 10 and 1200 min. The extent of reaction was monitored using the Phiβ assay. Data handling and analysis were carried out as before (section 5.2.3.3).

148

5.2.3.5   Effects of Quinoline Antimalarial Drugs on the Kinetics of β-Haematin Formation at the Lipid-Water Interface

Following the procedures outlined in section 5.2.3.3, the kinetics of β-haematin formation in the presence of various drug concentrations were recorded as follows: a series of 9 tubes, each containing the same drug concentration, ranging from zero to approximately three times the previously determined IC_{50} value, was incubated for different lengths of time in order to generate the data points for a single kinetic trace. Measurements at a particular drug concentration were performed at least three times (Figure 5.6). The absorbance value at 405 nm is a direct quantitative measure of the unreacted Fe(III)PPIX remaining after the reaction and consequently, the % β-haematin formed during the reaction could be determined.
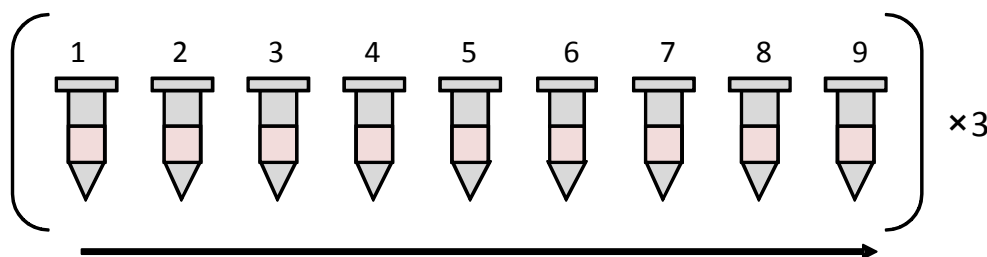
Figure 5.6 A schematic presentation of kinetic determinations. For each tube (1 – 9) the drug concentration was fixed and the incubation time varied with each time point determined three times.

The experimental procedure for the kinetic studies was the same as described in section 5.2.3.3, but with the following changes. In earlier work, 5 μL aliquot of Fe(III)PPIX solution (3.1 μM in 5.2 mL) for the IC_{50} determination were used. However, the publication of the kinetic studies of β-haematin formation[74] showed that a 2 μL aliquot (1.2 μM in 5.2 mL) of Fe(III)PPIX produced optimal yields of β-haematin. Thus these revised conditions were used in the kinetic studies on β-haematin inhibition. As a result, the premix solution delivered to each reaction contained 0.2 mL (200 μL) of lipid solution and 0.002 mL (2 μL) of Fe(III)PPIX solution.

Data were analysed by nonlinear least squares fitting of the data using GraphPad Prism 5 software,[164] which allowed the length of time required for the formation of β-haematin to proceed to half its extent, that is the half life ($t_{1/2}$), to be determined.

5.2.4   CQ and QD Adsorption to β-Haematin Crystals

5.2.4.1   Preparation of β-Haematin Crystals at the Pentanol-Water Interface

The pentanol-water interface system was used, since crystals grown from this environment have been shown to be of a better quality, largely due to the fact that traces of pentanol can be removed from the crystals if they are washed thoroughly. On the other hand, traces of lipid are routinely observed by SEM despite extensive washing of the crystals.

Experiments were carried out in Schott Duran crystallising dishes with an internal diameter of 9 cm. For the purpose of incubation, these glass vessels were partially immersed into a water bath set at 38 ^{o}C to ensure that the working temperature of the experiments remained close to 37 ^{o}C at all times. Aluminium foil was used to cover each vessel.

Regular citrate buffer (50.0 mL) was measured into each glass vessel after which 10 mL of 1-pentanol was layered on top of this aqueous layer. Vessels were then pre-incubated at 37 ^{o}C for 30 minutes while the Fe(III)PPIX solution was prepared. A solution of 1.0 mL Fe(III)PPIX (in acetone:methanol) was introduced close to the pentanol-water interface making use of a syringe with a needle diameter of 0.5 mm to deliver the solution dropwise over the whole interface. Once the Fe(III)PPIX had been loaded on to the interface, the experiments were left to incubate for a further 30 minutes.

At the end of the incubation period, the surface was agitated to release the product into the pentanol layer. The total volume of the pentanol layer ($\sim$ 11.0 mL) was transferred to a centrifuge tube and centrifuged at 6000 rpm. The supernatant was discarded and the pellet kept for further analysis. 1.0 mL of the 5:45:50 (*v/v*) pyridine: water: acetone solution (pH 7.5) was added to wash the pellet. After a second centrifugation, the remaining product (pellet) was dried in a desiccator being exposed to phosphorus pentoxide for up to 52 hours before further analysis.

5.2.4.2   CQ and QD Adsorption

To investigate adsorption of CQ and QD to the surface of β-haematin crystals, Eppendorf tubes containing 1.0 mg β-haematin crystals (prepared from the 1-pentanol-water interface) suspended in 2.0 mL of citric buffer with the desired drug concentration (prepared as

described in section 5.2.3.2) were setup and allowed to stand for a period of 3 days after which the absorbance of the supernatant was measured.

The amount of the drug that is proposed to be adsorbed by the crystal was calculated from Beer's law plots determined for CQ and QD respectively. From Beer's law, it is evident that there is a relationship between the transmission of light through a solution and the concentration of the solution being investigated (eq. 5.1).[147]

$$A = \varepsilon cl \qquad\qquad 5.1$$

In the above relationship, A is the measured absorbance, ε is the molar absortivity, c is the concentration of the compound in solution and l is the path length of the sample. By measuring the absorbance of the supernatant at 344 and 236 nm for CQ and QD respectively, and comparing to the initial absorbance reading of a drug solution of particular concentration, the extent of depletion was considered a measure of the adsorption of the drug to the β-haematin crystals. Studies were carried out in the presence of different drug concentrations, with each determination per drug concentration performed at least three times. Data were analysed by nonlinear least squares fitting using GraphPad Prism.[164]

5.3   Results

5.3.1   Formation and Characterisation of β-Haematin at the Lipid-Water Interface

Making use of the lipid-water interface system developed by Egan *et al.*, the first objective was to confirm that β-haematin could be reproducibly recovered using this method.[73] Before proceeding with an investigation of drug activity in this system, it was important to ensure that the material we were aiming to inhibit (β-haematin) could be successfully synthesised and characterised. Formation of β-haematin was brought about by incubating a premixed solution of Fe(III)PPIX (3.2 mM) and 1-monopalmitoyl-*rac*-glycerol (MPG) lipid (3.3 mM) for 30 min on the surface of 50 mL citrate buffer solution (50 mM, pH 4.8) pre-incubated at 37 $^{\circ}$C for 45 min. Following incubation, the reaction was quenched with pyridine. It has previously been shown in the pyridine hemichrome inhibition of β-haematin (Phiβ) assay, that 5% (*v/v*) aqueous pyridine solution, pH 7.5, can selectively react with free Fe(III)PPIX resulting in a characteristic orange-pink *bis*-pyridyl complex in solution with a distinctive absorbance maximum at 405 nm.[134] In the current work, the principles of the Phiβ assay were adapted for use with the lipid-water interface model system. Centrifugation allowed the β-haematin, which is not soluble in 5% (*v/v*) pyridine, to be recovered. β-Haematin yields a characteristic FT-IR spectrum as well as PXRD pattern and thus the final product obtained in these experiments was compared to literature standards.

Previously shown in Figure 1.9 (a), the centrosymmetric haemozoin dimer comes about due to the propionate group of one Fe(III)PPIX molecule coordinating to the Fe(III) centre of the second Fe(III)PPIX and *vice versa*.[35] The strong absorbance bands at 1211 cm^{-1} and 1664 cm^{-1} in the FT-IR spectrum, assigned by Slater *et al.*[30] to the C-O and C=O stretching frequencies of the coordinated propionate ligand are visible in the spectrum of the product recovered from the lipid-water interface (Figure 5.7). The ATR-IR spectrum and PXRD pattern of the product recovered from the interface are shown in Figure 5.7 and Figure 5.8 respectively, and confirm the formation of β-haematin.
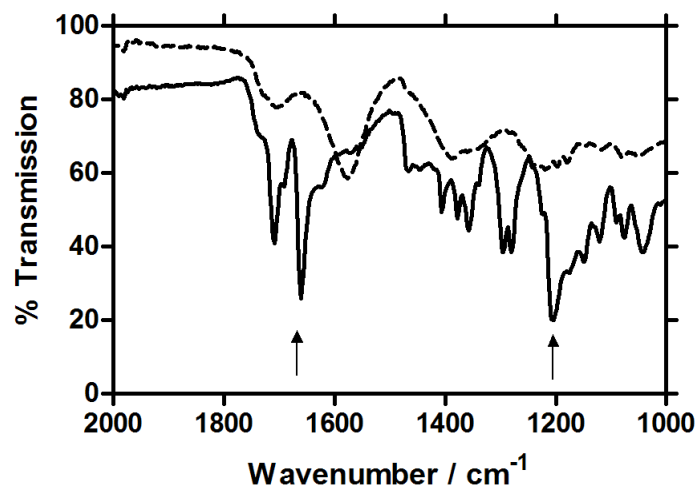
Figure 5.7 ATR-IR spectra of Fe(III)PPIX (dashed line) and β-haematin (solid line) recovered from the lipid-water interface. Characteristic peaks at 1211 and 1664 cm^{-1} in the spectrum of β-haematin are indicated with arrows and are absent in the spectrum of Fe(III)PPIX.
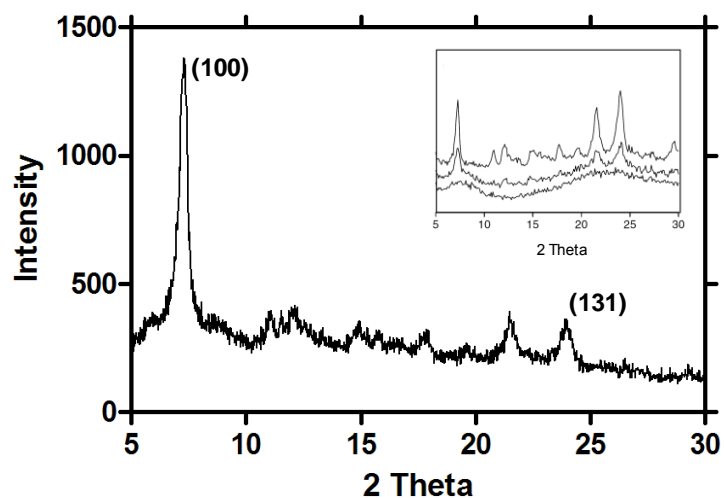
Figure 5.8 PXRD pattern of β-haematin recovered from the lipid-water interface. The (100) and (131) reflections are denoted. Comparison to the literature pattern previously reported by Egan *et al.*[71] (inset) supports the conclusion that β-haematin is indeed formed at the lipid-water interface.

5.3.2   Effect of Antimalarial Drugs on Lipid-Mediated Formation of β-Haematin

In order to validate the lipid-water interface system as a means of assaying antimalarial drug activity against β-haematin formation, the observed IC_{50} values were compared to the *in vitro* biological activities previously determined against CQ-sensitive (CQS) strains (3D7 and HB3) and CQ-resistant (CQR) strains (K1 and PH3) of the malaria parasite.[94]

5.3.2.1   Validation of the Lipid-Water Interface System as a Means of Assaying Drug Activity

The drug concentration required to inhibit β-haematin formation by 50% is referred to as the IC_{50} value. The more active a particular compound the lower its IC_{50} value. The dose-response curves for the inhibition of β-haematin formation by quinoline antimalarials amodiaquine (AQ), chloroquine (CQ), quinidine (QD), quinine (QN) and mefloquine (MQ) after 30 minutes incubation time in the lipid-water interface model system are shown in Figure 5.9. This incubation time was arbitrarily chosen as a starting point while the concentration of drug was systematically increased. In contrast to a previous study by Ncokazi *et al.*[134] in which drug concentrations were prepared as equivalents relative to Fe(III)PPIX and β-haematin formation was brought about in 4.5 M acetate (pH 4.5, 60 ^{o}C), the present study made use of actual molar concentrations. Following quenching of the reaction with 30% (*v/v*) aqueous pyridine to yield a final solution containing 5% (*v/v*) aqueous pyridine (pH 7.5), the extent of reaction was monitored by quantitating the remaining fraction of Fe(III)PPIX spectroscopically at 405 nm (Figure 5.9). The observed IC_{50} data are summarised in Table 5.2.
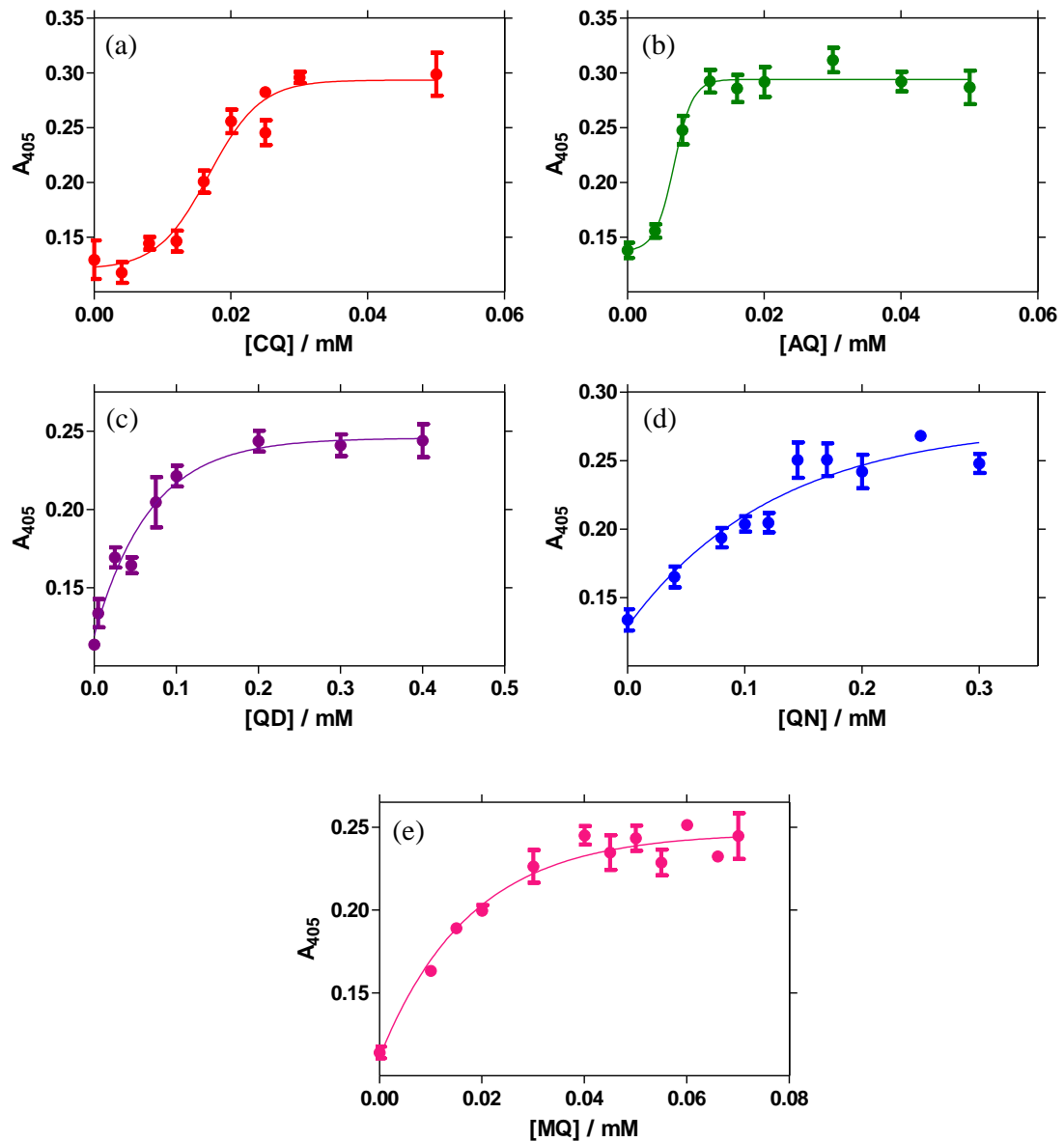
Figure 5.9 The inhibition of β-haematin formation by antimalarial drugs in a lipid-water interface model system. Dose-response curves determined after 30 minutes incubation as a function of increasing antimalarial drug concentration. The compounds investigated were (a) CQ, (b) AQ, (c) QD, (d) QN and (e) MQ. The solid line represents the best fit of the data to a sigmoidal (a and b) or simple hyperbolic (c, d and e) function in order to determine the IC_{50} for each drug.

Table 5.2 IC$_{50}$ data obtained for the inhibition of β-haematin at the lipid-water interface.

Antimalarial drug	Observed IC$_{50}$ (μM)
CQ	$16.4 \pm 0.5^*$
AQ	9.0 ± 0.4
QD	51.1 ± 5.8
QN	73.9 ± 12.8
MQ	12.2 ± 0.1

*Error calculated as standard error of the mean (SEM), following nine repeat measurements.

A corresponding increase in absorbance (A$_{405}$) is observed in each case as the concentration of the inhibitor is increased. This is expected due to an increase in the amount of free Fe(III)PPIX which is prevented from being incorporated into β-haematin. Notably, the inhibition profiles brought about in the presence of 4-aminoquinoline and quinoline methanol antimalarial drugs appear to differ. While AQ and CQ appear to induce a sigmoidal dose-response, the QD, QN and MQ dose-response curves conform to a simple hyperbola. Initially it was thought that the IC$_{50}$ results pointed to different mechanisms for the 4-aminoquinoline and quinoline methanol compounds, however, careful reconsideration as discussed below, suggests that this is not the case.

When comparing the observed IC$_{50}$ values to the *in vitro* biological activities previously determined against the CQ-sensitive (CQS) strains (3D7 and HB3) and CQ-resistant (CQR) strains (K1 and PH3) of the malaria parasite.[94] The results of the current study are in good agreement and show a linear correlation (Figure 5.10). In the case of the CQR correlation, data points for CQ have been omitted since the lipid-water interface cannot account for the CQR mechanism where the CQ concentration within the infected cell is diminished. This reduction is probably due to the removal of CQ by PfCRT.[178]
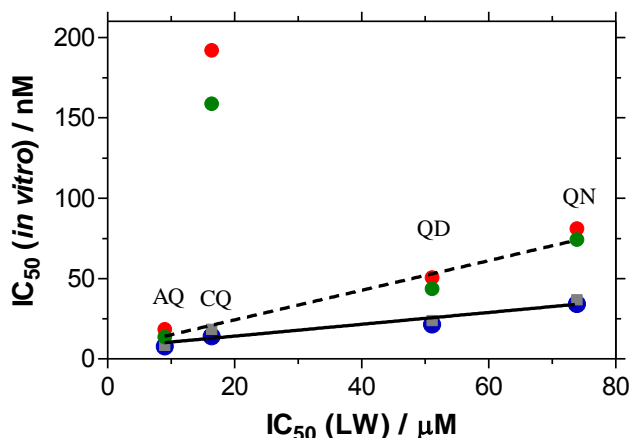
Figure 5.10 Inhibition of β-haematin formation by quinoline antimalarials at the lipid-water interface (LW). The correlation between the inhibitory activities of antimalarial drugs at the lipid-water interface (IC_{50} (LW) values obtained after 30 min incubation time), and their biological activity against CQ-susceptible strains, 3D7 (●) and HB3 (grey box), and CQ-resistant strains, K1 (●) and PH3 (●), of *P. falciparum*.[94] The r^2 values for CQS and CQR correlations are 0.92 and 0.96, respectively. The data points for CQ against the CQR strains indicate very poor activity and have not been included in the linear regression analysis. The slope values are different for the CQR and CQS strains: 0.92 ± 0.10 and 0.37 ± 0.04, respectively.

Since it is argued that MQ is the only drug which is not readily soluble in the aqueous layer, MQ has been excluded from the above correlation, and it is therefore difficult to compare its activity directly with the activity of other compounds. The statistical significance of the linear correlation observed between the biological activities of CQ, AQ, QN and QD against CQS and CQR strains of *P. falciparum* is good with r^2 values of 0.92 and 0.96 respectively. It is observed that different slopes are obtained for each correlation. The deviation from zero in each case is significant as indicated by a P value of < 0.05. However, the slope in the CQR correlation (slope $= 0.92 \pm 0.10$) is steeper when compared to the slope of the CQS correlation (slope $= 0.37 \pm 0.04$). Since the IC_{50} (LW) values are constant, the contributing factor to the differing slope values is simply the greater IC_{50} values reported for CQR compared to CQS strains. Overall, the correlations do indicate that the lipid-water interface system is a valid system in which to investigate drug activity.

5.3.2.2   Observed Kinetic Behaviour in the Presence of Quinoline Antimalarials

A detailed kinetic investigation of β-haematin formation at the lipid-water interface in the presence of quinoline antimalarial drugs CQ, QD, AQ and QN was subsequently undertaken. The rapid rate at which β-haematin forms in the lipid-water interface model system compared to 4.5 M acetate (pH 4.5, 60 ^{o}C) made it possible to investigate the kinetics for this process in the presence of antimalarial drugs. The observed kinetic behaviour in the presence of CQ is shown in Figure 5.11.
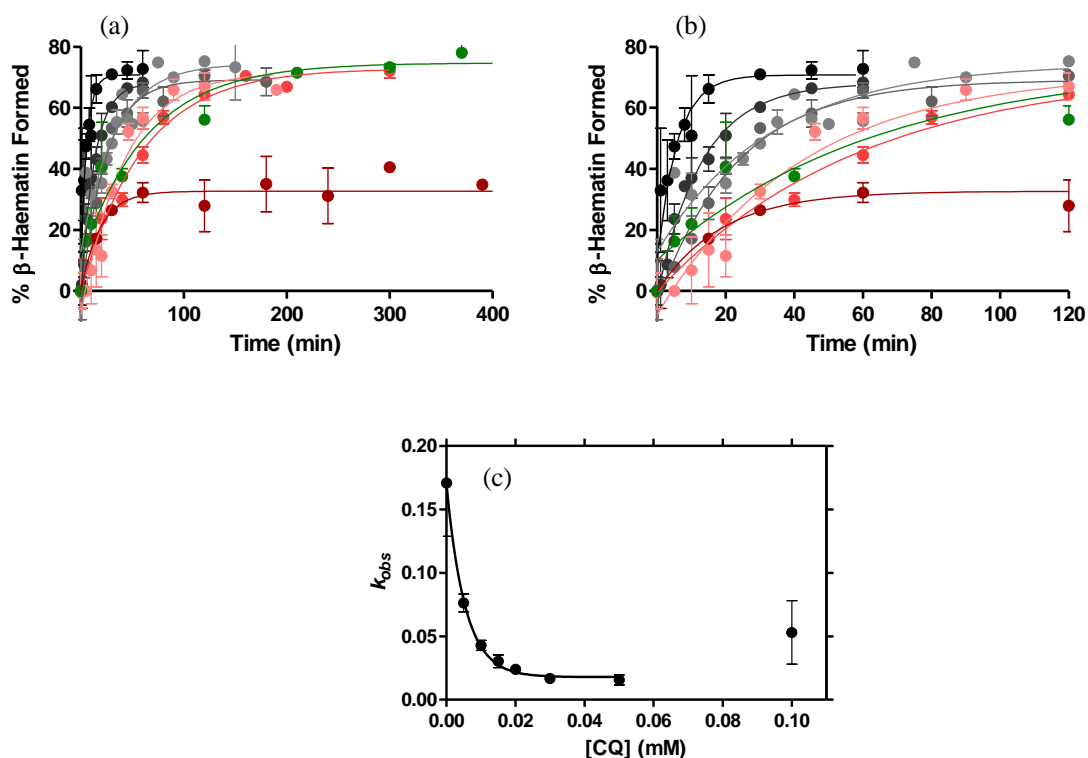
Figure 5.11 The effects of CQ on the kinetics of β-haematin formation. (a and b) In the absence (black circle) and presence of 0.005 (●), 0.01 (●), 0.015 (●), 0.02 (●), 0.03 (●), 0.05 (●) and 0.1 (●) mM CQ, differences in the rate of the reactions are observed as the drug concentration is increased. The absorbance readings at 405 nm were converted into % β-haematin formed after each reaction. At relatively low drug concentration, there is a decrease in the rate constant, with the same yield of β-haematin eventually forming after longer periods of time. However, when the drug concentration is increased, a decrease in the final yield of β-haematin is observed. (c) The observed decrease in the rate constant of β-haematin formation with an increase in drug concentration.

In studying the kinetic effect of the drug on the formation of β-haematin under biomimetic conditions (lipid-water interface), a decrease in the rate at which β-haematin is formed is

observed at low drug concentration. As the drug concentrations are increased further, a decrease in the final yield of β-haematin is observed. Similar results were obtained for the other quinoline antimalarial drugs.

It could be argued that the decrease in absorbance measured as a function of time may be due to the formation of an unknown higher aggregate of Fe(III)PPIX or a Fe(III)PPIX-drug complex which is also insoluble in pyridine. However, using both infrared spectroscopy and powder X-ray diffraction, the formation of β-haematin was confirmed as the cause of the lower absorbance values, even in the presence of lower drug concentrations. Infrared spectra of the product obtained in the presence of 18 μM CQ (roughly the IC$_{50}$ value for 30 minutes incubation time) and 50 µM QD (roughly the IC$_{50}$ value for 30 minutes incubation time) after 5, 30 and 300 minutes incubation time are shown in Figure 5.12 a and b respectively, where prominent β-haematin peaks at 1211 and 1664 cm^{-1} are clearly visible in the infrared spectra. No new peaks or significant shifts are observed with increasing time, confirming that only unreacted Fe(III)PPIX and β-haematin are present. Owing to the fact that the lipid (MPG) is only ~ 70% efficient in its conversion of Fe(III)PPIX to β-haematin, a significant fraction of unreacted Fe(III)PPIX remains. It is indicated in the IR spectrum as a large broad signal centred at approximately 1590 cm^{-1}.
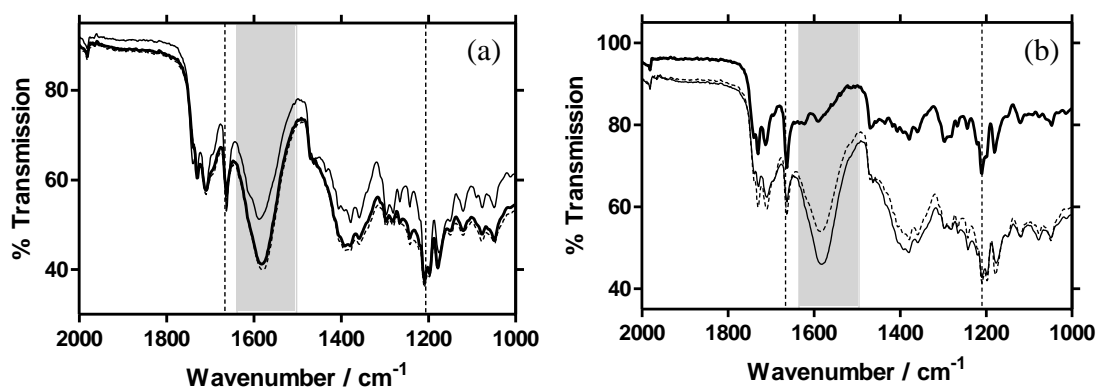
Figure 5.12 Infrared spectra of the Fe(III)PPIX species formed in the presence of (a) 18 µM CQ and (b) 50 µM QD after 5, 30 and 300 minutes (fine, medium and dashed lines respectively) incubation time. The two characteristic β-haematin bands at 1211 and 1664 cm^{-1} are indicated by dashed vertical lines. The signal for the unreacted Fe(III)PPIX in the grey block is expected owing to the lipid being only $\pm$ 70% efficient.[74]

PXRD patterns of the product obtained in the presence of 18 μM CQ and 50 μM QD after 5, 30 and 300 minutes incubation time are shown in Figure 5.13 a and b respectively. The PXRD patterns demonstrate the presence of β-haematin.
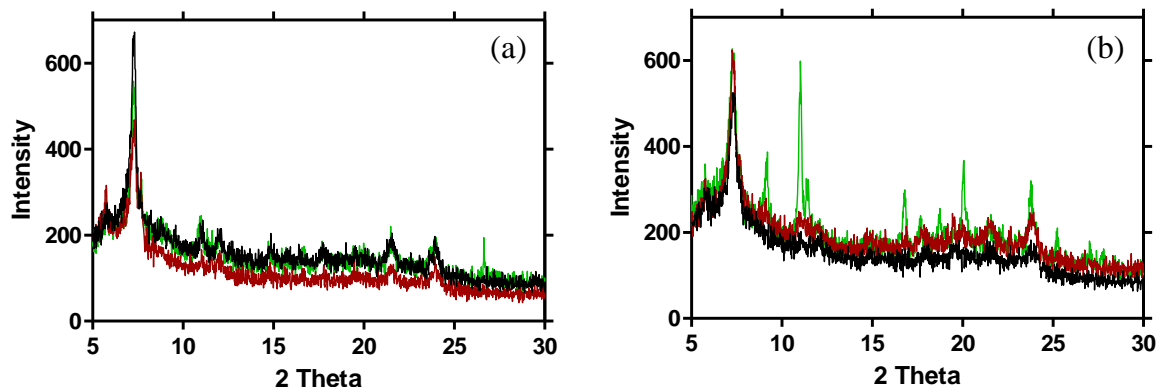
Figure 5.13 PXRD patterns of the Fe(III)PPIX species formed in the presence of (a) 18 μM CQ and (b) 50 μM QD after 5 minutes (green), 30 minutes (red) and 300 minutes (black) incubation time respectively. The PXRD patterns are characteristic of β-haematin.[71]

The quality of the PXRD pattern for Fe(III)PPIX species formed in the presence of 50 μM QD after 5 minute incubation time does not demonstrate the presence of β-haematin as clearly as at longer incubation times. This could be due to the fact that at short incubation time β-haematin crystal nucleation is still taking place and Fe(III)PPIX has not been converted to β-haematin or possibly due to a QD-Fe(III)PPIX complex forming.

5.3.2.3   Theoretical Model to Explain the Observed Kinetic Behaviour

Since simple kinetic models could not account for the observed effects of drug on the rate and yield of β-haematin formation, we set out to derive our own. In the first instance, an equilibrium in which the drug associates with free Fe(III)PPIX (haematin) in solution, and in the process reduces the concentration available to form β-haematin, was considered (Scheme 1). This equilibrium would account for the observed decrease in the rate of β-haematin formation, while the presence of an inhibiting drug may also be expected to promote a competing process that results in the irreversible precipitation of haematin, possibly as a drug complex. The latter would account for the decreased yield of β-haematin at higher drug concentrations. Irrespective of how strongly a drug compound associates with haematin in solution, as determined by the magnitude of the association constant K, the rate constant for the formation of β-haematin, k_1, is expected to dominate the rate constant for the precipitation of a drug-haematin complex, k_2, at low drug concentrations. Thus, the final yield of β-haematin would remain constant, but the rate of formation would decrease. However, as the concentration of drug is raised, k_2 will begin to have influence, and precipitation of the haematin (possibly as a drug complex) would begin to decrease the yield of β-haematin.
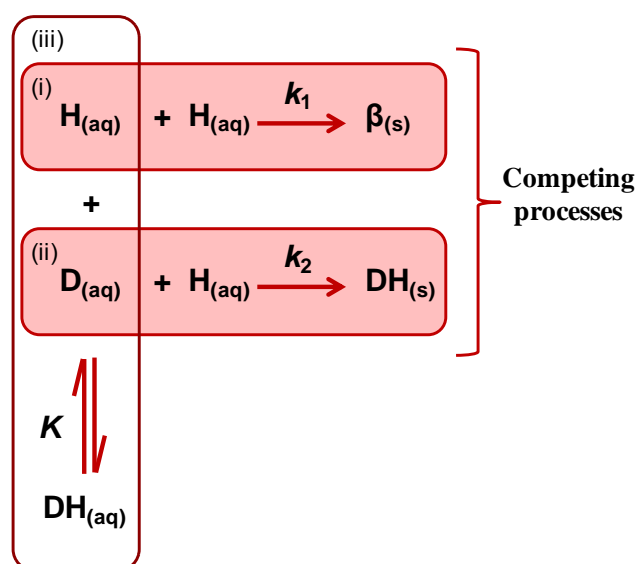
Scheme 1 A possible model to explain the effect of a drug on the rate of β-haematin formation. (i) Haematin ($H_{(aq)}$) dimerises in solution to form β-haematin ($β_{(S)}$) with rate constant k_1. (ii) The irreversible precipitation of a drug-haematin complex ($DH_{(s)}$), with rate constant k_2. (iii) Equilibruim reaction in which drug ($D_{(aq)}$) associates with free Fe(III)PPIX ($H_{(aq)}$) in solution forming a drug-haematin complex ($DH_{(aq)}$) with an association constant, K.

For this equilibrium reaction, the rate-determining step in the formation of β-haematin is a solution reaction, the rate of which is determined by the concentration of dissolved haematin species. Furthermore, if formation of the μ-propionato dimer of haematin (the precursor to β-haematin) in solution is rate-determining, the reaction would be expected to be second-order with respect to haematin. Alternative rate-limiting steps, such as dissociation of the axial ligand, would result in a process that is first order with respect to haematin.

While plausible, however, the mechanism presented in Scheme 1 is considered physically unrealistic for the process in question. A more likely scenario is that β-haematin crystal growth is rate determining. In this case the rate of β-haematin formation would be expected to depend on the rates of crystal nucleation and growth and not on the dissolved haematin concentration. While kinetics cannot definitively distinguish between this mechanism and the solution mechanism presented above, it was considered the more likely scenario, and therefore a crystal growth kinetic model was sought which may account for the observations.

The Avrami equation (eq. 5.2) has been used to model crystallisation processes, that is how solids transform from one phase into another at a constant temperature. It specifically describes the kinetics involved in crystallisation.[69,70]

$$\frac{m_R}{m_0} = e^{-zt^n} \tag{5.2}$$

In the above equation, m_R is the mass of Fe(III)PPIX remaining at time t compared to the initial mass m_0, z is an empirical rate constant and n is a constant known as the Avrami constant, which is usually an integer ranging between 1 and 4. In previous studies in which the kinetics of β-haematin formation were investigated in acetate medium, the yield of β-haematin formed were shown to exhibit sigmoidal time dependence. The best fit of the data to the Avrami model was when the Avrami constant was equal to 4. This indicates spontaneous nucleation and three dimensional crystal growth.[68]

The kinetic profile obtained for β-haematin formation in the lipid system conversely fits to an exponential function. When the Avrami constant is equal to 1, eq. 5.2 becomes mathematically indistinguishable from that of first order kinetics and thereby, accounts for the exponential shape observed. With a value equal to 1, the Avrami constant indicates that the process involves a fixed number of preformed nuclei, and that β-haematin crystal

growth takes place in approximately one dimension [1-D (linear) crystal growth]. This growth pattern is consistent with the observed morphology of β-haematin with crystals appearing as long needles.[179,180] Furthermore, the mode of nucleation is consistent with the proposed epitaxy model, with the lipid providing a fixed number of preformed nuclei (i.e. the nucleation sites are present before the reaction begins).[181]

In the model put forward by Leiserowitz and co-workers[40,180], the fastest-growing face of the β-haematin crystals was shown to contain a favourable binding site for quinoline antimalarial drugs (refer back to Figure 1.39, section 1.6.4). Their proposed mechanism for the inhibition of β-haematin formation by antimalarial drugs suggests that drug molecules are able to adsorb to sites on the surface of the growing crystal in order to impede further growth. Based on this hypothesis, a more realistic mechanistic explanation of the effect of drug on the rate of β-haematin formation was considered (Scheme 2).

In Scheme 2, [H] is the concentration of free Fe(III)PPIX (haematin). As the reaction progresses, there are two processes that compete for the starting material, namely the formation of β-haematin ($\beta_{(s)}$) or the precipitation of a haematin-drug complex ($DH_{(s)}$). The rate constant for the formation of β-haematin, z_{obs}, is expected to dominate the rate constant for the precipitation of a drug-haematin complex, k_2, at low drug concentrations. However, as the concentration of drug is raised, k_2 will begin to have an influence, and precipitation of the proposed complex will begin to decrease the yield of β-haematin.
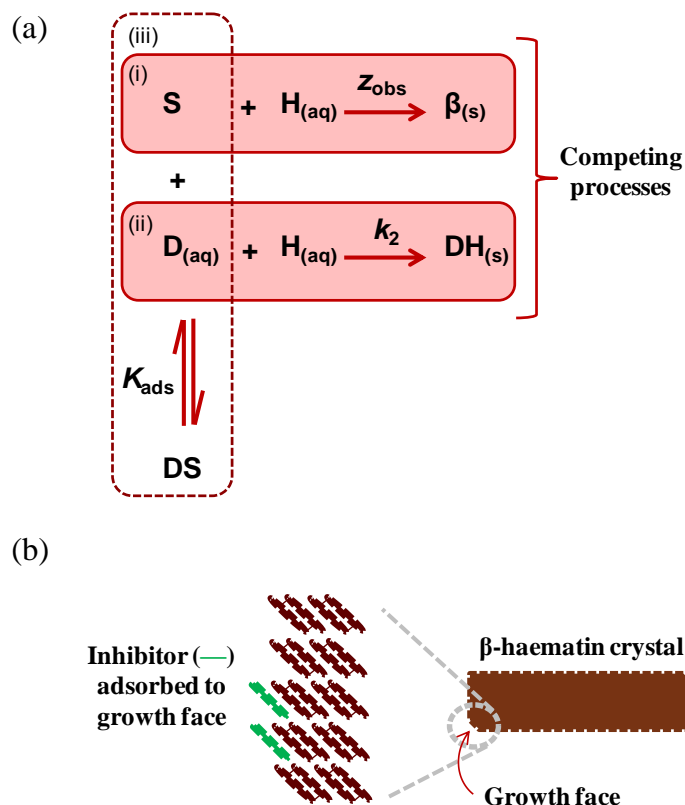
Scheme 2 Proposed model to explain the effect of drug molecules on the rate of β-haematin formation. (i) Haematin ($H_{(aq)}$) is added to the binding site (S) on the growing face of β-haematin ($\beta_{(s)}$), with a rate constant z_{obs} (ii) The irreversible precipitation of a drug-haematin complex ($DH_{(s)}$), with rate constant k_2. (iii) Equilibruim reaction in which drug ($D_{(aq)}$) adsorption onto the binding site (S) on the growing face of β-haematin crystals, form the adsorption complex (DS), with an adsorption equilibrium constant, K_{ads} (b) Representation of the formation of a drug monolayer on the fastest growing surface of β-haematin crystal by adsorption onto the binding sites. For the detailed model showing the docking of quinoline antimalarials into grooves on the fastest growing (001) face of a β-haematin crystal, please refer back to Figure 1.39.

The full derivation of the kinetic model discussed below is presented in Appendix 1. In this model, the process of adsorption of the drug onto the growing face of β-haematin was considered reminiscent of the Langmuir isotherm (eq. 5.3) where the extent of monolayer coverage of a solid surface is related to the partitioning of an adsorbant between the gas phase and the adsorbed state as a function of applied pressure.[182]

$$\theta = \frac{K_{ads}[P]}{1+K_{ads}[P]}$$
(5.3)

Here the Langmuir isotherm (eq. 5.3) relates the fraction of occupied binding sites on a solid surface θ to the pressure P of the adsorbing reactant in the gas phase and the equilibrium adsorption constant K_{ads}. The Langmuir isotherm can be used to characterise the adsorption of antimalarial drugs onto the growing face of β-haematin in a similar manner (eq. 5.4):

$$\theta = \frac{K_{ads}[D]}{1+K_{ads}[D]} \tag{5.4}$$

Here the drug concentration, [D], can be thought of in the same way as the pressure of the adsorbing reactant in the gas phase. The number of free sites that are available for continued crystal growth is therefore equal to $1 - \theta$. It is reasonable to propose that any continued growth of β-haematin is then dependent on the number of free sites $(1 - \theta)$, and therefore the growth rate of β-haematin, in the presence of a drug, z_{obs}, (Scheme 2) relative to its growth rate in the absence of drug, z, is proportional to the number of vacant binding sites. The rate constant for the formation of β-haematin in the presence of an inhibition drug, z_{obs}, is given by eq. 5.5; since $\frac{z_{obs}}{z} = 1 - \theta$, then

$$z_{obs} = z(1 - \theta) = \frac{z}{1+K_{ads}[D]} \tag{5.5}$$

In the above equation, z is the rate constant for β-haematin formation in the absence of drug while z_{obs} is the observed rate constant for β-haematin formation in presence of drug. From eq. 5.5, the observed rate constant is predicted to decrease with increasing drug concentration. Although this model is mathematically indistinguishable to that presented in Scheme 1, it is considered to be a more physically-realistic interpretation. It accounts for the observed decrease in the rate constant (Figure 5.11 c) of β-haematin formation with an increase in drug concentration in the experimental results where the kinetics of β-haematin formation in the presence of quinoline antimalarials at the lipid-water interface was studied as well as the fact that β-haematin crystals were able to form in the presence of an inhibitor.

A plot of the inverse of the observed rate constant, z_{obs}, as a function of drug concentration, yields a linear regression from which the values of z and K_{ads} can be determined from the values of the y-intercept and slope, respectively, according to eq.5.6.

$$\frac{1}{z_{abs}} = \frac{1+K_{ads}[D]}{z} = \frac{K_{ads}}{z}[D] + \frac{1}{z} \tag{5.6}$$

To explain the observed decrease in final yield of β-haematin formed at higher drug concentrations, it was necessary to incorporate a competing drug concentration-dependent process that would result in the irreversible precipitation of haematin, most likely as a drug complex (DH$_{(s)}$). The experimental kinetics show that such a process is required to fully account for the observations (Figure 5.11). While the details of this process have not been probed in this work, we found that satisfactory agreement with the experiment was achieved by incorporating the reaction included in Scheme 2. According to this mechanism, the rate of depletion of haematin in solution (H$_{(aq)}$) can be determined by eq. 5.7.

$$\frac{d[H_{(aq)}]}{dt} = -[H_{(aq)}]\left(z_{obs} + k_2[D_{(aq)}]^m\right)$$
(5.7)

In the above equation, k_2 is the rate constant for the irreversible precipitation of haematin brought about by interaction with the drug. $[D_{(aq)}]$ (simplified as $[D]$ in the equations below) and $[H_{aq}]$ are the respective concentrations of drug and haematin in solution and $m \geq 0$. It was found that the best agreement with the experimental results is achieved when m = 2 and this value is assumed for the remainder of the derivation. Assuming [D$_{(aq)}$] to be in large excess compared to haematin ($[D_{(aq)}] \gg [H_{aq}]$), the percentage yield of β-haematin (%β$_{(s)}$), as a function of time, *t*, is shown to depend on the rate of both competing reactions (eq. 5.8):

$$\%[\beta_{(S)}] = \frac{100z_{obs}}{(z_{obs} + k_2[D]^2)}\left(1 - e^{-(z_{obs} + k_2[D]^2)t}\right)$$
(5.8)

Substituting eq. 5.7 into the above relationship yields eq. 5.9:

$$\%[\beta_{(S)}] = \frac{100z}{(z + k_2[D]^2 + k_2 K_{ads}[D]^3)}\left(1 - e^{-\left(\frac{z + k_2[D]^2 + k_2 K_{ads}[D]^3}{1 + K_{ads}[D]}\right)t}\right)$$
(5.9)

To take into account that the lipid (MPG) is not able to convert $[H_{aq}]$ into a yield of 100% β-haematin, an additional term, Y was introduced to account for the fractional yield. It has been shown previously that in the absence of an inhibitor, MPG is capable of mediating β-haematin with approximately 70% efficiency.[74] Therefore, Y represents the fraction of the total theoretical yield that can physically be attained at any given drug concentration. To obtain identical lipid emulsion conditions is very difficult in practice: therefore this value exhibits a considerable degree of random variability. With no drug present in the system,

the value of Y is equal to 0.71 ± 0.03. Therefore during data fitting for all other experiments, Y was allowed to refine freely within three standard deviations of this value (i.e. between 0.62 and 0.8). It should also be noted that as the drug concentration is increased, the value of Y can start to decrease as a result of the irreversible precipitation of Fe(III)PPIX.

The values of K_{ads} and z were obtained from equation 5.6 and the values for [D] were the drug concentration used in each individual experiment. Since the competition reaction, which results in the precipitation of haematin, as something other than β-haematin, is poorly understood, an accurate value of k_2 could not be determined independently. However, since k_2 and Y are correlated, and understanding the limits of the experiment permitted us to select a sensible value for Y, a range of values for k_2 could be determined during the data analyses.

Taking all of the above consideration into account, the overall kinetic model is represented by eq. 5.10.

$$\%\beta_{(S)} = \frac{100Yz}{(z+k_2[D]^2+k_2 K_{ads}[D]^3)}\left\{1 - e^{-\left(\frac{z+k_2[D]^2+k_2 K_{ads}[D]^3}{1+K_{ads}[D]}\right)t}\right\} \tag{5.10}$$

Based on this model, it is possible to predict the kinetics of β-haematin formation in the absence and presence of an inhibiting drug. In order to apply the model, the experimental data was first fitted to a simple first-order equation to determine the values for z_{obs}. As shown in Figure 5.14 (a), the model predicts adherence to exponential behaviour. Furthermore, it is notable that at low drug concentrations, the final yield of β-haematin remains almost constant, however as the dose is increased further, the final yield begins to decrease. According to the adsorption model based on the Langmuir isotherm (eq. 5.6 above), a plot of the inverse of the observed rate constant as a function of drug concentration is predicted to be linear at low drug concentration (Figure 5.14 (b)). Linear regression in this region allows the adsorption equilibrium constant, K_{ads}, as well as the rate constant in the absence of an inhibitor, z, to be determined.
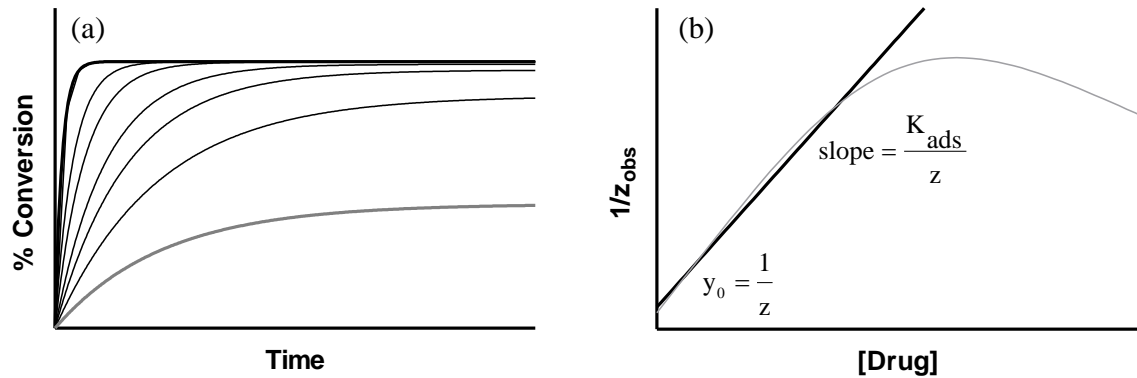
Figure 5.14 (a) The kinetics of β-haematin formation predicted by the model (eq. 5.10) in the absence and presence of an inhibiting drug. Drug concentrations range from 0 (black trace) through increasing doses to a relatively high final value (grey curve). (b) The plot of the inverse of the predicted behaviour of the observed rate constant z_{obs} as a function of drug concentration (grey line). Linear regression at relatively low concentration allows the values of the rate constant in the absence of drug (z) and the adsorption equilibruim constant (K_{ads}) to be determined from the values of the y-intercept and slope, as per eq.5.6.

It is also possible to predict the dose-response behaviour from the kinetic profiles by examining expected yields at various time points, as a function of drug concentration (Figure 5.15).
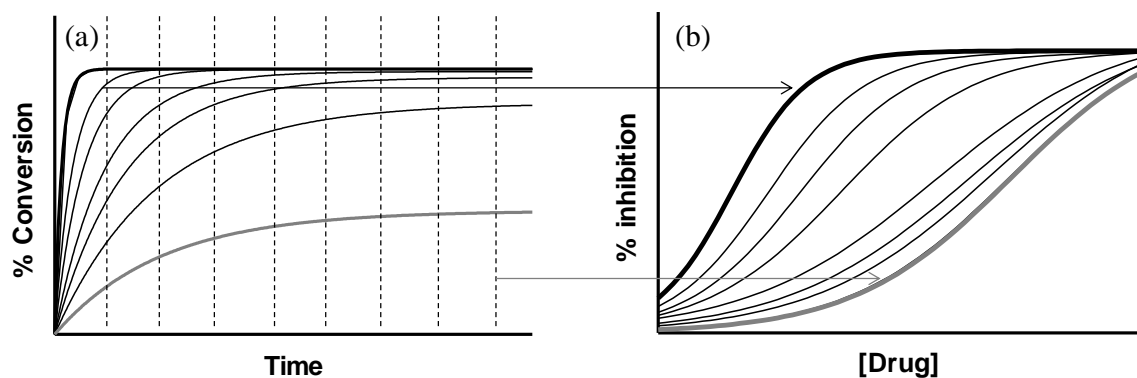
Figure 5.15 The kinetics of β-haematin formation predicted by the model (eq. 5.10). (a) Taking slices through the kinetic profiles at various time points (dashed lines), the dose-response behaviour can be predicted. (b) The best-fit of the numerical output generated at different times from (a). At short incubations times, dose-response curves tend towards a hyperbola, compared to sigmoidal dose-response curves observed at longer incubation times. It is shown that the curves eventually converge on a single IC_{50} value (grey line).

168

As shown above, the model gives rise to a sigmoidal dose-response curve, although this is more evident at longer incubation times. At shorter incubation times, on the other hand, the dose-response profile tends toward a hyperbolic function. According to this model, reproducing IC_{50} values from the dose-response behaviour (Figure 5.16) demonstrates that the IC_{50} value is dependent on incubation time at short times. At long incubation time however, the individual dose-response curves are predicted to converge with very little change in the expected IC_{50} value with further increase in incubation time, leading to a hyperbolic dependence of IC_{50} on time (Figure 5.16 (b)). This dependence of IC_{50} value on time would not occur in the absence of the drug-induced irreversible precipitation of haematin. Rather a linear relationship would be expected, since over longer periods of time, more and more drug would be required to inhibit β-haematin formation.
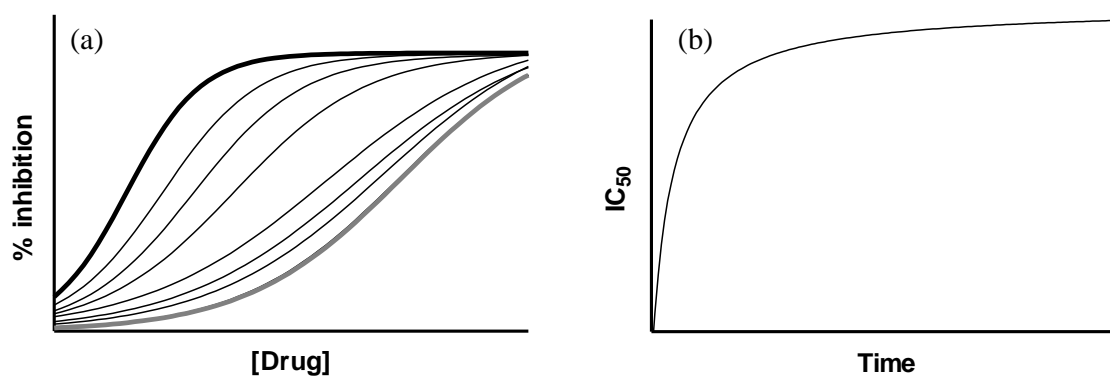
Figure 5.16 The dependence of IC_{50} value on incubation time. (a) The hyperbolic and sigmoidal dose-response curves produced from the numerical output generated at different times from the theoretical model (eq. 5.10). (b) Based on the theoretical outputs in (a), the corresponding IC_{50} values from the dose-response curves could be predicted. The data conform to a hyperbolic function as indicated, showing that at shorter incubation times, the effect on the IC_{50} values is more pronounced with there being little further increase at longer incubation times.

5.3.3   Observed Kinetics of β-Haematin Formation in the Presence of Antimalarial Quinolines

The observed kinetics of β-haematin formation in the presence of CQ shown above (Figure 5.11), are consistent with the theoretical behaviour predicted above; at low drug concentrations, the rate of β-haematin formation is decreasing with an increase in drug concentration. When the drug concentration is sufficiently high, a decrease in the final yield of β-haematin is observed. In the following section, the effects of CQ, AQ, QN and

QD on the kinetics of β-haematin formation are reported. Initially the kinetic data were fitted to a simple exponential equation in order to determine the observed rate constants (z_{obs}).

5.3.3.1 Kinetics of β-Haematin Formation in the Presence of CQ

In order to generate a plot of the inverse of z_{obs} as a function of increasing drug concentration (Figure 5.17 (a)), it was first necessary to fit the raw data to a simple exponential kinetic equation in order to determine the observed rate constants. Following the prediction of the proposed model based on the Langmuir isotherm, the inverse of z_{obs} versus drug concentration yields a linear correlation up to a concentration of 0.03×10^{-3} M. From the linear regression, the intercept and slope values were determined, which allowed the values for the observed rate constant of β-haematin formation in absence of CQ, z, and the adsorption equilibrium constant, K_{ads}, to be calculated according to eq. 5.6. These values are given in Table 5.3. The kinetic data were subsequently fitted to eq. 5.10, where the best fit value for the rate constant for the formation of $DH_{(s)}$, k_2, was found to be in the range between 0.3 and 0.6. Consequently, k_2 was set to a value of 0.45 in order to generate the best fit of the experimental kinetic data shown in Figure 5.17 (b). The r^2 values range between 0.74 and 0.96, indicating good agreement between the proposed kinetic model and the experimental results. There seems to be an increase in data scatter when the drug concentration increases. Therefore at a concentration of 0.1×10^{-3} M, the scatter is possibly due to drug interaction with lipid and the r^2 value is only 0.45.

Table 5.3 Best fit values to the kinetic model for β-haematin formation in the presence of CQ

Intercept (min)	**Slope** (min M^{-1})	z (min^{-1})	K_{ads} (M^{-1})	**Log K_{ads}**	k_2
5.15 ± 0.51	$(1.829 \pm 30) \times 10^3$	0.19 ± 0.02	$(3.55 \pm 0.06) \times 10^5$	5.55 ± 0.03	0.45

Shown in Figure 5.17 (c) is a dose-response curve extracted from the kinetic data at 30 min. It is very difficult to extract dose-response profiles from the kinetic data due to fairly large scatter in the experimental data and non-identical incubation times chosen for different CQ concentrations. However, the data at 30 min show a reasonable fit to a sigmoidal function. The observed IC$_{50}$ value ($0.019 \pm 0.005 \times 10^{-3}$ M) from the kinetic data are within one standard deviation of the value determined in the independent dose-response experiment ($0.016 \pm 0.001 \times 10^{-3}$ M). The dependency of the IC$_{50}$ value on

incubation time was also investigated. It is noted that at short incubation times there is a steep increase in the IC_{50} value, however it eventually converges on a value of ~0.045 × 10^{-3} M when the incubation time exceeds 500 min. The IC_{50} values can be fitted to a simple hyperbola (Figure 5.17 (d)) in accordance with the predicted theoretical model.
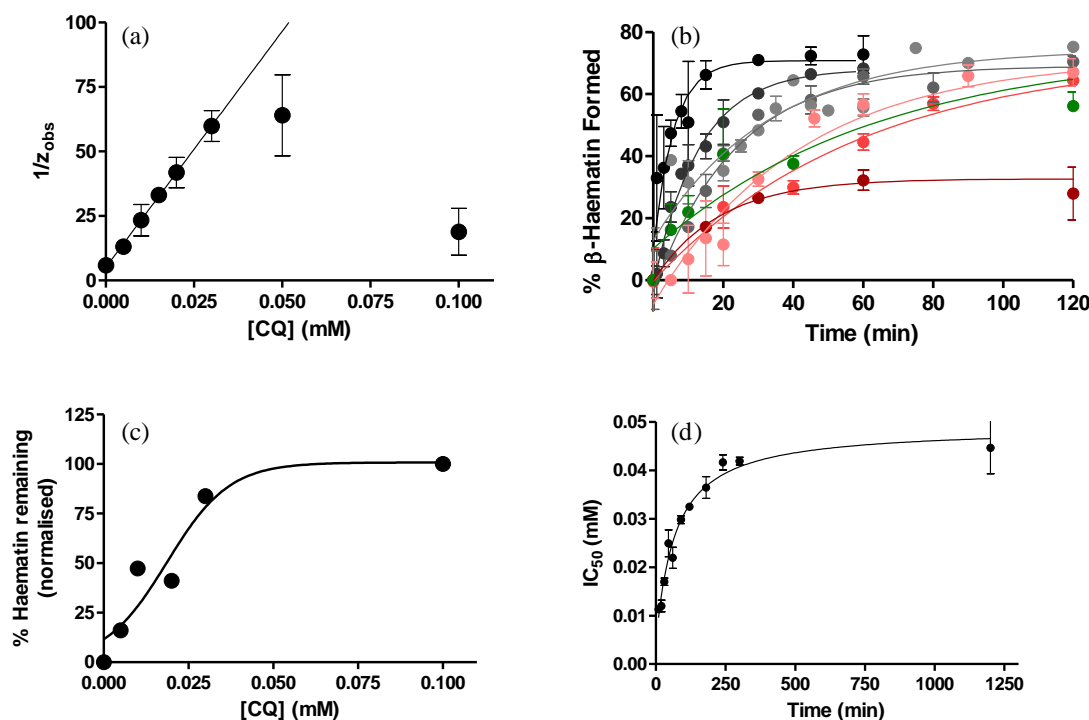
Figure 5.17 Kinetics of β-haematin formation in the presence of CQ. (a) As the kinetic model (eq. 5.10) predicts, the plot of the inverse of the rate constant z_{obs} as a function of drug concentration yields a linear correlation up to a concentration of 0.03 mM. The intercept value 5.15 ± 0.51 min and slope value of 1829 ± 30 × 10^{3} min M^{-1} were determined from the linear regression. Therefore, the values of z and K_{ads} were calculated to be 0.19 ± 0.02 min^{-1} and 3.55 ± 0.06 × 10^{5} M^{-1}, respectively. (b) Best fit of the experimental kinetic behaviour to the theoretical model (eq. 5.10), in the absence (black circle) and presence of 0.005 (●), 0.01 (●), 0.015 (●), 0.02 (●), 0.03 (●), 0.05 (●) and 0.1 (●) mM CQ. (c) A slice through the kinetic at an incubation time of 30 min generates a dose-response profile; the data have been fitted to a sigmoidal function (r^{2} = 0.90). (d) The IC_{50} values for the inhibition of β-haematin formation as a function of incubation time conform to a hyperbolic function. Error bars were taken as standard error of measurement (SEM).

5.3.3.2   Kinetics of β-Haematin Formation in the Presence of QD

The quinoline methanol antimalarials were also investigated. The kinetics of β-haematin formation in the presence of QD also follow the predicted behaviour. A plot of the inverse of the observed rate constant as a function of increasing drug concentration is in accordance with the model, and linear regression is possible up to a value of ~0.05×10^{-3} M (Figure 5.18 (a)). From the linear regression line, the intercept and slope values were determined as before. This allowed the values of the observed rate constant of β-haematin formation in the absence of QD, z, and the adsorption equilibrium constant, K_{ads}, to be determined according to eq. 5.6. These values are reported in Table 5.4.

Table 5.4 Best fit values to the kinetic model for β-haematin formation in the presence of QD.

Intercept (min)	**Slope** (min M^{-1})	z (min^{-1})	K_{ads} (M^{-1})	**Log** K_{ads}	k_2
5.92 ± 0.12	$(492 \pm 4) \times 10^3$	0.17 ± 0.01	$(8.36 \pm 0.06) \times 10^4$	4.92 ± 0.01	0.55

Fitting the kinetic data to the model, the value for k_2 was found in the range between 0.2 and 0.9. Therefore, a midrange value of 0.55 was used for the best fit of the experimental kinetics (Figure 5.18 (b)). A slice through the kinetics data at an incubation time of 30 min yields a dose-response curve, Figure 5.18 (c), which could be fitted to a sigmoidal function ($r^2 = 0.97$). The dependence of IC$_{50}$ values on incubation time is also shown (Figure 5.18 (d)), increasing markedly over relatively short periods of time and eventually converging on a value of approximately 0.15×10^{-3} M at incubation times greater than about 300 min.
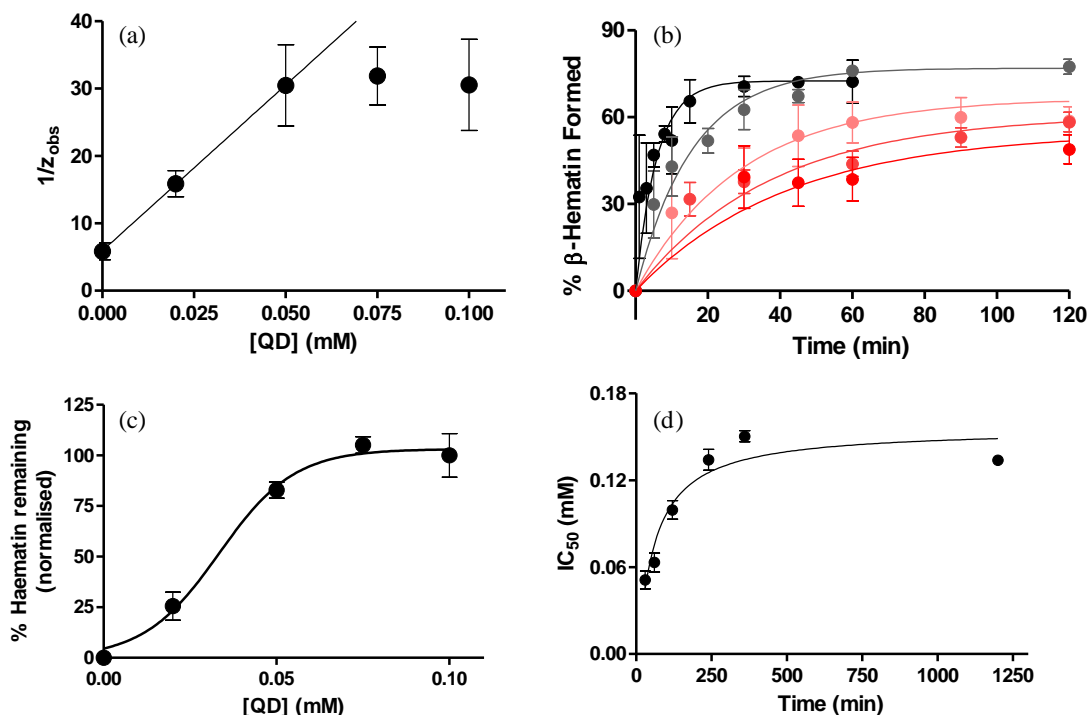
Figure 5.18 Kinetics of β-haematin formation in the presence of QD. (a) As the kinetic model (eq. 5.10) predicts, the plot of the inverse of the rate constant z_{obs} as a function of drug concentration yields a linear correlation up to a concentration of 0.05 mM. The intercept value 5.92 ± 0.12 min and slope value of $492 \pm 4 \times 10^3$ min M^{-1} were determined from the linear regression. Therefore, the values of z and K_{ads} were calculated to be 0.17 ± 0.01 min^{-1} and $8.36 \pm 0.06 \times 10^4$ M^{-1}, respectively. (b) Best fit of the experimental kinetic behaviour to the theoretical model (eq. 5.10), in the absence (black circle) and presence of 0.02 (●), 0.05 (●), 0.075 (●) and 0.100 (●) mM QD. (c) A slice through the kinetic at an incubation time of 30 min generates a dose-response profile; the data have been fitted to a sigmoidal function ($r^2 = 0.99$). (d) The IC$_{50}$ value for the inhibition of β-haematin formation as a function of incubation time by QD also conforms to a hyperbolic function. Error bars were taken as SEM.

5.3.3.3   Kinetics of β-Haematin Formation in the Presence of AQ

The kinetics of β-haematin formation in the presence of AQ were also investigated, and the results conform to the predicted kinetic behaviour. As shown previously for CQ and QD, a plot of the inverse of the observed rate constant as a function of increasing drug concentration agrees with the model, and can be linearised up to a value of $\sim 0.005 \times 10^{-3}$ M (Figure 5.19 (a)). From the linear regression, the intercept and slope values were determined, which subsequently allowed the values for the observed rate constant of β-

haematin formation in absence of AQ, z, and the adsorption equilibrium constant, K_{ads}, to be determined from eq. 5.6. The values are reported in Table 5.5. The value for k_2 was found to vary between 0.2 and 0.9. Therefore, a midrange value of 0.55 was used in the best fit of the experimental data (Figure 5.19 (b)).

Table 5.5 Best fit values to the kinetic model for β-haematin formation in the presence of AQ.

Intercept (min)	**Slope** (min M^{-1})	z (min^{-1})	K_{ads} (M^{-1})	**Log K_{ads}**	k_2
10.8 ± 3.8	$(5399 \pm 1268) \times 10^3$	0.09 ± 0.03	$(4.99 \pm 1.79) \times 10^5$	5.7 ± 0.4	0.55
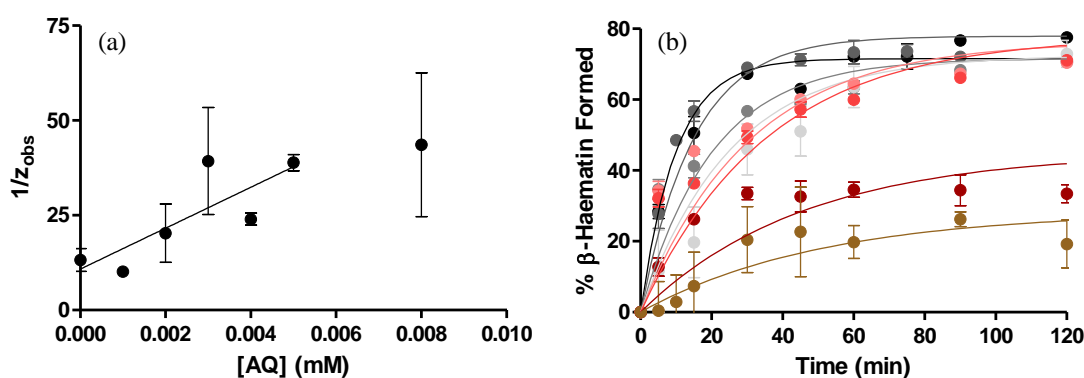
Figure 5.19 Kinetics of β-haematin formation in the presence of AQ. (a) As the kinetic model (eq. 5.10) predicts, the plot of the inverse of the rate constant z_{obs} as a function of drug concentration yields a linear correlation up to a concentration of 0.005 mM. The intercept value 10.8 ± 3.8 min and slope value of 5399 ± 1268 min M^{-1} were determined from the linear regression, from which the values of z and K_{ads} were calculated to be 0.09 ± 0.03 min^{-1} and $4.99 \pm 1.79 \times 10^5$ M^{-1}, respectively. (b) Best fit of the experimental data to the theoretical model (eq. 5.10), in the absence (black circle) and presence of 0.001 (●), 0.002 (●), 0.003 (○), 0.004 (●), 0.005 (●), 0.007 (●) and 0.008 (●) mM AQ. Error bars were taken as SEM.

5.3.3.4   Kinetics of β-Haematin Formation in the Presence of QN

Suspecting that the effect of QN may be similar to that of QD, the kinetics of β-haematin formation were followed in the presence of QN. The resultant kinetic data confirms this, as they are shown to follow the predicted behaviour. The plot of the inverse of the observed rate constant as a function of increasing drug concentration is consistent with the model, and is linear at concentrations less than 0.05×10^{-3} M (Figure 5.20 (a)). From the linear regression analysis, the intercept and the slope values were determined, which allowed the

values for the observed rate constant for β-haematin formation in the absence of QN, z, and the adsorption equilibrium constant, K_{ads}, to be calculated out according to eq. 5.6. These values are reported in Table 5.6. The value for k_2 was found to vary between 0.1 and 0.12, and a midrange value of 0.6 was therefore used in fitting the experimental data to the kinetic model (Figure 5.20 (b)).

Table 5.6 Best fit values to the kinetic model for β-haematin formation in the presence of QN.

| **Intercept** (min)	**Slope** (min M^{-1})	z (min^{-1})	K_{ads} (M^{-1})	**Log K_{ads}**	k_2
8.24 ± 4.27	$(857 \pm 118) \times 10^3$	0.12 ± 0.06	$(1.04 \pm 0.14) \times 10^5$	5.02 ± 0.14	0.6
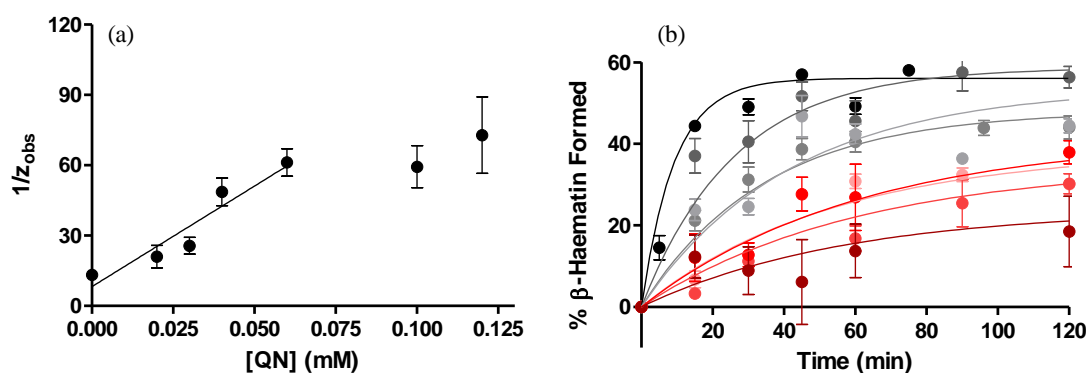
Figure 5.20 Kinetics of β-haematin formation in the presence of QN. (a) As the kinetic model (eq. 5.10) predicts, the plot of the inverse of the rate constant z_{obs} as a function of drug concentration yields a linear correlation up to a concentration of 0.075 mM. The intercept value 8.24 ± 4.27 min and slope value of $857 \pm 118 \times 10^3$ min M^{-1} were determined from the linear regression. Therefore, the values of z and K_{ads} were calculated to be 0.12 ± 0.06 min^{-1} and $1.04 \pm 0.14 \times 10^5$ M^{-1}, respectively. (b) Best fit of the experimental data to the theoretical model (eq. 5.10), in the absence (black circle) and presence of 0.02 (●), 0.03 (●), 0.04 (○), 0.06 (●), 0.08 (●), 0.1 (●), and 0.12(●) mM QN. Error bars were taken as SEM.

5.3.3.5   Validation of the Theoretical Kinetic Model

In order to assess whether the hypotheses underpinning the theoretical model could be related to the biological mechanism of the quinoline compounds investigated above, the K_{ads} values determined for each compound were compared against the IC$_{50}$ values for the biological activity previously determined against *P. falciparum* (chloroquine-sensitive 3D7

strain).[94] The correlation below indeed shows a significant agreement between the biological data and the experimental adsoption constants (Figure 5.21).
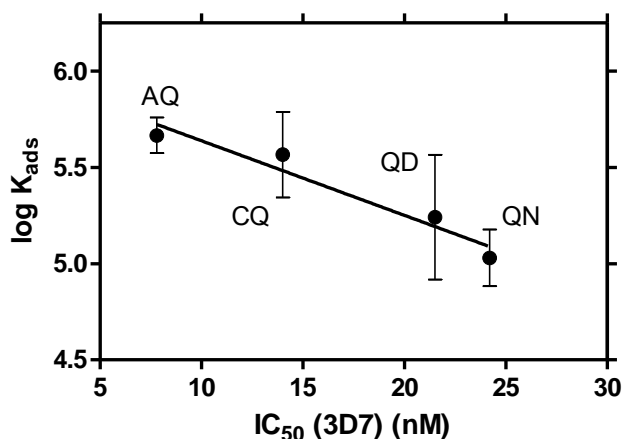
Figure 5.21 Linear correlation ($R^2 = 0.69$) between the observed equilibrium adsorption constant (log K_{ads}) and the IC_{50} for biological activity of 4-aminoquinoline (CQ and AQ) and quinoline methanol (QD and QN) compounds against *P. falciparum* (chloroquine-sensitive 3D7 strain).

5.3.4   Direct Adsorption of CQ and QD to β-Haematin Crystals

In order to investigate the adsorption of quinoline antimalarials onto the crystal surface of β-haematin directly, good quality crystals were required. The pentanol-water interface system was used since crystals grown from this environment have been shown to be of a better quality, due to the fact that traces of pentanol can be removed if they are washed thoroughly. Crystals formed in the presence of lipid often remain coated by the lipid despite extensive washing with acetone solution. β-Haematin formation was brought about by incubating a Fe(III)PPIX solution for 30 min at the pentanol-water interface. Following incubation, the pellet was recovered by centrifugation and washed with 5% (*v/v*) pyridine solution to dissolve unreacted Fe(III)PPIX. The formation of β-haematin was confirmed using both ATR-IR spectroscopy and PXRD (Figure 5.22).
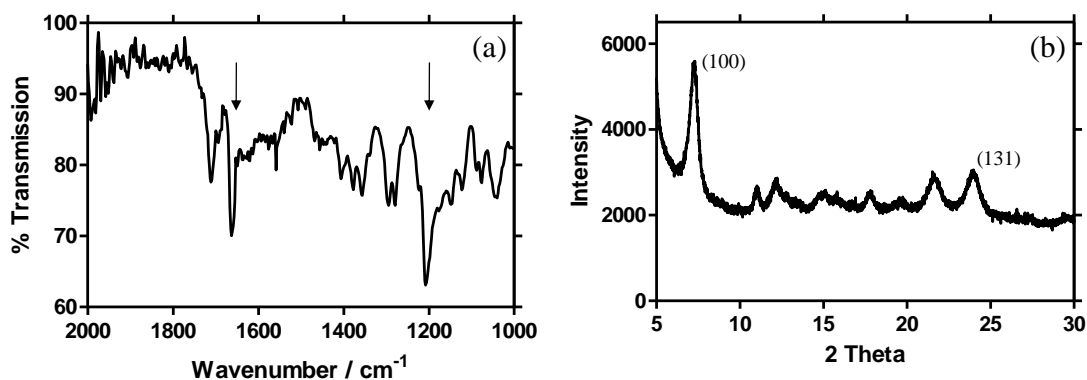
Figure 5.22 Characterisation of β-haematin recovered from the pentanol-water interface. (a) ATR-IR spectrum of β-haematin recovered from the pentanol-water interface. Characteristic peaks at 1211 and 1664 cm⁻¹ in the spectrum of β-haematin, confirming the formation of the μ-propionato coordination dimer, are indicated with arrows.[30] (b) PXRD pattern of β-haematin recovered from the pentanol-water interface. The (100) and (131) reflections are denoted.

The amount of a drug that is proposed to adsorb to the crystal was calculated using the Beer's law plots shown in Figure 5.23. By measuring the absorbance of the supernatant at 344 and 236 nm for CQ and QD respectively, and comparing to the initial absorbance reading of a drug solution of particular concentration, the extent of depletion was considered a measure of the adsorption of the drug to the β-haematin crystals. Studies were carried out in the presence of different drug concentrations, with each determination per drug concentration performed at least three times.
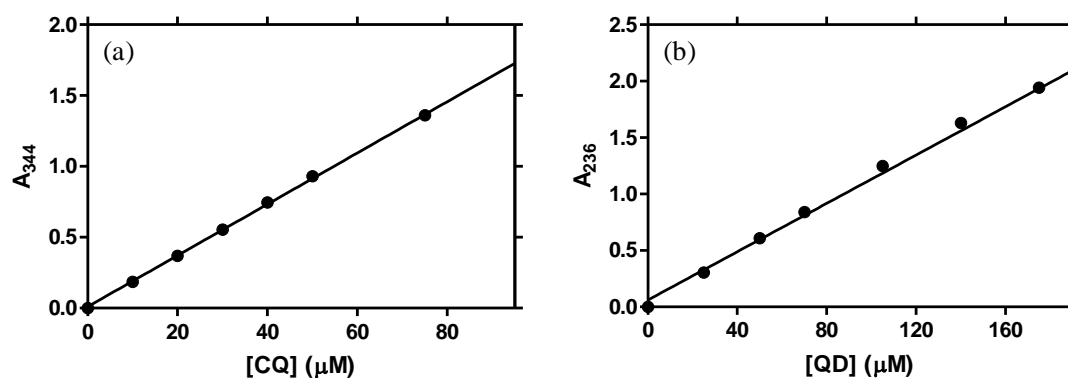
Figure 5.23 Beer's law plot of the maximum absorbance band of (a) CQ (measured at 344 nm) and (b) QD (measured at 236 nm) in citrate buffer (50 mM, pH 4.8). Corresponding r^2 values are 0.99 for both. Measurements were repeated three times. Error bars were taken as SEM.

177

A control study in which no β-haematin crystals were introduced into the CQ and QD solutions did not show any kind of decrease in the absorbance readings compared to their initial values. Thus the observed decrease in absorbance recorded in the presence of β-haematin crystals was attributed to some form of interaction between the drugs and the β-haematin crystals. The most likely interaction is considered to be adsorption. However, it could not be determined from these simple observations to which face, or more likely faces, the compounds were adsorbed to.
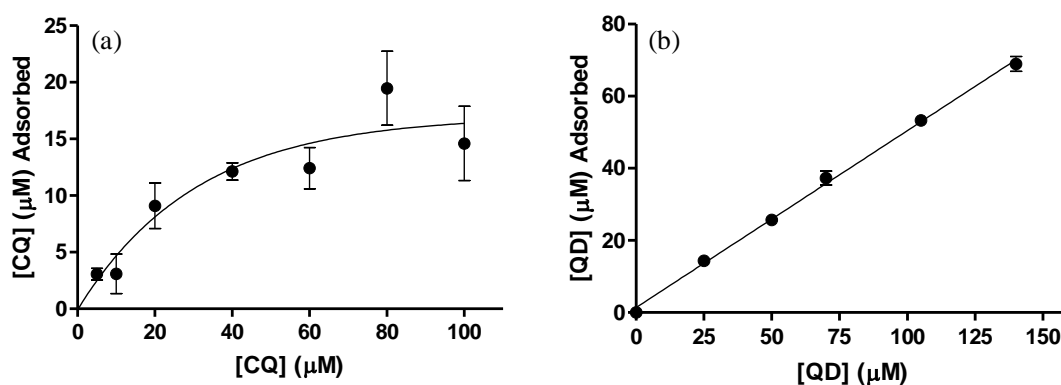
Figure 5.24 Extent of adsorption of (a) CQ and (b) QD by β-haematin. The crystals were placed in buffered aqueous solutions of the drugs for 3 days. The amount of drug adsorbed by the crystals was calculated from the Beer's law plots. Error bars were taken as SEM.

The difference in the adsorption profiles, QD being linear compared to CQ showing saturation, could be due to the fact that higher QD concentrations were too high to obtain meaningful UV readings.

5.4   Discussion

The discovery of haemozoin in association with neutral lipid bodies *in vivo* has revolutionised the way in which we think about the process of haemozoin formation and therefore inhibition. To date however, the mechanism of haemozoin formation has still not been fully explained and, in turn, neither has the mechanism of its inhibition by antimalarial drugs. The development of the lipid-water interface model has allowed the relevance of lipids in the formation of β-haematin (haemozoin) to be investigated *in vitro*.[74] As the focus of the current study was on the interaction between quinoline antimalarial drugs and ferrihaem which lead to the inhibition of β-haematin formation, the lipid-water interface system was used to probe drug activity under conditions which mimic the biological environment where haemozoin is now thought to take place. Aqueous-soluble antimalarial drugs were included into the aqueous buffer in order to investigate their inhibitory activities on the formation of β-haematin. The IC_{50} data obtained in the present study show a strong correlation with previously-determined biological activities for two CQS strains of the *P. falciparum*.[134] This indicates that the lipid-water interface provides a valid system in which to investigate drug activity.

It has previously been shown that quinoline antimalarials decrease the rate at which β-haematin formation occurs.[71,137] As evident from the time study on the formation of β-haematin, the results support the findings of Egan *et al*.[71], who showed that although quinoline drugs inhibit β-haematin formation when relatively short incubation times are used, β-haematin eventually forms after longer incubation times in 4.5 M acetate (pH 4.5, 60 ^{o}C). Chong and Sullivan[137] had made similar observations, recognising too that β-haematin formation eventually occurs in the presence of CQ and QD. Indeed the results presented in this chapter show that there is a correlation between incubation time and IC_{50} value; however, the relationship is not linear for either CQ or QD (Figure 5.17 (d) and Figure 5.18 (d) respectively). Shorter incubation times appear to have a more pronounced effect on the IC_{50} value while at longer incubation times little further change is observed. This growing body of evidence indicates that IC_{50} values for the inhibition of β-haematin by quinoline antimalarial drugs depend greatly on the incubation time. This must therefore be taken into consideration when investigating β-haematin inhibitors.

In the present study, the kinetic effects of quinoline antimalarial drugs on the formation of β-haematin show that, at low concentration of both 4-aminoquinoline (CQ and AQ) and quinoline methanol (QD and QN) compounds, there is a decrease in the rate at which β-haematin is formed under biomimetic (lipid-water interface) conditions. However, as drug concentrations were increased, a decrease in the final yield of β-haematin was observed. To explain the decrease in yield of β-haematin formed at higher drug concentrations, a competing process to the formation of β-haematin - the irreversible precipitation of Fe(III)PPIX, probably as its drug complex - was postulated. These drugs are thought to associate with free Fe(III)PPIX in solution by forming complexes, either through π-stacking or coordination,[85] and preventing its incorporation into β-haematin.[116,117,118] In the case of the quinoline methanol antimalarial drugs, the decrease in yield of β-haematin at higher drug concentrations may indeed be a direct consequence of complex formation. This would be consistent with the results presented in chapter 4, where direct coordination and intramolecular interactions were observed in the crystal structures of QN-Fe(III)PPIX and QD-Fe(III)PPIX. One shortcoming of the lipid-water interface methodology used in this study is the fact that it is not suitable for drug compounds insoluble in aqueous medium, therefore this system needs to be developed further in order for it to be of wider applicability.

It has previously been shown that the kinetics of β-haematin formation in a lipid-water emulsion conform to an apparent first-order process.[73,74] In the present study, a model was developed to explain the observations in yield of β-haematin with time in the presence of antimalarial drugs, as well as to explain the shape of the kinetics in the presence of the lipid-water interface. It was based on the Avrami model,[69,70] together with the Langmuir isotherm.[182,183] The best-fit to the experimental data was achieved by considering the process to be second order with respect to drug. However, this does not necessarily imply that the drug-F(III)PPIX complex would have a 2:1 stoichiometry. The nature of the quinoline-Fe(III)PPIX complexes formed in the lipid-water emulsions was not investigated in any detail, since it is reasonable to propose that the kinetic effect of the drugs, both at lower concentrations and shorter incubation times, is of greater biological relevance. To model the decreasing rates of β-haematin formation in the presence of low drug concentrations, the premises of the Langmuir isotherm were applied. The model proposes non-covalent adsorption of drug molecules to the fastest growing face of the β-haematin crystal (Scheme 2).

As the model predicts, the dose-response behaviour from the kinetic profiles gives rise to a sigmoidal dose-response curve at longer incubation times while, at shorter incubation times the dose-response profile tends toward a hyperbolic function. Interestingly, both dose-response profiles are observed in the experimental inhibition profiles for IC_{50} determination at 30 minutes incubation time; AQ and CQ appear to induce a sigmoidal dose-response, while QD and QN data conform to a simple hyperbola. Initially it was thought that this indicated a difference in mechanism, however it is now appreciated that the chosen incubation time for the IC_{50} study (30 min) may simply be a too short time for QD inhibition process, while sufficient time for CQ action.

CQ's adsorption equilibrium constant, K_{ads}, predicted by the model and the experimental conditions, is approximately 4 times greater than that of QD. The difference in the adsorption equilibrium constant for the 4-aminoquinoline and quinoline methanol drugs may be accounted for by considering the theoretical model of antimalarials being able to bind to the (001) face of β-haematin put forward by Leisorwitz *et al*.[40] They showed that antimalarial drugs such as the 4-aminoquinoline and quinoline methanol can adsorb onto the {001} surface of the β-haematin crystal *via* an (porphyrin)acid-(quinoline)amine salt bridge. They predicted that the side chain of CQ, being longer than that of either QN or QD, is able to interact more favourably with the free propionic acid groups at the surface of β-haematin resulting in a stronger interaction and offer an explanation for the observed results in the current work.

An interesting observation when comparing the value of the adsorption constant for CQ with the surface of β-haematin, log K_{ads} (5.55 $\pm$ 0.03), with the association constant of CQ with free Fe(III)PPIX in 40% (*v/v*) aqueous DMSO, log K (5.52 $\pm$ 0.03),[91] is these values are very close to one another. Therefore association constants can be linked to the drugs ability to adsorp onto the crystal surface of β-haematin for active compounds.

UV absorption spectra of CQ and QD, in the presence of β-haematin crystals, indicates some form of interaction, which is proposed to be adsorption of drugs onto β-haematin crystals. This form of inhibition by antimalarial drug was previously proposed by Buller *et al*. [40] Making use of the theoretical growth form of β-haematin, they suggested that the quinoline antimalarials are able to dock into grooves (binding sites) on the fastest growing face of the crystal as a result of being stabilised by interaction with surrounding functional groups. This proposed mechanism of inhibition of β-haematin formation by antimalarial

drugs is supported by the kinetic model developed in this study. However, other mechanisms of inhibition cannot be excluded and further studies are still needed to clarify these results.

5.5   Conclusion

The lipid-water emulsion provides a biologically-relevant medium to investigate the β-haematin inhibitory activity of antimalarial drugs. Based on the results reported in this chapter, both 4-aminoquinoline and quinoline methanol antimalarial drugs decrease the rate of β-haematin formation at low concentration and induce irreversible precipitation of Fe(III)PPIX at higher doses. A kinetic model was developed to account for the kinetic results, and it lends support to a mechanism of action where antimalarial drugs adsorb to the growing face of β-haematin. However, since kinetics alone cannot account for the mechanism of a chemical process, and the drug adsorption to β-haematin crystals as monitored using UV-vis spectroscopy cannot determine which face, or more likely faces, the drugs were adsorbed to, further studies are required to support these findings. Overall however, the kinetic data provides a basis for furthering our understanding of β-haematin inhibition processes under biomimetic conditions, which may in turn inform the rational design of novel antimalarial haemozoin inhibitors.

6   Single Crystal Diffraction of β-Haematin DMSO Solvate and Haemin

6.1   Introduction

Rational design of new drug candidates requires an in-depth understanding of the drug target, and in the case of quinoline antimalarials, it is widely accepted that this is haemozoin. While the structure of haemozoin and its synthetic counterpart β-haematin is known from powder X-ray diffraction,[35] the limitation of the technique have motivated ongoing efforts for a more definitive structure. Furthermore, the nature of the Fe(III)PPIX species with which antimalarial drugs interact to inhibit formation of haemozoin is not well understood. It is therefore essential to investigate the mechanism of the crystallisation process. More definitive knowledge of the crystal structure of haemozoin and its growth mechanism is likely to provide insight into the inhibition mechanisms of current quinoline antimalarials.

In this section, the first single crystal X-ray diffraction (SCD) structure of β-haematin as a DMSO solvate is reported. This structure provides the most accurate structural interpretation to date of a Fe(III)PPIX model of haemozoin. Additionally, extended X-ray absorption fine structure (EXAFS) spectroscopy was used to probe whether the structure determined in the solid state is also observed in solution. The nature of Fe(III)PPIX in solution must also be considered as it has important implications for understanding the nucleation and formation of β-haematin. In this work Fe(III)PPIX is proposed to exist in solution as a π-π dimer prior to β-haematin DMSO solvate crystallisation. The SCD structure of haemin, crystals of which were grown in the presence of the antimalarial drug AQ, shows Fe(III)PPIX as a π-π dimer. This structure was used to generate a model to which EXAFS data of the species in solution prior to nucleation of the β-haematin DMSO solvate was fitted. In addition, the structure refinement offers improvements compared to the previously-reported haemin structure.[79] Together, the structures presented in this chapter provide a basis for understanding and rationalising the nucleation and formation of haemozoin, the proposed target of quinoline antimalarial drugs.

6.2   Experimental Methods

This section describes the methods used to grow the single crystals of Fe(III)PPIX species (β-haematin DMSO solvate and haemin) as well as methods used to fully characterise their structures. The materials used have been listed in Table 3.1.

6.2.1   X-Ray Crystallography

The Crystallographic Information Files (CIF) along with the final SHELX ".res" and ".hkl" files for all crystal structures presented in this chapter can be found on the attached CD.

6.2.1.1   The Crystal Structure of β-Haematin DMSO Solvate: Crystallisation from Chloroquine Free Base

6.2.1.1.1   *Crystallisation Preparation*

A 0.76 mM stock solution of Fe(III)PPIX was prepared by dissolving Fe(III)PPIX (5.0 mg, 7.6 μmol) in 10.0 mL DMSO. A 1.56 mM stock solution of CQ free base (CQfb) was prepared by dissolving CQ 5.0 mg (15.6 μmol) in 10.0 mL DMSO. The crystallisation medium was prepared by adding 1.0 mL of Fe(III)PPIX stock solution to 1.0 mL of the CQfb stock solution in a small 5 mL glass vial. Hence the solution contained approximately 2 mol equiv of CQfb relative to Fe(III)PPIX. The mixture was stirred at 100 $^{\circ}$C for 30 min before it was allowed to stand in a water bath at 37 $^{\circ}$C for 24 hours. The solution was then filtered through a PTFE filter disc (0.45 *μm* pore size) into a clean vial which was covered with parafilm and left to stand at room temperature. The parafilm was punctured with one needle-sized hole to allow slow evaporation of solvent. Small rod-shaped crystals were observed on the bottom of the vial after two days. A single crystal of dimensions 0.15 × 0.05 × 0.01 mm was selected for X-ray diffraction.

6.2.1.1.2   *Structure Solution and Refinement*

All non-hydrogen atoms were refined with anisotropic temperature factors apart from some of the atoms of the disordered DMSO solvent molecule. The hydrogen atom located on the propionic acid group was located in the difference map and refined independently with a

simple bond length constraint. There is disorder displayed on the porphyrin pyrrole rings by the vinyl and methyl substituents. Each of the vinyl groups is disordered over two positions with site occupancy factors (s.o.f's) of 0.66 and 0.34. One of the DMSO solvent molecules is also disordered over two positions with s.o.f.'s of 0.92 and 0.08. The oxygen and carbon atoms of the minor component of the disorder were modelled isotropically and hydrogen atoms were not placed on the carbon atoms.

6.2.1.2   The Crystal Structure of β-Haematin DMSO Solvate: Crystallisation from Amodiaquine Free Base

6.2.1.2.1   *Crystallisation Preparation*

A 3.8 mM stock solution of Fe(III)PPIX was prepared by dissolving Fe(III)PPIX (5.0 mg, 7.6 μmol) in 2.0 mL DMSO. A 2.5 mM stock solution of AQ free base (AQfb) was prepared by dissolving 1.8 mg (5.06 μmol) in 2.0 mL DMSO. The crystallisation medium was prepared by adding 1.0 mL of Fe(III)PPIX stock solution to 1.0 mL of the AQ stock solution in a small 5 mL glass vial. Hence the solution contained approximately 0.6 mol equiv of AQfb relative to Fe(III)PPIX. The mixture was stirred at 100 $^{\circ}$C for 30 min and then covered with parafilm and left to stand at room temperature. The parafilm was punctured with one needle-sized hole to allow slow evaporation of solvent. Small rod-shaped crystals were observed on the bottom of the vial after one day. A single crystal of dimensions $0.28 \times 0.10 \times 0.03$ mm was selected for X-ray diffraction.

The free base form of AQ was prepared from an aqueous solution of the salt, using concentrated NaOH in order to yield a precipitate of the neutral species. The free base form of AQ was recovered by drying the precipitate in the presence of phosphorus pentoxide for 3 to 7 days.

6.2.1.2.2   *Structure Solution and Refinement*

All non-hydrogen atoms were refined with anisotropic temperature factors. The hydrogen atom located on the propionic acid group was located in the difference map and refined independently with a simple bond length constraint. There is disorder displayed on the porphyrin pyrrole rings by the vinyl and methyl substituents. Each of the vinyl groups is disordered over two positions with s.o.f's of 0.66 and 0.34, respectively. The S atom of one

of the DMSO solvent molecules is also disordered over two positions with s.o.f.'s of 0.93 and 0.07, respectively.

6.2.1.3   The Crystal Structure of Haemin

6.2.1.3.1   *Crystallisation Preparation*

A solution containing 0.806 mM AQ (salt form) and 1.59 mM haemin was prepared in 4.0 mL acetonitrile and 0.8 mL MeOH by dissolving AQ (1.8 mg, 3.87 μmol) and haemin (5.0 mg, 7.66 mmol). After stirring the solution for 30 minutes at 50 $^{\circ}$C, it was filtered through a PTFE filter disc (0.45 μm pore size) into a clean glass vial which was covered with parafilm and left to stand at room temperature. The parafilm was punctured with one needle-sized hole to allow slow evaporation of solvent. Small triangular-shaped crystals were observed on the bottom of the vial after two weeks. A single crystal of dimensions $0.02 \times 0.04 \times 0.125$ mm was selected for X-ray diffraction.

6.2.1.3.2   *Structure Solution and Refinement*

All non-hydrogen atoms were refined with anisotropic temperature factors. The hydrogen atom located on the propionic acid group was located in the difference map and refined independently with a simple bond length constraint. There is disorder displayed on the porphyrin pyrrole rings by the vinyl and methyl substituents. The vinyl group is disordered over two positions with s.o.f's of 0.52 and 0.48, respectively. The one acetonitrile solvent molecule and one water molecule which could be modelled were assigned s.o.f's of 0.5 each. The acetonitrile molecule was refined with simple bond length constraints and hydrogen atoms were not placed on the carbon atom of the acetonitrile molecule or the water molecule. There are additional solvent and/or water molecules in the structure, located in voids within and between the layers, which could not be unambiguously modelled. This structure was therefore analysed using SQUEEZE,[165] which showed a total void volume of 823.2 Å^3 and an electron count of 265 electrons.

6.2.2   EXAFS

6.2.2.1   Sample Preparation

The Fe K_α-edge EXAFS spectra were collected at the X-ray absorption spectroscopy (XAS) beamline at the Australian synchrotron. The β-haematin DMSO solvate crystals were prepared in advance according to the procedure described above. In order to investigate the solution species, it was necessary to increase the amount of haemin and drug relative to the initial crystallisation conditions so that a good quality signal could be detected. A final Fe(III)PPIX concentration of 10 mM and a final CQfb concentration of 20 mM, were used. The concentrated solution of the two species was prepared immediately before the EXAFS experiment was conducted and filtered through a PTFE filter disk (0.45 μm pore size) to remove undissolved solid. In the case of the crystals, they were placed in the sample holder with as much mother liquor removed as possible. All samples were flash frozen in liquid nitrogen and the cryogenic temperature of ∼ 18K was maintained for the duration of the measurement to limit thermal disorder and avoid sample degradation. Spectra were collected from several locations within the sample to ensure sample homogeneity and to limit sample damage due to continuous exposure to the X-ray beam.

6.2.2.2   Data Analyses

The raw EXAFS scans collected by the 100-channel Ge detector were merged using the AVERAGE program.[159] Data processing and background removal were achieved with ATHENA and AUTOBK respectively, while fitting of experimental data to the corresponding model was done with ARTEMIS.[160,161]

6.3   Results

6.3.1   β-Haematin DMSO Solvate Crystal

Crystals of the β-haematin DMSO solvate species were obtained from two separate crystallisation environments, one containing CQ free base (CQfb) and the other AQ free base (AQfb). Fe(III)PPIX was prepared in the presence of approximately 2 mol equivalent of CQfb in a DMSO solution in the one case and in the presence of approximately 0.6 mol equivalent of AQfb in DMSO solution in the other case. Both crystallisation solutions yielded small rod-shaped crystals, which proved to be unstable when the mother liquor was removed completely, collapsing into a tarry amorphous material. After analysing the single crystal X-ray diffraction data in both cases, the species in the solid state was determined to be a DMSO solvate of β-haematin. In both cases, the structure was shown to belong to the triclinic space group P$\overline{1}$. The repeating unit in both crystal structures is a centrosymmetric μ-propionato coordination dimer of Fe(III)PPIX (Figure 6.1). The structural refinement parameters are summarised in Table 6.1 and compared with the structural refinement parameters of β-haematin.[35]
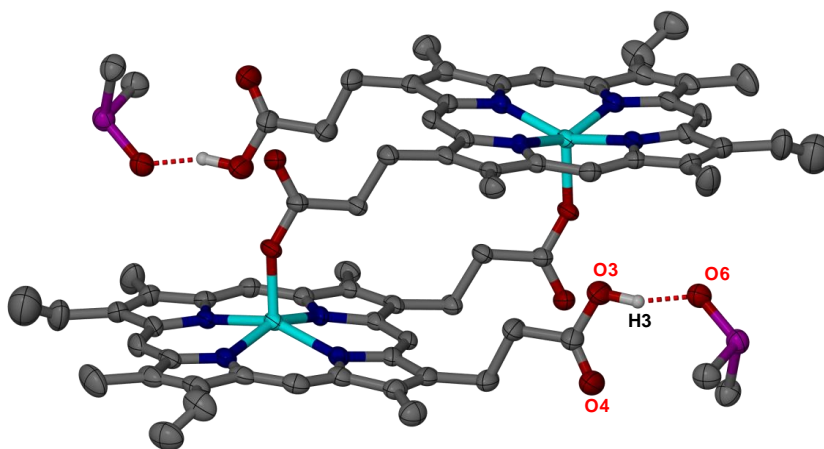
Figure 6.1 The μ-propionato dimer of Fe(III)PPIX, observed in the β-haematin DMSO solvate structure determined by single crystal X-ray diffraction. The crystals which yielded this structure were grown in the presence of either CQfb or AQfb, in DMSO solvent. The hydrogen bond (O3—H3····O6) between the free propionic acid group of Fe(III)PPIX and an included DMSO molecule is indicated with a dashed red line. Ellipsoids are drawn at 50% probability level and non-relevant solvent molecules and hydrogen atoms have been omitted for clarity. In the case of the disordered vinyl and methyl groups, only the position with highest occupancy has been shown for clarity. Atom colour labelling: grey – C, cyan – Fe, dark blue – N, red – O; white – H and purple – S.

Table 6.1 Experimental and refinement parameters for β-haematin DMSO solvate and β-haematin.

	β-haematin DMSO solvate (CQfb)*	β-haematin DMSO solvate (AQfb)*	β-haematin[#]
Molecular formula	$[C_{34}H_{31}FeN_4O_4.3(C_2H_6OS)]_2$	$[C_{34}H_{31}FeN_4O_4.3(C_2H_6OS)]_2$	$[C_{34}H_{31}FeN_4O_4]_2$
Formula weight / g mol^{-1}	849.96	843.81	615.50
Crystal system	Triclinic	Triclinic	Triclinic
Space group	$P\bar{1}$	$P\bar{1}$	$P\bar{1}$
a (Å)	9.7395(6)	9.7426(15)	12.196(2)
b (Å)	13.1930(7)	13.196(2)	14.864(2)
c (Å)	17.621(1)	17.635(3)	8.040(1)
α	110.641(3)	110.646(4)	90.22(1)
β	99.147(3)	99.110(4)	96.80(1)
γ	100.167(3)	100.144(4)	97.92(1)
V(Å^3)	2024.5(2)	2027.7(5)	1416.0(3)
Z	2	2	2
Temperature (K)	100	100	Room Temp
μ (mm^{-1})	2.369	0.580	-
Independent reflections	6892	7152	-
R_{int}	0.0884	0.1220	-
Goodness of fit, S	1.073	0.997	-
Final R indices [$I>2\sigma(I)$]	$R_1 = 0.0463$ $wR_2 = 0.1241$	$R_1 = 0.0674$ $wR_2 = 0.1978$	-

*This study. Structures determined by single crystal X-ray diffraction
[#]From Pagola *et al*. Structure determined by Rietveld refinement of powder X-ray diffraction data. [35]

Refinement of the β-haematin DMSO solvate crystal structures reveal that three DMSO solvent molecules are included in the crystal packing per molecule of Fe(III)PPIX. Two of the DMSO molecules simply occupy the free space between adjacent columns of stacked μ-propionato dimers, and are not involved in hydrogen bonding. The third DMSO molecule is hydrogen-bonded to the free propionic acid group of each Fe(III)PPIX molecule (Figure 6.1), for which the hydrogen bond geometries are reported in Table 6.2.

Both CQfb and AQfb, which were present in the crystallisation media, are not observed in the crystal structures.

Table 6.2 Hydrogen bond geometry in the β-haematin DMSO solvate crystal structure.

Species	D—H····A	D—H····Å	H····A/Å	D—H····A/ Å	D—H····A/ ^{o}
From CQfb	O3—H3····O6	1.000(5)	1.56(2)	2.531(4)	162(6)
From AQfb	O3—H3····O6	1.00	1.54	2.537	175.2

As a result of the solvent included in the structures, the unit cell parameters for both β-haematin DMSO solvate crystals are larger when compared to those reported for β-haematin, which was determined to be void of solvent.[35] Despite the presence of solvent molecules in the β-haematin DMSO solvate crystals however, the external morphology of the crystals observed by scanning electron microscopy (SEM), is very similar to the observed growth form of haemozoin (Figure 6.2).[179,180]
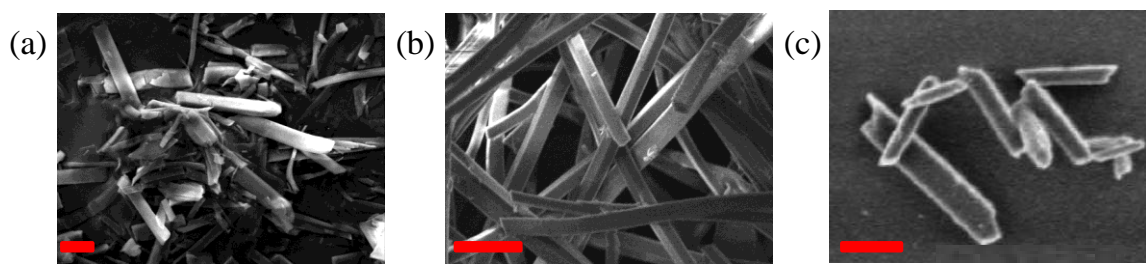
Figure 6.2 SEM micrographs of β-haematin DMSO solvate crystals and haemozoin. β-haematin DMSO solvate crystals grown in the presence of (a) CQfb and (b) AQfb. (c) Haemozoin crystals from *P. falciparum*, reproduced from reference.[184] Scale bar represents 20 μm, 10 μm and 200 nm for (a), (b) and (c) respectively.

An interesting observation is that the crystals grown in the presence of CQfb and AQfb do not show any signs of having tapered ends as has been reported in the presence of 10% CQ (mol/mol Fe(III)PPIX) in DMSO-MeOH and CHCl$_3$.[180]

The infrared spectrum of the bulk material confirmed that the single crystal selected for analysis was representative of the bulk sample (Figure 6.3). The crystal grown from the solution containing AQfb had a significant amount of mother liquor present and therefore the absorbance bands are not so intense (Figure 6.3 (b)). The bands attributed to coordination of the propionate group to the iron centre appear at 1205 and 1651 cm^{-1},

shifted to lower wavenumbers relative to their characteristic positions of 1211 and 1664 cm^{-1} respectively, in β-haematin. This is also the case for the band at 1703 cm^{-1}, which is assigned to the carbonyl stretch of the free carboxylic acid groups in the crystals grown in the presence of CQfb. The use of DMSO as the crystallisation medium for these crystals, and the fact that it is included in the structure of the β-haematin DMSO solvate and participates in hydrogen bonding to the free propionic acid group, may account for these observed differences in the IR spectra. A study by Nie *et al.*[185] provides some explanation. Making use of *ab initio* computational studies, the authors demonstrated that there is a correlation between the C=O stretching frequency in hydrogen-bonded carboxylic acid moieties and the hydrogen bond strength. They showed that the stronger the hydrogen-bonding interactions, the larger the red shift in the C=O stretching frequency. Using Gaussian03 for structural optimisation and energy calculations in the presence of a dielectric medium, the frequencies were also shown to be sensitive to the dielectric constant of the environment, where a hydrogen-bonding interaction is expected to remain strong in a medium with a dielectric constant between 1 and 5.6. Interestingly, the characteristic peaks of the µ-propionato coordination dimer are not visible in the IR spectrum of dried crystals (i.e. when no solvent is present). This points to the instability of the crystals when removed from the crystallisation medium. Due to this instability, all attempts to use powder X-ray diffraction to confirm that the bulk sample has the same structure as the single crystal were unsuccessful. In each case the crystals rapidly collapsed into a tarry substance that yielded an amorphous solid when dry. The instability of these crystals probably arises from rapid desolvation or absorption of water from the atmosphere.
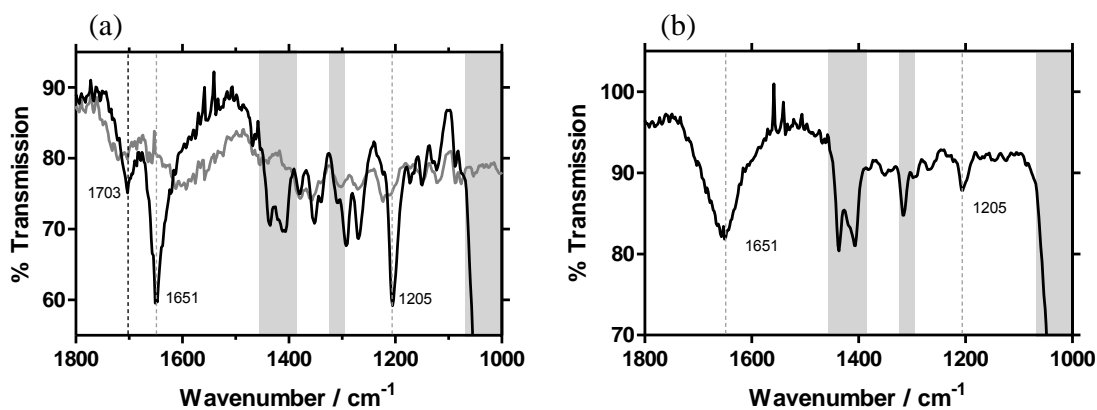
Figure 6.3 ATR-IR spectra of the β-haematin DMSO solvate crystals (a) from CQfb and (b) from AQfb. A sample of the bulk material was removed from the mother liquor, excess solvent was removed manually and the spectrum was recorded immediately in attenuated total reflectance (ATR) mode (black solid line). Peaks arising from DMSO have been highlighted in grey. These do not, however, interfere with the characteristic IR peaks attributed to μ-propionato coordination at 1205 and 1651 cm^{-1}, which correspond to the coordinated carboxylate C=O and C─O stretches respectively.[30] The peak at 1703 cm^{-1} in the spectrum of the material from CQfb corresponds to the C=O stretch of the free carboxylic acid group. For the crystals grown from AQfb, this peak is included in the broad peak centered at 1651 cm^{-1}. The ATR-IR spectrum of dried β-haematin DMSO solvate crystals is shown for comparison in (a) (solid grey line).

6.3.1.1   Disorder in the Positions of the Methyl and Vinyl Substituents

The vinyl and methyl substituents on the pyrrole rings B and C (Figure 6.4) are disordered. This disorder has been modelled over two sites, labeled as α and β for the upper molecule of the μ-propionato dimer, and γ and δ for the lower molecule. The α and γ positions are shown in green while the β and δ positions are shown in orange. In the refinement process, the site occupancies of the two vinyl groups at each position (i.e., the two α, the two β, the two γ, and the two δ vinyl groups) were set equal to each other, while the sum of the site occupancies of the α and β vinyl groups and the γ and δ vinyl groups was set equal to 1.0. In this way, the site occupancies of the vinyl substituents refined to 0.66 for the α and γ positions, and 0.34 for the β and δ positions. The result was the same for both β-haematin DMSO solvate structures, irrespective of whether the crystals were grown in CQfb or AQfb.
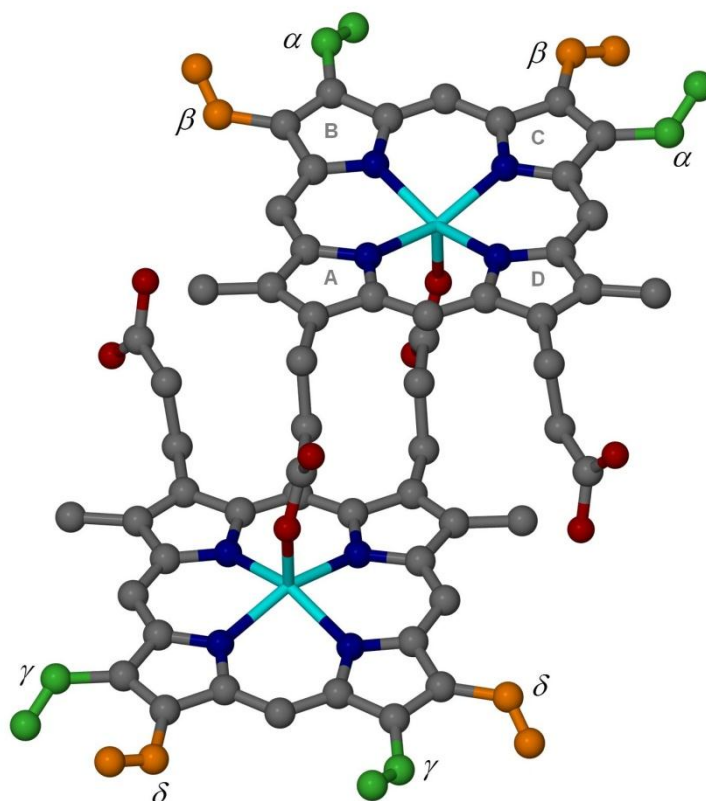
Figure 6.4 Illustration of the vinyl disorder in the single crystals of the β-haematin DMSO solvate. The site occupancies of the α and γ positions (shown in green) refined to 0.66, while the site occupancies of the β and δ position (shown in orange) refined to 0.34. Atom colour labelling for the porphyrin: grey – C; blue – N; red – O; cyan – Fe.

6.3.2 Comparison of Crystal Packing in β-Haematin DMSO Solvate and β-Haematin

The structure of haemozoin (β-haematin) was solved from powder X-ray diffraction (PXRD),[35] and the structural information was accessed *via* the Cambridge Structural Database (reference code XETXUP).[84] We were able to compare the structural similarities between the β-haematin DMSO solvate, solved with SCD, and β-haematin solved from PXRD, by viewing the data through XSEED.[143]

Firstly, an overlay of the porphyrin cores of the β-haematin DMSO solvate and β-haematin[35] show that there is a close agreement between the structures of the repeating units (Figure 6.5).
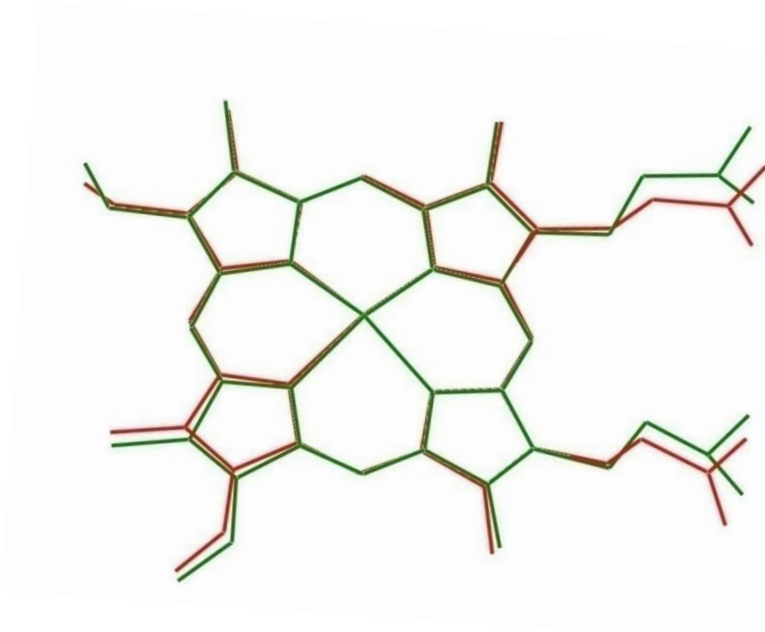
Figure 6.5 An overlay of the porphyrin core as present in the μ-propionato dimer of the β-haematin DMSO solvate (red) and β-haematin[35] (green).

While the structural features of the repeating μ-propionato dimer and the external crystal morphology of the β-haematin DMSO solvate (Figure 6.2) appear to be almost indistinguishable from β-haematin,[179,180] examination of the crystal packing reveals interesting differences. The unit cell of each structure contains two molecules of Fe(III)PPIX, which are related to one another through a centre of inversion. In the case of the β-haematin DMSO solvate crystals, the unit cell contains a π-π dimer in which the unligated faces of the two Fe(III)PPIX molecules interact with one another (Figure 6.6), with three solvent molecules included in the crystal packing per molecule of Fe(III)PPIX. In contrast to this, the unit cell of β-haematin, was placed so as to contain a μ-propionato dimer of Fe(III)PPIX, Figure 6.7, and no solvent molecules are present in the crystal packing.[35]
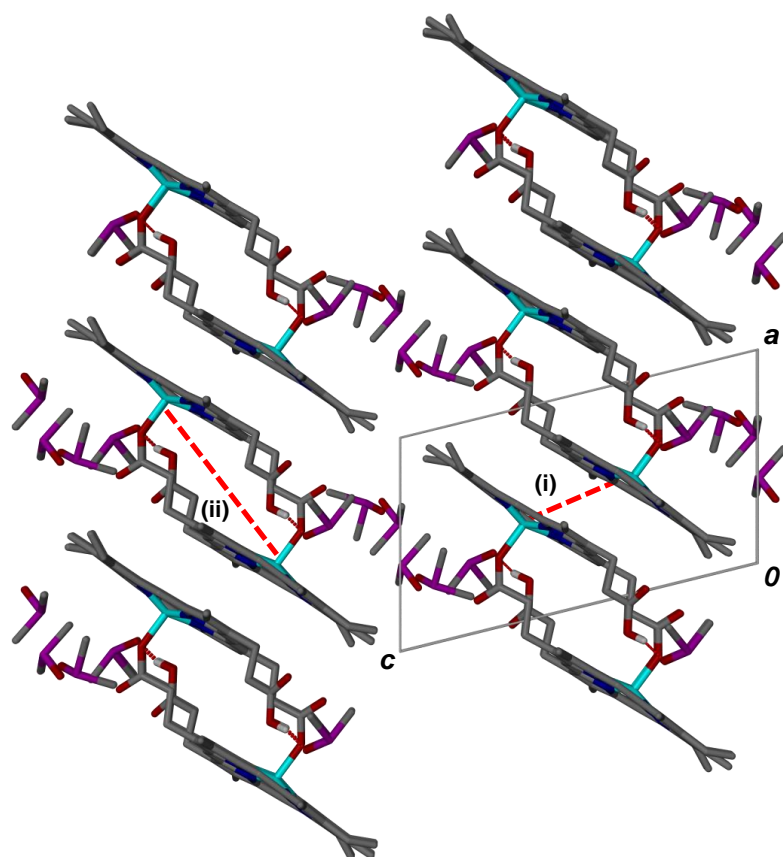
Figure 6.6 Crystal packing of β-haematin DMSO solvate viewed along the crystallographic *b*-axis. The unit cell (outlined in grey) contains a pair of Fe(III)PPIX molecules in which the two Fe atoms are separated by an interdimer distance of 5.380 Å (i). Packing of the Fe(III)PPIX molecules along the *a*-axis is brought about by μ-propionato–Fe coordination resulting in the formation of a centrosymmetric μ-propionato dimer in which the two Fe atoms are separated by an intradimer distance of 8.982 Å (ii). Atom colour labelling: grey – C; white – H; blue – N; red – O; cyan – Fe; purple –S.
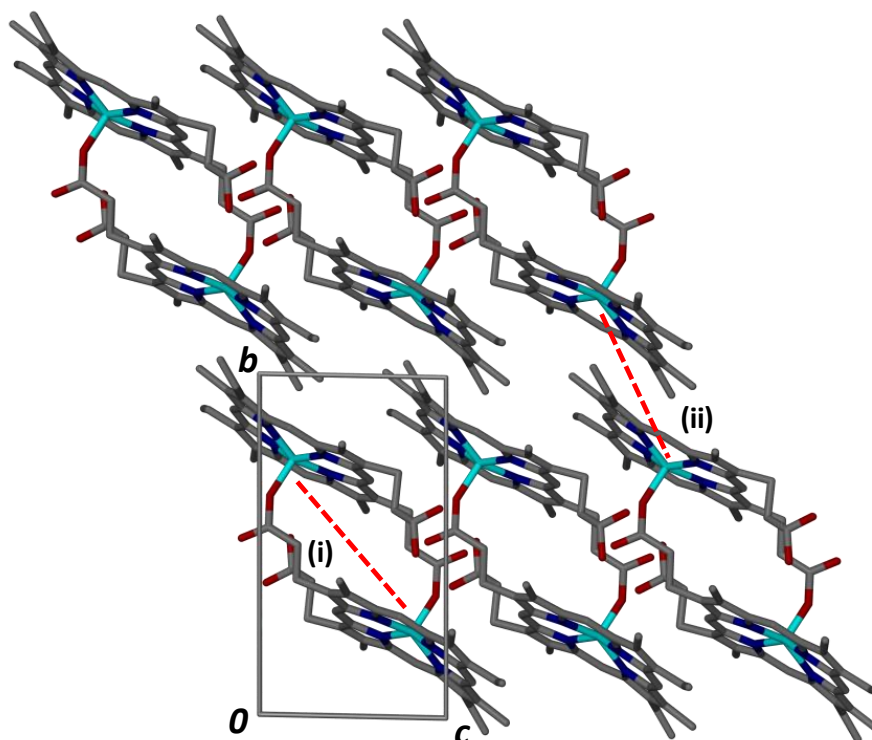
Figure 6.7 Crystal packing of β-haematin viewed along the crystallographic *a*-axis. The unit cell (outlined in grey) contains a μ-propionato dimer in which the two Fe atoms are separated by an intradimer distance of 9.047 Å (i). Stacking of the dimers along the *b*-axis by means of non-covalent (π-π) interactions between the unligated Fe(III)PPIX faces, results in the two Fe atoms being separated by an interdimer distance of between 7.859 and 8.040 Å (ii). Atom colour labelling: grey – C; blue – N; red – O; cyan – Fe; purple –S.

When considering only the stacked (π-π) dimer, the metal centres are offset relative to one another. For the β-haematin DMSO solvate dimers, there is considerable overlap of the porphyrin cores (Figure 6.8 (a)). However, given the larger offset between the porphyrin planes, there is much less lateral overlap between the porphyrin cores in β-haematin (Figure 6.8 (b)). The observed Fe–Fe distance between adjacent μ-propionate dimers (referred to as the interdimer distance) for the β-haematin DMSO solvate is 5.380 Å for both the CQfb and AQfb structures (Figure 6.8 (a)), while an interdimer Fe-Fe distance of between 7.859 and 8.040 Å was measured for β-haematin (Figure 6.8 (b)).
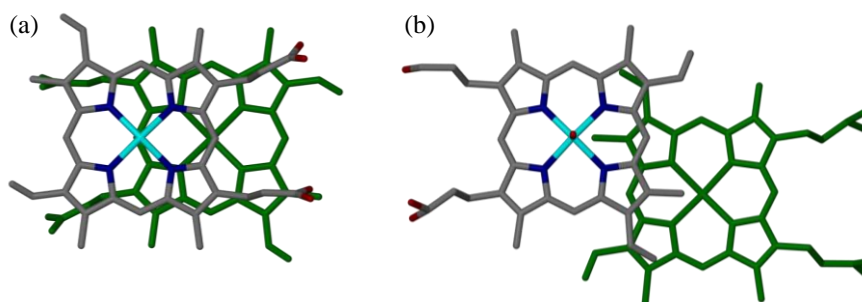
Figure 6.8 A view down the Fe–O bonds of two adjacent μ-propionato dimers. (a) In the β-haematin DMSO solvate, the two porphyrin cores are laterally shifted relative to one another, with an observed interdimer Fe–Fe distance of 5.380 Å. (b) The corresponding view in β-haematin.[35] In this case, the interdimer Fe–Fe distances vary between 7.859 and 8.040 Å. For clarity the porphyrin at the back has been shaded green. Atom colour labelling of the front porphyrin: grey – C; blue – N; red – O and cyan – Fe.

In the β-haematin DMSO solvate structure, stacked Fe(III)PPIX pairs interact with one another through μ-propionate-Fe coordination along the a-axis, resulting in formation of μ-propionato dimers in which the observed intradimer Fe–Fe distance is 8.982 Å and 8.991 Å, respectively (Figure 6.9 (a)). Given the geometrical constraints of the μ-propionato dimer, it was not unexpected that a very similar intradimer Fe-Fe distance of 9.047 Å is observed in the β-haematin structure (Figure 6.9 (b)). These dimers π-stack along the *b*-axis.
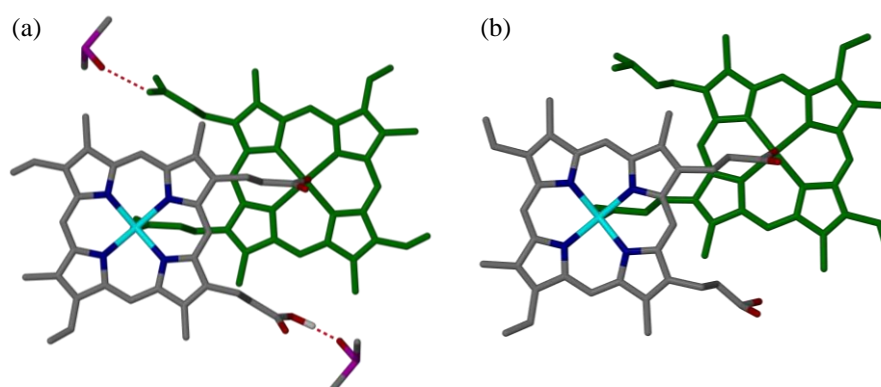
Figure 6.9 A view down the Fe—O bonds of the μ-propionato dimer of Fe(III)PPIX in (a) the β-haematin DMSO solvate and (b) the β-haematin[35] structures. The intra-dimer Fe-Fe distances are 8.982 Å and 9.047 Å, respectively. The porphyrin molecule at the back has been shaded green for clarity. Atom colour labelling of the front porphyrin: grey – C; white – H; blue – N; red – O; cyan – Fe and purple –S.

6.3.3   The Crystal Structure of Haemin

Crystals of haemin (Cl-Fe(III)PPIX) were obtained by dissolving haemin in the presence of approximately 0.5 mol equivalents of amodiaquine dihydrochloride dihydrate (AQ) in a 5:1 (*v:v*) solution of acetonitrile: methanol. After two weeks, small triangular-shaped crystals were observed on the bottom of the vial. A single crystal of dimensions $0.02 \times 0.04 \times 0.125$ mm was selected for X-ray diffraction. The asymmetric unit for haemin is shown in Figure 6.10. The crystal and structural refinement parameters are reported in Table 6.3 and compared to those determined previously for α-chlorohaemin.[82] Despite the inclusion of the antimalarial compound, analysis of the crystals by SCD showed that they contained only haemin. At first this was not considered interesting since the structure of haemin (α-chlorohaemin) has been known since 1965,[82] however, having compared the two structures, there are notable differences.
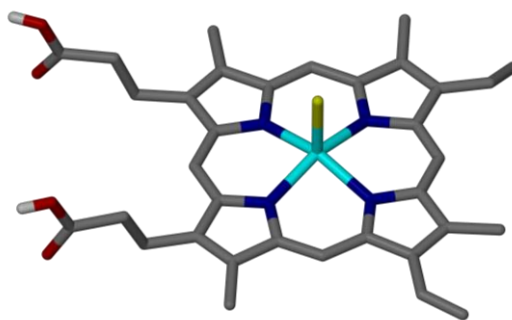
Figure 6.10 The haemin structure. Solvent molecules and non-relevant H atoms have been omitted for clarity. In the case of the disordered vinyl and methyl substituents, only the position with the highest site occupancy has been shown for clarity. Atom colour labelling: grey – C, cyan – Fe, dark blue – N, red – O; white – H and yellow – Cl.

198

Table 6.3 The crystal data, experimental and refinement parameters for haemin and α-chlorohaemin.

	Haemin*	α-Chlorohaemin[#]
Molecular formula	$C_{34} H_{28} N_4 O_4 Cl_1 Fe_1$	$C_{34} H_{18} N_4 O_4 Cl_1 Fe_1$
Formula weight / g mol^{-1}	684.44	637.84
Crystal system	Monoclinic	-
Space group	C 2/m	P$\bar{1}$ or P1
a (Å)	17.3355(15)	11.494
b (Å)	23.005(2)	14.097
c (Å)	11.5284(11)	10.854
α	90.00	98.56
β	122.195(5)	108.48
γ	90.00	107.48
V(Å^3)	3890.7(6)	1529.99
Z	1	2
Temperature(K)	100	173
μ (mm^{-1})	0.497	-
Independent Reflections	3667	-
R_{int}	0.2295	-
Goodness of fit, S	1.030	-
Final R indices [I>2σ(I)]	R_1 = 0.0815	-
	wR_1 = 0.2310	

*This study. Structure determined by SCD.
[#]From Koenig. Structure determined by SCD.[82]

Intermolecular hydrogen bonding between the propionic acid group of adjacent Fe(III)PPIX molecules is observed. Specifically, carboxylic acid moieties from adjacent Fe(III)PPIX molecules hydrogen bond to form the carboxylic acid dimer motif as shown in Figure 6.11. The hydrogen bonding geometries are reported in Table 6.4 and the crystal packing is outlined in section 6.3.4.
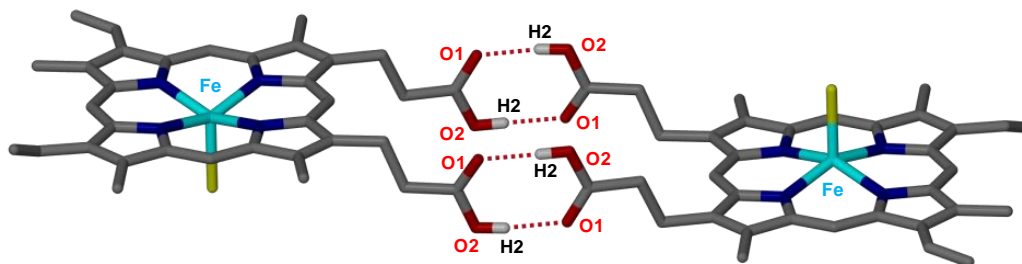
Figure 6.11 The hydrogen bonding observed in the crystal structure of haemin. The atoms involved in hydrogen bonding and the Fe(III) centre are labelled. The hydrogen bonds between the propionic acid group of adjacent Fe(III)PPIX molecules are indicated with dashed red lines. Solvent molecules and non-relevant H atoms have been removed for clarity. Atom colour coding: grey – C, cyan – Fe, dark blue – N, red – O; white – H and yellow – Cl.

Table 6.4 Hydrogen bond geometry in haemin.

D—H····A	D—H····Å	H····A/Å	D—H····A/ Å	D—H····A/ °
O2—H2····O1A	0.986	1.697	2.636	157.84

6.3.3.1   Comparison Between Haemin and α-Chlorohaemin

Crystals of α-chlorohaemin formed on the surface of a dialysis tube which was filled with a concentrated aqueous solution of NaCl, coated with mineral oil and perforated with pinholes, before being placed in test tube containing dissolved haemin in 1.0 mL pyridine, 1.4 mL tetrachloroethane and 14 mL of glacial acetic acid and incubated at 120 °C.[82] Even though a structure for haemin was solved in 1965,[82] it is known that the conformation adopted by porphyrins may be strongly influenced by the crystal packing forces.[186] As a result of the different solvents and environments used to grow the crystals of haemin (this work) and α-chlorohaemin (previous study), the unit cell parameters for haemin are notably different to the unit cell parameters reported for α-chlorohaemin (Table 6.3).

Comparing the structure of haemin to the published structure of α-chlorohaemin,[82] obvious differences in the packing of the porphyrins can be seen by simply comparing the adopted conformations of two adjacent porphyrins. Viewed from the side, the porphyrin core of haemin is planar (Figure 6.12 (a)), while that of α-chlorohaemin is noticeably domed (Figure 6.12 (b)).[82] Given that the closest contact between adjacent porphyrin cores at a

distance of approximately 3.54 and 3.465 Å respectively, some π-stacking is likely between the two aromatic porphyrin macrocycles. Interestingly, Fe(III)PPIX has been shown to exist in aqueous solution as a π-π dimer, with a proposed structure similar to the structures shown below.[79] This π-π dimer (where the axial ligand is H_2O) is thought to be the precursor in the formation of β-haematin.[73] Therefore, the structure of this species is of interest in understanding the mechanism of β-haematin formation, and the π-π dimers in haemin and α-chlorohaemin (Figure 6.12) provide the most accurate (SCD data) structural interpretations to support this model. In the aqueous environment, the axial ligand Cl of haemin would be substituted by either H_2O or HO^-.[79] In the parasite's digestive vacuole, which has an estimated pH of 4.8, H_2O would be expected to be the axial ligand.
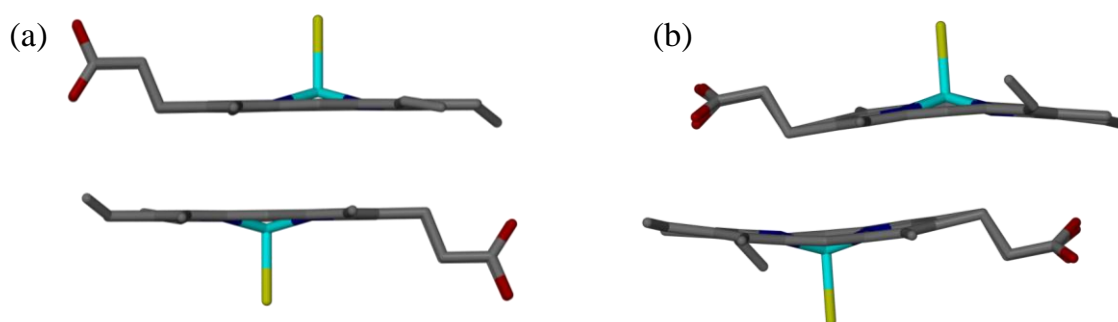
Figure 6.12 Conformation of π-π dimers. A view from the side of two haemin molecules stacking on top of each other with the unligated faces facing one another and the axial ligands directed outward, for (a) haemin and (b) α-chlorohaemin[82]. The planar and domed conformations adopted by the Fe(III)PPIX molecules is observed for the two structures respectively. Atom colour coding: C – grey; N – blue; O – red; Fe – cyan and Cl – yellow.

An overlay of the porphyrin cores in the two structures, viewed down the Fe-Cl bonds (Figure 6.13), shows that there is a much greater overlay in haemin compared to α-chlorohaemin. The resulting interdimer Fe-Fe distance is 4.592 Å in haemin compared to 6.666 Å in α-chlorohaemin.
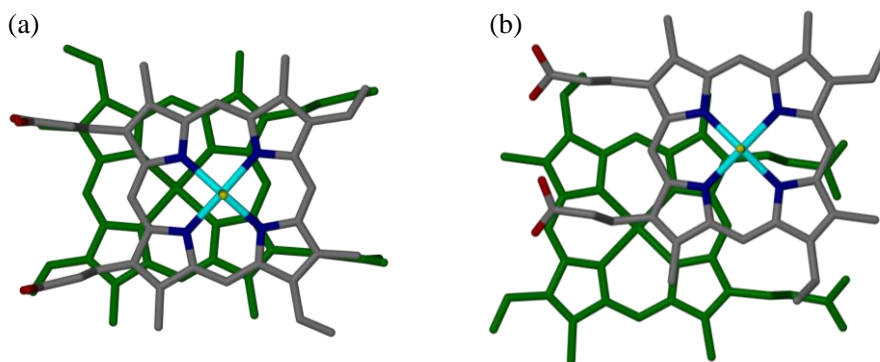
Figure 6.13 A view down the Fe—Cl bonds of (a) haemin and (b) α-chlorohaemin[82]. The interdimer Fe-Fe distance between two π-stacked porphyrins is 4.597 and 6.666 Å, respectively. These Fe-Fe distances may be more easily appreciated from the side view shown in Figure 6.12. The porphyrin molecule at the back has been shaded green for clarity. Atom colour coding in the front porphyrin: C – grey; N – blue; O – red; Fe – cyan and Cl – yellow.

Closer inspection of the packing of haemin viewed along the crystallographic c-axis reveals large channels filled with disordered solvent molecules.
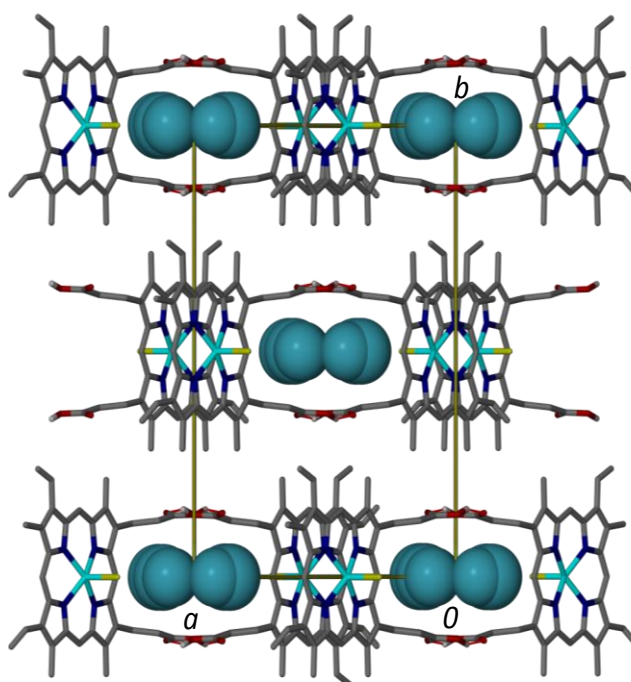
Figure 6.14 Crystal packing of haemin viewed down the crystallographic c-axis as indicated by the unit cell. Disordered acetonitrile and water molecules are shown in light blue (space-filling). Atom colour coding: C – grey; H – white; N – blue; O – red; Fe – cyan and Cl – yellow.

The π-π stacking observed in haemin is best appreciated when viewed along the crystallographic *b*-axis (Figure 6.15).
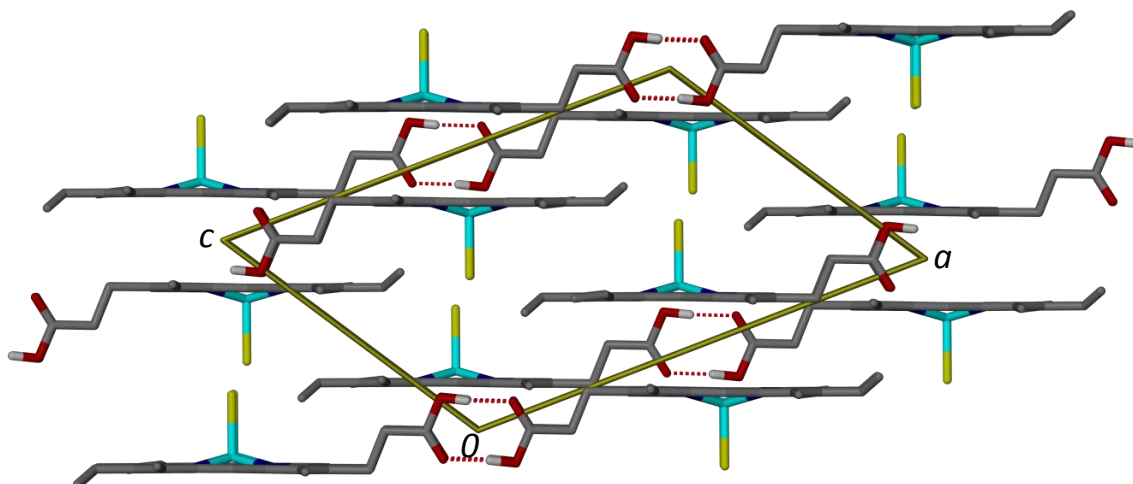
Figure 6.15 Crystal packing of haemin viewed down the crystallographic *b*-axis indicated by the unit cell. Solvent molecules and non-relevant hydrogen atoms have been removed for clarity. Atom colour coding: C – grey; H – white; N – blue; O – red; Fe – cyan and Cl – yellow.

The difference in the packing of haemin and α-chlorohaematin can be appreciated when looking at comparative views of the packing of the latter species (Figure 6.16) down the *b*-axis and down the *c*-axis. When considering the ligated faces of the porphyrins in the packing diagrams, the atoms surrounding the Cl atom in the α-chlorohaemin structure are packed closer together. Therefore, comparing distances between Cl atoms in the crystal packing, the observed distances between two closest packed Cl atoms is 6.237 Å in α-chlorohaemin compared to 7.807 Å in haemin.

(a)

(b)
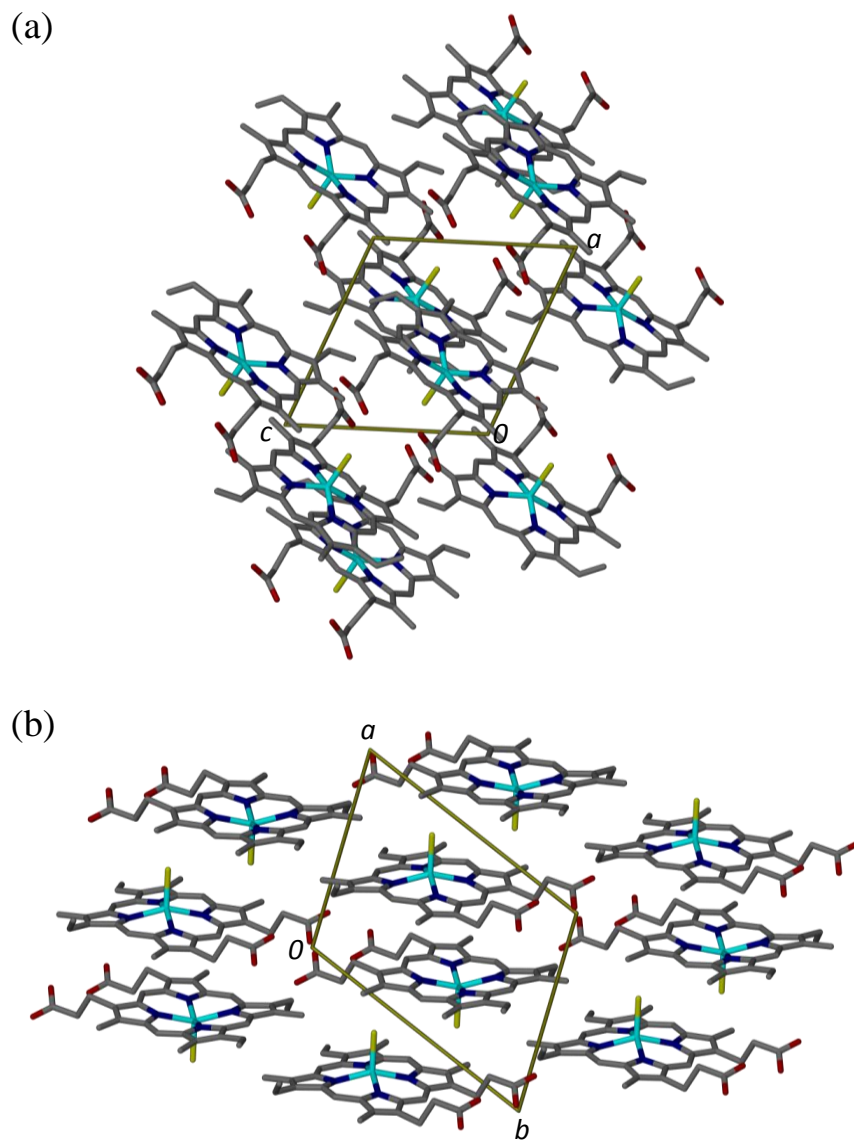
Figure 6.16 The crystal packing of α-chlorohaemin viewed down the crystallographic (a) *b*-axis and (b) *c*-axis as indicated by the unit cell. Atom colour coding: C – grey; N – blue; O – red; Fe – cyan and Cl – yellow.

6.3.4   EXAFS

X-ray absorption spectroscopy was used to investigate the Fe(III)PPIX species in the crystallisation medium of β-haematin DMSO solvate in order to determine whether the species observed in the solid state also exists in solution. EXAFS is a very powerful tool that can give information about the local structure around an absorbing atom. The location and distance between atoms relative to an absorbing atom within a molecule can be determined, and can also provide information about disorder. Unfortunately, EXAFS is not suitable to study drug-treated parasite samples. Due to the high concentration of iron in haemoglobin, this would overpower the signal arising from any Fe(III)PPIX interacting with CQ. In this study, crystal of the β-haematin DMSO solvate and the crystallisation medium containing CQfb were investigated to study the interaction between Fe(III)PPIX and CQ at much higher concentrations.

As mentioned previously, a reasonable starting model of the atoms around the absorbing Fe atom is needed to analyse EXAFS data. As an obvious starting point, the single crystal diffraction data determined for the β-haematin DMSO solvate was used to generate coordinates for these atoms from which a model was built to account for atoms in a sphere of ≤ 5.0 Å around the central Fe atom of one of the porphyrin molecules in the μ-propionato dimer. These included the four nitrogen atoms directly bonded to the Fe centre, the α and *meso* carbon atoms, and the β-carbon atoms (refer back to Figure 2.13 in section 2.5.4). Atoms anticipated to be involved in coordination to the Fe centre, namely those of the propionate group of Fe(III)PPIX involved in coordination to form the μ-propionato dimer, as well as atoms of DMSO, CQfb and H_2O which could compete in solution and preferentially coordinate to the Fe(III) centre in the crystallisation medium, are referred to as axial atoms (a.a.). Atoms involved in backscattering from a second Fe(III)PPIX molecule as a result of π-π interactions or stacking between adjacent Fe(III)PPIX molecules are labelled as atoms outside the ring (a.o.). These atomic positions based on the known crystal structure were used to compare to the atomic positions determined from the EXAFS refinement, and were used to rationalise whether the solid-state structure is represented in solution or not.

6.3.4.1   EXAFS of β-Haematin DMSO Solvate

The EXAFS spectra of the β-haematin DMSO solvate crystallisation medium and the crystals of β-haematin DMSO solvate were fitted to a starting model which was based on the SCD structure of the β-haematin DMSO solvate. Atoms involved in the EXAFS refinement are indicated in Figure 6.17. The EXAFS oscillations χ(q) and the corresponding Fourier transforms obtained for the crystallisation medium and the crystals respectively are shown Figure 6.19.
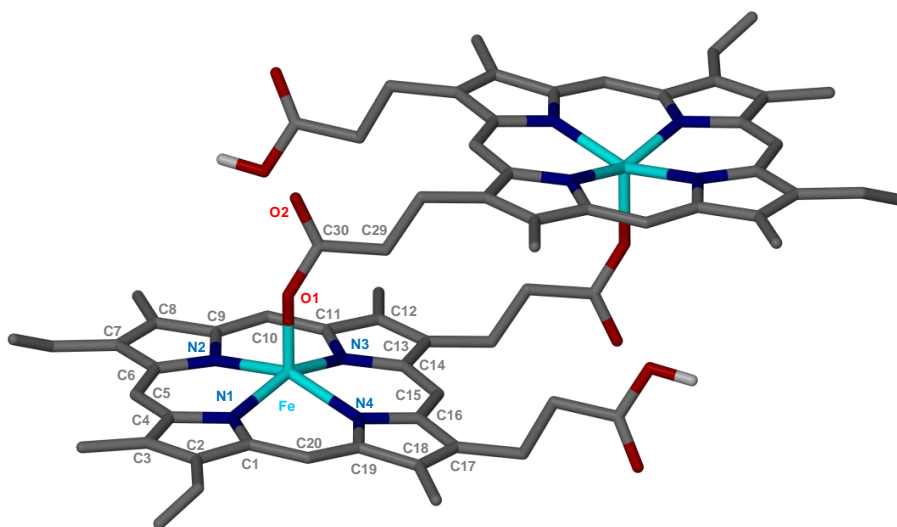
Figure 6.17 The μ-propionato dimer as observed in the crystal structure of β-haematin DMSO solvate. The atoms considered in the EXAFS model refinement are labelled. Atom colour labelling: grey – C, cyan – Fe, dark blue – N, red – O and white – H.

Due to the fact that some mother liquor remained in the sample of crystals of the β-haematin DMSO solvate, some scattering from partner Fe(III)PPIX molecules was also considered in the model. As expected, there was very good agreement between the experimental spectrum of the crystals of β-haematin DMSO solvate and the model based on the SCD. In the case of the crystals of β-haematin DMSO solvate, the R factor for the best fit of the experimental data to the model was 0.029. In the case of the crystallisation medium however, the fit to the SCD model was poor and other models of Fe(III)PPIX, including cases with DMSO and CQfb as ligands, were considered. For this purpose the model of the local environment around the Fe centre was modified assuming the absence or existence of additional atoms. All plausible models were considered before the best fit was selected.

In an independent attempt to rationalise which Fe(III)PPIX species might exist in the crystallisation medium, a UV-vis spectrum of the crystallisation medium was collected. The concentration of Fe(III)PPIX used in the crystallisation medium was too high to obtain a meaningful UV reading, and therefore the concentrations of both Fe(III)PPIX and CQfb were adjusted to 7.638×10^{-3} mM and 1.56×10^{-2} mM, respectively for the investigation of the Soret band, Figure 6.18 (a), and 9.54×10^{-2} mM and 1.95×10^{-1} mM, respectively to investigate the charge transfer and Q bands, Figure 6.18 (b). Both solutions contained approximately 2 mol equiv of CQfb relative to Fe(III)PPIX. In the UV spectra obtained, the sharp and intense absorbance peak close to 400 nm indicates the presence of a monomeric Fe(III)PPIX species.[155] No change in the speciation of Fe(III)PPIX was observed even after 10 days. While providing some insight, the low Fe(III)PPIX concentration used compared to the EXAFS study, may influence the Fe(III)PPIX speciation.
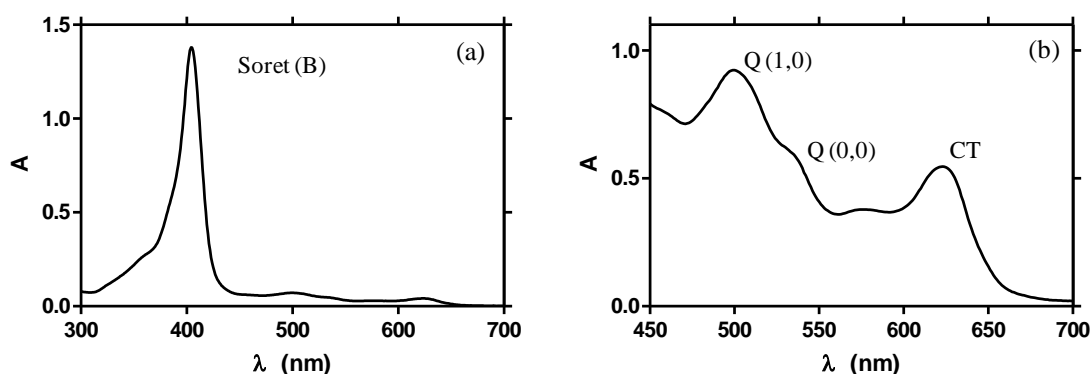
Figure 6.18 The UV-vis spectrum of the crystallisation medium of β-haematin DMSO solvate. (a) The concentrations of Fe(III)PPIX and CQfb were 7.638×10^{-3} mM and 1.56×10^{-2} mM respectively, to investigate the Soret band. (b) The concentration of Fe(III)PPIX and CQfb were 9.54×10^{-2} mM and 1.95×10^{-1} mM respectively, to investigate the charge transfer and Q bands. The soret band in the spectrum is characteristic of monomeric Fe(III)PPIX, suggesting that this is the species present in solution.

According to the UV study (Figure 6.18), the speciation of Fe(III)PPIX in the presence of CQfb in DMSO is consistent with a monomeric Fe(III)PPIX species. However, since the concentration of Fe(III)PPIX in the EXAFS experiment was increased to 10 mM compared to 0.38 mM in the crystallisation experiment and 7.6×10^{-3} mM in the UV experiments (in order to record a spectrum), it was possible that other species such as a π-π dimer or even

the μ-oxo dimer of Fe(III)PPIX could have been in the crystallisation solution environment owing to aggregation. Therefore these species were also considered together with monomeric Fe(III)PPIX.

If Fe(III)PPIX is monomeric, it is reasonable to consider the case in which DMSO could coordinate to form a 6-coordinate Fe(III)PPIX species. Given that the DMSO solvent was not dried before use, water is also a possible axial ligand along with the CQfb present in the crystallisation solution environment. Even though no drug molecules were observed in the SCD data, Fe(III)PPIX-drug moieties in the crystallisation medium were considered. Despite these other possibilities, the 6-coordinate monomeric Fe(III)PPIX with two DMSO molecules coordinating to the Fe centre, through either the oxygen or sulphur atom was considered the likely species. However, modelling did not refine with acceptable values of interatomic distances, r, or the statistical parameters R, and χ^2.

The μ-oxo dimer between two Fe(III)PPIX molecules was also considered. Again this model did not refine with acceptable values of the Fe-Fe distance and R and χ^2 fitting indices.

The model proposed to exist in aqueous solution comprises two 5-coordinate Fe(III)PPIX molecules interacting non-covalently through their unligated faces, with the axial ligand pointing outward being either H_2O or HO^-.[79] Judging from the R and χ^2 values, 0.014 and 1.06 respectively, there is excellent agreement of the experimental data to this model. Although a somewhat surprising result given what is known about Fe(III)PPIX speciation is solution, the π-π dimer has been proposed to be one of the precursor steps in the formation of β-haematin.[73]
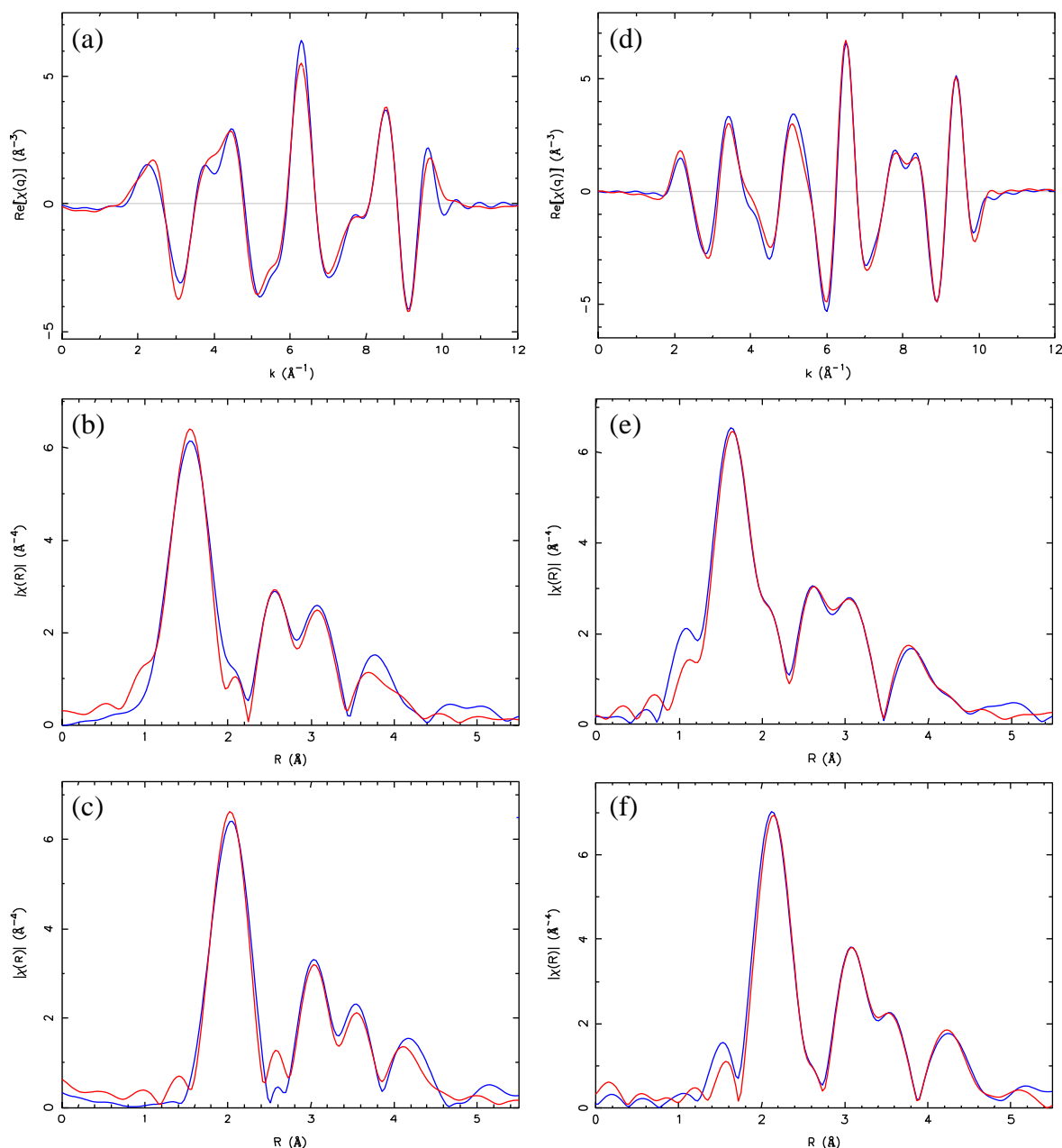
Figure 6.19 EXAFS spectra. The Fe K_α-edge k^3-weighted experimental (blue) and the best fit (red) spectra (a and d), the corresponding Fourier transform (b and e) and the corresponding Fourier transform with phase correction (c and f), for crystals of β-haematin DMSO solvate (a, b and c) and the corresponding crystallisation medium (d, e and f). The R factor for the best fit to the model is 0.029 in the case of the crystals of the β-haematin DMSO solvate fitted to the SCD data as a model, and 0.014 for the crystallisation solution fitted to a model of a π-π dimer with the axial ligand being either H_2O or HO^- pointing outward.

The EXAFS oscillations χ(q), refined for the crystals of β-haematin DMSO solvate and the corresponding Fourier transforms spectra (Figure 6.19), indicate that there is good agreement between the model built from the SCD data of the β-haematin DMSO solvate and the fitted EXAFS. This is the same in the case of the crystallisation medium, where a model was built based on the π-π dimer of Fe(III)PPIX with H_2O or HO^- as the axial ligand.

In the case of the β-haematin DMSO solvate crystal, the EXAFS oscillation spectrum (Figure 6.19 (a)) shows differences in the shape between the model and the experimental results in the ranges 2.5–4.5 $Å^{-1}$ and an increase in the peak intensity at 6.2 $Å^{-1}$ for the experimental data. This could be as a result of the mother liquor that was present in the sample. The Fourier transformed spectrum shows similarities for the resolved atomic coordination spheres (Figure 6.19 (b)), again the small differences in the spectrum of the experimental and best fit to the model could be attributed to mother liquor present in the sample collection. The first peak from 1.4 to 2.4 Å, present in the Fourier transformed spectrum with phase corrections (Figure 6.19 (c)), is attributed to the scattering contributions from the axial oxygen (as a result of propionate coordination from a partner Fe(III)PPIX) and the four pyrrolic nitrogen atoms of Fe(III)PPIX. From Table 6.5 the distances assigned to the scattering atoms agree with the distance at which they will contribute to the peak observed in the spectrum in Figure 6.19 (c). The EXAFS data for the crystallisation medium indicate that the Fe(III)PPIX species present in solution prior to β-haematin DMSO solvate crystallisation is a π-π dimer with either H_2O or HO^- as the axial ligand. From the EXAFS oscillation spectrum (Figure 6.19 (d)) there are minor differences in the range of 3.5–6 $Å^{-1}$, which is expected since molecules in solution are able to move more freely. The Fourier transformed spectrum for the crystallisation medium shows a good fit to the predicted model. Therefore, the precursor to the formation of β-haematin is proposed in Figure 6.20.

(a) (b)
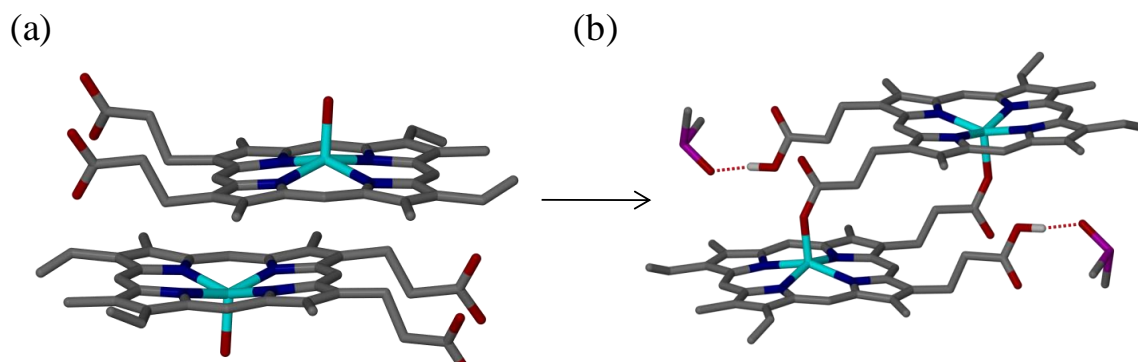
Figure 6.20 Proposed precursor to β-haematin DMSO solvate formation. (a) The π-π dimers predicted by EXAFS to be in the crystallisation medium of β-haematin DMSO solvate. (b) In order to form the µ-propionato linkages in the crystal structure of β-haematin DMSO solvate, the π-π dimers need to shift laterally, forming the µ-propionato dimer *via* propionate coordination and loss of the axial H_2O or HO^- molecule.

The refined EXAFS parameters are shown in Table 6.5.

Table 6.5 Refined EXAFS parameters of β-haematin DMSO solvate crystallisation solution and crystals of β-haematin DMSO solvate.

	β-haematin DMSO solvate (SCD)[#]			β-haematin DMSO Solvate Crystal EXAFS				β-haematin DMSO Solvate Crystallisation Medium EXAFS			
ΔE_0(eV)	-			2.8(1.6)				9.5(5)			
$S_o{}^2$	-			0.8(1)				1.000(1)			
n_{ind}	-			20.2				25.15			
n_{var}	-			16				10			
R	-			0.029				0.013			
χ^2	-			2.59				1.06			
EXAFS labelling[##]	Atom in SCD	Distance from Fe (Å)	Average	Atom (X)	N(X)	Distance from Fe (Å)	σ^2 (Å^2)	Atom (X)	N(X)	Distance from Fe (Å)	σ^2 (Å^2)
N1	N1	2.064		N1	1	2.020(7)	0.006(4)	N1	1	2.07(6)	0.0045(4)
N2	N2	2.063		N2	1	2.061(7)	0.006(4)	N2	1	2.11(6)	0.0045(4)
N3	N3	2.057		N3	1	2.046(7)	0.006(4)	N3	1	2.10(6)	0.0045(4)
N4	N4	2.055		N4	1	2.036(7)	0.006(4)	N4	1	2.09(6)	0.0045(4)
C2	**C1α**	**3.079**	**3.085**	**C2**	**4**	**3.07(4)**	**0.004(2)**	**C2**	**4**	**3.1(1)**	**0.0008(7)**
C2	**C4 α**	**3.101**									
C2	**C6 α**	**3.088**									
C2	**C9 α**	**3.072**									
C3	C11 α	3.089	3.089	C3	4	3.04(4)	0.004(2)	C3	4	3.07(7)	0.0008(7)
C3	C14 α	3.091									
C3	C16 α	3.094									
C3	C19 α	3.080									
C5	**C2 β**	**4.314**	**4.313**	**C5**	**4**	**4.32(9)**	**0.004(5)**	**C5**	**4**	**4.25(1)**	**0.008(7)**
C5	**C3 β**	**4.319**									
C5	**C7 β**	**4.314**									
C5	**C8 β**	**4.306**									
C4	C12 β	4.323	4.314	C4	4	4.32(9)	0.004(5)	C4	4	4.3(1)	0.0008(7)
C4	C13 β	4.314									
C4	C17 β	4.311									
C4	C18 β	4.311									
C6	**C5 meso**	**3.45**	**3.443**	**C6**	**4**	**3.47(9)**	**0.004(5)**	**C6**	**4**	**3.5(1)**	**0.006(3)**
C6	**C10 meso**	**3.43**									
C6	**C15 meso**	**3.445**									
C6	**C20 meso**	**3.445**									

Tabel 6.5 Continued from previous page

EXAFS labelling[##]	Atom in SCD	Distance from Fe (Å)	Average	Atom (X)	N(X)	Distance from Fe (Å)	σ^2 (Å^2)	Atom (X)	N(X)	Distance from Fe (Å)	σ^2 (Å^2)
	Fe(III)PPIX										
O1	O1 a.a.	1.892		O1	1	1.97(4)	0.006(5)				
C7	C30 a.a.	3.037		C7	1	3.10(5)	0.004(2)				
O2	O2 a.a.	4.056		O2	1	4.05(2)	0.006(4)				
C8	C29 a.a.	3.520		C8	1	3.8(2)	0.004(5)				
Fe	Fe o.r.							Fe	1	4.6(-1)	0.007(0.01)
Cp1				Cp1	6	3.83(4)	0.003(5)	Cp1	3	3.8(4)	0.010 (3)
Cp2	**C15 o.r.**	**3.811**	**4.163**	**Cp2**	**4**	**4.5(2)**	**0.005(7)**	**Cp2**	**4**	**4.6(3)**	**0.004(0.01)**
Cp2	**C16 o.r.**	**3.98**									
Cp2	**N4 o.r.**	**4.438**									
Cp2	**C17 o.r.**	**4.4**									
Cp2	**C14 o.r.**	**4.186**									
Cp3	N3 o.r.	4.644	4.71	Cp3	2	4.73(8)	0.003(.01)	Cp3	6	4.8(1)	0.004(5)
Cp3	C13 o.r	4.769									
Cn				Cn	4	3.96(-7)	0.003(6)	Cn	2	3.8(-2)	0.010(3)
	H$_2$O[*]										
oh	O a.a.							oh	1	2.5(-2)	0.001(2)

[#]The model was built from the SCD data of the β-haematin DMSO solvate determined in this work. The atoms used to model distances from the Fe centre of the porphyrin are included to compare with the distances refined in the EXAFS data.

[##] If atoms have the same EXAFS labelling it indicates that the atoms were refined at the same distance from the absorbing atom.

[*] In the crystallisation solution, coordination to the Fe(III) centre through H$_2$O or HO$^-$ was also modelled.

[**]Abbreviations: atoms marked a.a. - axial atoms belonging to the propionate side chains of the second Fe(III)PPIX coordinating to the Fe(III) centre to form the μ-propionato dimer. Atoms marked o.r. – atoms outside the Fe(III)PPIX ring, belonging to the partner porphyrin which is involved in π-π stacking in the crystal structure. α, β and *meso* labels indicate the atoms respective position in the Fe(III)PPIX ring.

6.3.4.1   [1]H Nuclear Magnetic Resonance Spectroscopy

In order to further investigate the Fe(III)PPIX species present in solution prior to crystallising out as β-haematin DMSO solvate crystals, ^{1}H NMR spectra of the crystallisation solution used in the EXAFS experiment, with and without CQfb were recorded in DMSO-d_6 (Figure 6.21). With only Fe(III)PPIX dissolved in DMSO, a spectrum consistent with that reported for a high-spin six coordinate species is observed (Figure 6.21 (a)). When the CQfb is added to the solution, the peaks in the 40-70 ppm region are still observed in the base line (Figure 6.21 (b)), but when the solution was spiked with D_2O, no peaks were observed in this region.
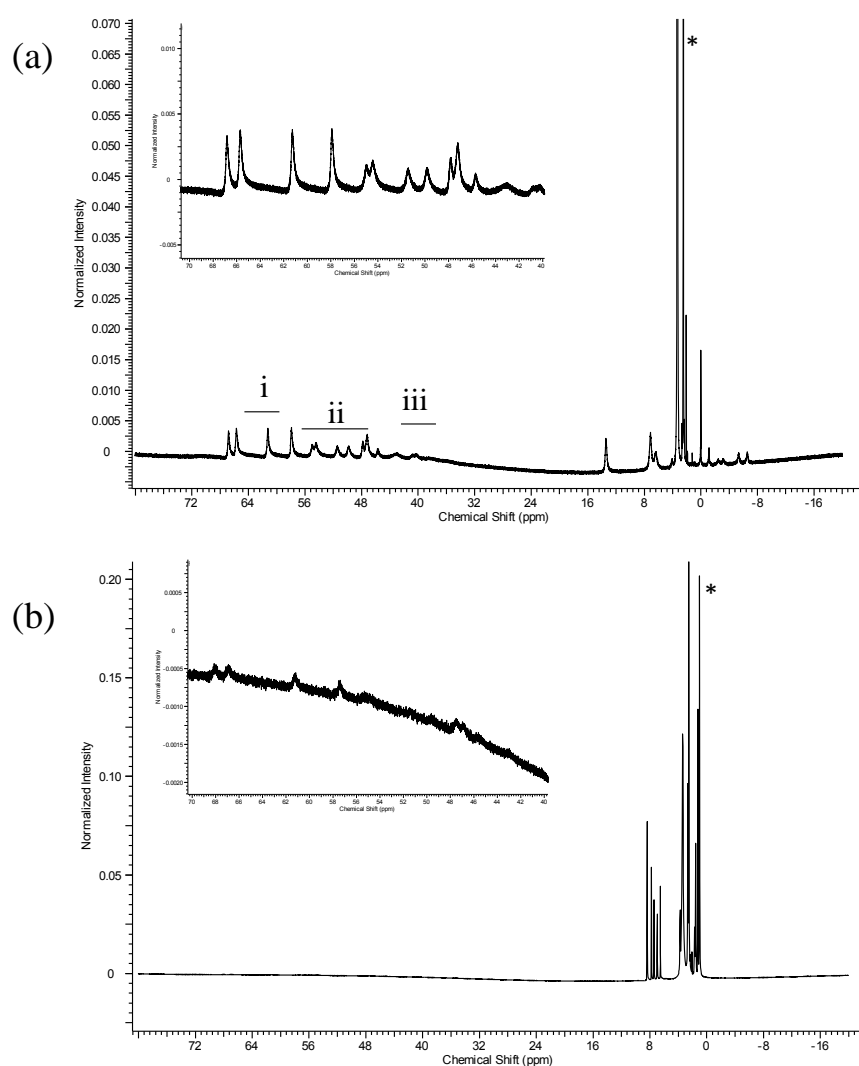
**Figure 6.21** (a) The ^{1}H NMR spectrum of Fe(III)PPIX in DMSO-d_6. Peaks are assigned based on the spectrum reported by Budd et al,[81] *i* methyl groups, *ii* vinyl α-CH, *iii* porphyrin *meso* H, *iv* propionic acid COOH group, *v* propionyl β-CH_2 and *vi cis* and *trans* vinyl β-CH_2. Asterisks indicate solvent signals. (b) The ^{1}H NMR spectrum of Fe(III)PPIX and CQfb in DMSO-d_6.

6.3.4.2 Haemin Structure Compared to EXAFS Data of Fe(III)PPIX π-π Dimers

In unpublished work by our collaborator, Dr. Victor Streltsov, at the CSIRO in Australia, X-ray absorption spectroscopy (XAS) was used to study aggregated Fe(III)PPIX in aqueous suspension. Analysing the XAS data confirmed that the samples contained a substantial amount of π-π dimers as was proposed for the Fe(III)PPPIX species to exist in aqueous solution.[79] Therefore, it was proposed that crystallisation of β-haematin may be initiated by the formation of π-π dimers. The distances calculated in this EXAFS investigation were compared to the distances in the crystal structure of both haemin and α-chlorohaemin in Table 6.6. The numbering of the EXAFS is the same as in Figure 2.13, section 2.5.4.

Table 6.6 The best fit of EXAFS for Fe(III)PPIX with the distance from the Fe (Å) centre, comparing with the same distances observed in the crystal structure of haemin and α-chlorohaemin.

EXAFS labelling[#]	EXAFS*	Haemin	α-Chlorohaematin
	Distance from Fe (Å)	Distance from Fe (Å)	Distance from Fe (Å)
N, N=4	2.055 (4)	2.055	2.056
C_α, N=8	3.08 (2)	3.086	3.091
C_{meso}, N=4	3.46 (3)	3.433	3.456
C_β, N=8	4.27 (5)	4.304	4.313
Fe, N=1	4.50 (3)	4.597	6.666
[##]Cp1 N=3	3.80 (5)	4.139 (N=2)	3.898 (N=2)
[##]Cp2 N=2	3.90 (5)	4.246 (N=4)	4.356 (N=2)
[##]Cp3 N=6	4.68 (3)	4.783 (N=2)	4.828 (N=3)

*Data collected by Dr Victor Streltsov.
[#] EXAFS labelling is the same as in Table 6.5, N indicates the number of atoms at the same distance from the Fe centre.
[##] Is the labelling for atoms back scattered from an partner Fe(III)PPIX molecule. Same meaning as in Tabel 6.5.

The distances of scattering atoms from the Fe(III) centre in Fe(III)PPIX in the EXAFS data were compared to the distances in the crystal structures of haemin and α-chlorohaemin. The distance to the Fe centre of the adjacent Fe(III)PPIX moiety, as a result of π-stacking is highlighted in light grey (Table 6.6). The crystal structure of haemin determined in this work (where crystals were grown from a acetonitrile-methanol solvent system) showed a Fe to Fe distance of 4.597 Å compared to the Fe to Fe distance of 6.666 Å in the case of α-

chlorohaemin which is closer to the structure observed in aqueous solution with a distance of 4.50 Å between the Fe centres (Table 6.6, highlighted in light grey). Therefore the haemin SCD structure presented in this work is the closest structure (to date) to represent the back to back π-π structure believed to exist in aqueous solution with the only difference being that the position occupied by the axial ligand is Cl as opposed to H_2O/HO^-.[79]

6.4   Discussion

When the crystal structure of β-haematin was solved from powder X-ray diffraction in 2000,[35] it came as a surprise that it was not in fact a polymer but rather a cyclic dimer of Fe(III)PPIX in which the propionic acid groups linked these dimers through hydrogen bonding. It is recognised that the information which can be obtained from powder X-ray diffraction is far less than from SCD. There are limitations of the PXRD technique when applied to a large organic molecule like Fe(III)PPIX which has 43 non-hydrogen atoms.[35,42] However, growing crystals of a suitable size for SCD has not been accomplished to date. The material which was used in the PXRD study was prepared from a solution containing haemin and 2,6-lutidine, where it seems reasonable that the base facilitated the dehydrohalogenation reaction necessary to yield a propionate which is then free to coordinate to the Fe(III) centre of a partner molecule and *vice versa*. [45]

In the current study, several attempts to grow single crystals of 4-aminoquinoline antimalarial drugs, in particular CQ given its success in clinical treatment, complexing with Fe(III)PPIX were undertaken without success. However, a experiment in which we used the free base of CQ (CQfb) in place of the salt yielded single crystals of β-haematin that were suitable for analysis by SCD. The crystal structure of the β-haematin DMSO solvate is the closest Fe(III)PPIX analogue (to date) of β-haematin. Even though it has been crystallised as its DMSO solvate, the structures still provide conclusive insight into the molecular nature of the synthetic counterpart of haemozoin. The repeating unit is confirmed to be a μ-propionato coordination dimer of Fe(III)PPIX, as we have come to appreciate for β-haematin based on the original PXRD structure determination.[35] The porphyrin planes are laterally shifted in two dimensions relative to one another, which results in an intradimer Fe-Fe distance of 8.982 and 8.991 Å for the species grown from CQfb and AQfb, respectively. These values agree closely with the intradimer distance reported for β-haematin (9.047 Å), which is not surprising given the geometric constraints imposed upon formation of the centrosymmetric dimer. We also showed that the geometry of the porphyrin core within the dimers determined by SCD and PXRD are in very good agreement (Figure 6.5). When comparing the five-coordinate species, the Fe(III)–O bond lengths in the two structures solved from SCD are 1.891(2) Å and 1.886(2) Å, respectively and 1.893 Å for the PXRD structure. The metal centre resides 0.42 Å out of the mean porphyrin plane for both β-haematin DMSO solvate structures and only slightly further

(0.47 Å) in the case of β-haematin. As mentioned in the introduction, section 1.5.1, Bohle and Dodd[46] recently reported the SCD structure of a propionate-linked dimer as found in haemozoin. This cyclic dimer of Ga(III)PPIX, in which the propionate side chain of one protoporphyrin unit coordinates to the Ga(III) centre of the second and *vice versa*, has a Ga(III) centre and is six-coordinate with a pyridine ligand bound *trans* to the propionate. The free propionic acid forms an intradimer hydrogen bond with its partner propionate of the same porphyrin unit. With the obvious dissimilarities between β-haematin and the Ga(III)PPIX species, the crystal structure of the β-haematin DMSO solvate determined in this work is able to provide far greater insight into the structure of β-haematin and therefore haemozoin.

Due to the enantio-facial symmetry of Fe(III)PPIX, isomers of the μ-propionato dimer can form upon coordination due to the random choice of face *via* which the incoming propionate ligand binds the iron centre. Straaso and co-workers have proposed four different Fe–O cyclic stereoisomers relevant to β-haematin, which differ in the site occupancies of the vinyl and methyl substituents.[41] There are two achiral centrosymmetric dimers labelled $cd\bar{1}_1$ and $cd\bar{1}_2$, and two chiral noncentrosymmetric enantiomers labelled $cd2(+)$ and $cd2(-)$ (Figure 6.22).
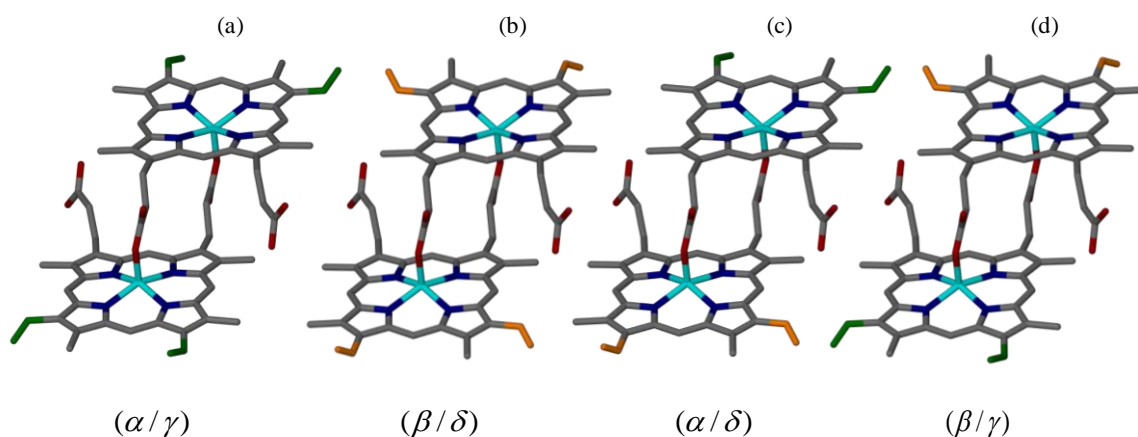
Figure 6.22 A schematic representation of the four isomers of the β-haematin μ-propionato dimer.[41] The two achiral centrosymmetric dimers, (a) and (b) have been termed cd$\bar{1}_1$, and cd$\bar{1}_2$, respectively, while the two chiral non-centrosymmetric dimers, (c) and (d) have been termed cd2(+) and cd2(-), respectively. The vinyl substituents shown in green occupy the α (top porphyrin and γ (bottom porphyrin) sites, while those shown in orange occupy the β (top porphyrin) and δ (bottom porphyrin) sites. Atom colour coding: C – grey; N – blue; O – red; Fe – cyan and vinyl groups – green and orange. Redrawn from reference.[41]

In these four isomers, the vinyl substituents are located at the α/γ, β/δ, α/δ and β/γ positions, respectively. The authors proposed that a major phase of β-haematin exists, and that it primarily consists of $cd\overline{1}_1$, and the minor phase of $cd\overline{1}_2$, with $cd2(+)$ and $cd2(-)$ included in both, giving rise to the disorder. Alternatively it has been proposed that there is only one single phase and that disorder is caused by the presence of all four isomers.[42] The latter authers also state that powder X-ray diffraction cannot distinguish between the vinyl/methyl disorder and that SCD would provide insight into resolving the issue.

In the β-haematin DMSO solvate crystals grown from either CQfb or AQfb, there is no evidence of major and minor phases. Rather, IR analysis suggests a homogenous (single phase) sample. The single crystals selected for analysis out of both samples display disorder in the positions of the vinyl and methyl substituents, and we consider combinations of the four stereoisomers to be the most likely explanation. The observed α, β, γ and δ site occupancies of 0.66, 0.34, 0.66 and 0.34 were obtained for both structures. These values can be rationalised by considering various ratios of the four isomers. For example, the observed site occupancies may arise due to 0.66 $cd\overline{1}_1$ and 0.34 $cd\overline{1}_2$ (with no contribution from $cd2(+)$ and $cd2(-)$). On the other hand 0.33 $cd\overline{1}_1$ and 0.33 each of $cd2(+)$ and $cd2(-)$, would give the same result. Taking into account that for the overall structure to remain centrosymmetric, a requirement of the space group $P\overline{1}$, equal contributions of $cd2(+)$ and $cd2(-)$ must be included, many more ratios are in fact possible. Essentially, the contribution of $cd\overline{1}_1$ can vary from 0.66 to 0.34, while that of $cd\overline{1}_2$ can vary from 0.34 to 0. At the same time, contributions from both $cd2(+)$ and $cd2(-)$ can range from 0 to 0.33 (i.e. their contribution increases while that of $cd\overline{1}_1$ and $cd\overline{1}_2$ decreases). In the original proposed structure of β-haematin, the sites at α and γ were fully occupied while the β and δ sites were empty.[35] The β-haematin DMSO solvate structure highlights the value of SCD analysis over PXRD, and provide insight into this disorder. SCD cannot, however, shed light on which ratio of the four isomers accounts for the observed site occupancies. Furthermore, whether the disorder issue is relevant or present at all in the parasite still remains questionable.

In the SCD structure of the β-haematin DMSO solvate, an intramolecular hydrogen bond is observed between the free propionic acid group of each molecule of Fe(III)PPIX and an included molecule of DMSO. Bohle and co-workers have reported the same interaction in the PXRD structure of the Fe(III) mesoporphyrin IX analogue of β-haematin, prepared

from a DMSO solution containing 2,6-lutidine.[47] When compared to the structures of β-haematin[35] and haemozoin,[36] both solved from PXRD data by means of Rietveld refinement (and maximum-entropy-based fitting in the case of haemozoin), it is interesting to note that neither of these structures contain solvent molecules. In both structures, the μ-propionato dimers of Fe(III)PPIX hydrogen bond through their free carboxylic acid groups to form a common supramolecular homosynthon, the carboxylic acid dimer (Figure 6.22 (a)).[187]

A detailed study on the hierarchy of supermolecular synthons by Zaworotko and co-workers[187] reported that out of 5690 entries in the Cambridge Structural Database (CSD) that had at least one carboxylic acid moiety present, only 34% included homosynthons (the dimer accounting for 31% of these entries and the catemer the remaining 3%). This indicates that heterosynthons are preferred in the presence of a competing hydrogen bonding moiety. In structures in which no other hydrogen bonding partners (donors or acceptors) are present, the authors showed that the characteristic carboxylic acid dimer accounts for 93%.[187] In the case of the β-haematin DMSO solvate, we see that the heterosynthon is preferred. However, closer inspection reveals that a cyclic dimer like motif is still more-or-less preserved (Figure 6.23 (b, c)).
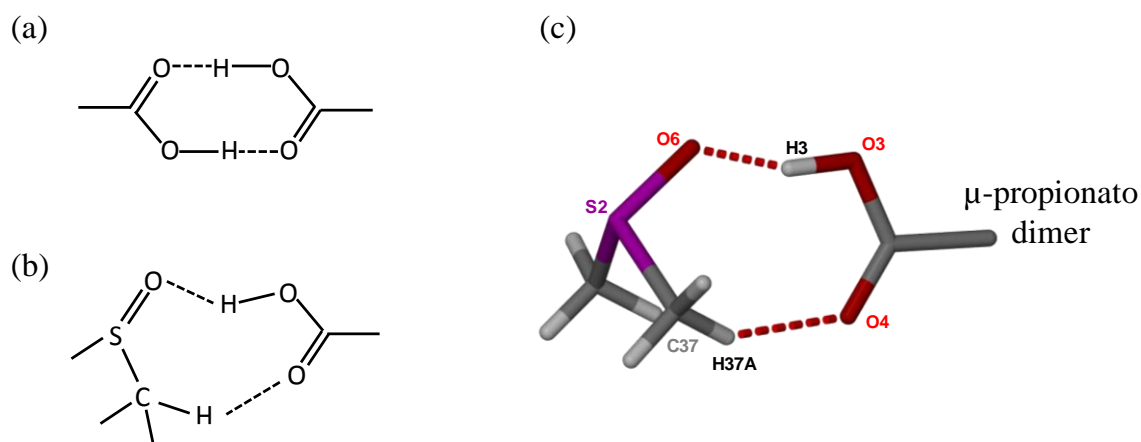

Figure 6.23 (a) The carboxylic acid dimer, present in the structure of haemozoin. (b) The preserved dimer structure in β-haematin DMSO solvate. (c) Interactions between the DMSO solvent and the free carboxylic acid group in the μ-propionato dimer of Fe(III)PPIX as found in the β-haematin DMSO solvate crystal are shown, with the atoms involved in the hydrogen bonded "dimer" labelled.

Hydrogen bonding is a well-known intermolecular interaction X-H⋯A, with X being the donor and A the acceptor. This interaction can be classified as very strong, strong and weak depending on the contact distances between atoms.[188] The O3—H3⋯⋯O6 hydrogen bond in the crystal structure of the β-haematin DMSO solvate is considered to be a strong interaction with a distance of 2.531 Å between O3 and O6. If we consider the C_{methyl} atom of the solvent to be a hydrogen bond donor, then the resulting hydrogen bond is considered to be much weaker, with the distance between C37 and O4 in the crystal structure being 3.393 Å, and the bond angle 28.97^{o} (Figure 6.23).

Each β-haematin DMSO solvate crystal contains three molecules of solvent (DMSO) per molecule of Fe(III)PPIX. As mentioned in the introduction, it is interesting that malaria pigment is able to reversibly absorb up to 14% of its mass in water (a mol ratio of 4.78 H_2O molecules compared to Fe(III)PPIX).[189] PXRD data has shown that upon hydration, samples of haemozoin become more ordered, which suggests that water molecules may be present in haemozoin and β-haematin, where they contribute to the crystallinity. Even though it is still unclear where the water that is absorbed resides in the crystal, the possibility that we could exchange the DMSO in the β-haematin DMSO solvate structure for water was considered. However, all attempts to do so with either water or methanol were not successful. Since the original structural interpretation of β-haematin did not show any solvent molecules, the role played by the solvents (DMSO or water) is yet to be fully appreciated. It may well have great implications for our understanding of the biological target haemozoin, proposed to grow at a lipid-water interface,[60] however, further evidence is still required in order to substantiate this.

The fact that β-haematin DMSO solvate crystals were grown in the presence of inhibitor drugs, CQfb or AQfb, is interesting and brings up a few questions. How is it possible for β-haematin DMSO solvate to grow in the presence of an inhibitor? And what role is the drug molecule playing? At first one would assume that in the absence of another base, CQfb or AQfb would simply act as the base which is required for overall dehydrohalogenation. However looking at the kinetic effect of CQ and AQ on the rate of β-haematin formation investigated in this work (Chapter 5), and previously demonstrated in aqueous acetate medium,[71,137] suggests that CQ and AQ, in addition to acting as a base in the crystallisation medium, may also be acting kinetically to slow down the rate of β-haematin, thereby enabling the formation of single crystals of β-haematin DMSO solvate.

The crystal structure of haemin shown in this work gives us valuable insight into the structure of a π-π dimer. In this structure, disorder in the vinyl occupancies was also found. The observed α and β site occupancies are 0.48 and 0.52, respectively. In the α-chlorohaemin it was only mentioned that the vinyl group may be on either the α or β position, but not on both at once.[82] Another related structure which has been used to model the π-π dimer previously is that of the aqua-iron(III)octaethylporphyrin perchlorate (Fe(OEP)(H$_2$O))ClO$_4$ (Figure 6.24).[83] However this structure has only ethyl groups located around the porphyrin with no methyl, vinyl or propionic acid groups as found in Fe(III)PPIX, and the interdimer Fe–Fe distance of stacking molecules in (Fe(OEP)(H$_2$O))ClO$_4$ is 5.083 Å, compared to 4.592 Å and 6.666 Å for haemin and α-chlorohaemin respectively.

(a)   (b)
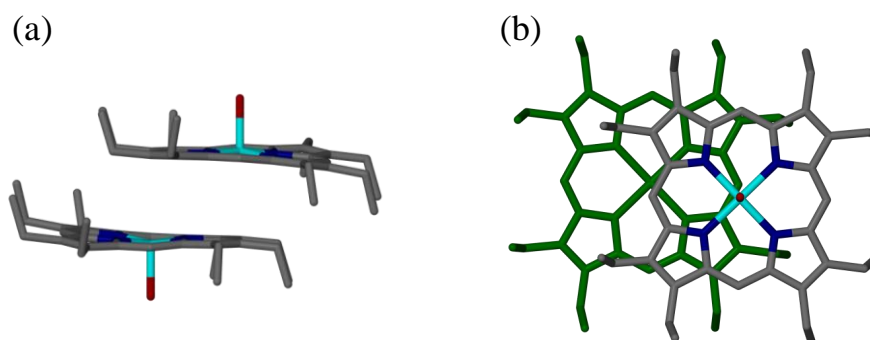
Figure 6.24 The SCD structure of aqua-iron(III)octaethylporphyrin perchlorate (a) side view, (b) top view. The structure was extracted from the Cambridge Structural Database,[84] (reference code HECZUK) and displayed in XSEED.[143]

Haemin being able to form in the presence of AQ is interesting, since it has been proposed that 4-aminoquinoline antimalarials promote *μ*-oxo dimer formation.[122] Comparing the method used to grow the crystals which yielded the haemin structure, namely a solution of acetonitrile/methanol AQ present in its salt form, to the method used to grow β-haematin DMSO solvate, where AQfb was used in the DMSO crystallisation medium, not one of the crystal structures have the drug molecule included in the crystal structure. The results indicate that the protonation state of the drug can influence Fe(III)PPPIX speciation.

Utilizing the ability of the EXAFS to model the local atomic structure around the Fe centre of Fe(III)PPIX, the species of Fe(III)PPIX present in solution prior to β-haematin DMSO solvate crystallisation has been investigated in the current work. It is shown that in this

environment, the species present in solution prior to crystal formation is a back to back (π-π) dimer of Fe(III)PPIX with the unligated faces facing one another and either H_2O or HO^- as the axial ligand directed outwards. The distance of the offset π-π dimers Fe centres in solution is 4.6 Å, therefore it does not appear that the μ-oxo dimer is formed in the presence of the CQfb and the EXAFS data indicate no interaction between CQ and the Fe(III) centre of Fe(III)PPIX. A similar investigation of mesohaematin anhydride (synthetic analogue of haemozoin) to probe the structure in the presence and absence of CQfb was carried out by Walczak *et al.*[162] In contrast to their findings where the authors contributed the additional features in the EXAFS spectra at 2.5 Å to a CQ-ferrimesoporphyrin IX complex (refer back to Figure 1.19, section 1.5.1), our results for the EXAFS spectrum of the β-haematin DMSO solvate crystals do not support the formation of a CQ-Fe(III)PP IX complex.

Since an understanding of the speciation of Fe(III)PPIX in solution has direct implications for understanding the nucleation and formation of haemozoin, this SCD data of the π-π dimer and the β-haematin DMSO solvate gives us structural insight into the proposed formation of haemozoin at the lipid-water interface.[73,79] Therefore, the formation of the haemozoin precursor dimer (exemplified by the β-haematin DMSO solvate structure), Figure 6.25, only requires that the π-π dimer of Fe(III)PPIX in aqueous solution simply changes in a lateral shift of the two porphyrins when entering the lipid environment to adopt the correct conformation to coordinate. This model is supported in the crystal growth mechanism of the β-haematin DMSO solvate. The EXAFS data suggest that Fe(III)PPIX starts out as a back to back π-π dimer in the crystallisation solution, and provides us with valuable insight in understanding the formation of β-haematin from Fe(III)PPIX.
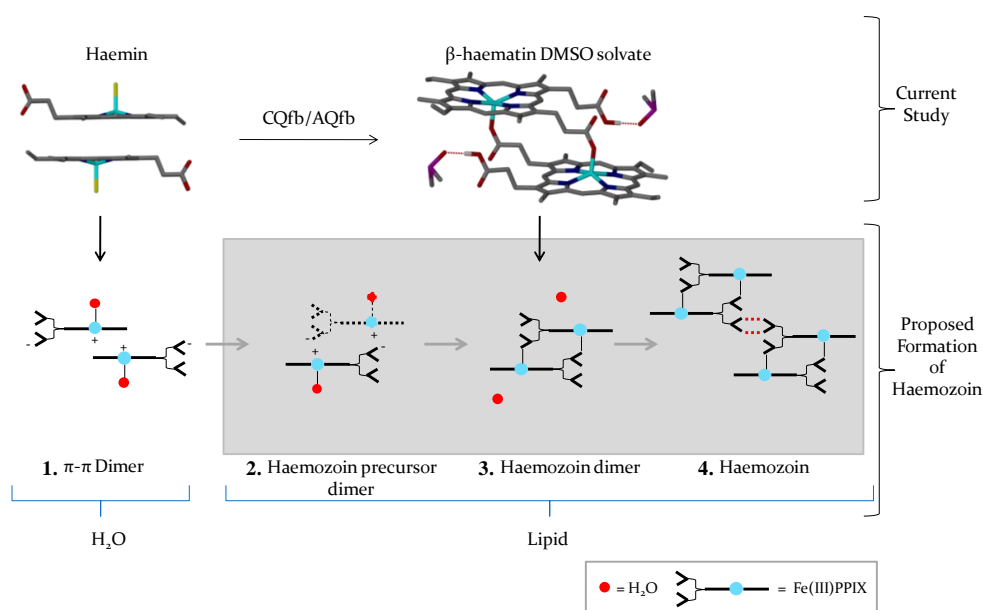
Figure 6.25 The proposed mechanism of the formation of haemozoin at the lipid water interface. Starting in the aqueous where Fe(III)PPIX is proposed to exist as a π-π dimer (1) supported by the structure of haemin. When the π-π dimer enters the lipid environment, the formation of the haemozoin precursor dimer (2) only requires the coordination of the positively charge propionate to coordinate to the negatively charged Fe centre to form the haemozoin dimer (3), supported by the structure of β-haematin DMSO solvate dimer. In order to form haemozoin, all that is required is the loss of the H_2O and the hydrogen bonding between the haemozoin dimers (4).

6.5   Conclusions

To develop new antimalarial drugs, it is imperative to understand the crucial pathway of haemozoin formation. The crystals of the β-haematin DMSO solvate reported in this work are the first Fe(III)PPIX model of haemozoin to be studied by SCD. These crystals provide the most accurate structural insight to date for a Fe(III)PPIX model of haemozoin and the π-π dimer predicted in aqueous solution. Though the crystallisation environment does not represent that of the parasite, it is still very relevant in gaining deeper insight into the nucleation and formation of β-haematin. The EXAFS results indicate that the back to back π-π dimer of Fe(III)PPIX is present in solution as the precursor to the formation of the β-haematin DMSO solvate. This π-π dimer can be thought of as the building block in the nucleation initiation of β-haematin DMSO solvate crystals and the crystal structure of haemin provides the insight into the molecular structure of the precursor. These SCD structures may aid in probing Fe(III)PPIX drug interactions in the design of novel antimalarial drugs.

7   Overall Conclusion and Future Work

7.1   Overall Conclusion

Haemozoin, the characteristic pigment observed in the blood of victims suffering from malaria, still remains a validated drug target for quinoline antimalarial drug development.[55,190] With widespread resistance to drugs currently used in treatment, there are extensive attempts to design novel haemozoin inhibitors. Given that the large majority of quinoline antimalarials have been shown to inhibit the formation of synthetic haemozoin (β-haematin), this process has been the focus of the current study. Understanding the pharmacophore of quinolines, as well as how β-haematin formation is mediated and inhibited, were the main objectives. In particular, the work in this dissertation gives insight into the different interactions which are possible between ferrihaem (Fe(III)PPIX), be it in solution or the solid-state (β-haematin), and clinically-relevant quinoline antimalarial drugs.

Prior to this study, very little structural information existed to conclusively demonstrate how antimalarial drugs interact with Fe(III)PPIX, either in its free form or as haemozoin. The structures of the QD-Fe(III)PPIX, QN-Fe(III)PPIX and MQ-Fe(III)PPIX complexes determined in this work by single crystal X-ray diffraction provide detailed insight into the key interactions formed between the drug molecule and Fe(III)PPIX, at least in the case of the quinoline methanol antimalarial drugs. By targeting free Fe(III)PPIX in solution, which is a precursor to β-haematin formation, the three structures provide conclusive experimental evidence for a three-point binding mode which includes direct coordination of the drug to the Fe(III) centre through their benzylic alcohol functional group, π-stacking between drug and porphyrin aromatic systems, and finally intramolecular hydrogen bond formation. In the case of the *Cinchona* alkaloids (QD and QN), this was observed between the porphyrin propionate group and the protonated quinuclidine nitrogen atom of the drug, while in the MQ complex, a network of intramolecular hydrogen bonding between the propionate and propionic acid side chains of Fe(III)PPIX, with further two between each of these groups and the piperidinium nitrogen atom of the drug was observed. The intramolecular hydrogen bonds are proposed to play an important part in stabilising these crystal structures, and are in fact considered fundamental to be able to rationalise activity. It has been shown computationally, that the ease by which the active and inactive *Cinchona* alkaloids form this intramolecular hydrogen bond is directly correlated to their

biological and β-haematin inhibitory activity.[85] Given that the intramolecular hydrogen bond was observed in the QD-Fe(III)PPIX crystals which were grown from a solvent system rich in hydrogen bonding partners (3:7 DMSO-methanol), this support a previous hypothesis that QD may be suitably pre-organised given its stereochemical configuration.[89] It has long been thought that stereochemical effects are the key to the greater activity of QD compared to QN. However, this current study has provided conclusive evidence in favour of a proposal that it is not the stereochemistry of the drug alone which is important, but rather the impact of the drug's stereochemistry on its ability to form the key interactions with Fe(III)PPIX described above. The EXAFS data indicate that the coordination complexes are also present in solution, however, due to the distance of the atoms involved in intramolecular hydrogen bond formation from the Fe centre exceeding the analysed coordination sphere, we are not in a position to comment on whether the intramolecular hydrogen bonds persist in solution or not. Given that the coordination complexes do exist in solution, we propose that this mode of interaction may contribute to the antimalarial action of these drugs, since binding to free Fe(III)PPIX would limit haemozoin formation.

Due to increasing interest in the lipid-mediated mechanism of β-haematin formation, and the fact that drug activity is likely to take place in this non-aqueous environment, a biomimetic system was used in this study to model the lipid-water interface. Drug activity was investigated under conditions that are more biologically-relevant than previous assays, and experimentally-determined IC_{50} values for CQ, AQ, QN and QD show excellent correlation with biological data determined against CQ-sensitive parasite strains, 3D7 and HB3. The lipid-water interface system was also used to investigate the effect of quinoline antimalarial drugs on the kinetics of β-haematin formation. Previous studies performed under non-biological conditions have shown that quinoline antimalarial drugs decrease the rate at which β-haematin is formed, rather than thermodynamically inhibit its formation.

The kinetic investigation of β-haematin formation under biomimetic (lipid-water interface) conditions in the presence of antimalarial drugs shows that at low concentration of both 4-aminoquinoline and quinoline methanol compounds, a decrease in the rate at which β-haematin is formed is effected by the drug. However, as the drug concentration is increased, a decrease in the final yield of β-haematin is observed. This dual mode of action has not been considered before by other investigators. In order to explain the exponential

kinetics of β-haematin formation observed in the presence of lipid, a model was developed in an attempt to explain these observations.

The kinetic model is based on the Avrami model,[69,70] and incorporates the premises of the Langmuir isotherm.[182,183] The experimental data strongly support a mechanism of antimalarial drug action by adsorption to the growing face of β-haematin, and the strength of interaction between a drug and the surface is measurable (log K_{ads}). At significantly high drug concentration, precipitation of Fe(III)PPIX was included to account for the observed decrease in yield of β-haematin, and it is possible that a Fe(III)PPIX-drug complex is formed. The kinetic model provides a basis for furthering our understanding of β-haematin inhibition processes under biomimetic conditions, although it is recognised that a kinetic model cannot necessarily predict a mechanism.

Finally, the single crystal X-ray diffraction structures of the β-haematin DMSO solvate and haemin determined in this study provide the most accurate structural insight to date for a Fe(III)PPIX model of haemozoin and the π-π dimer predicted in protic solution. Based on the reported EXAFS data, a model in support of the π-π dimer with the outward axial ligands being either H_2O of HO^- is postulated to be the precursor species in the formation of β-haematin. Furthermore, the inclusion of a free base species that is also antimalarially active supports the kinetic data which indicate that a reduction in the crystal growth rate is achieved in the presence of a β-haematin inhibitor.

Overall, this body of work provides valuable structural insight into the possible mode of inhibition, by quinoline antimalarials as well as structural insight into the proposed target, β-haematin (Figure 7.1), and thus contributes to the growing literature which may inform the rational design of novel antimalarial haemozoin inhibitors.
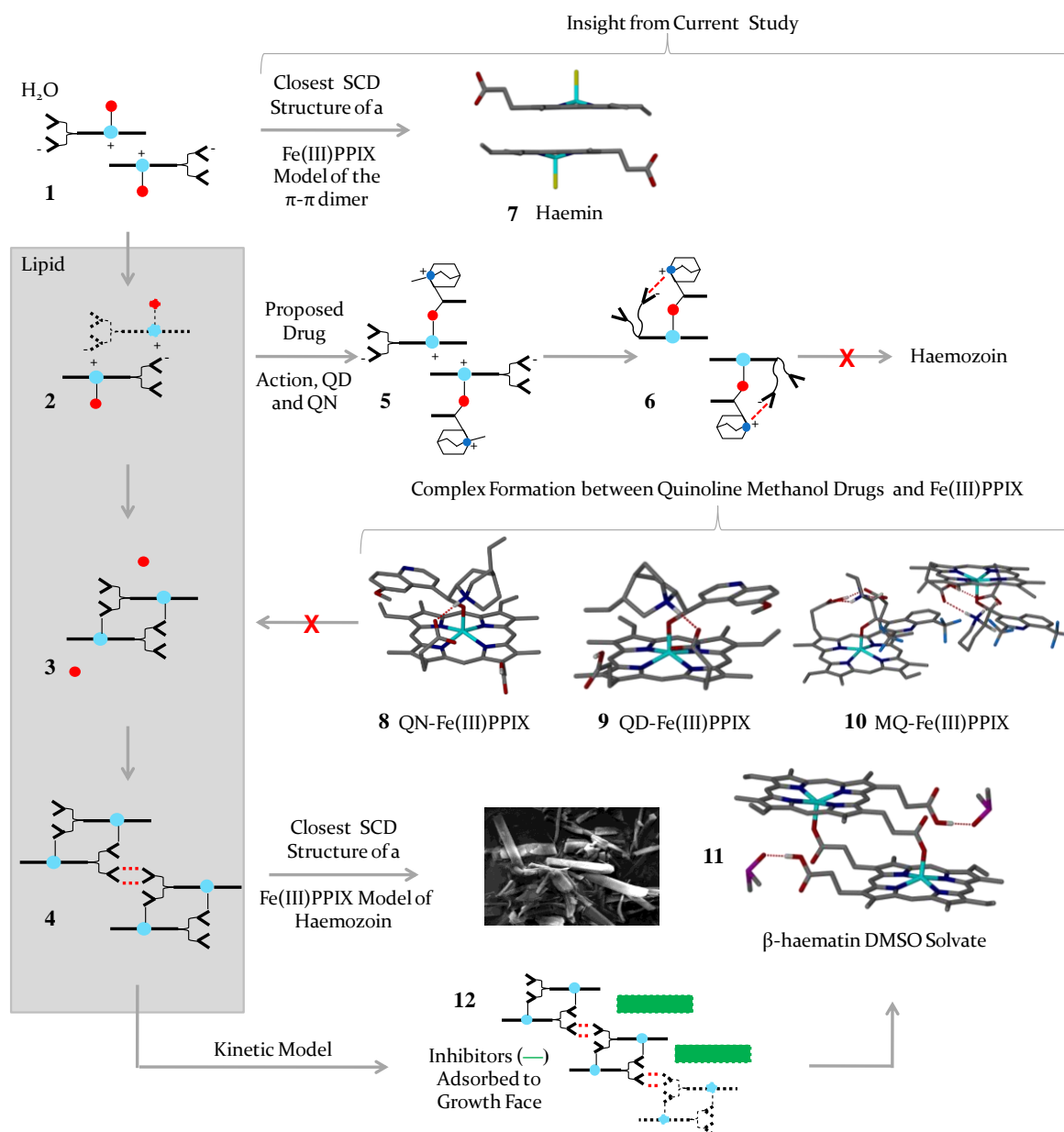
Figure 7.1 The main conclusions reached from this study. For a description of the proposed route of haemozoin formation (1-4) and inhibition (5 and 6), refer back to Figure 1.34 and Figure 1.50, respectively. (7) The SCD structure of haemin provides structural insight into the π-π dimer shown to exist in aqueous solution. (8-10) The Fe(III)PPIX-drug complexes shown, inhibit haemozoin formation *via* coordination, π-π interactions and intramolecular hydrogen bonding. (11) The β-haematin DMSO solvate SCD structure provides the most accurate structural insight to date of a Fe(III)PPIX model of haemozoin. (12) The kinetic model developed provides essential insight for furthering our understanding of β-haematin inhibition processes under biomimetic conditions. The data strongly support a mechanism of antimalarial drug action by adsorption to the growing face of haemozoin, as well as precipitation of haematin at high drug concentration, possibly as a Fe(III)PPIX-drug complex (8-10).

7.2 Future Work

The elucidation of the crystal structures of the quinoline methanol antimalarial drug (QN, QD and MQ) complexes of Fe(III)PPIX indicate that drug activity may involve three key interactions. The intramolecular hydrogen bond is thought to be the key interaction for determining activity, at least when considering the active and inactive *Cinchona* alkaloids. An understanding of how antimalarial compounds interact with Fe(III)PPIX, specifically within the food vacuole of the malaria parasite, has important implications in future drug development. In order to address the biological relevance of the complexes obtained in this work, the following studies are proposed:

- Investigate drug-treated parasites spectroscopically in an attempt to characterise and locate the Fe(III)PPIX-drug species as they occur *in vivo*. One technique which may offer insight in this regard may be Resonance Raman Spectroscopy (RRS), due to its high sensitivity and selectivity. Webster *et al.*[191] have shown that RRS is able to resolve structural changes in haemozoin after incubation with CQ in infected erythrocytes. This technique has important implications for monitoring the effect of antimalarials on their proposed target Fe(III)PPIX, and may thus be the link between the crystal structures and their biological relevance *in vivo*.

- Continue ongoing experimental efforts to crystallise Fe(III)PPIX complexes with the inactive *Cinchona* alkaloids, namely 9-epiquinidine and 9-epiquinine.

- An EXAFS investigation of the crystallisation solutions of QD-Fe(III)PPIX and QN-Fe(III)PPIX complexes, in which the active alkaloids are replaced with the inactive alkaloids (EQN and EQD), may provide insight into whether the inactive compounds coordinate to the Fe centre or not. If coordination does take place, intramolecular hydrogen bonding would not be expected,[85] and the protonated quinuclidine nitrogen atom, and propionate group would most likely be involved in hydrogen bonding to solvent molecules. This may be the reason for our unsuccessful attempts to date to crystallise these complexes.

- Use the Fe(III)PPIX-drug complexes as a scaffold for synthesising novel new antimalarial haemozoin inhibitors, based on the interactions shown to exist in the solid state, and test their antimalarial activity against *P. falciparum*.

In this work, the lipid-water interface system was validated as a means to investigate the inhibition activities of quinoline antimalarial drugs. One drawback of the system is the fact

that only aqueous soluble drugs can be tested using the current approach. In the same system, the observed kinetics of β-haematin formation in the presence of quinoline antimalarial drug led to the development of a kinetic model, which proposes that the biologically-relevant mode of drug action is when inhibitor molecules adsorb onto the crystal surface. To investigate the relevance of the adsorption onto β-haematin crystals, and to further modify the procedures so that non-aqueous soluble compounds can be studied using the lipid-water interface, the following studies are proposed:

- Develop the methodology of the lipid-water interface assay further in order to be able to investigate drugs not soluble in the aqueous medium. It is necessary to investigate means of testing the activities of aqueous insoluble compounds such as mefloquine (MQ), lumefantrine (Lf) and halofantrine (Hf) using the lipid-water interface assay. One solution may be to incorporate these and other such drugs into the Fe(III)PPIX-lipid premix, which is prepared in a 1:9 (*v/v*) acetone:methanol solution (as was attempted for MQ). The total volume of the premix is only 200 μL which means that the active compound is essentially added directly to the interface, whereas previously it was necessary to first concentrate the drug at the interface out of the bulk aqueous phase (5 mL). Since we have already shown in this study that incubation time has a significant impact on the IC_{50} value, this would need to be carefully investigated.

- Making us of LynxTag-CQ, where a fluorescent marker was successfully tagged to CQ, [192,193] attempts to visualise CQ adsorbed to β-haematin crystals may provide definitive insight into the mechanism of drug action. By using the fluorescent-labelled CQ in inhibition studies, the result may possibly confirm adsorbance of CQ onto the growing crystal surface of β-haematin (haemozoin), by use of fluorescence microscopy.

Based on the crystal structure of β-haematin DMSO solvate, solvent in the crystal is relevant in stabilising the structure. To investigate how the β-haematin DMSO solvate crystal may be used in drug development, and to further probe the relevance of solvent, if any, in haemozoin crystal formation, the following studies are proposed:

- Since it has been possible to predict the face of β-haematin that would most likely support drug adsorption,[40] it should also be possible to compute the attachment energies for the different faces of the DMSO solvate crystal and hence use their

structure as a model in the rational design of novel probes for controlling the crystallisation process.

- Since the original structure interpretation of β-haematin does not show any included solvent molecules, the role played by solvents (DMSO or water) is yet to be fully appreciated. Therefore, attempts to crystallise β-haematin from other solvents are ongoing and may aid in furthering our understanding of the role played in the structure of malarial pigment.

Appendix I – Derivation of the Kinetic Model

The Avrami equation (eq. 1), has been used to model crystallisation processes, that is how solids transform from one phase into another at a constant temperature. It specifically describes the kinetics involved in crystallisation.[69,70]

$$\frac{m_R}{m_0} = e^{-zt^n} \tag{1}$$

In the above equation, m_R is the mass of Fe(III)PPIX remaining at time t compared to the initial mass m_0, z is an empirical rate constant, and n is a constant known as the Avrami constant, which is usually an integer ranging between 1 and 4.

The Langmuir isotherm (eq. 2), where the extent of monolayer coverage of a solid surface θ, is related to the partitioning of an adsorbant between the gas phase and the adsorbed state as a function of applied pressure P of the adsorbing reactant and the equilibrium adsorption constant K_{ads}.[182]

$$\theta = \frac{K_{ads}[P]}{1+K_{ads}[P]} \tag{2}$$

The Langmuir isotherm can be used to characterise the adsorption of antimalarial drugs onto the growing face of β-haematin in a similar manner (eq. 3). Here, the drug molecules are in contact with the solid surface of β-haematin at a fixed temperature and the drug concentrations [D] can be thought of in the same way as the pressure of the adsorbing reactant in the gas phase.

$$\theta = \frac{K_{ads}[D]}{1+K_{ads}[D]} \tag{3}$$

To generate the equation in the context of β-haematin crystal growth in the presence of an inhibitor, the adsorption of drug D to binding sites S were considered in the light of Scheme 2 (Chapter 5), on the surface of β-haematin in a similar manner to the Langmuir behaviour. Arriving at the following equilibrium:

$$D + S \underset{\rightleftharpoons}{\overset{K}{}} DS \tag{4}$$

In eq. 4, D is an inhibitor (such as CQ), S is an empty surface site where an inhibitor may adsorb, and is equivalent to the $(1-\theta)$, DS is the filled adsorption sites and is equivalent to θ. It is important to note that by writing this equilibrium equation, we are making an

inherent assumption that there is a fixed number of adsorption sites present on the surface of the crystal. The extent of adsorption S (θ), would be dependent on the concentration of the inhibiting drug [D]. Thus the adsorption process between the drug molecules [D], and the number of free sites $(1 - \theta)$, and adsorbed sites θ, can be presented by a forward reaction governed by the rate of adsorption eq. 5:

$$rate\ of\ adsorption = k_a \times [D] \times N \times (1 - \theta) \tag{5}$$

where N is the total number of sites available for adsorption, and k_a is the adsorption rate constant. The reverse direction is governed by the rate of desorption eq. 6:

$$rate\ of\ desorption = k_d \times N \times \theta \tag{6}$$

where k_d is the desorption rate constant. At equilibrium, the rates of adsorption and desorption are expected to be equal:

$$k_a \times [D] \times N \times (1 - \theta) = k_d \times N \times \theta$$

$$K_{ads} = \frac{k_a}{k_d} = \frac{\theta}{(1 - \theta)[D]}$$

$$K_{ads} = \frac{\theta}{(1 - \theta)[D]}$$

Solving θ finally yields eq. 7, which is reminiscent of the Langmuir isotherm, with the equilibrium adsorption constant, K_{ads}.

$$\theta = \frac{K_{ads}[D]}{1 + K_{ads}[D]} \tag{7}$$

The number of sites that are available for continued crystal growth is equivalent to $1 - \theta$. It is reasonable to propose that any continued growth of β-haematin is then dependent on the number of free sites, $(1 - \theta)$. Therefore:

$$1 - \theta = 1 - \frac{K_{ads}[D]}{(1 + K_{ads}[D])} \tag{8}$$

Rearranging eq. 8 generates eq. 9:

$$1 - \theta = \frac{1}{1 + K_{ads}[D]} \tag{9}$$

The growth rate of β-haematin in the presence of a drug, z_{obs}, (Chapter 5, Scheme 2) relative to its growth rate in the absence of drug (z) is proportional to the number of vacant binding sites. Therefore, the rate constant for the formation of β-haematin in the presence of an drug z_{obs}, is given by eq. 10. Since, $\frac{z_{obs}}{z} = 1 - \theta$, therefore

$$z_{obs} = z(1 - \theta) = \frac{z}{1 + K_{ads}[D]} \tag{10}$$

where z is the rate constant for β-haematin formation in the absence of drug and z_{obs} is the observed rate constant for β-haematin formation in the presence of drug.

The plot of the inverse of the observed rate constant, z_{obs}, as a function of drug concentration yields a linear regression, from which the values of z and K_{ads} can be determined from the values of the y-intercept and slope respectively, as shown in eq.11.

$$\frac{1}{z_{abs}} = \frac{1 + K_{ads}[D]}{z} = \frac{K_{ads}}{z}[D] + \frac{1}{z} \tag{11}$$

To explain the observed decrease in final yield of β-haematin formed at higher drug concentrations, it was necessary to incorporate a competing drug concentration-dependent process that would result in the irreversible precipitation of haematin, most likely as a drug complex ($DH_{(s)}$), (Scheme 2, Chapter 5). According to this mechanism, the rate of depletion of haematin in solution ($H_{(aq)}$) can be determined by eq. 12.

$$\frac{d[H_{(aq)}]}{dt} = -z_{obs}[H_{(aq)}] - k_2[H_{(aq)}][D_{(aq)}]^m \tag{12}$$

Rearranging eq. 12 generates eq. 13.

$$\frac{d[H_{(aq)}]}{dt} = -[H_{(aq)}]\left(z_{obs} + k_2[D_{(aq)}]^m\right) \tag{13}$$

where k_2 is the rate constant for the irreversible precipitation of haematin brought about by interaction with the drug. $[D_{(aq)}]$ (simplified as $[D]$ in the equations below) and $[H_{aq}]$ are the respective concentrations of drug and haematin in solution, and $m \geq 0$. It was found that the best agreement with the experimental results is achieved when m = 2, this value is assumed for the remainder of the derivation. Assuming $[D_{(aq)}]$ to be in large excess compared to haematin ($[D_{(aq)}] \gg [H_{aq}]$), and therefore essentially a constant, the concentration of haematin remaining in solution as a function of time can be determined by integration, to generate eq. 14.

$$\int \frac{1}{[H_{(aq)}]} d[H_{(aq)}] = -\left(z_{obs} + k_2[D]^2 \int_0^t dt\right)$$

$$ln[H_{(aq)}] - ln[H_{(aq)}]_0 = ln\frac{[H_{(aq)}]}{[H_{(aq)}]_0} = -(z_{obs} + k_2[D]^2)t$$

$$[H_{(aq)}] = [H_{(aq)}]_0 \cdot e^{-(z_{obs}+k_2[D]^2)t} \tag{14}$$

Since the formation of β-haematin is directly dependent on the concentration of haematin in solution, eq.14 is a useful expression to determine the rate of the formation of β-haematin (eq. 15a). It follows from the corresponding integral eq. 15b of eq. 15a that the yield of β-haematin, $[\beta_{(s)}]$, is given by eq. 15c.

$$\frac{d[\beta_{(s)}]}{dt} = z_{obs}[H_{(aq)}] = z_{obs} \cdot [H_{(aq)}]_0 \cdot e^{-(z_{obs}+k_2[D]^2)t} \tag{15a}$$

$$\int d[\beta_{(s)}] = z_{obs}[H_{(aq)}]_0 \int_0^t e^{-(z_{obs}+k_2[D]^2)t} dt \tag{15b}$$

$$[\beta_{(S)}] = \frac{-z_{obs}[H_{(aq)}]_0}{(z_{obs}+k_2[D]^2)} e^{-(z_{obs}+k_2[D]^2)t} \Bigg]_0^t$$

$$[\beta_{(S)}] = \frac{z_{obs}[H_{(aq)}]_0}{(z_{obs}+k_2[D]^2)} - \frac{z_{obs}[H_{(aq)}]_0}{(z_{obs}+k_2[D]^2)} e^{-(z_{obs}+k_2[D]^2)t}$$

$$[\beta_{(S)}] = \frac{z_{obs}[H_{(aq)}]_0}{(z_{obs}+k_2[D]^2)} \left(1 - e^{-(z_{obs}+k_2[D]^2)t}\right) \tag{15c}$$

As written above, eq. 15c implies that the yield of β-haematin will be measured as an actual concentration, but in practice, the yield is determined as a fraction relative to the initial amount of haematin in the system (i.e. $\left([H_{aq}]_0 = 100\%\right)$) eq. 16.

$$\%[\beta_{(S)}] = \frac{100z_{obs}}{(z_{obs}+k_2[D]^2)} \left(1 - e^{-(z_{obs}+k_2[D]^2)t}\right) \tag{16}$$

Acknowledging this, and substituting the expression derived above for the observed rate constant (eq. 10), into eq. 16, the kinetic model is reached (eq. 17).

$$\%[\beta_{(S)}] = \frac{100z}{(z+k_2[D]^2+k_2K_{ads}[D]^3)} \left(1 - e^{-\left(\frac{z+k_2[D]^2+k_2K_{ads}[D]^3}{1+K_{ads}[D]}\right)t}\right) \tag{17}$$

To take into account that the lipid (MPG) is not able to convert $[H_{aq}]$ into a yield of 100% β-haematin, an additional term Y, was introduced to account for the fractional yield (0.7), and the overall kinetic model is reached (eq. 18).

$$\%\beta_{(S)} = \frac{100Yz}{(z+k_2[D]^2+k_2K_{ads}[D]^3)}\left\{1 - e^{-\left(\frac{z+k_2[D]^2+k_2K_{ads}[D]^3}{1+K_{ads}[D]}\right)t}\right\} \tag{18}$$

Eq. 18 incorporates both the adsorption of drug to the surface of β-haematin as well as the drug-induced precipitation of haematin, most likely as a drug complex (DH$_{(s)}$).

References

(1)   Webb, J. L. A., Jr *Humanity's burden :a global history of malaria*; Cambridge University Press, **2009**.

(2)   World Health Organisation, World Malaria Report,; www.who.int/malaria/world_malaria_report_2009/en/index.html, accessed on 01-2013.

(3)   Wellems, T. E.; Plowe, C. V. *J. Infect. Dis.* **2001**, *184*, 770-776.

(4)   Center for Disease Control and Prevention,;http://www.cdc.gov/malaria/ history/ index.htm

(5)   Lancisi, G. M. *De noxiis paludum effluvius eorumque remediis*; Salvioni, J M: Rome, 1717.

(6)   Laveran , C. L. A. *A newly discovered parasite in the blood of patients suffering form malaria. Parasitic etiology of attacks of malaria*; Cornell University Press: Ithaca, New Yorc, **1978**.

(7)   Ross, R. *Br. Med. J.* **1897**, *ii*, 1736-1788.

(8)   Klayman, D. L. *Science* **1985**, 6, 1049-1055.

(9)   Wright, D. F. *Nature* **2002**, *419*, 495-496.

(10)   Frederich, M.; Dogne, J. M.; Angenot, L.; De Mol, P. *Curr. Med. Chem.* **2002**, *9*, 1435-1456.

(11)   Ashley, E.; McGready, R.; Proux, S.; Nosten, F. *Travel Med. Infect. Dis.* **2006**, *4*, 159-73.

(12)   Kumar, A.; Katiyar, S. B.; Agarwal, A.; Chauhan, P. M. S. *Curr. Med. Chem.* **2003**, *10*, 1137-1150.

(13)   Bannister, L. H.; Hopkins, J. M.; Fowler, R. E.; Krishna, S.; Mitchell, G. H. *Parasitol. Today* **2000**, *16*, 427-433.

(14)   Eggleson, K. K.; Duffin, K. L.; Goldberg, D. E. *J. Biol. Chem.* **1999**, *274*, 32411-32417.

(15)   Banerjee, R.; Liu, J.; Beatty, W.; Pelosof, L.; Klemba, M.; Goldberg, D. E. *Proc. Natl. Acad. Sci. U.S.A.* **2002**, *99*, 990-995.

(16)   Rosenthal, P. J.; McKerrow, J. H.; Aikawa, M.; Nagasawa, H.; Leech, J. H. *J. Clin. Invest.* **1988**, *82*, 1560-1566.

(17)   Krugliak, M.; Zhang, J.; Ginsburg, H. *Mol. Biochem. Parasitol.* **2002**, *199*, 249-256.

(18)   Hayward, R.; Saliba, K. J.; Kirk, K. *J.Cell sci.* **2006**, *119*, 1016-1025.

(19)   Ursos, L. M. B.; Roepe, P. D. *Med. Res. Rev.* **2002**, *22*, 465-491.

(20)   Egan, T. J.; Combrinck, J. M.; Egan, J.; Hearne, G. R.; Marques, H. M.; Ntenteni, S.; Sewell, B. T.; Smith, P. J.; Taylor, D.; van Schalkwyk, D. A.; Walden, J. C. *Biochem. J.* **2002**, *365*, 343-347.

(21)   Egan, T. J. *Mol. Biochem. Parasitol.* **2008**, *157*, 127-136.

(22)   Olliaro, P. L.; Yuthavong, Y. *Pharmacol. Ther.* **1999**, *81*, 91-110.

(23)   Oliveira, M. F.; Silva, J. R.; Dansa-Petretski, M.; de Souza, W.; Lins, U.; Braga, C. M. S.; Masuda, H.; Oliveira, P. L. *Nature* **1999**, *400*, 517-518.

(24)   Chen, M. M.; Shi, L.; Sullivan, D. J., JR. *Mol. Biochem. Parasitol.* **2001**, *113*, 1-8.

(25)   Oliveira, M. F.; d'Avila, J. C. P.; Torres, C. R.; Oliveira, P. L.; Tempone, A. J.; Rumjanek, F. D.; Braga, C. M. S.; Silva, J. R.; Dansa-Petretski, M.; Oliveira, M. A.; de Souza, W.; Ferreira, S. T. *Mol. Biochem. Parasitol.* **2000**, *111*, 217-221.

(26)   Pisciotta, J. M.; Ponder, E. L.; Fried, B.; Sullivan, D. *Int. J. Parasitol.* **2005**, *35*, 1037-1042.

(27)   Hamsik, A. *Z. Physiol. Chem.* **1936**, *190*, 199-215.

(28)   Bohle, D. S.; Dinnebier, R. E.; Madsen, S. K.; Stephens, P. W. *J. Biol. Chem.* **1997**, *272*, 713-716.

(29)   Fitch, C. D.; Kanjananggulpan, P. *J. Biol. Chem.* **1987**, *262*, 15552-15555.

(30)   Slater, A. F. G.; Swiggard, W. J.; Orton, B. R.; Flitter, W. D.; Goldberg, D. E.; Cerami, A.; Henderson, G. B. *Proc. Natl. Acad. Sci. USA* **1991**, *88*, 325-329.

(31)   Wood, B. R.; Langford, S. J.; Cooke, B. M.; Glenister, F. K.; Lim, J.; McNaughton, D. *FEBS Lett.* **2003**, *554*, 247-252.

(32)   Brown, W. H. *J. Esp. Med.* **1911**, *13*, 290-299

(33)   Ashong, J. O.; Blench, I. P.; Warhurst, D. C. *Trans. R. Soc. Trop. Med. Hyg.* **1989**, *83*, 167-172.

(34)   Bohle, D. S.; Dinnebier, R. E.; Madsen, S. K.; Stephens, P. W. *J. Biol. Chem.* **1997**, *272*, 713-716.

(35)   Pagola, S.; Stephens, P. W.; Bohle, D. S.; Kosar, A. D.; Madsen, S. K. *Nature* **2000**, *404*, 307-310.

(36)   Klonis, N.; Dilania, R.; Hanssen, E.; Darmanin, C.; Streltsov, V.; Deed, S.; Quiney, H.; Tilley, L. *Biochem.* **2010**, *49*, 6804-6811.

(37)   Walczak, M. S.; Lawniczak-Jablonska, K.; Sienkiewicz, A.; Klepka, M. T.; Suarez, L.; Kosar, A. J.; Bellemare, M. J.; Bohle, D. S. *J. Non-Cryst. Solids* **2010**, *356*, 1908-1913.

(38)   Walczak, M.; Lawniczak-Jablonska, K.; Sienkiewicz, A.; Demchenko, I. N.; Piskorska, E.; Chatain, G.; Bohle, D. S. *Nucl. Instrum. Meth. Phys. Res. B* **2005**, *238*, 32-38.

(39)   Hartman, P.; Perdok, W. G. *Acta. Crystal.* **1955**, *8*, 49-52.

(40)   Buller, R.; Peterson, M. L.; Almarsson, O.; Leiserowitz, L. *Crystal Growth & Design* **2002**, *2*, 553-562.

(41)   Straaso, T.; Kapishnikov, S.; Kato, K.; Takata, M.; Als-Nielsen, J.; Leiserowitz, L. *Crys. Growth Des.* **2011**, *11*, 3342-3350.

(42)   Bohle, D. S.; Dodd, E. L.; Stephens, P. *Chem. Biodivers.* **2012**, *9*, 1891-1902.

(43)   IUPAC; www.chem.qmul.ac.uk/iupac/tetrapyrrole/TP1.html#p1.

(44)   Marom, N.; Tkatchenko, A.; Kapishnikov, S.; Kronik, L.; Leiserowitz, L. *Cryst. Growth Des.* **2011**, *11*, 3332-3341.

(45)   Bohle, D. S.; Kosar, A. D.; Stephens, P. W. *Can.J.Chem.* **2003**, *81*, 1285-1291.

(46)   Bohle, D. S.; Dodd, E. L. *Inorg. Chem.* **2012**, *51*, 4411-3.

(47)   Bohle, D. S.; Dodd, E. L.; Kosar, A. J.; Sharma, L.; Stephens, P. W.; Suarez, L.; Tazoo, D. *Angew. Chem. Int. Ed.* **2011**, *50*, 6151-6154.

(48)   Behere, D. V.; Goff, H. M. *J. Am. Chem. Soc.* **1984**, *106*, 4945-4950.

(49)   Marques, H. M.; Vester, K.; Egan, T. J. *J. Inorg. Biochem.* **1996**, *64*, 7-23.

(50)   Walczak, M. S.; Lawniczak-Jablonska, K.; Wolska, A.; Sienkiewicz, A.; Suarez, L.; Kosar, A. J.; Bohle, D. S. *J. Phys. Chem. B* **2011**, *115*, 1145-1150.

(51)   Walczak, M. S.; Lawniczak-Jablonska, K.; Wolska, A.; Sikora, M.; Sienkiewicz, A.; Suarez, L.; Kosar, A. J.; Bellemare, M.-J.; Bohle, D. S. *J. Phys. Chem. B* **2011**, *115*, 4419-4426.

(52)   Hempelmann, E.; Egan, T. J. *Trends Parasitol* **2002**, *18*, 11-11.

(53)   Sullivan, D. J., JR.; Gluzman, I. Y.; Goldberg, D. E. *Science* **1996**, *271*, 219-222.

(54)   Papalexis, V.; Siomos, M.-A.; Campanale, N.; Guo, X.-g.; Kocak, G.; Foley, M.; Tilley, L. *Mol. Biochem. Parasitol.* **2001**, *115*, 77-86.

(55)   Sullivan, D. J. *Int. J. Parasitol.* **2002**, *32*, 1645-1653.

(56)   Jani, D.; Nagarkatti, R.; Beatty, W.; Angel, R.; Slebodnick, C.; Andersen, J.; Kumar, S.; Rathore, D. *PLoS Pathog.* **2008**, *4*. e 1000053

(57)   Fitch, C. D.; Cai, G. Z.; Chen, Y. F.; Shoemaker, J. D. *Biochim. Biophys. Acta* **1999**, *1454*, 31-37.

(58)   Jackson, K. E.; Klonis, N.; Ferguson, D. J. P.; Adisa, A.; Dogovski, C.; Tilley, L. *Mol. Microbiol.* **2004**, *54*, 109-122.

(59)   Coppens, I.; Vielemeyer, O. *Int. J. Parasitol.* **2005**, *35*, 597-615.

(60)   Pisciotta, J. M.; Coppens, I.; Tripathi, A. K.; Scholl, P. F.; Shuman, J.; Bajad, S.; Shulaev, V.; Sullivan, D. J., Jr. *Biochem. J.* **2007**, *402*, 197-204.

(61)   Oliveira, M. F.; Kycia, S. W.; Gomez, A.; Kosar, A. J.; Bohle, D. S.; Hempelmann, E.; Menezes, D.; Vannier-Santos, M. A.; Oliveira, P. L.; Ferreira, S. T. *FEBS Lett.* **2005**, *579*, 6010-6016.

(62)   Kapishnikov, S.; Berthing, T.; Hviid, L.; Dierolf, M.; Menzel, A.; Pfeiffer, F.; Als-Nielsen, J.; Leiserowitz, L. *Proc. Natl. Acad. Sci. U. S. A.* **2012**, *109*, 11184-11187.

(63)   Kapishnikov, S.; Weiner, A.; Shimoni, E.; Guttmann, P.; Schneider, G.; Dahan-Pasternak, N.; Dzikowski, R.; Leiserowitz, L.; Elbaum, M. *Proc. Natl. Acad. Sci. U. S. A.* **2012**, *109*, 11188-11193.

(64)   Hempelmann, E. *Parasitol. Res.* **2007**, *100*, 671-676.

(65)   Ketchum, M. A.; Olafson, K. N.; Petrova, E. V.; Rimer, J. D.; Vekilov, P. G. *J. Chem. Phys.* **2013**, *139*, 121911-121919.

(66)   Bohle, D. S.; Helms, J. M. *Biochem. Biophys. Res. Commun.* **1993**, *193*, 504-508.

(67)   Blauer, G.; Akkawi, M. *Arch. Biochem. Biophys.* **2002**, *398*, 7-11.

(68)   Egan, T. J.; Mavuso, W. W.; Ncokazi, K. K. *Biochem.* **2001**, *40*, 204-213.

(69)   Avrami, M. *J. Chem. Phys.* **1939**, *7*, 1103-1112.

(70)   Avrami, M. *J. Chem. Phys.* **1940**, *8*, 212-224.

(71)   Egan, T. J.; Ncokazi, K. K. *J. Inorg. Biochem.* **2005**, *99*, 1532-1539.

(72)   Egan, T. J.; Tshivhase, M. G. *Dalton Trans.* **2006**, 5024-5032.

(73)   Egan, T. J.; Chen, J. Y.-J.; de Villiers, K. A.; Mabotha, T. E.; Naidoo, K. J.; Ncokazi, K. K.; Langford, S. J.; McNaughton, D.; Pandiancherri, S.; Wood, B. R. *FEBS Lett.* **2006**, *580*, 5105-5110.

(74)   Hoang, A. N.; Ncokazi, K. K.; de Villiers, K. A.; Wright, D. W.; Egan, T. J. *Dalton Trans.* **2010**, *39*, 1235-1244.

(75)   Huy, N. T.; Shima, Y.; Maeda, A.; Men, T. T.; Hirayama, K.; Hirase, A.; Miyazawa, A.; Kamei, K. *PLOS ONE* **2013**, *8*, e70025-e70025.

(76)   Carter, M. D.; Phelan, V. V.; Sandlin, R. D.; Bachmann, B. O.; Wright, D. W. *Combinatorial Chem. High Throughput Scr.* **2010**, *13*, 285-292.

(77)   Sandlin, R. D.; Carter, M. D.; Lee, P. J.; Auschwitz, J. M.; Leed, S. E.; Johnson, J. D.; Wright, D. W. *Antimicrob. Agents. Chemother.*, *55*, 3363-3369.

(78)   Brown, S. B.; Dean, T. C.; Jones, P. *Biochem. J.* **1970**, *117*, 733-739.

(79)   de Villiers, K. A.; Kaschula, C. H.; Egan, T. J.; Marques, H. M. *J. Biol. Inorg. Chem.* **2007**, *12*, 101-117.

(80)   Okeeffe, D. H.; Smythe, G. A.; Fuchsman, W. H.; Moss, T. H.; Lilienthal, H. R.; Caughey, W. S.; Barlow, C. H. *Bioinorg. Chem.* **1975**, *5*, 125-147.

(81)   Budd, D. L.; Lamar, G. N.; Langry, K. C.; Smith, K. M.; Nayyirmazhir, R. *J. Am. Chem. Soc.* **1979**, *101*, 6091-6096.

(82)   Koenig, D. F. *Acta cryst.* **1965**, *18*, 663-673.

(83)   Cheng, B.; Safo, M. K.; Orosz, R. D.; Reed, C. A.; Debrunner, P. G.; Scheidt, W. R. *Inorg. Chem.* **1994**, *33*, 1319-1324.

(84)   Cambridge Structural Database; V S26; Cambridge Crystallographic Data Centre: Cambridge, **2004**.

(85)   de Villiers, K. A.; Marques, H. M.; Egan, T. J. *J. Inorg. Biochem.* **2008**, *102*, 1660-1667.

(86)   Asher, C.; de Villiers, K. A.; Egan, T. J. *Inorg. Chem.* **2009**, *48*, 7994-8003.

(87)   Pasternack, R. F.; Munda, B.; Bickford, A.; Gibbs, E. J.; Scolaro, L. M. *J. Inorg. Biochem.* **2010**, *104*, 1119-1124.

(88)   Karle, J. M.; Karle, I. L.; Gerena, L.; Milhous, W. K. *Antimicrob. Agents Chemother.* **1992**, *36*, 1538-1544.

(89)   Warhurst, D. C.; Craig, J. C.; Adagu, I. S.; Meyer, D. J.; Lee, S. Y. *Malar. J.* **2003**, *2*, 1-14.

(90)   Egan, T. J.; Ross, D. C.; Adams, P. A. *FEBS Lett.* **1994**, *352*, 54-57.

(91)   Egan, T. J.; Mavuso, W. W.; Ross, D. C.; Marques, H. M. *J. Inorg. Biochem.* **1997**, *68*, 137-145.

(92)   Egan, T. J.; Hempelmann, E.; Mavuso, W. W. *J. Inorg. Biochem.* **1999**, *73*, 101-107.

(93)   Dorn, A.; Vippagunta, S. R.; Matile, H.; Jaquet, C.; Jonathan.L., V.; Ridley, R. G. *Biochem. Pharmacol.* **1998**, *55*, 727-736.

(94)   Hawley, S. R.; Bray, P. G.; Mungthin, M.; Atkinson, J. D.; O'Neill, P. M.; Ward, S. A. *Antimicrob. Agents Chemother.* **1998**, *42*, 682-686.

(95)   Egan, T. J.; Hunter, R.; Kaschula, C. H.; Marques, H. M.; Misplon, A.; Walden, J. *J. Med. Chem.* **2000**, *43*, 283-291.

(96)   Kaschula, C. H.; Egan, T. J.; Hunter, R.; Basilico, N.; Parapini, S.; Taramelli, D.; Pasini, E.; Monti, D. *J. Med. Chem.* **2002**, 3531-3539.

(97)   Nosten, F.; Terkuile, F.; Maelankiri, L.; Chongsuphajaisiddhi, T.; Nopdonrattakoon, L.; Tangkitchot, S.; Boudreau, E.; Bunnag, D.; White, N. J. *J. Infect. Dis.* **1994**, *169*, 595-603.

(98)   Schlagenhauf, P.; Adamcova, M.; Regep, L.; Schaerer, M. T.; Rhein, H.-G. *Malar. J.* **2010**, *9*.

(99)   Coatney, G. R. *Am. J. Trop. Med. Hyg.* **1963**, *12*, 121-8.

(100)   Slater, A. F. G. *Pharmacol. Ther.* **1993**, *57*, 203-235.

(101)   Yayon, A.; Cabantchik, Z. I.; Ginsburg, H. *EMBO J.* **1984**, *3*, 2695-2700.

(102)   Saliba, K. J.; Folb, P. I.; Smith, P. J. *Biochem. Pharm.* **1998**, *56*, 313-320.

(103)   Schlesinger, P. H.; Krogstad, D. J.; Herwaldt, B. L. *Antimicrob. Agents Chemother.* **1988**, *32*, 793-798.

(104)   Sanchez, C. P.; Stein, W. D.; Lanzer, M. *Trends Parasitol.* **2007**, *23*, 332-339.

(105)   World Health Organisation; www.who.int/mediacentre/factsheets/fs194/en/

(106)   Bathurst, I.; Hentschel, C. *Trends Parasitol.* **2006**, *22*, 301-307.

(107)   Krogstad, D. J.; Gluzman, I. Y.; Kyle, D. E.; Oduola, A. M. J.; Martin, S. K.; Milhous, W. K.; Schlesinger, P. H. *Science* **1987**, *238*, 1283-1285.

(108)   Fidock, D. A.; Nomura, T.; Talley, A. K.; Cooper, R. A.; Dzekunov, S. M.; Ferdig, M. T.; Ursos, L. M. B.; Sidhu, A. B. S.; Naude, B.; Deitsch, K. W.; Su, X. Z.; Wootton, J. C.; Roepe, P. D.; Wellems, T. E. *Mol. Cell* **2000**, *6*, 861-871.

(109)   Cowman, A. F.; Karcz, S.; Galatis, D.; Culvenor, J. G. *J. Cell Biol.* **1991**, *113*, 1033-1042.

(110)   Cowman, A. F.; Galatis, D.; Thompson, J. K. *Proc. Natl Acad. Sci. USA* **1994**, *91*, 1143-1147.

(111)   Ferdig, M. T.; Cooper, R. A.; Mu, J. B.; Deng, B. B.; Joy, D. A.; Su, X. Z.; Wellems, T. E. *Mol. Microbiol.* **2004**, *52*, 985-997.

(112)   Slater, A. F. G.; Cerami, A. *Nature* **1992**, *355*, 167-169.

(113)   Dorn, A.; Stoffel, R.; Matile, H.; Bubendorf, A.; Ridley, R. G. *Nature* **1995**, *374*, 269-271.

(114)   Sullivan, D. J.; Gluzman, I. Y.; Russell, D. G.; Goldberg, D. E. *Proc. Natl. Acad Sci. USA* **1996**, *93*, 11865-11870.

(115)   Sullivan, D. J.; Matile, H.; Ridley, R. G.; Goldberg, D. E. *J. Biol. Chem.* **1998**, *273*, 31103-31107.

(116)   Cohen, S. N.; Phifer, K. O.; Yielding, K. L. *Nature* **1964**, *202*, 805-&.

(117)   Chou, A. C.; Chevli, R.; Fitch, C. D. *Biochem.* **1980**, *19*, 1543-1549.

(118) Egan, T. J. *J. Inorg. Biochem.* **2006**, *100*, 916-926.

(119) Leed, A.; DuBay, K.; Ursos, L. M. B.; Sears, D.; de Dios, A. C.; Roepe, P. D. *Biochem.* **2002**, *41*, 10245-10255.

(120) de Dios, A. C.; Tycko, R.; Ursos, L. M. B.; Roepe, P. D. *J. Phys. Chem. A.* **2003**, *107*, 5821-5825.

(121) de Dios, A. C.; Casabianca, L. B.; Kosar, A.; Roepe, P. D. *Inorg. Chem.* **2004**, *43*, 8078-8084.

(122) Casabianca, L. B.; An, D.; Natarajan, J. K.; Alumasa, J. N.; Roepe, P. D.; Wolf, C.; de Dios, A. C. *Inorg. Chem.* **2008**, *47*, 6077-6081.

(123) Casabianca, L. B.; Kallgren, J. B.; Natarajan, J. K.; Alumasa, J. N.; Roepe, P. D.; Wolf, C.; Dios, A. C. d. *J. Inorg. Biochem.* **2009**, *103*, 745-748.

(124) Warhurst, D. C. *Biochem. Pharmacol.* **1981**, *30*, 3323-3327.

(125) Alumasa, J. N.; Gorka, A. P.; Casablanca, L. B.; Comstock, E.; de Dios, A. C.; Roepe, P. D. *J. Inorg. Biochem.* **2011**, *105*, 467-475.

(126) Asghari-Khiavi, M.; Vongsvivut, J.; Perepichka, I.; Mechler, A.; Wood, B. R.; McNaughton, D.; Bohle, D. S. *J. Inorg. Biochem.* **2011**, *105*, 1662-1669.

(127) Hoard, J. L.; Hamor, M. J.; Hamer, T. A.; Caughey, W. S. *J. Am. Chem. Soc.* **1965**, *87*, 2312-2319.

(128) Lecomte, C.; Chadwick, D. L.; Coppens, P.; Stevens, E. D. *Inorg. Chem.* **1983**, *22*, 2982-2992.

(129) Hatano, K.; Uno, T. *Bull. Chem.Soc. Jpn* **1990**, *63*, 1825-1827.

(130) Johnson, M. R.; Seok, W. K.; Ma, W. P.; Slebodnick, C.; Wilcoxen, K. M.; Ibers, J. A. *J. Org. Chem.* **1996**, *61*, 3298-3303.

(131) Einstein, F. W. B.; Willis, A. C. *Inorg. Chem.* **1978**, *17*, 3040-3045.

(132) Gans, P.; Buisson, G.; Duee, E.; Regnard, J. R.; Marchon, J. C. *J. Chem. Soc. Chem. Commun.* **1979**, 393-395.

(133) Kappe, S. H. I.; Vaughan, A. M.; Boddey, J. A.; Cowman, A. F. *Science*, *328*, 862-866.

(134) Ncokazi, K. K.; Egan, T. J. *Anal. Biochem.* **2005**, *338*, 306-319.

(135) Marques, H. M.; Munro, O. Q.; Crawcour, M. L. *Inorg. Chim. Acta* **1992**, *196*, 221-229.

(136) Parapini, S.; Basilico, N.; Pasini, E.; Egan, T. J.; Olliaro, P.; Taramelli, D.; Monti, D. *Exp Parasitol* **2000**, *96*, 249-256.

(137) Chong, C. R.; Sullivan, D. J., Jr. *Biochem. Pharmacol.* **2003**, *66*, 2201-2212.

(138) Geochemical Instrumentation and Analysis;http://serc.carleton.edu/research_ education/geochemsheets/techniques/SXD.html, accessed on 07-201

(139) Jauncey, G. E. M. Proc. Natl. Acad Sci USA. **1924**, *10(2)*, 57-60.

(140) Electron Microscopy; http://www.microscopy.ethz.ch/bragg.htm, accessed on 07-2013

(141) Bruker; Bruker AXS Inc.: Madison, Winsconsin, USA, **2009**.

(142) Sheldrick, G. M. Göttingen, Germany, **1997**.

(143) Barbour, L. J. *J. Supramol. Chem.* **2001**, *1*, 189-191.

(144) POV-RAY; Persistence of Vision Raytracer Pty. Ltd.: **2003-2008**.

(145) Farrugia, L. J. *J. Appl. Cryst.* **1999**, 837-838.

(146) Van der Sluis, P.; Spek, A. L. *Acta Crystallogr., Sect. A* **1990**, *46*, 194-201.

(147) Skoog, D. A.; West, D. M.; Holler, F. J.; Crouch, S. R. *Fundametnals of Analytical Chemistry*; Thomson Brooks/Cole, **2004**.

(148) ATR-IR;http://www.nuance.northwestern.edu/KeckII/Instruments/FTIR/keckii%20 pages1. html, accessed on 06-2013

(149) Modern Chemical Tachniques; http://media.rsc.org., accessed on 05-2013

(150) Giovannetti, R. *The Use of Spectrophotometry UV-Vis for the Study of Porphyrins, Macro To Nano Spectroscopy*; InTech, **2012**.

(151) Wood, B. R.; McNaughton, D. *Expert Rev. Proteomics* **2006**, *3*, 525-544.

(152) Gouterman, M. *J. Chem. Phys.* **1959**, *30*, 1139-1161.

(153) Gouterman, M. *J. Mol. Spectroscopy* **1961**, *6*, 138-163.

(154) Marcelli, A.; Badovinac, I. J.; Orlic, N.; Salvi, P. R.; Gellini, C. *Photochem. Photobiol. Sci.* **2013**, *12*, 348-355.

(155) Egan, T. J.; Ncokazi, K. K. *J. Inorg. Biochem.* **2004**, *98*, 144-152.

(156) Australian Synchrotron; www.synchrotron.org.au, **2013**

(157) Newville, M. *Fundamentals of XAFS* Revision 1.7 July 23, **2004**.

(158) Levina, A.; Armstrong, R. S.; Lay, P. A. *Coord. Chem. Rev.* **2005**, *249*, 141-160.

(159) Average Program; http://anbf2.kek.jp

(160) Ravel, B.; Newville, M. *J. Synchrotron Radiat.* **2005**, *12*, 537-541.

(161) Ravel, B.; Newville, M. *Phys. Scr.* **2005**, *T115*, 1007-1010.

(162) Walczak, M. S.; Lawniczak-Jablonska, K.; Wolska, A.; Sienkiewicz, A.; Suarez, L.; Kosar, A. J.; Bohle, D. S. *J. Physcal Chem. B.* **2010**, *115*, 1145-1150.

(163) Walczak, M. S.; Lawniczak-Jablonska, K.; Wolska, A.; Sikora, M.; Sienkiewicz, A.; Suarez, L.; Kosar, A. J.; Bellemare, M. J.; Bohle, D. S. *J. Phys. Chem. B* **2011**, *115*, 4419-4426.

(164) GraphPad Prism; v 0.3; GraphPad Software, Inc.: San Diego.

(165) Spek, A. L. *J. Appl. Crystallogr.* **2003**, *36*, 7-13.

(166) Endnote; Windows v 4.0; ISI ReasearchSoft: Berkeley.

(167) Stiebler, R.; Hoang, A. N.; Egan, T. J.; Wright, D. W.; Oliveira, M. F. *Plos One* **2010**, *5*.

(168) Flack, H. D. *Acta Crystallogr. Sect. A* **1983**, *39*, 876-881.

(169) Sarma, B.; Reddy, L. S.; Nangia, A. *Cryst. Growth Des.* **2008**, *8*, 4546-4552.

(170) Dassonville-Klimpt, A.; Jonet, A.; Pillon, M.; Mullie, C.; Sonnet, P. *Science against Microbial Pathogens: Communicating Current Research and Technological Advances* Formatex Research Centet, 2011; Vol. 1.

(171) Kyu, H. H.; Fernandez, E. *Bull. World Health Organ.* **2009**, *89*, 896-904.

(172) Constantinidis, I.; Satterlee, J. D. *J. Am. Chem. Soc.* **1988**, *110*, 927-932.

(173) Menger, F. M.; Ladika, M. *J. Am. Chem. Soc.* **1987**, *109*, 3145-3146.

(174) Marques, H. M. *Inorg. Chem.* **1990**, *29*, 1597-1599.

(175) Karle, J. M.; Karle, I. L. *Antimicrob. Agents. Chemother.* **2002**, *46*, 1529-1534.

(176) Skorska, A.; Sliwinski, J.; Oleksyn, B. J. *Bioorg. Med. Chem. Lett.* **2006**, *16*, 850-853.

(177) Pisciotta, J. M.; Sullivan, D. *Parasitol. Int.* **2008**, *57*, 89-96.

(178) Warhurst, D. C. *Curr. Sci.* **2007**, *92*, 1556-1560.

(179) Bohle, D. S.; Kosar, A. D.; Stephens, P. W. *Acta Cryst.* **2002**, *D58*, 1752-1756.

(180) Solomonov, I.; Osipova, M.; Feldman, Y.; Baehtz, C.; Kjaer, K.; Robinson, I. K.; Webster, G. T.; McNaughton, D.; Wood, B. R.; Weissbuch, I.; Leiserowitz, L. *J. Am. Chem. Soc.* **2007**, *129*, 5779-5779.

(181) de Villiers, K. A.; Osipova, M.; Mabotha, T. E.; Solomonov, I.; Feldman, Y.; Kjaer, K.; Wcissbuch, I.; Egan, T. J.; Leiserowitz, L. *Cryst. Growth Des.* **2009**, *9*, 626-632.

(182) Langmuir, I. *J. Am. Chem. Soc.* **1916**, *38*, 221-2295.

(183) Langmuir, I. *J. Am. Chem. Soc.* **1917**, *39*, 1848-1906.

(184) Noland, G. S.; Briones, N.; Sullivan, D. J. *Mol. Biochem. Parasitol.* **2003**, *130*, 91-99.

(185) Nie, B. N.; Stutzman, J.; Xie, A. H. *Biophys. J.* **2005**, *88*, 2833-2847.

(186) Neal, T. J.; Cheng, B. S.; Ma, J. G.; Shelnutt, J. A.; Schulz, C. E.; Scheidt, W. R. *Inorg. Chim. Acta* **1999**, *291*, 49-59.

(187) Shattock, T. R.; Arora, K. K.; Vishweshwar, P.; Zaworotko, M. J. *Cryst. Growth Des.* **2008**, *8*, 4533-4545.

(188) Desiraju, G. R.; Steiner, T. *The Weak Hydrogen Bond In Structural Chemistry and Biology*, Oxford University Press, **2006**.

(189) Bohle, D. S.; Kosar, A. D.; Stephens, P. W. *Can. J. Chem.* **2003**, *81*, 1285-1291.

(190) Egan, T. J. *Drug Des. Rev.-Online* **2004**, *1*, 93-110.

(191) Webster, G. T.; Tilley, L.; Deed, S.; McNaughton, D.; Wood, B. R. *FEBS Letters* **2008**, *582*, 1087-1092.

(192) Ch'ng, J. H.; Kotturi, S. R.; Chong, A.-L.; Lear, M. J.; Tan, K. S. W. *Cell Death Dis.* **2010**, *1*, e26.

(193) Ch'ng, J. H.; Liew, K.; Goh, A. S. P.; Sidhartha, E.; Tan, K. S. W. *Cell Death Dis.* **2011**, *2*, e216.

"If you think you are too small to make a difference,

try sleeping with a mosquito."

-Dalai Lama XIV-